Theoretical study on nonequilibrium transport phenomena induced by biological nanomachines

生体分子マシンが誘起する非平衡輸送現象の理論的研究（英文）

By

Yuto Hosaka

Under the Supervision of

Professor Masahiko Hada

Professor Shigeyuki Komura

A Thesis Submitted in Fulfillment of Requirements for the Degree of Doctor of Philosophy in Science of Tokyo Metropolitan University

TOKYO METROPOLITAN UNIVERSITY

東京都立大学

Department of Chemistry, Faculty of Science

Tokyo Metropolitan University

March 2022

List of Publications

1. K. Yasuda, A. Kobayashi, L.-S. Lin, Y. Hosaka, I. Sou, S. Komura, "The Onsager-Machlup integral for non-reciprocal systems with odd elasticity," J. Phys. Soc. Jpn. **91**, 015001 (2022).

2. Y. Hosaka, S. Komura, and D. Andelman, "Hydrodynamic lift of a two-dimensional liquid domain with odd viscosity," Phys. Rev. E **104**, 064613 (2021).

3. K. Yasuda, Y. Hosaka, I. Sou, and S. Komura, "Odd microswimmer," J. Phys. Soc. Jpn. **90**, 075001 (2021).

4. Y. Hosaka, S. Komura, and D. Andelman "Nonreciprocal response of a two-dimensional fluid with odd viscosity," Phys. Rev. E **103**, 042610 (2021).

5. K. Era, Y. Koyano, Y. Hosaka, K. Yasuda, H. Kitahata, and S. Komura, "Autonomous elastic microswimmer," EPL (Europhysics Letters) **133**, 34001 (2021).

6. Y. Hosaka, S. Komura, and A. S. Mikhailov, "Mechanochemical enzymes and protein machines as hydrodynamic force dipoles: the active dimer model," Soft Matter **16**, 10734-10749 (2020).

7. I. Sou, Y. Hosaka, K. Yasuda, and S. Komura, "Irreversibility and entropy production of a thermally driven micromachine," Physica A **562**, 125277 (2021).

8. Y. Hosaka, S. Komura, and D. Andelman, "Shear viscosity of two-state enzyme solutions," Phys. Rev. E **101**, 012610 (2020).

9. I. Sou, Y. Hosaka, K. Yasuda, and S. Komura, "Nonequilibrium probability flux of a thermally driven micromachine," Phys. Rev. E **100**, 022607 (2019).

10. Y. Ota, Y. Hosaka, K. Yasuda, and S. Komura, "Three-disk microswimmer in a supported fluid membrane," Phys. Rev. E **97**, 052612 (2018).

11. Y. Hosaka, K. Yasuda, I. Sou, R. Okamoto, and S. Komura, "Thermally driven elastic micromachines," J. Phys. Soc. Jpn. **86**, 113801 (2017).

12. K. Yasuda, Y. Hosaka, M. Kuroda, R. Okamoto, and S. Komura, "Elastic three-sphere microswimmer in a viscous fluid," J. Phys. Soc. Jpn. **86**, 093801 (2017).

13. Y. Hosaka, K. Yasuda, R. Okamoto, and S. Komura, "Lateral diffusion induced by active proteins in a biomembrane," Phys. Rev. E **95**, 052407 (2017).

Acknowledgements

I would deeply like to express thankful to my supervisors Prof. Masahiko Hada from Tokyo Metropolitan University and Prof. Shigeyuki Komura from University of Chinese Academy of Sciences (China), for their generous support, advice, foresight, and guidance. I have greatly benefitted from their incredible insight, intuition, and knowledge. I am very thankful to Prof. Masahiko Hada for supervising me during my last year of Ph.D. Especially, Prof. Komura has broadened my horizons not only in physical chemistry but also in general culture, and properly guided me during my Ph.D. studies.

I am very thankful to Prof. Alexander S. Mikhailov from Kanazawa University (Japan) for offering many suggestions in the beginning of my studies, and especially for his hospitality during my visit to Berlin and being a guide for a beginner in biophysics. It was my pleasure to have worked with Prof. David Andelman and to have visited his group in Tel Aviv University. David's generous hospitality made my visits to Israel a highlight of my Ph.D. studies. I am very thankful to David for teaching me the importance of independence in studies and for his vast knowledge on soft matter theory.

My work has benefited greatly from discussions with Prof. Tadashi Kato, Prof. Naoki Nakatani, Dr. Yohei Kawabata, and Dr. Takuma Hoshino from Tokyo Metropolitan University. During my Ph.D. studies, I have worked jointly with several students and colleagues. I would like to thank Prof. Hiroyuki Kitahata from Chiba University (Japan), Dr. Yuki Koyano from Kobe University (Japan), Dr. Ryuichi Okamoto from Okayama University (Japan), Dr. Isamu

Sou from Tokyo Metropolitan University, Dr. Kento Yasuda from Kyoto University (Japan), Yui Ota, and Katsutomo Era for our collaborations.

I would like to express my deepest gratitude to my parents and partner for their endless support and for their genuine interest in what I study.

Support from JSPS Research Fellowships for Young Scientists (Grant No. 19J20271, 2019-2022), Graduate Students Participation in International Academic Conferences Financial Support Program from Tokyo Metropolitan University (2019), and Bilateral Student Exchange Program between Tokyo Metropolitan University and Tel Aviv University (2019) is gratefully acknowledged.

Contents

Chapter 1

General Background

1.1 Physical chemistry of biological matter

1.1.1 Biological nanomachines

Biological nanomachines are nanometer-size proteins that catalyze chemical reactions in the presence of substrate molecules, e.g., adenosine triphosphate (ATP) [1.1]. During chemical reactions, nanomachines or motor proteins change their shapes to generate forces to surrounding environments such as the cytoplasm or biological membranes. For example, the myosin proteins are responsible for muscle contraction by generating directional movement along actin filaments, while kinesins and dyneins that walk along microtubules are important for vesicle trafficking (see Fig. 1.1 for the schematic illustration of a dynein). In addition to these translational motors that are responsible for motile processes in a biological cell [1.2], there are rotor proteins called ATP synthase or F_0F_1 ATPase that exhibits rotational motions to allow proteins or other materials to pass through the membrane (Fig. 1.2). These rotary enzymes are classified as membrane proteins because they are embedded in biological membranes to be responsible for various life-sustaining processes [1.2].

One of the characters of these motor proteins is that they consume chemical energy in order to deliver mechanical work such as unidirectional movements.

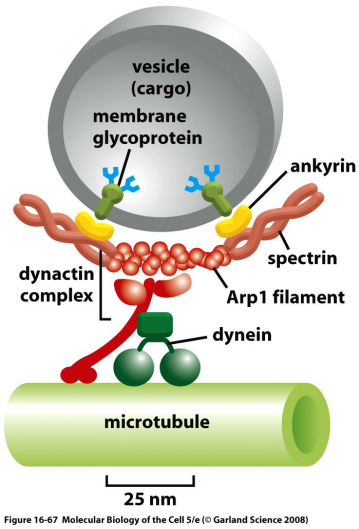

Figure 1.1: Dynein motor is a large macromolecular assembly that plays a role in organelle transport along microtubule. Adapted from Ref. [1.1].

Each mechanical step is related to free energy of ATP hydrolysis ΔE and one can roughly estimate the force f exerted by a motor protein as [1.2]

$$f = \frac{\Delta E}{\ell} \approx \frac{20\ k_{\mathrm{B}}T}{8\ \mathrm{nm}} \approx 10\ \mathrm{pN}, \tag{1.1}$$

where $\ell = 8$ nm is the typical distance traveled by a kinesin motor and $k_{\mathrm{B}}T \approx 4$ pN with k_{B} and T being the Boltzmann constant and the temperature, respectively. Furthermore, by assuming that motor proteins or enzymes consist of an elastic spring, one can estimate motor's elastic constant k and characteristic relaxation timescale τ as

$$k = \frac{f}{a} \approx \frac{10\ \mathrm{pN}}{10\ \mathrm{nm}} \approx 10^{-3}\ \mathrm{N/m}, \qquad \tau = \frac{\zeta}{k} \approx \frac{10^{-7}\ \mathrm{N \cdot s/m}}{10^{-3}\ \mathrm{N/m}} \approx 10^{-4}\ \mathrm{s}, \tag{1.2}$$

respectively. Here, we have chosen the protein size as $a \approx 10$ nm and the friction coefficient of a motor as $\zeta = 10^{-7}$ N·s/m. These estimates give characteristic physical quantities for motor proteins at the small scales.

Since their mechanical work are allowed by attaching themselves to some biological structures such as filaments or membranes, as shown in Figs. 1.1 and 1.2, motile behavior was not reported for enzymatic molecules that are freely dispersed in aqueous solutions or cytoplasm and are not attached to surround-

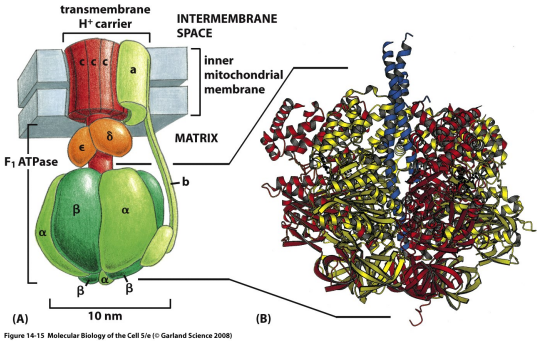

Figure 1.2: (Left) F_0F_1 ATPase bounded in biological membranes, which rotates in the presence of the hydrogen ion gradient and drives the chemical synthesis of ATP from ADP. Adapted from Ref. [1.1]. (Right) The three-dimensional (3D) structure of the F_1 ATPase, determined by x-ray crystallography. Adapted from Ref. [1.1].

ing structures. However, it has been experimentally shown that enzymes also exhibit mechanical motions and their dependency on substrate concentrations or theoretical modelings have attracted much attention.

1.1.2 Biocatalysis by enzymatic molecules

Enzymes are functional macromolecular proteins, each of which consists of amino acids in a particular sequence [1.1]. The assembly of amino acids folds into a precise 3D conformation with reactive sites on its surface [see Fig. 1.3(Left) for lysozyme] [1.1]. Therefore, these amino acids polymers bind with high specificity to other molecules, and act as enzymes catalyzing chemical processes that make or break covalent bonds of other molecules, as schematically illustrated in Fig. 1.3(Right) [1.1]. Moreover, these proteins play other roles such as maintaining structures, generating movements, and sensing signals, which are essential for cellular metabolism and homeostasis [1.1, 1.2].

To exhibit specific functions in cells, the shapes of most biological macromolecules are highly constrained [1.1]. In principle, however, most of the covalent bonds in a macromolecule allow rotation of atoms, and gives the polymer chain great flexibility. This allows a macromolecule to adopt an almost unlimited number of conformations caused by random thermal motions of surrounding en-

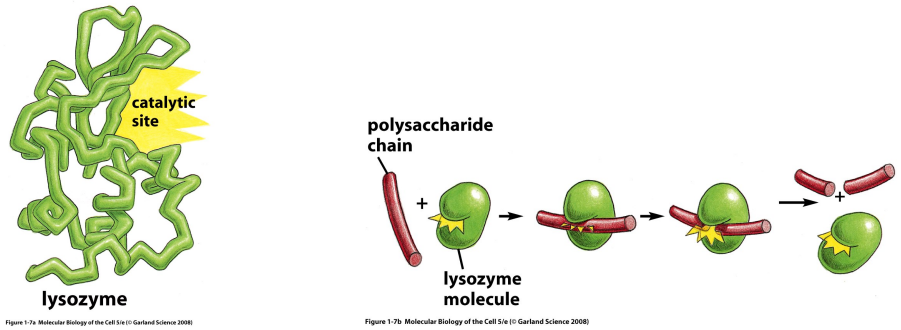

Figure 1.3: (Left) The enzyme lysozyme having a 3D conformation with the catalytic site on its surface. Adapted from Ref. [1.1]. (Right) Lysozyme molecule breaks a covalent bond of polysaccharide chain in the catalytic cycle. Adapted from Ref. [1.1].

vironments. [1.1]. In fact, macromolecules can fold tightly into highly preferred conformations because of many weak noncovalent bonds that form between different parts of the same molecule [1.1].

The four types of noncovalent interactions (hydrogen bonds, van der Waals attractions, hydrophobic forces, and electrostatic attractions) are essential for biological molecules. Although the strength of these noncovalent bonds is 20 times weaker than that of a covalent bond, they provide tight binding once many of such weak interactions are formed simultaneously [1.1]. In addition, they can also add up to create a strong attraction between two different molecules when these molecules fit together very closely [1.1]. Since the strength of the binding depends on the number of noncovalent bonds that are formed between molecules, interactions of almost any affinity are possible [1.1]. This allows rapid dissociation of a molecule, which drives catalytic chemical cycles followed by the dissociation of product molecules [1.1, 1.2].

Recent advances in fluorescence microscopy have allowed studies of single molecules observation. In 1988, Lu *et al.* investigated enzymatic turnovers of single cholesterol oxidase molecules in real time by monitoring the emission from the enzymes fluorescent active site [1.3]. Moreover, they derived the waiting time distribution of the enzymes, and showed that the obtained distribution agrees well with that derived from real-time trajectories of enzymes (see Fig. 1.4).

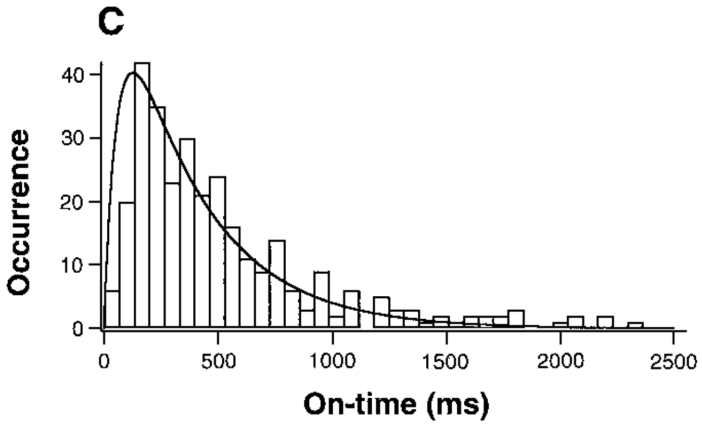

Figure 1.4: The histogram of occurrence as a function of on-time, which corresponds to the waiting time for the reduction of cholesterol oxidases' active sites. The solid line denotes the waiting time distribution derived from the single enzyme kinetics. Adapted from Ref. [1.3].

Later, it was shown that the reaction velocity for single-enzyme observations coincides with that for ensemble-enzyme observations as long as the factor of the total concentration of enzymes are neglected [1.4, 1.5]. This relation originates from the equivalence between the average over the long time trace of a single molecule and that over a large ensemble of identical molecules.

1.1.3 Conformational dynamics during chemical reactions

Motor proteins such as myosin and kinesin undergo unidirectional motion that is responsible for autonomously contracting muscles and the transport of materials within cells [1.1]. By catalyzing ATP hydrolysis, they achieve sufficient energy to exhibit the motile behavior. On the other hand, most of enzymes do not exhibit such behavior although both motor proteins and enzymes catalyze chemical reactions. In particular, enzymes exhibit a distinctive type of dynamics, i.e., conformational change, which is generally induced by substrate binding and product release [1.6]. Then, it follows that enzymes undergo a conformational change in each turnover cycle of the chemical reactions in the presence of substrate molecules.

These conformational dynamics have been taken into account to mimic actual

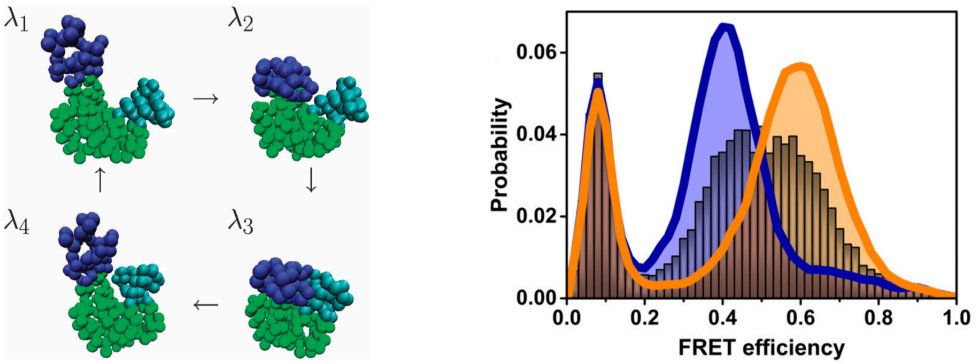

Figure 1.5: (Left) Conformational changes of the coarse-grained enzyme, adenylate kinase, from the fully open (λ_1) to fully closed (λ_3) conformations in the sequential binding mechanism. Adapted from Ref. [1.7]. (Right) FRET efficiency histograms of adenylate kinase in the absence of substrate (blue) and in the presence of saturating substrate concentrations (1 mM ATP, 1 mM AMP, and 160 μM ADP, orange), suggesting mostly open and closed conformations, respectively. Adapted from Ref. [1.8].

enzymes in a framework of the elastic network model. Togashi *et al.* analyzed nonlinear conformational relaxation dynamics of proteins in elastic networks, and found that motions of these proteins are robust against external perturbations [1.9]. Also, they constructed an example of an artificial elastic network, operating as a cyclic machine powered by substrate binding with the use of evolutionary optimization methods. Later, Echeverria *et al.* presented a multiscale coarse-grained description of protein conformational dynamics in a solvent, which is described by multiparticle collision dynamics [see Fig. 1.5(Left)] [1.7]. They found that hydrodynamic interactions have important effects on the large scale conformational motions of the protein, and significantly affect the translational diffusion coefficients and orientational correlation times [1.7].

Recently, using direct observation techniques Aviram *et al.* studied the relationship between conformational dynamics and the chemical steps of enzymes [1.8]. They labelled adenylate kinase, which is responsible for cellar energy homeostasis, from *E. coil* with FRET dyes at positions of CORE and LID domains, and derived open and closed conformations of the enzyme from histograms of FRET efficiency [1.8]. The obtained histograms show a peak FRET efficiency value of

0.4 in the absence of substrates, while the peak shifts to at 0.6 in the saturating concentrations of ATP, as shown in Fig. 1.5(Right) [1.8]. By comparing these conformational dynamics and chemical steps, they found that substrate binding increases dramatically domain closing and opening times, which are 100-200 times faster than the enzymatic turnover rate [1.8].

ATP synthase or F_0F_1 ATPase is composed of two different rotary motors (F_0 and F_1) connected to a shaft (Fig. 1.2) and shows another type of the conformational change, i.e., rotational motion [1.2]. The F_0 motor uses the gradient of hydrogen ions to rotate, while the F_1 motor uses APT hydrolysis to rotate in the opposite direction of F_0 [1.2]. When the transmembrane electrochemical gradient is strong, F_0 generates more torque than F_1 and, so that F_1 rotate in reverse to synthesize ATP [1.2]. When the electrochemical gradient is weak, on the other hand, the torque that F_1 generates dominates over that of F_0 and the APT hydrolysis occurs, which pump hydrogen ions out of the cell [1.2]. These different mechanisms for rotation are summarized in Fig. 1.6 [1.1]. By direct observation of the motion of F_1, Noji *et al.* showed that the motor rotates in distinct steps of 120° and the induced torque is the order of 10 pN·nm [1.1, 1.10]. Given the nanometer-size rotary motor, one can see that the observed torque is comparable to the force exerted by a motor protein, which is estimated in Eq. (1.1).

1.1.4 Diffusion enhancement in enzyme solutions

To explicitly focus on enzyme-driven phenomena, diffusion in enzyme solutions has been experimentally studied in recent years [1.11–1.17]. Muddana *et al.* first reported the enhanced diffusion of enzyme urease in the presence of substrate urea (Fig. 1.7) [1.11]. Later, it was shown that enzymes exhibit collective motions towards the direction of higher or lower concentrations of substrates, i.e., chemotaxis and antichemotaxis, respectively [1.12, 1.16, 1.18].

It was also claimed that the enhanced diffusion have been observed even during catalysis at the Ångstöm scale, which is much smaller than a system of

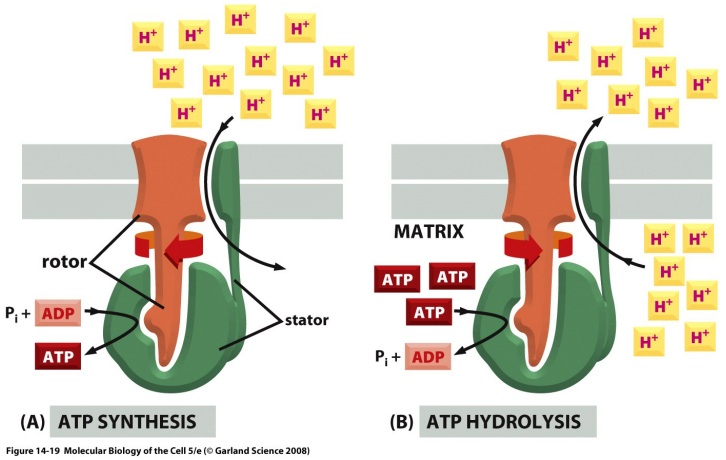

Figure 1.6: The ATP synthase can either (A) synthesize ATP by harnessing the gradient of proton ions or (B) pump proton ions against their electrochemical gradient by hydrolyzing ATP. Adapted from Ref. [1.1].

molecular enzymes [1.17, 1.18]. Since the used catalyst shows less conformational dynamics due to its rigidity compared with that of molecular proteins, a different mechanism, such as transfer of momentum from the active catalyst molecules, was proposed to account for the enhanced diffusion. Moreover, it was also reported that enhanced diffusion in molecular-scale systems was due to a convection artifact [1.19], and enhancement in diffusivity is still a matter of debate [1.20].

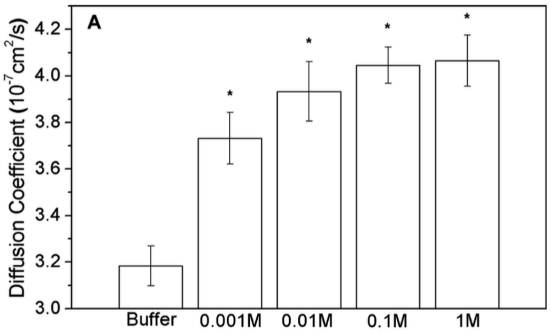

Figure 1.7: The diffusion coefficient of urease increased with the increasing substrate concentration. Adapted from Ref. [1.11].

To identify the mechanism of the observed enhanced diffusion and chemotactic phenomena, several people have suggested theories that account for the roles

of heat or hydrodynamic interaction caused by enzymes [1.21–1.24]. Mikhailov *et al.* discussed the collective hydrodynamic flows induced by active force dipoles, and analytically derived the diffusion enhancement of a tracer particle, which depends linearly on the activity of enzymes [1.21, 1.22]. Then, Golestanian proposed four mechanisms for the enhanced diffusion of enzymes, namely self-thermophoresis, boost in kinetic energy, stochastic swimming, and collective heating, and concluded that only the last two descriptions can account for the phenomenon [1.23]. Later, Illien *et al.* took into account the hydrodynamic effects induced by conformational changes of enzymatic domains, and demonstrated that a single enzyme can diffuse faster even at equilibrium [1.24]. However, a recent experiment pointed out the difficulty to quantitatively account for the observed enhanced diffusion within the suggested theoretical approaches [1.25].

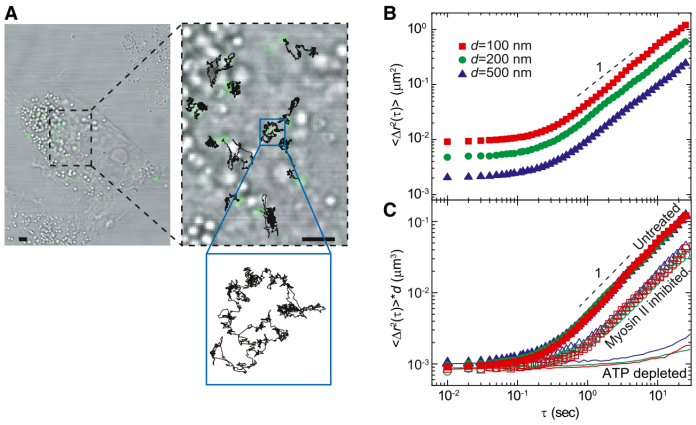

Figure 1.8: (A) Bright-field image of an A7 cell with microinjected 200-nm-diameter fluorescence particles (green) and 2 min trajectories (black) superimposed on top. Scale bar, 5 μm. (B) Two-dimensional ensemble-averaged mean-square displacement of tracer particles of various sizes are plotted against lag time on a log-log scale, in living A7 cells. Red, green, and blue symbols and lines represent particles that are 100, 200, and 500 nm in diameter, respectively. (C) Ensemble-averaged mean-square displacement scaled with particle diameter, in untreated (solid symbols), blebbistatin treated (open symbols), and ATP-depleted (solid lines) A7 cells. Adapted from Ref. [1.26].

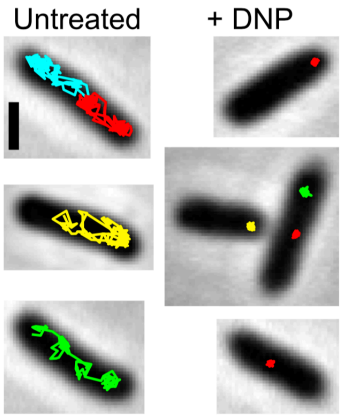

Figure 1.9: 2D trajectories of GFP-LacI-labeled mini-RK2 plasmids overlaid on corresponding phase-contrast images of metabolically active and DNP-treated *E. coli* cells (JP924). Scale bar is 1 μm. Adapted from Ref. [1.27].

1.2 Nonequilibrium phenomena in living systems

1.2.1 Active transport in biological cells

In recent years, to better understand nonequilibrium phenomena in biological cells, the diffusive properties of tracer particles *in vivo* have been experimentally studied [1.26, 1.27]. Guo *et al.* microinjected submicron colloidal particles into A7 melanoma cells, and measured their time-dependent motion to calculate ensemble-averaged mean-square displacement (Figs. 1.8A and 1.8B) [1.26]. In Fig. 1.8B, the mean-square displacement shows constant behavior at small timescales, whereas at large timescales the quantity increases approximately linearly with time [1.26]. Although this linearly increasing behavior is consistent with Brownian motion in a purely viscous liquid and at thermal equilibrium, these ideas can not be applied to the cytoplasm [1.26]. They also observed the mean-square displacement in cells whose activity is inhibited, and found no change of the displacement compared to that in active cells at small timescales as shown in Fig. 1.8C [1.26]. At large timescales, on the other hand, the quantity exhibits increasing and nearly time-independent behaviors when myosin is inhib-

ited and ATP is depleted, respectively [1.26]. These results suggest that not only motor proteins but also ATP-driven proteins such as enzymes play important roles in the motion of particles in cells. Parry *et al.* performed similar experimental studies in the bacterial cytoplasm, and observed the enhanced diffusion of plasmids in untreated cells, which is termed anomalous diffusion compared with the Brownian diffusion due to thermal motions of solvent molecules (see Fig. 1.9) [1.27].

These experimental findings demonstrate that passive particles diffuse faster when cells function properly in the presence of substrate molecules, and imply that nonequilibrium fluctuations driven by energy supplied to cells contribute to nonthermal diffusion. At the same time, ATP-dependent diffusion observed in the cytoplasm suggests that enzymes that catalyze chemical reactions using substrate molecules also have some contribution to the anomalous diffusion. However, due to the complexity of cellular environments, which contain structures and materials such as cytoskeletons and viscoelastic media, the mechanism of anomalous diffusion has not yet been definitively identified.

1.2.2 Rheology of sub- and multicellular systems

Biomolecular machines exhibit mechanical motions in fluid environments such as cytoplasm or biological membranes, and the physical properties of the fluid with these active constituents are important for biomolecular transports and chemical reactions [1.28]. Hence, the effect of enzymatic activity on rheological properties of such active fluids has gathered much attention in recent years.

Before proceeding to reviewing some experimental findings in this field, we first review the concept of the rheological properties of ordinary passive fluids. In general, the rheological properties of fluids are characterized by the fourth-rank viscosity tensor $\eta_{ijk\ell}$ that connects the linear relation between the strain

rate tensor $v_{ij} = (\partial_i v_j + \partial_j v_i)/2$ and the fluid stress tensor σ_{ij} [1.29]:

$$\sigma_{ij} = \eta_{ijk\ell} v_{k\ell}, \tag{1.3}$$

where the indices $i, j, k, \ell = x, y, z$ and we assume summation over repeated indices throughout this chapter. In the above, $\mathbf{v}$ is the fluid velocity field and the viscosity tensor for a 3D isotropic fluid is given by [1.29]

$$\eta_{ijk\ell} = \eta_{\rm d}\delta_{ij}\delta_{k\ell} + \eta_{\rm s}\left(\delta_{ik}\delta_{j\ell} + \delta_{i\ell}\delta_{jk} - \frac{2}{3}\delta_{ij}\delta_{k\ell}\right), \tag{1.4}$$

where δ_{ij} is the Kronecker delta and $\eta_{\rm d}$ and $\eta_{\rm s}$ are the dilatational and shear viscosities, respectively. Experimentally, the viscosity is measured through the autocorrelation functions of the viscous stress σ_{xy} on the basis of the linear response theory

$$\eta_{\rm s} = \frac{1}{k_{\rm B}TV}\int_0^\infty dt\, \langle \sigma_{xy}(t)\sigma_{xy}(0)\rangle, \tag{1.5}$$

where V is the volume and $\langle \cdots \rangle$ denotes the average over the steady-state ensemble of trajectories. For a passive fluid, its viscosities can be modified, e.g., by the density of immersed particle, the system temperature, or applied shear forces [1.28]. On the other hand, these rheological properties can be modified by other contributions for the cytoplasm or biological membranes where metabolic activities are present and the systems are strongly driven out of equilibrium.

Nishizawa *et al.* experimentally studied the shear viscosity of cytoplasm for various concentrations of macromolecules [1.30]. The viscosity of cell extracts without metabolic activation rapidly increased with the macromolecule concentration, which shows diverging viscosity at critical concentrations $c^* \sim$ 0.34 g/mL, as shown in Fig. 1.10 [1.30]. The concentrations are close to the physiological concentration in living cells ($\sim$ 0.3 g/mL) [1.30]. On the other hand, metabolically active living cells showed moderate fluidity [1.30]. These experimental findings suggest that metabolic activities are important for finite fluidity that facilitates the efficient transport of molecules in living cells [1.30].

In more macroscopic scales, the shear viscosity of bacterial suspensions have

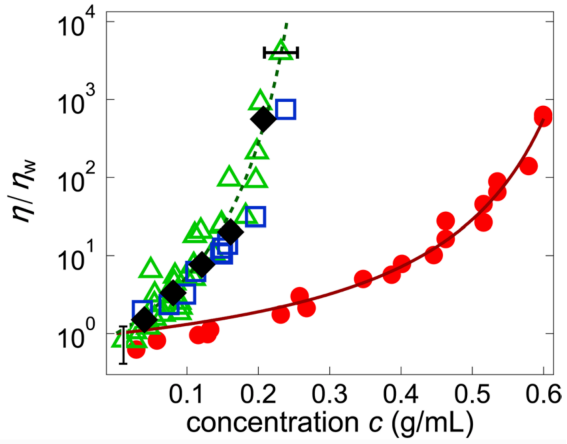

Figure 1.10: The effective viscosity η of BSA solutions (red circles) and cell extracts (green triangles: *E. coli*, blue squares: Xenopus eggs, and black diamonds: HeLa cells) as a function of the macromolecules concentration c. The viscosity η is rescaled by the water viscosity η_w. Adapted from Ref. [1.30].

been studied [1.28, 1.31, 1.32]. Rafaï *et al.* performed experiments on the rheology of suspensions of live cells, *Chlamydomonas Reinhardtii* and revealed that the obtained viscosity was greater than for suspensions with the same volume fraction of dead cells [1.32]. Later, López *et al.* investigated the response of an *E. coli* suspension under the shear flow and showed that the suspension viscosity decreases with the increasing bacterial density at low shear rate [1.31]. These experimental findings suggest that active constituents that convert chemical energy into mechanical work contribute to rheological signatures dependent of their internal activity [1.28]. Although such active macroscopic properties are expected to exist also in enzymatic solutions, much less work has been done in such systems.

1.2.3 Emergent macroscopic patterns in active chiral systems

In addition to the above peculiar rheological properties, the emergent macroscopic patterns have been investigated in active fluids [1.33–1.36]. Experimentally, such active systems have been realized in nanoscale molecular motors [1.33, 1.35] or multicellular biological systems [1.34, 1.36]. Sumino *et al.* investigated

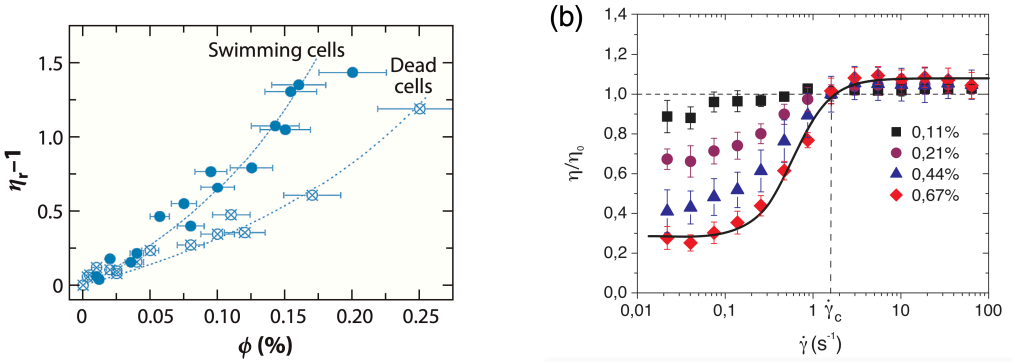

Figure 1.11: (Left) Effective viscosity of live (solid) and dead (crossed) *Chlamydomonas Reinhardtii* suspensions as a function of the volume fraction ϕ. Adapted from Ref. [1.28]. (Right) Effective viscosity of *E. coli* suspensions as a function of the applied shear rate $\dot{\gamma}$ for various values of the volume fraction ϕ. Adapted from Ref. [1.31].

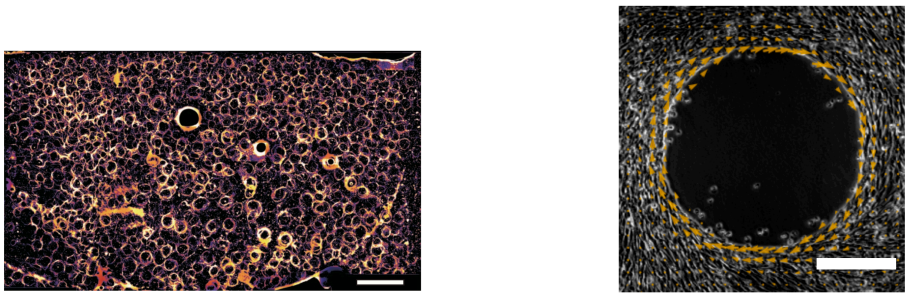

Figure 1.12: (Left) Large-scale lattice of vortices. Vortices can be observed everywhere on the surface of the flow cell. Scale bar is 2 mm. Adapted from Ref. [1.33]. (Right) Phase contrast image with the circular flow observed at the edges of open circles (500 μm diameter) of neural progenitor cell culture. Orange arrows are proportional to the velocity of cell flow calculated by averaging the cell displacements within 30 μm square regions. Scale bar is 200 μm. Adapted from Ref. [1.34].

the behavior of microtubules that are propelled by surface-bound dyneins and observed that self-organization of the microtubules due to the alignment mechanism results in vortices at high densities [Fig. 1.12(Left)] [1.33]. In addition, a spatiotemporal pattern was found in the monolayer of synthetic molecular motors [1.35]. For larger scales such as multicellular systems, edge flows were observed at the boundary of active nematic cells [Fig. 1.12(Right)] [1.34]. In the bacterial suspensions, Beppu *et al.* showed that edge currents grow stronger as the increasing bacterial density [1.36].

The common feature of these emergent chiral patterns is that the parity symmetry is broken due to the collective effect of motor proteins [1.33], the chiral structure of molecules [1.35], or the surrounding geometries [1.34, 1.36]. Moreover, these active constituents continuously consume energy and hence the time-reversal symmetry is apparently broken. Since both the time-reversal and parity symmetries are violated in these biological environments, they are called active chiral systems and in particular, active chiral fluids within the hydrodynamic description [1.37]. In these out-of-equilibrium systems, the equilibrium concept such as free energy, detailed balance, and time-reversal symmetry are invalidated [1.38] and new physical quantities that characterize the systems are necessary.

1.3 Coarse-grained modeling of biological nanomachines

1.3.1 Continuum hydrodynamic description

For the passive case without activity, the disturbance flow arises only when an external force or flow field is imposed on a fluid [1.28]. For the active case, however, the disturbance flow is indued even in a quiescent fluid because of the mechanical work driven by motor proteins or enzymatic molecules. Over the length scale of molecular proteins where the inertial effect is negligible, the hydrodynamic behavior is governed by the well-known Stokes equation

$$-\nabla p(\mathbf{r}) + \eta_{\mathrm{s}} \nabla^2 \mathbf{v}(\mathbf{r}) + \mathbf{F}(\mathbf{r}) = 0, \tag{1.6}$$

and the incompressibility condition

$$\nabla \cdot \mathbf{v}(\mathbf{r}) = 0, \tag{1.7}$$

with the 3D differential operator $\nabla = (\partial_x, \partial_y, \partial_z)$ and the position $\mathbf{r} = (x, y, z)$. In the above, p is the hydrostatic pressure, η_{s} is the shear viscosity, $\mathbf{v}$ is the fluid velocity field, and $\mathbf{F}$ is any other arbitrary force density on the fluid.

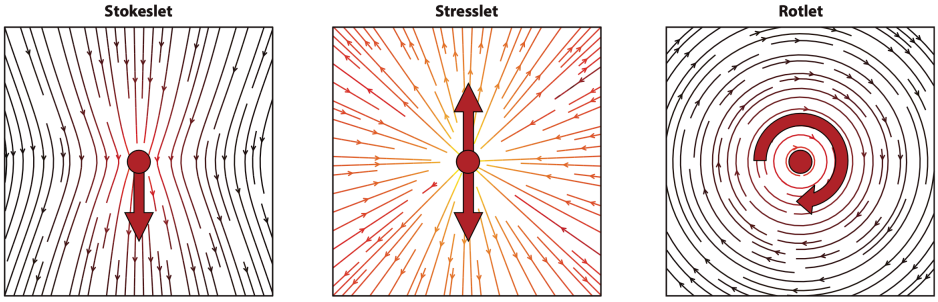

Figure 1.13: Streamlines induced by (left) Stokeslet for $n = 0$ and (middle) stresslet and (right) rotlet for $n = 1$ in Stokes flows. Adapted from Ref. [1.28].

In this Stokes regime, the disturbance flow at the position $\mathbf{r}$ induce by $\mathbf{F}$ at $\mathbf{r}_0$ is expressed as $v_i(\mathbf{r}) = -\int_{\partial V} dA\, G_{ij}\left(\mathbf{r}-\mathbf{r}_0\right) F_j\left(\mathbf{r}_0\right)$, where the Green's function or the propagator for a 3D unbounded fluid, namely the Oseen tensor is [1.39]

$$G_{ij}(\mathbf{r}) = \frac{1}{8\pi\eta_s r}\left(\delta_{ij} + \frac{r_i r_j}{r^2}\right), \tag{1.8}$$

with $r = |\mathbf{r}|$. If the position of the point $\mathbf{r}$ is far from that of $\mathbf{F}$, a Taylor expansion of the Green's function provides a far-field representation of the flow in terms of multipole moments $\mathbf{M}^{(n)}$ of the tractions and velocities, which drive a superposition of singular flows expressed in terms of $\mathbf{G}$ and its derivatives [1.28, 1.40]:

$$v_i(\mathbf{r}) \approx \sum_{n=0}^{\infty} \partial_k^{(n)} G_{ij}(\mathbf{r}) M_{jk}^{(n)}. \tag{1.9}$$

Figure 1.13 represents the streamlines that are induced by the Stokeslet $\mathbf{M}^{(0)} = \mathbf{F}$ when $n = 0$ and the symmetric (stresslet, $\mathbf{S}$) and antisymmetric (rotlet, $\mathbf{L}$) parts of $\mathbf{M}^{(1)}$ when $n = 1$.

In a biological context, no force and torque act on nanomachines as they function autonomously in the presence of chemical energy, requiring the condition $\mathbf{F} = \mathbf{L} = 0$ to hold in general. Hence, the stresslet $\mathbf{S}$ and the torque dipole $\mathbf{M}^{(2)}$ have been used to model enzymatic molecules [1.21, 1.22] and rotary proteins [1.41, 1.42], respectively, as will be discussed in more detail later. For biological membranes, moreover, one has to derive the mobility tensor for free [1.43, 1.44], confined [1.45], or curved [1.46] geometries of a 2D fluid, which

requires the revisiting the 2D version of Eq. (6.4) [1.47–1.49].

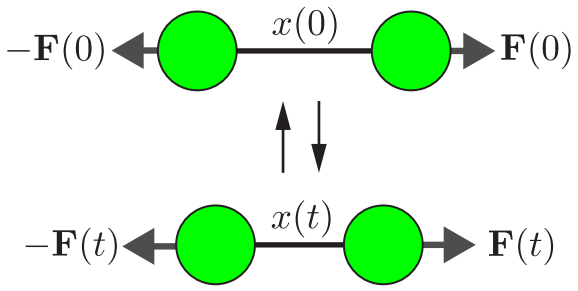

Figure 1.14: The active force dipole for a molecular enzyme that undergoes the conformational change cyclically in the presence of substrate molecules. In the model, the time-dependent distance and the force of the enzyme are $x(t)$ and $\mathbf{F}(t)$, respectively.

1.3.2 Active force dipole model

In this section, we shall present more detailed descriptions of the active force dipole model that was originally proposed by Mikhailov and Kapral [1.21, 1.22]. As explained in Sec. 1.1, each actual enzyme has a specific 3D conformation that depends on its biological function and surrounding environments such as the cytoplasm and biological membranes. At large scales, however, any enzyme can be regarded as an active force dipole as shown in Fig. 1.14. The active force dipole consists of two domains, representing enzymatic domains, connected with a shaft, and its length cyclically varies in time to mimic the conformational dynamics of enzymes during chemical reactions.

Since a dipole exerts the time-dependent force, $\mathbf{F}(t)$, in its axis direction, the dipole induces the hydrodynamic flow in surrounding environments. If the force dipole is immersed in a 3D fluid, the generated flow field can be calculated from Eq. (1.9) when $n = 1$:

$$v_i(\mathbf{r}) = -F(t)x(t)\hat{x}_k\partial_k G_{ij}(\mathbf{r})\hat{x}_j, \tag{1.10}$$

where $\mathbf{F}(t) = F(t)\hat{\mathbf{x}}$ with $\hat{\mathbf{x}}$ being a unit vector in the direction of the enzyme axis. In a context of self-propelled microswimmers, $F > 0$ ($F < 0$) denotes a pusher (puller) type of a micromachine. The resultant flow is the stresslest that is plotted in Fig. 1.13. When multipole dipoles are immersed in fluids, they

induce collective hydrodynamic flows in their surroundings, which can lead to nonthermal fluctuations in the system. Considering these hydrodynamic effects, Mikhailov *et al.* derived the diffusion coefficient of a passive tracer in a solution where dipoles are homogeneously distributed in space and the directions of their long axes are randomly distributed. Moreover, when the concentration gradient of dipoles are present, the tracer exhibits chemotaxis, which was observed in experiments [1.12]. Later, Koyano *et al.* discussed the situation where dipoles are aligned and concentrated in a liquid domain that corresponds to lipid rafts in biological membranes [1.50].

The hydrodynamic interactions and clustering mechanisms of active force dipoles were also investigated in flat [1.51] or curved [1.52] biological membranes. Manikantan examined the phase behavior of a pair of hydrodynamically interacting force dipoles and showed that bulk confinement plays a striking role in clustering of dipoles [1.51]. Moreover, it was demonstrated that multiple dipoles exhibit the collective dynamics that can be tuned by the confinement on the membrane [1.51]. In a curved geometry, aggregation effects of dipoles were confirmed in regimes of both low and high curvatures [1.52]. One of the features of 2D fluid membrane geometries is that they have hydrodynamic screening lengths that make the short distance hydrodynamic behavior significantly different from the long one [1.43–1.45].

1.3.3 Fluctuation-induced hydrodynamic coupling

So far, the hydrodynamic flow induced by a single or multiple enzymes have been discussed in terms of the active force dipole model [1.21, 1.22]. Next, we review some of the theories that account for the internal hydrodynamics between the domains of a single enzyme [1.24, 1.53–1.55]. Since an actual macromolecular enzyme is asymmetric in general, its internal degrees of freedom are coupled to its center of mass diffusion, which would give rise to the change in the diffusion coefficient [1.54].

Considering the effect of conformational fluctuations of an asymmetric dumb-

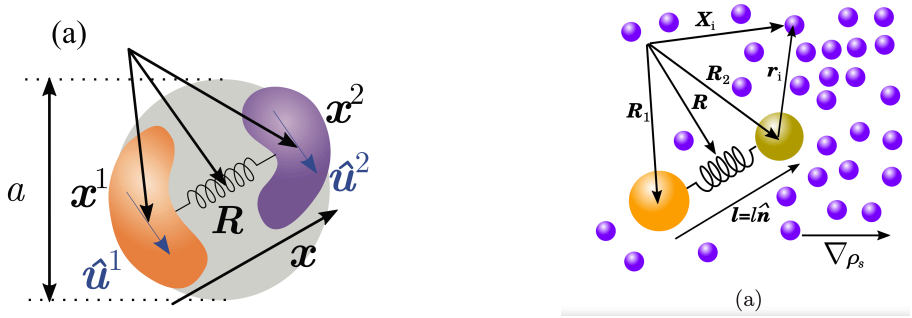

Figure 1.15: (Left) The asymmetric dumbbell model with the typical size of the protein a, which is made of two subunits with orientations $\hat{\mathbf{u}}_1$ and $\hat{\mathbf{u}}_2$, and located at positions $\mathbf{x}^1$ and $\mathbf{x}^2$. The vector $\mathbf{R}$ denotes the center of mass of the protein and $\mathbf{x}$ its elongation. Adapted from Ref. [1.24]. (Right) An enzyme in a gradient of substrate molecules. The enzyme interacts with substrates in the bulk via pairwise hydrodynamic and noncovalent surface interactions. Adapted from Ref. [1.55].

bell model (Fig. 1.15), Illien *et al.* showed that thermal fluctuations can give rise to negative contributions to the overall diffusion coefficient [1.24]. In addition, the time dependence of the diffusion coefficient of the dumbbell was derived with the use of the path integral formulation [1.24]. Later, Adeleke-Larodo *et al.* studied the anisotropy effect on the enzyme diffusive behavior and derived the long-time diffusion coefficient of an asymmetric dumbbell by using the moment expansion technique [1.53]. They also studied the response of an asymmetric dumbbell enzyme to an inhomogeneous substrate concentration and showed that the enzyme exhibits a tendency to align parallel or antiparallel to the gradient, depending on the enzyme affinity to the substrate (Fig. 1.15) [1.55]. Moreover, they found that the hydrodynamic interaction plays an important role in the collective behavior of many interacting enzyme molecules [1.55]. These theoretical findings suggest that hydrodynamic interactions lead to the interaction between the enzyme and substrate molecules as well as the diffusion enhancement of a single enzyme even at equilibrium states [1.24, 1.53–1.55].

1.3.4 New concept for nonequilibrium systems: Nonreciprocity

Active systems are driven strongly out of equilibrium because of the energy input that is continuously consumed by their constituents. This implies the absence of equilibrium concepts such as free energy, detailed balance, time-reversal symmetry, and Newton's third law [1.38]. The violation of Newton's third law means that interactions between the objects are nonreciprocal, which is a key feature of chemical interactions between two different species, e.g., synthetic catalytic colloids, biological enzymes, or whole cells or microorganisms [1.56]. For a 3D fluid, the hydrodynamic interaction between the two object separated by the distance r is described by the Oseen tensor $G_{ij}(\mathbf{r})$ of Eq. (1.8) as long as r is large enough [1.39]. Under the exchange of the index $i \leftrightarrow j$, $G_{ij}(\mathbf{r})$ remains the same and the symmetry relation, $G_{ij} = G_{ji}$, holds. This is known as the reciprocal theorem in fluid dynamics [1.57]. In active fluids driven by biological nanomachines, however, the reciprocal relations is expected to be violated, i.e., $G_{ij} \neq G_{ji}$, which leads to peculiar collective behavior in out-of-equilibrium systems.

Agudo-Canalejo and Golestanian theoretically studied mixtures of chemically interacting particles and unveiled the existence of a new class of active phase separation phenomena where action-reaction symmetry or reciprocal relation is broken [1.56]. Suppose that the concentration field of chemical around a chemically active particle of species i is $c \sim \alpha_i/r$ with the activity α_i and the distance to the particle's center r, the motion of a particle of species j in response to gradients of the chemical is given by a velocity $\mathbf{V}_{ij} \sim -\mu_j \nabla c = \alpha_i \mu_j \mathbf{r}_{ij}/r_{ij}^3$. Here, μ_j is the mobility of the species and $\mathbf{r}_{ij} = \mathbf{r}_i - \mathbf{r}_j$ with $r_{ij} = |\mathbf{r}_{ij}|$. Since the nonreciprocal relation, $\mathbf{V}_{ij} \neq \mathbf{V}_{ji}$, holds in general, an action-reaction symmetry is broken, which can not been seen at equilibrium states. Such a nonreciprocity leads to a variety of active phase separation phenomena, as shown in Fig. 1.16.

Later, Ouazan-Reboul *et al.* extended the above model by considering size

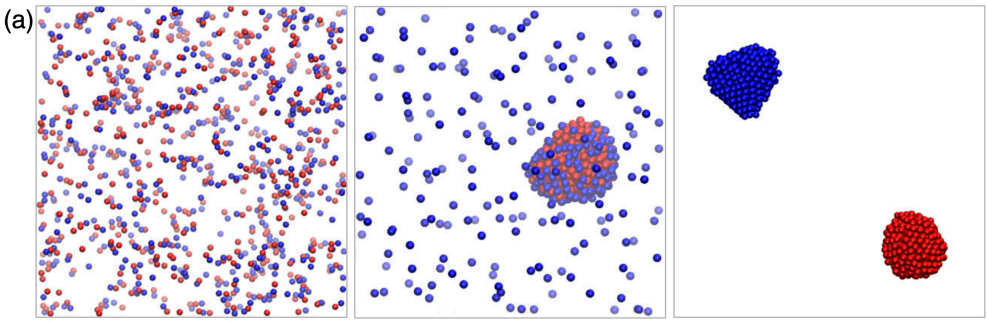

Figure 1.16: Binary mixtures of producer ($\alpha_1 > 0$, blue) and consumer ($\alpha_2 < 0$, red) species show (left) homogeneous states with association of particles into small aggregation, (middle) a static dense phase that coexists with a dilute phase, and (right) separation into two static collapsed clusters. Adapted from Ref. [1.56].

dispersity of the catalytically active particles and the dependence of catalytic activity on the substrate concentration [1.58]. In addition, a continuum model of pattern formation due to nonreciprocal interaction was proposed and a traveling density wave was confirmed, which is a clear signature of broken time-reversal symmetry in this active system [1.59]. Despite these theoretical findings, studies on physical quantities that lead to the emergence of the nonreciprocal relation in active systems are sparse and further investigations are needed to estimate the extent of nonreciprocity in a biological context.

1.4 Time-reversal symmetry and parity breaking transport coefficient: Odd viscosity

1.4.1 Microscopic and macroscopic origins of odd viscosity

Odd viscosity is a rheological property that exists only when the time-reversal and parity symmetries are broken. Although the concept was known for gasses or plasmas in an external magnetic field [1.60], Avron *et al.* showed in 1995 that the odd viscosity is present in a quantum Hall fluid and connected the viscosity with Berry curvature [1.61]. Since this study, the odd viscosity has been discussed in

a fractional quantum Hall or chiral super fluidic systems [1.62]. Since the odd viscosity can be a new measure that characterizes a type of the quantization or universality in these systems, this transport coefficient has gained much more attention not only in condensed matter but also in active matter contexts that deal with living systems.

For a passive isotropic fluid, $\eta_{ijk\ell}$ is symmetric under the exchange of $i \leftrightarrow j$, while $\eta_{ijk\ell} = \eta_{ij\ell k}$ holds from the definition of the symmetric tensor $v_{k\ell}$, as can be inferred from Eq. (1.4). Extending the above symmetry argument, Avron *et al.* introduced a new type of index exchange $ij \leftrightarrow k\ell$, which implies time-reversal transformation [1.61, 1.63]. For the passive case, the symmetry relation holds, i.e., $\eta_{ijk\ell} = \eta_{k\ell ij}$, as can be seen in Eq. (1.4), whereas the asymmetric (odd) part that satisfies $\eta_{\mathrm{o},ijk\ell} = -\eta_{\mathrm{o},k\ell ij}$ is a new contribution to the viscosity tensor. For a 2D isotropic fluid, the odd part of the viscosity tensor can be written solely in terms of the scalar transport coefficient called *odd viscosity* η_{o} as [1.64, 1.65]

$$\eta_{\mathrm{o},ijk\ell} = \frac{1}{2}\eta_{\mathrm{o}} \left(\epsilon_{ik}\delta_{j\ell} + \epsilon_{j\ell}\delta_{ik} + \epsilon_{i\ell}\delta_{jk} + \epsilon_{jk}\delta_{i\ell}\right), \tag{1.11}$$

where ϵ_{ij} is the 2D Levi-Civita tensor with $\epsilon_{xx} = \epsilon_{yy} = 0$ and $\epsilon_{xy} = -\epsilon_{yx} = 1$. The above viscosity tensor $\eta_{\mathrm{o},ijk\ell}$ is parity-even because both σ_{ij} and $v_{k\ell}$ are parity-even, whereas terms that include odd number of ϵ_{ij} are parity-odd. Hence, it is concluded from Eq. (1.11) that η_{o} exists only if both time-reversal and parity symmetries are broken [1.37].

Using the Poisson-Bracket approach, Markovich *et al.* presented a first-principles microscopic Hamiltonian theory for odd viscosity and showed that the viscosity is present both in 2D and 3D systems [1.66]. Through the relation between the angular momentum density $\boldsymbol{\ell}$ of rotating particles and odd viscosity [1.66], they also showed that $\boldsymbol{\ell} = \mathbf{I} \cdot \boldsymbol{\tau}/\Gamma$ at the steady state, which is in agreement with the hydrodynamic derivation [1.37]. Here, $\mathbf{I}$ is the momenta of inertia tensor, $\boldsymbol{\tau}$ is the torque density, and Γ is the rotational friction coefficient of a particle. On the other hand, Khain *et al.* systematically studied all possible

viscosity coefficients that violate parity in a 3D fluid [1.67] and showed that in some cases, their obtained coefficients correspond to $\boldsymbol{\ell}$ obtained in Ref. [1.66].

Moreover, the Green-Kubo formulas that relate $\eta_{\rm o}$ to the stress tensor was derived as [1.65, 1.68]

$$\eta_{\rm o} = \frac{1}{k_{\rm B}TV}\int_0^\infty dt\ [\langle\sigma_{xx}(t)\sigma_{yx}(0)\rangle - \langle\sigma_{yx}(t)\sigma_{xx}(0)\rangle + \langle\sigma_{xy}(t)\sigma_{yy}(0)\rangle - \langle\sigma_{yy}(t)\sigma_{xy}(0)\rangle]\,. \tag{1.12}$$

Note here that when the time-reversal symmetry is preserved, i.e., $\boldsymbol{\sigma}(t) = \boldsymbol{\sigma}(-t)$, and under the assumption of the time translational invariance, i.e., $\langle\boldsymbol{\sigma}(t)\boldsymbol{\sigma}(t')\rangle = \langle\boldsymbol{\sigma}(t-t')\boldsymbol{\sigma}(0)\rangle$ [1.69], the odd viscosity $\eta_{\rm o}$ vanishes. This means that the violation of the time-reversal symmetry is essential for the existence of odd viscosity and the active chiral system with the broken symmetries inherently possesses the odd transport coefficient [1.37, 1.66]. By using molecular dynamics simulations and Eq. (1.12), odd viscosity has been measured [1.65, 1.68].

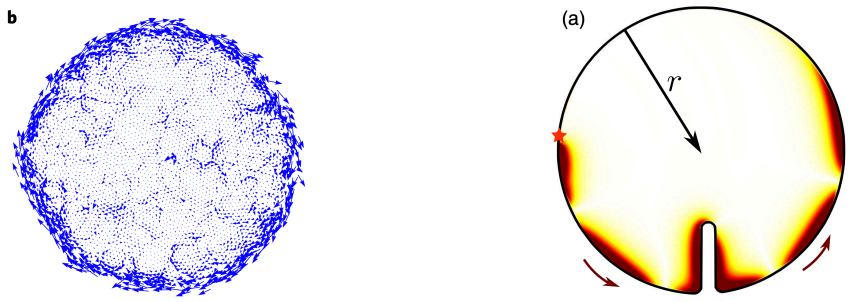

Figure 1.17: (Left) Unidirectional edge flows of the droplet of chiral spinner fluid. Adapted from Ref. [1.70]. (Right) Topological waves in fluids with odd viscosity. Color shows density deviations. Adapted from Ref. [1.71].

1.4.2 Unidirectional edge waves at fluid boundaries

From the experimental point of view, odd viscosity was measured for a fluid consisting of self-spinning particles [1.70, 1.72–1.74]. Soni *et al.* considered an active chiral fluid that includes spinning colloidal magnets and studied the fluid flow with a focus on its surface dynamics [1.70]. They found that unidirectional waves emerged at the fluid boundary [Fig. 1.17(Left)] and further related the

surface tension to odd viscosity, which is the first experimental verification of odd viscosity [1.70]. Similar robust surface flows were also observed at the macroscopic scale, e.g., active chiral granular systems with centimeter-scale toys called Hexbug [1.72] or gear-like particles [1.73]. Later, by taking into account the inter-particle hydrodynamic lubrications, the first normal stress difference turned out to related to odd viscosity in the sheared active chiral system [1.74].

In quantum systems, odd viscosity has been discussed in relation to topological systems, such as quantum Hall fluids [1.61], whereas in classical systems, the viscosity has been rarely investigated. Recently, it has been shown that the odd viscosity characterizes topological edge modes even in a classical fluid with odd viscosity [1.71, 1.75, 1.76]. Souslov *et al.* demonstrated that the topological properties of linear waves [Fig. 1.17(Right)] in a fluid is affected by odd viscosity and the number of chiral edge states depend on the signs of both odd viscosity and the rotational property of the fluid [1.71]. They also found that the behavior can be related with a bulk topological invariant Chern number, which is given by

$$\mathcal{C} = \mathrm{sign}(\eta_\mathrm{o}) + \mathrm{sign}(\omega), \tag{1.13}$$

where ω is the intrinsic rotation angular frequency of the fluid constituent. Later, it was shown that edge modes depend on the boundary conditions of the fluids [1.75, 1.76].

1.4.3 Inertialess hydrodynamic effects due to odd viscosity

Next, we shall explain the hydrodynamic consequences of odd viscosity, which have been examined so far [1.63–1.65, 1.77, 1.78, 1.78]. Through the momentum balance equation, $\nabla \cdot \boldsymbol{\sigma} - \nabla p = 0$, at low Reynolds number, where inertia is negligible [1.69], one can obtain the hydrodynamic equation for a 2D incompressible fluid with odd viscosity as [1.63]

$$-\nabla p + \eta_\mathrm{s} \nabla^2 \mathbf{v} + \eta_\mathrm{o} \nabla^2 \boldsymbol{\epsilon} \cdot \mathbf{v} = 0, \tag{1.14}$$

together with the 2D version of the incompressibility condition $\nabla \cdot \mathbf{v} = 0$ of Eq. (1.7). The third term on the left-hand side of Eq. (1.14) is a new contribution due to the presence of nonvanishing odd viscosity. Since the antisymmetric tensor $\boldsymbol{\epsilon}$ accounts for the clockwise rotation by $\pi/2$, one can see that odd viscosity contributes to the fluid flow that is perpendicular to the one generated by shear viscosity η_s.

The hydrodynamic forces acting on various objects have been studied theoretically for a 2D incompressible fluid in the presence of odd viscosity [1.64, 1.77, 1.78]. Ganeshan *et al.* showed that if boundary conditions depend only on the velocity field, it does not depend on η_o [1.64]. The force exerted on a unit length of a contour of the object is given by the traction force $f_j = n_i \sigma_{ij}$ where $\mathbf{n}$ is a unit vector normal to the contour in the direction of the fluid. From the relation $f_j = 2\eta_o \partial_s v_j$ with $\mathbf{s} = -\boldsymbol{\epsilon} \cdot \mathbf{n}$, the total force on the object becomes [1.64]

$$F_j = 2\eta_o \int ds\, v_j = 0, \tag{1.15}$$

which means that the net force acting on an arbitrarily shaped object does not depend on η_o [1.64]. This implies that one should include appropriate boundary conditions in a 2D incompressible fluid in order to reveal the presence of odd viscosity [1.64, 1.77, 1.78]. In that sense, an expanding bubble with a no-stress boundary condition has been considered and it was shown that the odd viscosity is responsible for a torque acting on the bubble [1.64, 1.65, 1.77, 1.78].

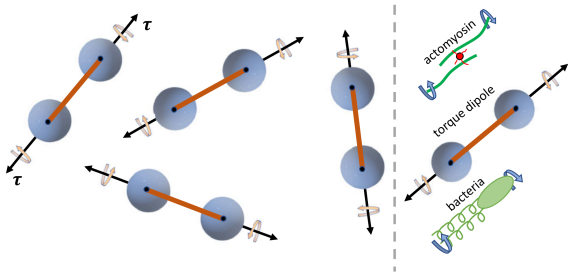

Figure 1.18: (Left) A fluid of torque dipoles that represents inhomogeneous odd viscosity. (Right) Torque dipole as a model for toque exerted by bacteria and for a myosin twisting two actin filaments. Adopted from Ref. [1.66].

1.4.4 Odd viscosity in biological systems

Active chiral systems are abundant in living systems where the energy-consuming agents and their inherent asymmetry play important roles. For instance, biological nanomachines such as ion pumps break both the time-reversal and parity symmetries due to ATP-driven motions and autonomous rotation, which would give rise to odd viscosity in biological membranes [1.37]. In microscopic approaches, it was shown that the odd viscosity also exists in 3D fluids, which extends the applicability of odd viscosity in living matter such as actomyosin gels [Fig 1.18(Right)] [1.66].

As mentioned in Sec. 1.3.1, no external force acts on biological nanomachines and hence the force-free or torque-free conditions should be taken into account for enzymes and micromachines [1.21, 1.79, 1.80] or rotary proteins [1.66], respectively. In living systems, moreover, heterogeneity plays an important role and hence, odd viscosity can vary in space [Fig 1.18(Left)] [1.66]. Despite these recent developments in the theory of odd viscosity [1.37, 1.64–1.66, 1.71, 1.77, 1.78], there has been no experiment that observes odd viscosity in living systems. This is because experimental protocols that allow for the measurement of odd viscosity in a biological context are still sparse and hence further theoretical studies are needed to relate odd viscosity to actual physical phenomena.

1.5 Purpose and organization of the thesis

In recent years, to better understand the complex nonequilibrium phenomena observed in living systems such as the cytoplasm and biological membranes, various studies have been performed in an interdisciplinary field involving chemistry, physics, biology, and engineering [1.28, 1.38]. Experimental studies demonstrate that by harnessing chemical energy, biological nanomachines give rise to nonequilibrium transport phenomena such as diffusion enhancement [1.11, 1.13–1.15, 1.17, 1.26, 1.27], chemotaxis [1.12] or antichemotaxis [1.16, 1.18], and substantial change in rheological properties [1.30–1.32]. Although several model-

ings of biological nanomachines have been conducted [1.21–1.24, 1.50], there has been no unifying theory that quantitatively accounts for the experimental findings [1.25]. In addition, equilibrium concepts such as the time-reversal symmetry and reciprocal relation do not hold in nonequilibrium living systems, and hence further developments in universal physical properties that characterize the systems are needed.

In this thesis, we theoretically investigate the nonequilibrium transport properties in living systems with a special emphasis on active diffusive dynamics and rheological properties that are induced by conformational dynamics of biological nanomachines. To this aim, we employ the *active force dipole* [1.21, 1.22] as a general model for enzymatic molecules and discuss its single and collective hydrodynamic effects on surrounding media, and connect the obtained results to existing experiments. Furthermore, we focus on the peculiar rheological property called *odd viscosity* [1.63] and study its hydrodynamic effects for various situations. The viscosity coefficient emerges only when the time-reversal and parity symmetries are broken in aqueous environments and are expected to exist in living systems [1.37, 1.66].

The three following Chaps. 2-4 deal with the active force dipole that is a minimum model for biological nanomachines. We discuss the statistical property of a single force dipole by means of numerical simulations and provide the estimate of the diffusion enhancement in relation to actual enzymes in Chap. 2. We show in Chap. 3 that the shear viscosity of an enzyme solution decreases with the increasing concentration of substrate molecules, and demonstrate the diffusion enhancement in physiological conditions. In Chap. 4, we discuss the hydrodynamic collective effects due to active force dipoles in free and confined geometries of biological membranes. These obtained results provide a perspective on modeling nonequilibrium phenomena that involve a single or collective biological nanomachines.

The next two following Chaps. 5 and 6 are concerned with odd viscosity that

characterizes active chiral systems. Chapter 5 deals with the hydrodynamic linear response of a 2D fluid monolayer with the odd viscosity to a point force, force dipole, and finite-sized object that moves laterally in the fluid. Then, Chap. 6 provides the hydrodynamic force of a liquid domain with odd viscosity, which is immersed in a 2D fluid having another odd viscosity. These findings can serve as experimental protocols to observe odd viscosity in living systems.

Finally, in Chap. 7, we summarize this thesis and discuss future prospects.

References

[1.1] B. Alberts, A. Johnson, J. Lewis, M. Raff, K. Roberts, and P. Walter, *Molecular Biology of the Cell* (Garland Science, New York, 2008).

[1.2] R. Phillips, J. Kondev, J. Theriot, H. G. Garcia, and N. Orme, *Physical Biology of the Cell* (Garland Science, New York, 2012).

[1.3] H. P. Lu, L. Xun, and X. S. Xie, Science **282**, 1877 (1998).

[1.4] S. C. Kou, B. J. Cherayil, W. Min, B. P. English, and X. S. Xie, J. Phys. Chem. B **109**, 19068 (2005).

[1.5] B. P. English, W. Min, A. M. Van Oijen, K. T. Lee, G. Luo, H. Sun, B. J. Cherayil, S. Kou, and X. S. Xie, Nature Chem. Bio. **2**, 87 (2006).

[1.6] M. Gerstein, A. M. Lesk, and C. Chothia, Biochemistry **33**, 6739 (1994).

[1.7] C. Echeverria, Y. Togashi, A. S. Mikhailov, and R. Kapral, Phys. Chem. Chem. Phys. **13**, 10527 (2011).

[1.8] H. Y. Aviram, M. Pirchi, H. Mazal, Y. Barak, I. Riven, and G. Haran, Proc. Natl. Acad. Sci. (USA) **115**, 3243 (2018).

[1.9] Y. Togashi and A. S. Mikhailov, Proc. Natl. Acad. Sci. (USA) **104**, 8697 (2007).

[1.10] H. Noji, R. Yasuda, M. Yoshida, and K. Kinosita, Nature **386**, 299 (1997).

[1.11] H. S. Muddana, S. Sengupta, T. E. Mallouk, A. Sen, and P. J. Butler, J. Am. Chem. Soc. **132**, 2110 (2010).

[1.12] S. Sengupta, K. K. Dey, H. S. Muddana, T. Tabouillot, M. E. Ibele, P. J. Butler, and A. Sen, J. Am. Chem. Soc. **135**, 1406 (2013).

[1.13] C. Riedel, R. Gabizon, C. A. M. Wilson, K. Hamadani, K. Tsekouras, S. Marqusee, S. Pressé, and C. Bustamante, Nature **517**, 227 (2015).

[1.14] P. Illien, X. Zhao, K. Dey, P. J. Butler, A. Sen, and R. Golestanian, Nano Lett. **17**, 4415 (2017).

[1.15] X. Zhao, K. K. Dey, S. Jeganathan, P. J. Butler, U. M. Córdova-Figueroa, and A. Sen, Nano Lett. **17**, 4807 (2017).

[1.16] A.-Y. Jee, S. Dutta, Y.-K. Cho, T. Tlusty, and S. Granick, Proc. Natl. Acad. Sci. (USA) **115**, 14 (2018).

[1.17] K. K. Dey, Angew. Chem. Int. Ed. **58**, 2208 (2019).

[1.18] H. Wang, M. Park, R. Dong, J. Kim, Y.-K. Cho, T. Tlusty, and S. Granick, Science **369**, 537 (2020).

[1.19] T. S. MacDonald, W. S. Price, R. D. Astumian, and J. E. Beves, Angew. Chem. **131**, 19040 (2019).

[1.20] N. Rezaei-Ghaleh, J. Agudo-Canalejo, C. Griesinger, and R. Golestanian, arXiv preprint arXiv:2110.12819 (2021).

[1.21] A. S. Mikhailov and R. Kapral, Proc. Natl. Acad. Sci. USA **112**, E3639 (2015).

[1.22] R. Kapral and A. S. Mikhailov, Physica D **318–319**, 104 (2016).

[1.23] R. Golestanian, Phys. Rev. Lett. **115**, 108102 (2015).

[1.24] P. Illien, T. Adeleke-Larodo, and R. Golestanian, Eur. Phys. Lett. **119**, 40002 (2017).

[1.25] M. Xu, J. L. Ross, L. Valdez, and A. Sen, Phys. Rev. Lett. **123**, 128101 (2019).

[1.26] M. Guo, A. J. Ehrlicher, M. H. Jensen, M. Renz, J. R. Moore, R. D. Goldman, J. Lippincott-Schwartz, F. C. MacKintosh, and D. A. Weitz, Cell **158**, 822 (2014).

[1.27] B. R. Parry, I. V. Surovtsev, M. T. Cabeen, C. S. O'Hem, E. R. Dufresne, and C. Jacobs-Wagner, Cell **156**, 183 (2014).

[1.28] D. Saintillan, Annu. Rev. Fluid Mech. **50**, 563 (2018).

[1.29] L. D. Landau and E. M. Lifshitz, *Fluid mechanics* (Pergamon Press, Oxford, 1987).

[1.30] K. Nishizawa, K. Fujiwara, M. Ikenaga, N. Nakajo, M. Yanagisawa, and D. Mizuno, Scientific reports **7**, 1 (2017).

[1.31] H. M. López, J. Gachelin, C. Douarche, H. Auradou, and E. Clément, Phys. Rev. Lett. **115**, 028301 (2015).

[1.32] S. Rafaï, L. Jibuti, and P. Peyla, Phys. Rev. Lett. **104**, 098102 (2010).

[1.33] Y. Sumino, K. H. Nagai, Y. Shitaka, D. Tanaka, K. Yoshikawa, H. Chaté, and K. Oiwa, Nature **483**, 448 (2012).

[1.34] L. Yamauchi, T. Hayata, M. Uwamichi, T. Ozawa, and K. Kawaguchi, arXiv preprint arXiv:2008.10852 (2020).

[1.35] Y. Tabe and H. Yokoyama, Nat. Mater. **2**, 806 (2003).

[1.36] K. Beppu, Z. Izri, T. Sato, Y. Yamanishi, Y. Sumino, and Y. T. Maeda, Proc. Natl. Acad. Sci. (USA) **118** (2021).

[1.37] D. Banerjee, A. Souslov, A. G. Abanov, and V. Vitelli, Nat. Commun. **8**, 1573 (2017).

[1.38] G. Gompper, R. G. Winkler, T. Speck, A. Solon, C. Nardini, F. Peruani, H. Löwen, R. Golestanian, U. B. Kaupp, L. Alvarez, *et al.*, J. Phys.: Condens. Matter **32**, 193001 (2020).

[1.39] M. Doi and S. F. Edwards, *The Theory of Polymer Dynamics* (Oxford University Press, New York, 1986).

[1.40] S. Kim and S. J. Karrila, *Microhydrodynamics: Principles and Selected Applications* (Courier Corporation, 2013).

[1.41] N. Oppenheimer, D. B. Stein, and M. J. Shelley, Phys. Rev. Lett. **123**, 148101 (2019).

[1.42] P. Lenz, J.-F. Joanny, F. Jülicher, and J. Prost, Phys. Rev. Lett. **91**, 108104 (2003).

[1.43] P. G. Saffman and M. Delbrück, Proc. Natl. Acad. Sci. (USA) **72**, 3111 (1975).

[1.44] P. G. Saffman, J. Fluid Mech. **73**, 593 (1976).

[1.45] E. Evans and E. Sackmann, J. Fluid Mech. **194**, 553 (1988).

[1.46] M. L. Henle and A. J. Levine, Phys. Rev. E **81**, 011905 (2010).

[1.47] N. Oppenheimer and H. Diamant, Biophys. J. **96**, 3041 (2009).

[1.48] N. Oppenheimer and H. Diamant, Phys. Rev. E **82**, 041912 (2010).

[1.49] S. Ramachandran, S. Komura, K. Seki, and G. Gompper, Eur. Phys. J. E **34**, 46 (2011).

[1.50] Y. Koyano, H. Kitahata, and A. S. Mikhailov, Phys. Rev. E **94**, 022416 (2016).

[1.51] H. Manikantan, Phys. Rev. Lett. **125**, 268101 (2020).

[1.52] S. Bagaria and R. Samanta, arXiv preprint arXiv:2110.05460 (2021).

[1.53] T. Adeleke-Larodo, P. Illien, and R. Golestanian, Eur. Phys. J. E **42**, 1 (2019).

[1.54] R. Golestanian, arXiv preprint arXiv:1909.03747 (2019).

[1.55] T. Adeleke-Larodo, J. Agudo-Canalejo, and R. Golestanian, J. Chem. Phys. **150**, 115102 (2019).

[1.56] J. Agudo-Canalejo and R. Golestanian, Phys. Rev. Lett. **123**, 018101 (2019).

[1.57] H. Masoud and H. A. Stone, J. Fluid Mech. **879**, 1 (2019).

[1.58] V. Ouazan-Reboul, J. Jaime Agudo-Canalejo, and R. Golestanian, Eur. Phys. J. E **44** (2021).

[1.59] S. Saha, J. Agudo-Canalejo, and R. Golestanian, Phys. Rev. X **10**, 041009 (2020).

[1.60] E. Lifshitz and L. Pitaevskii, *Physical Kinetics* (Pergamon Press, Oxford, 1981).

[1.61] J. Avron, R. Seiler, and P. G. Zograf, Phys. Rev. Lett. **75**, 697 (1995).

[1.62] N. Read, Phys. Rev. B **79**, 045308 (2009).

[1.63] J. E. Avron, J. Stat. Phys. **92**, 543 (1998).

[1.64] S. Ganeshan and A. G. Abanov, Phys. Rev. Fluids **2**, 094101 (2017).

[1.65] J. M. Epstein and K. K. Mandadapu, Phys. Rev. E **101**, 052614 (2020).

[1.66] T. Markovich and T. C. Lubensky, Phys. Rev. Lett. **127**, 048001 (2021).

[1.67] T. Khain, C. Scheibner, M. Fruchart, and V. Vitelli, arXiv preprint arXiv:2011.07681 (2020).

[1.68] M. Han, M. Fruchart, C. Scheibner, S. Vaikuntanathan, J. J. de Pablo, and V. Vitelli, Nat. Phys. **17**, 1260 (2021).

[1.69] M. Doi, *Soft Matter Physics* (Oxford University Press, 2013).

[1.70] V. Soni, E. S. Bililign, S. Magkiriadou, S. Sacanna, D. Bartolo, M. J. Shelley, and W. T. M. Irvine, Nat. Phys. **15**, 1188 (2019).

[1.71] A. Souslov, K. Dasbiswas, M. Fruchart, S. Vaikuntanathan, and V. Vitelli, Phys. Rev. Lett. **122**, 128001 (2019).

[1.72] X. Yang, C. Ren, K. Cheng, and H. Zhang, Phys. Rev. E **101**, 022603 (2020).

[1.73] Q. Yang, H. Zhu, P. Liu, R. Liu, Q. Shi, K. Chen, N. Zheng, F. Ye, and M. Yang, Phys. Rev. Lett. **126**, 198001 (2021).

[1.74] Z. Zhao, B. Wang, S. Komura, M. Yang, F. Ye, and R. Seto, Phys. Rev. Res. **3**, 043229 (2021).

[1.75] C. Tauber, P. Delplace, and A. Venaille, J. Fluid Mech. **868**, R2 (2019).

[1.76] C. Tauber, P. Delplace, and A. Venaille, Phys. Rev. Res. **2**, 013147 (2020).

[1.77] A. Souslov, A. Gromov, and V. Vitelli, Phys. Rev. E **101**, 052606 (2020).

[1.78] M. F. Lapa and T. L. Hughes, Phys. Rev. E **89**, 043019 (2014).

[1.79] A. Najafi and R. Golestanian, Phys. Rev. E **69**, 062901 (2004).

[1.80] R. Golestanian and A. Ajdari, Phys. Rev. E **77**, 036308 (2008).

Chapter 2

Statistical Properties of Enzymes as Active Force Dipoles †

2.1 Introduction

Ligand-induced mechanochemical motions are typical for enzymes. Binding or dissociation of a ligand (i.e., substrate or product) to such proteins, as well as chemical reactions within the ligand-bound state, are often accompanied by conformational transitions in them. Thus, these macromolecules would repeatedly change their shapes in each next turnover cycle. The primary role of mechanochemical motions is to enable and facilitate catalytic reaction events. In the enzymes that operate as protein machines or molecular motors and catalytically convert ATP or GTP, such motions are moreover employed to bring about the required machine function or to generate work.

Since enzymes are in solution, their active conformational changes are accompanied by flows in the fluid around them. Such nonequilibrium flows can affect internal mechanical motions in the enzymes and also influence translational and rotational diffusion of such proteins, as demonstrated by MD simulations for a model protein [2.1] and adenylate kinase [2.2]. It has been discussed whether

†The material presented in this chapter was published in: Y. Hosaka, S. Komura, and A. S. Mikhailov, Soft Matter **16**, 10734 (2020).

hydrodynamic self-propulsion of enzymes could furthermore occur, in the models where either instantaneous transitions [2.3, 2.4] or ligand-induced continuous conformational motions take place [2.5–2.7].

Lipid bilayers, forming biological membranes, behave as two-dimensional (2D) fluids on submicrometer scales [2.8, 2.9]. Biomembranes often include many active protein inclusions, such as ion pumps or transporters. Essentially, they represent protein machines powered by ATP hydrolysis or other catalytic reactions in them. Within each operation cycle, the shapes of their membrane domains typically change, inducing 2D fluid flows in the lipid bilayer around them [2.10]. As a result, active protein inclusions might even propel themselves through biomembranes [2.11].

Collective conformational activity of enzymes and protein machines leads to the development of nonthermal fluctuating flows in solution or a lipid bilayer. Other particles (i.e., passive tracers) are advected by these nonequilibrium flows, and, as previously shown [2.12] increased mixing in such systems and diffusion enhancement should therefore arise. Additionally, chemotaxis-like effects in the presence of spatial gradients in the concentration or the activity of enzymes can take place [2.12]. Remarkably, such phenomena persist even if mechanochemical motions are reciprocal; they do not rely on the presence of self-propulsion for proteins, which is predicted to be weak [2.5–2.7].

Following the original publication [2.12], extensive further research has been performed [2.13–2.20]. The effects of rotational diffusion and of possible nematic ordering for enzymes were considered [2.14], the phenomena in biomembranes were extensively analyzed [2.15, 2.16], and the theory was extended to viscoelastic media as well [2.17, 2.18]. Recently, it was shown that viscosity in dilute solutions of mechanochemically active enzymes should become also reduced [2.19]. Multiparticle numerical simulations of active oscillatory colloids, explicitly including hydrodynamic effects, were furthermore undertaken and principal theoretical predictions could thus be verified [2.20].

At low Reynolds numbers, the flow distribution produced by an object, changing the shape due to internal forces within it, can be characterized in the far field as that corresponding to a hydrodynamical force dipole. If the time-dependent stochastic force dipole of an enzyme is known, the collective hydrodynamic effects in solution of such enzymes are predicted by the mean-field theory [2.12]. The difficulty, however, is that experimental measurements and precise theoretical estimates for intensities and statistical properties of the force dipoles corresponding to actual enzymes are not available yet. Lacking this knowledge, only rough quantitative estimates for the considered collective hydrodynamic effects could be made so far.

Our present study has two aims and, respectively, it includes two parts. Section 2.2 corresponds to the first part. Here, the active dimer model is formulated. The active dimer represents a minimal model where ligand-induced mechanochemical motions are reproduced [2.12, 2.20–2.22]. After presenting the model, we undertake an approximate analytical investigation of statistical properties of the force dipoles corresponding to active dimers in subsection 2.2.2, followed by a numerical study in subsection 2.2.3. Quantitative estimates for the intensity of hydrodynamical force dipoles in real enzymes are obtained in subsection 2.2.4.

Section 2.3 corresponds to the second part. Based on the active dimer results, we obtain in subsection 2.3.1 more precise analytical and numerical estimates for the maximal diffusion enhancement for passive particles in solutions of active enzymes, taking into account fast rotational diffusion of enzymes. Similar estimates for diffusion enhancement of passive particles in lipid bilayers are derived in subsection 2.3.2.

The results are discussed in Sec. 2.4. There, we analyze the available experimental and computational data for diffusion enhancement in, respectively, subsections 2.4.1 and 2.4.2. Conclusions and an outline for the perspectives of further research are provided in Sec. 2.5.

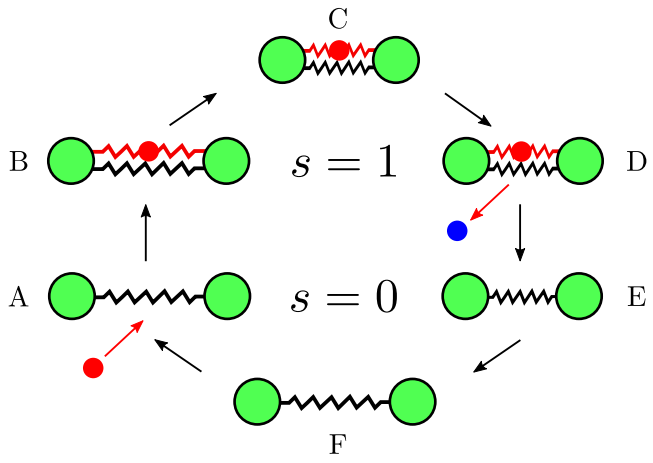

Figure 2.1: The turnover cycle and mechanochemical motions in the active dimer model of an enzyme (see the text).

2.2 Statistical properties of force dipoles

2.2.1 The active dimer model

The simplest mechanical system that gives rise to a hydrodynamical force dipole is a dimer. It consists of two beads 1 and 2 interacting via a potential $u(r)$ that depends on the distance $r = |\boldsymbol{r}_1 - \boldsymbol{r}_2|$ between them. The forces acting on the particles are $\boldsymbol{f}_1 = -\partial u/\partial \boldsymbol{r}_1 = \boldsymbol{f}$ and $\boldsymbol{f}_2 = -\boldsymbol{f}$. If the dimer is immersed into a viscous fluid, the velocity $\boldsymbol{V}$ of the hydrodynamic flow far enough from the dimer is approximately given by [2.12]

$$V_\alpha = \frac{\partial G_{\alpha\beta}}{\partial R_\gamma} e_\beta e_\gamma m, \tag{2.1}$$

where $G_{\alpha\beta}(\boldsymbol{R})$ is the mobility tensor depending on the position $\boldsymbol{R}$ of the dimer with respect to the observation point, $\boldsymbol{e} = (\boldsymbol{r}_1 - \boldsymbol{r}_2)/r$ is the unit orientation vector of the dimer, and $m = fr$ is the magnitude of the force dipole. Summation over repeated indices is assumed. The force dipole is present only if there are nonvanishing net interaction forces, i.e., if the distance between the particles in a dimer continues to change. As in the study [2.12], we assume that the Oseen approximation holds. For a dimer, it is justified if the distance between the beads is much larger than their size.

The minimal active dimer model has been proposed [2.12, 2.21] (see also

review [2.23]) to imitate mechanochemical conformational motions accompanying a catalytic turnover cycle in an enzyme. Note that the dimer model, with nonreactive dissociation of substrate additionally included, was also considered in the study [2.22].

The operation mechanism is illustrated in Fig. 2.1. Two identical beads (green) of radius a are connected by an elastic link with a certain natural spring length ℓ_0 and stiffness k_0. A substrate particle (red) arrives (A) and binds as a ligand to the dimer by forming an additional elastic link with stiffness κ that connects the two beads (B). The natural length ℓ_c of this additional link is taken to be shorter than ℓ_0. Therefore, it tends to contract the dimer until a new equilibrium conformation (C) with a certain distance ℓ_1 between the beads is reached. Once this has taken place, a chemical reaction, that converts the ligand from the substrate to the product, occurs and the product (blue) is instantaneously released (D). Following the product release, the dimer is in the state E with the spring length ℓ_1 that is shorter than the natural length ℓ_0. Therefore, the spring expands and the domains move apart until the equilibrium state (F) is approached again. After that, a new substrate can bind, repeating the turnover cycle.

It is assumed that products are immediately evacuated and therefore we do not consider reverse product binding events. Moreover, possible dissociation events for the substrate are neglected assuming that its affinity is high. Note that, since the product is immediately released once it has been formed, the ligand inside our model enzyme is always only in the substrate form. Therefore, the dimer can be either in the ligand-free ($s = 0$) or the ligand-bound ($s = 1$) states.

The elastic energies in these two states are

$$E_0(x) = \frac{k_0}{2}(x - \ell_0)^2, \tag{2.2}$$

and

$$E_1(x) = \frac{k_0}{2}(x-\ell_0)^2 + \frac{\kappa}{2}(x-\ell_c)^2 = A + \frac{k_1}{2}(x-\ell_1)^2, \tag{2.3}$$

where x is the distance between the beads and

$$A = \frac{\kappa k_0}{2(k_0+\kappa)}(\ell_0-\ell_c)^2, \qquad k_1 = k_0+\kappa, \qquad \ell_1 = \frac{k_0\ell_0+\kappa\ell_c}{k_0+\kappa}. \tag{2.4}$$

The overdamped dynamics of the dimer in the ligand state s is described by the Langevin equation

$$\frac{dx}{dt} = -\gamma\frac{\partial E_s}{\partial x} + \xi(t), \tag{2.5}$$

where γ is the mobility coefficient. To account for thermal fluctuations, this equation includes thermal noise,

$$\langle \xi(t_1)\xi(t_2)\rangle = 2\gamma k_B T\delta(t_1-t_2), \tag{2.6}$$

where k_B is the Boltzmann constant and T is the temperature.

In Eq. (2.5), we have omitted hydrodynamic interactions between the beads. They were taken into account in the study [2.22] of diffusion enhancement for a single dimer itself. In the Oseen approximation, such interaction terms are proportional to the small parameter a/ℓ_0, leading to corrections of the same order for the force dipoles, neglected by us.

Stochastic transitions between the two ligand states take place at constant rates v_0 and v_1 within narrow windows of width ρ near $x = \ell_0$ and $x = \ell_1$. If probability distributions $p_s(x,t)$ are introduced, they obey a system of two coupled Fokker-Planck equations

$$\frac{\partial p_0}{\partial t} = \frac{\partial}{\partial x}[\gamma k_0(x-\ell_0)p_0] + \gamma k_B T\frac{\partial^2 p_0}{\partial x^2} + u_1(x)p_1(x) - u_0(x)p_0(x), \tag{2.7}$$

and

$$\frac{\partial p_1}{\partial t} = \frac{\partial}{\partial x}[\gamma k_1(x-\ell_1)p_1] + \gamma k_B T\frac{\partial^2 p_1}{\partial x^2} + u_0(x)p_0(x) - u_1(x)p_1(x), \tag{2.8}$$

where $u_0(x) = v_0$ for $\ell_0-\rho < x < \ell_0+\rho$ and vanishes outside of this interval; $u_1(x) = v_1$ for $\ell_1-\rho < x < \ell_1+\rho$ and zero outside the interval. Note that the rate v_0 of substrate binding is proportional to the substrate concentration.

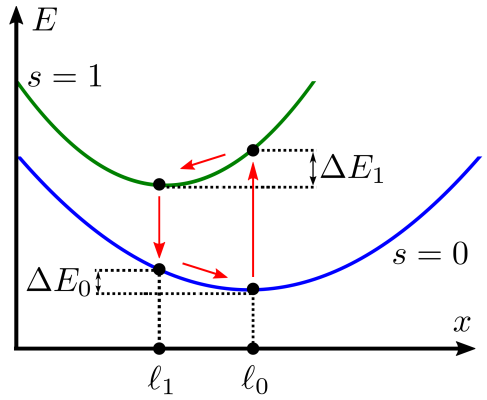

Figure 2.2: The energy diagram of the active dimer.

If the transition windows are very narrow, i.e., $\rho \ll \ell_0$ and $\rho \ll \ell_1$, one can use the approximation

$$u_0(x) = \nu_0 \delta(x - \ell_0), \qquad u_1(x) = \nu_1 \delta(x - \ell_1), \tag{2.9}$$

where $\nu_0 = 2v_0\rho$ and $\nu_1 = 2v_1\rho$.

Figure 2.2 shows the energy diagram of the model. Within each cycle, the dimer dissipates in mechanochemical motions the energy $\Delta E = \Delta E_0 + \Delta E_1$ which is furthermore equal to the difference $E_{\text{sub}} - E_{\text{prod}}$ of the energy $E_{\text{sub}} = E_1(\ell_0) - E_0(\ell_0)$ supplied with the substrate and the energy $E_{\text{prod}} = E_1(\ell_1) - E_0(\ell_1)$ removed with the product. We have

$$\Delta E = \frac{1}{2}(k_0 + k_1)(\ell_0 - \ell_1)^2. \tag{2.10}$$

The energy difference ΔE is always positive and, hence, the considered active dimer represents an exothermic enzyme.

The force dipole of the active dimer is $m = k_0(\ell_0 - x)x$ for $s = 0$ and $m = k_1(\ell_1 - x)x$ for $s = 1$. Note that therefore $m \le k_0\ell_0^2/4$ for $s = 0$ and $m \le k_1\ell_1^2/4$ for $s = 1$.

When the transition windows are narrow, the probability rate w_0 that substrate binding, i.e., a transition to state $s = 1$, occurs per unit time in the state $s = 0$ is approximately

$$w_0 = \nu_0 \sqrt{\frac{k_0}{2\pi k_{\text{B}} T}}. \tag{2.11}$$

On the other hand, the probability rate w_1 that product release, i.e., a transition to state $s = 0$, occurs per unit time in the state $s = 1$ is then approximately given by

$$w_1 = \nu_1 \sqrt{\frac{k_1}{2\pi k_{\mathrm{B}} T}}. \tag{2.12}$$

These equations are derived in Appendix 2.A. Moreover, the characteristic relaxation times of the dimer in the states $s = 0$ and $s = 1$ are, respectively, $\tau_0 = (\gamma k_0)^{-1}$ and $\tau_1 = (\gamma k_1)^{-1}$.

The parameter combinations $w_0\tau_0$ and $w_1\tau_1$ play an important role in determining the kinetic regimes. If the condition $w_0\tau_0 \ll 1$ is satisfied, equilibration to thermal distribution in the state $s = 0$ usually takes place before a transition to the state $s = 1$, i.e., binding of a substrate, occurs. If the opposite condition $w_0\tau_0 \gg 1$ holds, such transition takes place immediately after the transition window at $x = \ell_0$ is reached. If $w_1\tau_1 \ll 1$, the equilibration takes place in the state $s = 1$ before a transition to the state $s = 0$, i.e., the reaction and the product release, occurs. In the opposite limit with $w_1\tau_1 \gg 1$, the reaction takes place and product becomes released immediately once the respective window at $x = \ell_1$ is reached.

Note that, because the rate w_0 is proportional to substrate concentration, the condition $w_0\tau_0 \gg 1$ corresponds to the substrate saturation regime for the considered model enzyme. The condition $w_1\tau_1 \ll 1$ implies that the enzyme waits a long time before the product is released.

2.2.2 Approximate analytical results for force dipoles

At thermal equilibrium in the absence of substrate, $p_1(x) = 0$ and

$$p_0(x) = \sqrt{\frac{k_0}{2\pi k_{\mathrm{B}} T}} \exp\left[-\frac{k_0}{2k_{\mathrm{B}} T}(x - \ell_0)^2\right]. \tag{2.13}$$

Since $m = k_0(\ell_0 - x)x$, one can easily find the equilibrium statistical distribution for force dipoles by using the condition $P_{\mathrm{eq}}(m)dm = p_0(x)dx$. Using, for convenience, the dimensionless force dipole magnitude $\widetilde{m} = m/(k_0\ell_0^2)$ and

dimensionless temperature $\theta = k_{\mathrm{B}}T/(k_0\ell_0^2)$, we get

$$P_{\mathrm{eq}}(\widetilde{m}) = \frac{1}{\sqrt{2\pi(1-4\widetilde{m})\theta}}\Bigg\{\exp\left[-\frac{1}{8\theta}(1+\sqrt{1-4\widetilde{m}})^2\right] + \exp\left[-\frac{1}{8\theta}(1-\sqrt{1-4\widetilde{m}})^2\right]\Bigg\}. \tag{2.14}$$

If $\theta \ll 1$, this distribution is approximately Gaussian and localized at $m = 0$, i.e.,

$$P_{\mathrm{eq}}(\widetilde{m}) = \frac{1}{\sqrt{2\pi\theta}}\exp\left(-\frac{\widetilde{m}^2}{2\theta}\right). \tag{2.15}$$

Using the distribution in Eq. (2.14), one finds that the mean force dipole is

$$\langle m\rangle_{\mathrm{eq}} = -k_{\mathrm{B}}T. \tag{2.16}$$

The correlation function $C(t) = \langle\Delta m(t)\Delta m(0)\rangle$ for variations $\Delta m = m - \langle m\rangle$ of force dipoles is [2.20]

$$C_{\mathrm{eq}}(t) = k_0\ell_0^2 k_{\mathrm{B}}T e^{-|t|/\tau_0} + 2(k_{\mathrm{B}}T)^2 e^{-2|t|/\tau_0}, \tag{2.17}$$

where $\tau_0 = (\gamma k_0)^{-1}$ is the characteristic relaxation time for the dimer in the state $s = 0$. As shown in Appendix 2.B, the exact relation $\langle m\rangle = -k_{\mathrm{B}}T$ holds for the dimer in any steady state and, therefore, in any of these limits.

For an active dimer, approximate analytical estimates can be obtained in the four characteristic limits described below. The two of them (A and C) correspond to low substrate concentrations, with rare turnover cycles controlled by the substrate supply. In regime B, mechanochemical motions are limiting the overall catalytic rate. In other words, product formation and its release occur once an appropriate conformation ($x = \ell_1$) has been reached. In regime D, the overall kinetic rate is, on the other hand, limited by the waiting time for product formation and release.

A The limit of $w_0\tau_0 \ll 1$ and $w_1\tau_1 \ll 1$

If these conditions are satisfied, binding of the substrate and product release have large waiting times. In this limit, there are two almost independent equilibrium subpopulations of dimers in the states $s = 0$ and $s = 1$. The relative

weights of the subpopulations are $w_1/(w_1+w_0)$ and $w_0/(w_1+w_0)$. Therefore, all statistical properties are given by the sums of contributions from different states taken with the respective weights. Particularly, the correlation function of force dipoles is

$$C(t) = \frac{w_1}{w_0+w_1}\left[k_0\ell_0^2 k_{\rm B}T e^{-|t|/\tau_0} + 2(k_{\rm B}T)^2 e^{-2|t|/\tau_0}\right] + \frac{w_0}{w_0+w_1}\left[k_1\ell_1^2 k_{\rm B}T e^{-|t|/\tau_1} + 2(k_{\rm B}T)^2 e^{-2|t|/\tau_1}\right]. \tag{2.18}$$

We can use the above equation to determine the nonequilibrium part of the fluctuation intensity of force dipoles

$$\langle \Delta m^2\rangle_{\rm A} = \langle \Delta m^2\rangle - \langle \Delta m^2\rangle_{\rm eq}. \tag{2.19}$$

Because $\langle \Delta m^2\rangle = C(0)$, we have

$$\langle \Delta m^2\rangle_{\rm A} = \frac{w_0}{w_0+w_1}\left(k_1\ell_1^2 - k_0\ell_0^2\right)k_{\rm B}T. \tag{2.20}$$

As follows from Eq. (2.17), the equilibrium fluctuation intensity is

$$\langle \Delta m^2\rangle_{\rm eq} = k_0\ell_0^2 k_{\rm B}T + 2(k_{\rm B}T)^2. \tag{2.21}$$

Since the effective binding rate w_0 of the substrate is proportional to its concentration c, i.e., $w_0 = \eta c$, Eq. (2.20) yields the Michaelis-Menten form of the dependence of $\langle \Delta m^2\rangle_{\rm A}$ on the substrate concentration.

Remarkably, the catalytic activity of the model enzyme can thus lead not only to some enhancement, but also to *reduction* of fluctuations of the force dipoles. According to Eq. (2.20), reduction should be observed if $k_1\ell_1^2 < k_0\ell_0^2$. Under this condition, the ligand-bound dimer ($s=1$) is characterized by a lower fluctuation intensity of force dipoles than the free dimer ($s=0$).

B The limit of $w_0\tau_0 \gg 1$ and $w_1\tau_1 \gg 1$

In this limit, transitions take place once the respective transitions windows are entered. If additionally the conditions $k_0\ell_0^2 \gg k_{\rm B}T$ and $k_1\ell_1^2 \gg k_{\rm B}T$ are satisfied, thermal fluctuations can be neglected and the dimer essentially behaves as a deterministic oscillator. Then, the solution can be obtained by integrating

Eq. (2.5) with appropriate boundary conditions. This yields $x(t) = \ell_1 + (\ell_0 - \ell_1 - \rho)e^{-t/\tau_1}$ for $0 < t < T_1$ and $x(t) = \ell_0 + (\ell_1 - \ell_0 + \rho)e^{-(t-T_1)/\tau_0}$ for $T_1 < t < T_c$. Here, T_c is the oscillation period of the active dimer and T_1 is the duration of the cycle time when the dimer is in the ligand-bound state $s = 1$. If transition windows are narrow, i.e., the condition $\rho \ll (\ell_0 - \ell_1)$ is satisfied, we approximately have

$$T_1 = \tau_1 \ln\left(\frac{\ell_0 - \ell_1}{\rho}\right), \tag{2.22}$$

and

$$T_c = (\tau_0 + \tau_1) \ln\left(\frac{\ell_0 - \ell_1}{\rho}\right). \tag{2.23}$$

The respective time-dependent force dipole is $m(t) = k_1(\ell_1 - x)x$ for $0 < t < T_1$ and $m(t) = k_0(\ell_0 - x)x$ for $T_1 < t < T_c$. Hence, it is negative for $s = 1$ and positive for $s = 0$.

The force dipole varies within the interval $m_{\min} < m < m_{\max}$, where the minimum value $m_{\min} = -k_1\ell_0(\ell_0 - \ell_1)$ is taken at $t = 0$, i.e., in the state $s = 1$ just after substrate binding, and the maximum value $m_{\max} = k_0\ell_1(\ell_0 - \ell_1)$ is reached at $t = T_1$, in the state $s = 0$ just after product release (here we again assume that transition windows are narrow). Note that, if thermal fluctuations were present, the force dipoles could however have also taken the values outside of this interval.

It can be checked by direct integration that the period-averaged force dipole for the deterministic active dimer is $\langle m(t)\rangle_{\rm det} = 0$. The correlation function for the deterministic oscillating dimer is defined as the period average

$$C_{\rm det}(t) = \frac{1}{T_c}\int_0^{T_c} dh\, m(t+h)m(h). \tag{2.24}$$

The explicit analytical form of this periodic correlation function is too complicated and we do not give it (analytical results for correlation functions are also omitted below in the limits C and D).

The mean-square intensity of force dipoles is $\langle m(t)^2\rangle_{\rm det} = C_{\rm det}(0)$. In the

limit $\rho \to 0$, we approximately have

$$\langle m(t)^2 \rangle_{\rm det} = \frac{k_0 k_1}{12(k_0+k_1)} \left[\ln\left(\frac{\ell_0 - \ell_1}{\rho} \right) \right]^{-1} (\ell_0 - \ell_1)^2 \times \Big[k_0(\ell_0^2 + 2\ell_0\ell_1 + 3\ell_1^2) + k_1(3\ell_0^2 + 2\ell_0\ell_1 + \ell_1^2) \Big]. \quad (2.25)$$

When $k_1 \sim k_0$, this equation yields the scaling $\langle m(t)^2 \rangle_{\rm det} \sim k_0^2$.

C The limit of $w_0\tau_0 \ll 1$ and $w_1\tau_1 \gg 1$

If these conditions are satisfied, the model enzyme waits a long time for binding of a substrate (because the substrate concentration is low), but then it performs a rapid reaction cycle. An approximate solution in this regime can be obtained if, additionally, the conditions $k_0\ell_0^2 \gg k_{\rm B}T$ and $k_1\ell_1^2 \gg k_{\rm B}T$ are satisfied, i.e., that thermal fluctuations are weak. Moreover, we shall assume that the transition window for substrate binding is narrow, i.e., the approximation in Eq. (2.9) holds for $u_0(x)$.

In this case, the dependence $x(t)$ consists of a sum of statistically independent rare pulses, each corresponding to one reaction cycle:

$$x(t) = \sum_j z(t - t_j), \quad (2.26)$$

where $z(t) = \ell_1 + (\ell_0 - \ell_1)e^{-t/\tau_1}$ for $0 < t < T_1$ and $z(t) = \ell_0 + (\ell_1 - \ell_0)e^{-(t-T_1)/\tau_0}$ for $t > T_1$, with T_1 given by Eq. (2.22). The pulses appear at random time moments t_j and the probability of their appearance per unit time is w_0.

Moreover, we also have

$$m(t) = \sum_j \zeta(t - t_j), \quad (2.27)$$

where $\zeta(t) = k_1(\ell_1 - z(t))z(t)$ for $0 < t < T_1$ and $\zeta(t) = k_0(\ell_0 - z(t))z(t)$ for $t > T_1$.

Hence, this represents a random Poisson process. Its first two statistical moments are approximately $\langle m(t) \rangle = 0$ and

$$\langle m^2(t) \rangle = w_0 \int_0^\infty dt\, \zeta^2(t) = \frac{1}{12} w_0 \tau_0 (\ell_0 - \ell_1)^2 \left[k_0^2(\ell_0^2 + 2\ell_0\ell_1 + 3\ell_1^2) + k_0 k_1 (3\ell_0^2 + 2\ell_0\ell_1 + \ell_1^2) \right]. \quad (2.28)$$

Taking into account Eq. (2.11), we notice that, when $k_1 \sim k_0$, the scaling $\langle m^2(t)\rangle \sim k_0^{3/2}$ should hold.

D The limit of $w_0\tau_0 \gg 1$ and $w_1\tau_1 \ll 1$

This situation corresponds to substrate saturation and a long waiting time for the reaction and product release in the ligand-bound state. A derivation, similar to that given above, shows that, if $k_0\ell_0^2 \gg k_\mathrm{B}T$ and $k_1\ell_1^2 \gg k_\mathrm{B}T$, we approximately have $\langle m(t)\rangle = 0$ and

$$\langle m^2(t)\rangle = \frac{1}{12} w_1\tau_1(\ell_0-\ell_1)^2\left[k_1^2(3\ell_0^2+2\ell_0\ell_1+\ell_1^2)+k_0k_1(\ell_0^2+2\ell_0\ell_1+3\ell_1^2)\right]. \tag{2.29}$$

If we take into account Eq. (2.12), it can be noticed that, when $k_1 \sim k_0$, scaling $\langle m^2(t)\rangle \sim k_0^{3/2}$ is again obtained.

2.2.3 Numerical simulations

Numerical simulations can yield statistical properties of force dipoles for selected parameter values in the regions where there are no approximate analytical results. Below in this section, we focus on the situation under substrate saturation, but with the waiting time for product release comparable to the conformational relaxation time (thus, lying between the limits B and D). We shall consider a situation where the condition $k_\mathrm{B}T \ll k_0\ell_0^2$ is satisfied, so that thermal fluctuations are relatively weak.

Before proceeding to simulations, the model was nondimensionalized. The dimensionless variables were $\tilde{t} = t/\tau_0$, $\tilde{x} = x/\ell_0$, and $\widetilde{m} = m/(k_0\ell_0^2)$. The dimensionless transition rates were $\tilde{v}_0 = v_0\tau_0$ and $\tilde{v}_1 = v_1\tau_0$, while the dimensionless temperature was $\theta = k_\mathrm{B}T/(k_0\ell_0^2)$. Stochastic differential equation (2.5) was numerically integrated, complemented by transitions between the ligand states [see the source code in Appendix 2.E].

In the simulations, we had $\ell_1 = 0.55\ell_0$, $k_1 = 2k_0$, and $\rho = 0.01\ell_0$. We have kept constant $\tilde{v}_1 = 2$, but varied the parameter $\tilde{v}_0$. A relatively low dimensionless temperature $\theta = 0.0018$ was chosen to satisfy the condition $k_\mathrm{B}T \ll k_0\ell_0^2$. Under

such choice, $\langle m(t)^2\rangle_{\rm det}/\langle \Delta m^2\rangle_{\rm eq} = 19.3$ and $w_1\tau_1 = 0.27$.

Note that, because of the last condition, there was a significant random variation in the waiting times for substrate conversion and product release. Moreover, waiting times for substrate binding, characterized by the rate w_0, could also vary. These effects kept the model stochastic even when thermal noise was small.

Figure 2.3 shows typical time dependences of the force dipoles. In Fig. 2.3(a), the waiting time for substrate binding is long. Therefore, the dimer spends most of the time in the ligand-free state $s = 0$. Within the time shown, only one turnover cycle has taken place. For the force dipole, the cycle consists of a negative spike, just after binding of the substrate, and the following positive spike, just after the product release. In Fig. 2.3(b), the substrate binding rate is increased. As a result, the dimer is frequently cycling, already resembling an oscillator. Nonetheless, the random variation of the times between the cycles is relatively large.

Probability distributions of force dipoles are shown in Fig. 2.4. The black curve is the distribution for passive dimers in the absence of the substrate, given by Eq. (2.14). It represents a narrow Gaussian peak at $m = 0$. The distribution at $\tilde{v}_0 = v_0\tau_0 = 0.03$ (red) is almost indistinguishable from it. The blue curve is the distribution for active dimers corresponding to Fig. 2.3(b). Now, the distribution is more broad and the central peak is smaller. The tail on the left side from the peak and the shoulder on its right side are due to the nonequilibrium activity of force dipoles.

The dependence of the nonequilibrium part of the fluctuation intensity of force dipoles, Eq. (2.19), on the substrate binding rate v_0, proportional to substrate concentration, is shown in Fig. 2.5. It can be well fitted to the Michaelis-Menten function (the solid curve). The saturation magnitude is close to the value of 0.033 predicted at such parameters for the deterministic dimer by Eq. (2.25).

Normalized correlation functions of force dipoles at different substrate binding rates are shown in Fig. 2.6. In the absence of the substrate (for $v_0 = 0$)

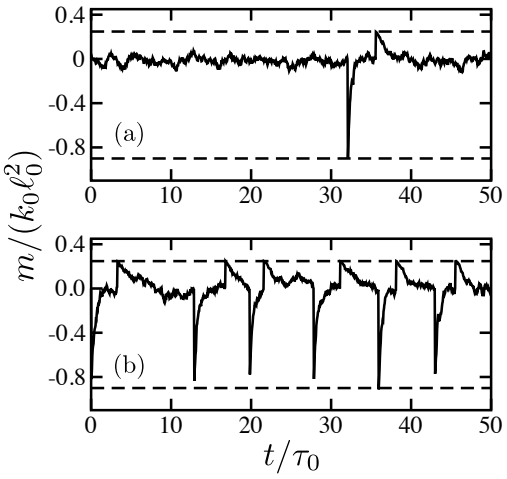

Figure 2.3: Time dependence of dimensionless force dipoles $\widetilde{m} = m/(k_0\ell_0^2)$ on time for (a) $\tilde{v}_0 = 0.03$ and (b) $\tilde{v}_0 = 3$. Dashed lines show the lower bound $\widetilde{m}_{\min} = -0.9$ for the deterministic oscillatory dimer and the absolute upper bound $\widetilde{m}_{\max} = 0.25$ for force dipoles.

the dependence is monotonous (it is given by Eq. (2.17)). As the substrate concentration is increased, damped oscillations in the correlation function become observed, thus signaling the onset of the active oscillatory behavior that prevails over the thermal noise.

The correlation functions could be fitted (dashed curves in Fig. 2.6) to the dependence

$$C(t)/C(0) = \frac{1}{\cos\alpha}\exp(-\Gamma|t|)\cos(\Omega|t| - \alpha). \tag{2.30}$$

Figure 2.7 shows how the dimensionless relaxation time $1/(\Gamma\tau_0)$, the dimensionless oscillation period $2\pi/(\Omega\tau_0)$ and the phase shift α depend on the substrate binding rate. The oscillation period under saturation conditions is still larger than $T_c/\tau_0 = 5.7$ for the deterministic dimer according to Eq. (2.23). This is because of an additional waiting time for product release. The characteristic relaxation time is about $1/(\Gamma\tau_0) = 2$.

It should be stressed that the form in Eq. (2.30) of the correlation function would not hold in the deterministic limit. Indeed, the oscillations stay harmonic in the limit of an infinite correlation time. However, the deterministic oscillations are actually nonharmonic, as seen in Fig. 2.3.

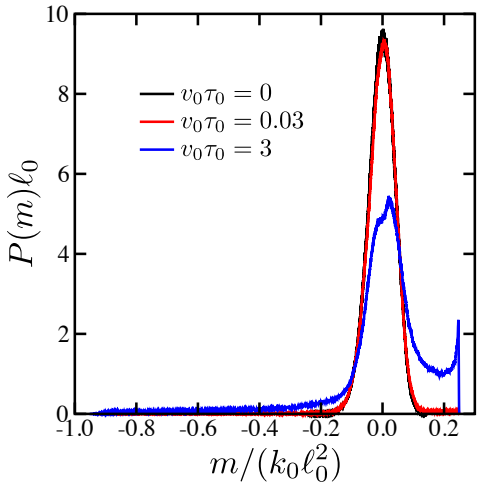

Figure 2.4: Probability distributions of force dipoles $\widetilde{m}$ for passive (black curve, $v_0 = 0$) and active (red curve, $\tilde{v}_0 = 0.03$, and blue curve, $\tilde{v}_0 = 3$) dimers.

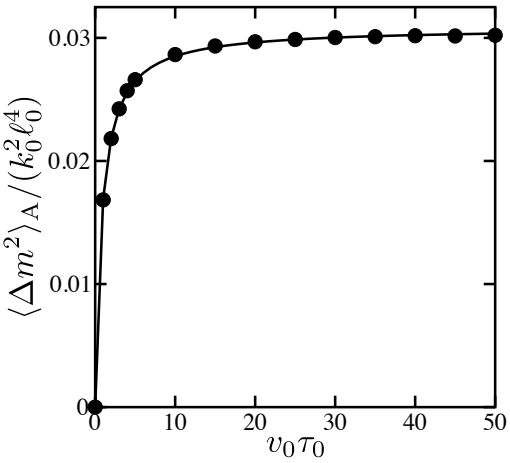

Figure 2.5: Dependence of the nonequilibrium part $\langle \Delta m^2 \rangle_{\rm A}$ of the fluctuation intensity of force dipoles on the substrate binding rate v_0 (dots). The solid curve is a fit to the Michaelis-Menten function.

There are two effects that make the dimer model stochastic, i.e., the thermal noise in the dynamical equation (2.5) and random transitions between the ligand states $s = 0$ and $s = 1$. When $\theta \to 0$, the thermal noise vanishes, but random transitions between the states nonetheless remain. This second stochastic effect is responsible for the decay in the correlation function. As shown in Appendix 2.C, the dependence of the correlation function in Eq. (2.30) corresponds to an approximate solution of the master equations (2.7) and (2.8).

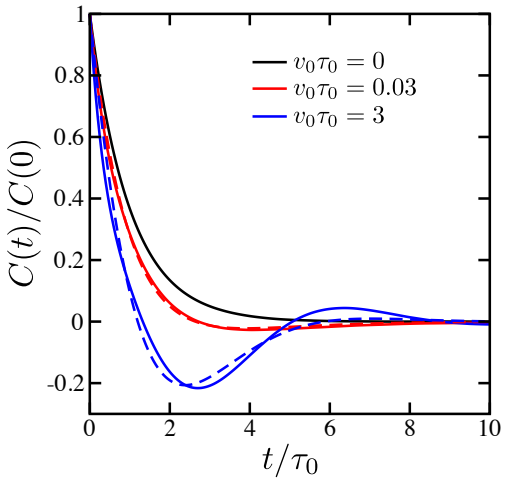

Figure 2.6: Normalized correlation functions of force dipoles at different substrate binding rates: $v_0 = 0$ (absence of substrate, black), $\tilde{v}_0 = 0.03$ (red), and $\tilde{v}_0 = 3$ (blue). The correlation function for passive dimers (black) is given by Eq. (2.17). Dashed curves are fits to the dependence in Eq. (2.30).

2.2.4 Estimates for hydrodynamic force dipoles of enzymes

Above, statistical properties of force dipoles were analyzed in the framework of an idealized model of the active dimer. Now, the obtained results can be applied to approximately estimate the force dipoles for real enzymes and protein machines. To do this, the relationship between such a simple model and the actual proteins needs to be first discussed.

Proteins fold into a definite conformation that however incorporates many different substates. Slow dynamics of proteins represents wandering over a Markov network of such metastable conformational substates [2.24]. In all-atom molecular dynamics (MD) simulations, transitions within tens of nanoseconds to the nearest metastable states can be clearly seen. Long MD simulations show motions over a set of these states extending to the millisecond timescales [2.25]. Single-molecule fluorescence correlation spectroscopy experiments with cholesterol oxidase revealed that thermal conformational fluctuations in this enzyme, in the absence of the substrate, had correlations persisting even over about 1.5 s time [2.26, 2.27]. In the coarse-grained structure-based simulations of proteins,

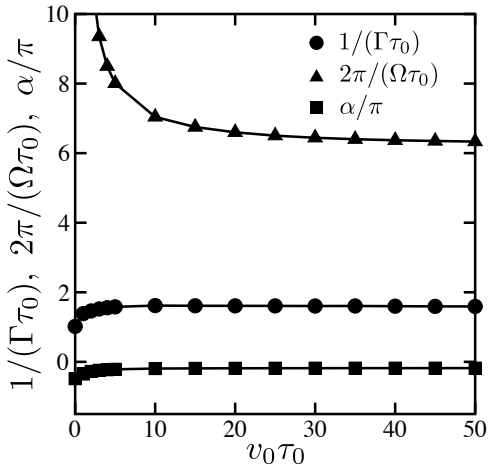

Figure 2.7: The dependences of the relaxation time $1/\Gamma$ (circles), oscillation period $2\pi/\Omega$ (triangles) and phase shift α (squares) on substrate binding rate v_0.

such as modeling based on elastic networks, the rugged atomic energy landscape becomes smoothed [2.28], thus yielding continuous slow conformational dynamics described by a set of effective collective coordinates.

In a detailed study of adenylate kinase [2.29], combining all-atom MD simulations with single-molecule fluorescence resonance energy transfer and NMR, it was found that, in this characteristic mechanochemical enzyme, conformational substates lie along a trajectory that connects the initial open apo conformation to the final catalytically efficient closed state. Thus, the energy landscape has a valley that guides towards the optimal protein state; the motion along such a valley can be described by a single coordinate. Similar organization of the energy landscape has been noticed in structure-based coarse-grained modeling of protein machines and molecular motors, such as myosin V and F_1-ATPase [2.30] and HCV helicase [2.31].

Typically, mechanochemical enzymes and molecular machines represent proteins with domain structure. Slow functional conformational dynamics in these proteins consists in relative motions of the domains that can be often characterized by a single coordinate, such as a hinge angle or a distance between the centers of mass of two protein domains. This leads to the reduced models for

proteins, with just one or a few mechanical coordinates [2.23]. The active dimer is a model belonging to this class. Note that previously a similar simple model with three beads was employed to estimate the magnitude of self-propulsion effects in the enzymes [2.7]. In the framework of the active dimer model, statistical properties of force dipoles in different kinetic regimes can be analyzed and characteristic order-of-magnitude estimates for the intensity of such dipoles for typical enzymes and protein machines can be derived.

In Sec. 2.2.2, four kinetic regimes have been outlined. The two of them (A and C) correspond to low substrate concentrations, with rare turnover cycles controlled by the substrate supply. Below, we focus on the substrate saturation regimes B and D where high catalytic activity and, thus, the strongest nonequilibrium force dipoles can be expected.

In regime B, mechanochemical motions are limiting the overall catalytic rate. In other words, product formation and its release occur once an appropriate conformation ($x = \ell_1$) has been reached. Such regime is characteristic, for example, for adenylate kinase where the turnover time is limited by the time (about 1 ms) of the conformational transition from the open to the closed state, with the reaction AMP + ATP $\rightarrow$ 2ADP rapidly occurring once the latter state is reached [2.29].

In regime D, the overall kinetic rate is, on the other hand, limited by the waiting time for product formation and release. This regime is typical for protein machines and motors such as myosin V. In each operation cycle of this molecular motor, catalytic hydrolysis of substrate ATP into product ADP takes place. The cycle duration of 66 ms under ATP saturation is limited by waiting for ADP release [2.32]. The conformational transition from the open to the closed state, i.e., the lever-arm swing after ATP binding, takes place within a much shorter millisecond time.

The principal parameters of the active dimer model are stiffness constants k_0 and k_1 and inter-domain distances ℓ_0 and ℓ_1 in the open ($s = 0$) and closed

($s = 1$) conformations, respectively. The typical size of a protein is of the order of tens of nanometers and this would be also the characteristic distances ℓ_0 and ℓ_1 between the domains. Moreover, if the open and closed states are distinctly different, as, for example, in adenylate kinase or myosin, the change $\Delta\ell = \ell_0 - \ell_1$ is comparable in magnitude to ℓ_0 and ℓ_1. As characteristic values for order-of-magnitude estimates, one can, for example, choose $\ell_0 = 10\,\mathrm{nm}$ and $\ell_1 = 5\,\mathrm{nm}$ in the open and the closed states, respectively.

In the active dimer, two domains (beads) are connected by a spring. In real proteins, they can be, instead, connected by a hinge with the elastic energy

$$E = \frac{1}{2}K(\Theta - \Theta_0)^2, \tag{2.31}$$

which depends on the deviation of the hinge angle Θ from the equilibrium angle Θ_0. This can also be approximately written as

$$E = \frac{1}{2}k(x - \ell_0)^2, \tag{2.32}$$

so that the hinge is described as an elastic spring with $x = \ell\Theta$, $\ell_0 = \ell\Theta_0$ and the effective stiffness $k = K/\ell^2$, where ℓ is the characteristic linear size of the domains connected by the hinge.

The stiffness of the converter hinge in myosin V was estimated in single-molecule experiments by Kinoshita with coworkers [2.33] to be about $K = 5\,k_\mathrm{B}T/\mathrm{rad}^2$ both in the open and the closed states. On the other hand, the data of high-speed AFM observations by Ando with coworkers [2.34] corresponds to a higher value of $K = 23\,k_\mathrm{B}T/\mathrm{rad}^2$. The difference may be due to the fact that the hinge becomes softer for larger angles. In our estimates below, we take $K = 10\,k_\mathrm{B}T/\mathrm{rad}^2$. Choosing $\ell = 10\,\mathrm{nm}$, this leads to $k = 0.1\,k_\mathrm{B}T/\mathrm{nm}^2$.

As noticed above, in adenylate kinase, the overall turnover rate under substrate saturation in an enzyme is limited by conformational transitions between the open and closed states (and hence the turnover rate is about $10^3\,\mathrm{s}^{-1}$). The maximum intensity of force dipoles can be estimated by using Eq. (2.25). If the parameter values $k_0 = k_1 = 0.1\,k_\mathrm{B}T/\mathrm{nm}^2$, $\ell_0 = 10\,\mathrm{nm}$, $\ell_1 = 5\,\mathrm{nm}$ and $\rho = 1\,\mathrm{nm}$

are chosen, the nonequilibrium mean-square fluctuation intensity $\langle \Delta m^2 \rangle_{\mathrm{A}}$ of force dipoles in such enzymes is estimated as approximately $80\,[\mathrm{pN{\cdot}nm}]^2$. This is similar to the previous estimate of $100\,[\mathrm{pN{\cdot}nm}]^2$ in Ref. [2.12] based on typical stall forces in molecular motors.

In more slow enzymes and protein machines with the turnover numbers of tens per second, the turnover is limited by product formation and its release. In this case, the intensity of force dipoles can be estimated using Eq. (2.29). There, the rate w_1 of product formation and release is approximately the same as the overall turnover rate, whereas τ_1 corresponds to the conformational transition time. Choosing the turnover rate of $15\,\mathrm{s}^{-1}$, as in myosin V, and the conformational transition time of 1 ms and keeping the same other parameters as above, the nonequilibrium mean-square fluctuation intensity of force dipoles can then be estimated as about $4\,[\mathrm{pN{\cdot}nm}]^2$. This is much smaller than the above estimate for fast enzymes because nonthermal mechanical forces are only generated in conformational transitions of about 1 ms in duration. It represents only a small fraction of the entire cycle time of tens of milliseconds in such enzymes or protein machines.

While typical enzymes have turnover times between milliseconds and tens of milliseconds, there are also very slow enzymes, such as tryptophan synthase with the turnover time of 0.5 s [2.35], and enzymes that are very fast, such as catalase ($17\,\mu$s) or urease ($59\,\mu$s) [2.36]. Moreover, transition times from open to close confirmations can be also very short in some enzymes. For example, for phosphoglycerate kinase (PGK), neutron spin-echo spectroscopy yields conformational transition times of the order of tens of nanoseconds [2.37]. This was also observed in coarse-grained MD simulations for PGK [2.38]. Therefore, it is interesting to discuss under what general conditions stronger force dipoles can be expected in enzymes.

Equation (2.10) relates the energy (generally, enthalpy) dissipated in mechanochemical motions within the turnover cycle of an active dimer to the stiffness of the

dimer and the magnitude of conformational changes in it. While it has been derived for an idealized model, it can also be used for order-of-magnitude estimates in real enzymes. Taking, for example, $k_0 = k_1 = 0.1\,k_{\rm B}T/{\rm nm}^2$ and $\ell_0 - \ell_1 = 10\,{\rm nm}$ for myosin, we obtain $\Delta E = 10\,k_{\rm B}T$, which is in reasonable agreement with the energy of about $20\,k_{\rm B}T$ supplied to this molecular motor with ATP (only half of this energy is used in the power stroke).

Note that, assuming for simplicity that $k_0 = k_1 = k$, Eq. (2.10) can be also written as

$$k = \frac{\Delta E}{\Delta \ell^2}, \tag{2.33}$$

thus expressing the stiffness in terms of the energy ΔE dissipated in mechanochemical motions and the conformational change $\Delta\ell = \ell_0 - \ell_1$. An enzyme is stiffer if the same energy is dissipated within a conformational transition of a smaller magnitude.

Suppose that conformational changes are indeed small in an enzyme and, moreover, its turnover rate is limited by conformational transitions within the cycle. Then, Eq. (2.25) can be used to estimate the intensity of force dipoles. For approximate numerical estimates, it can be written in the form

$$\langle \Delta m^2 \rangle = \zeta_0 k^2 \ell_0^2 (\ell_0 - \ell_1)^2, \tag{2.34}$$

where ζ_0 is a dimensionless factor of order unity that also includes the logarithmic term and we have taken $k_0 = k_1 = k$. Note that this estimate holds assuming that the force dipoles in the catalytically active enzyme are much stronger than those due to thermal fluctuations in the absence of substrate.

Substituting k from Eq. (2.33), a simple order-of-magnitude estimate is obtained

$$\langle \Delta m^2 \rangle = \zeta_1 \left(\frac{\ell_0}{\Delta \ell} \right)^2 \Delta E^2, \tag{2.35}$$

where ζ_1 is another dimensionless factor of order unity. Moreover, by using

Eq. (2.21) and (2.33), we furthermore get

$$\frac{\langle \Delta m^2 \rangle}{\langle \Delta m^2 \rangle_{\mathrm{eq}}} = \zeta_1 \frac{\Delta E}{k_{\mathrm{B}} T}, \tag{2.36}$$

if the condition $k\ell_0^2 \gg k_{\mathrm{B}}T$ holds.

These results show that the intensity of force dipoles is strongly sensitive to the magnitude of mechanochemical motions within the turnover cycle. Moreover, they show that, in strongly exothermic enzymes, force dipoles are greatly enhanced when catalytic activity takes place.

The above-mentioned catalase and urease enzymes are not only exceptionally fast, but also highly exothermic, with $\Delta H = 100\,\mathrm{kJ/mol}$ for catalase and $\Delta H = 59.6\,\mathrm{kJ/mol}$ for urease [2.36]. Hence, large energies of $42\,k_{\mathrm{B}}T$ or $25\,k_{\mathrm{B}}T$ are released in them and dissipated into heat within very short microsecond cycle times. Furthermore, at least for catalase, it is known that functional conformational changes are involved within the turnover cycle, but their magnitude is small [2.39]. It has been previously proposed [2.36] that chemoacoustic intramolecular effects caused by strong heat release may even lead to hydrodynamic self-propulsion of these enzymes, although subsequent examination could not confirm this [2.7]. These enzymes do not have a domain structure and therefore the results of our analysis based on the dimer model are not directly applicable to them. Nonetheless, they suggest that hydrodynamic force dipoles in them may be very strong.

2.3 Diffusion enhancement for passive particles in active enzyme solutions

The most important application of the obtained results for force dipoles is that they allow to obtain more accurate analytical and numerical estimates for diffusion enhancement of passive particle in solutions of active enzymes. In the previous studies [2.12, 2.14], the magnitude of diffusion enhancement has been expressed in terms of the statistical properties of hydrodynamic force dipoles.

However, because these properties were only poorly known, precise estimates for such magnitude could not be obtained. This has led to difficulties in the interpretation of experimental results and in the analysis of the computational data. In this section, we use the statistical properties of force dipoles for active dimers, determined above in Sec. 2.2, to estimate the diffusion enhancement effects for enzymes in water solution and for active protein inclusions in biomembranes.

2.3.1 Diffusion effects of enzymes in water solutions

As previously shown [2.12, 2.14], the change $D_{\rm A}$ in the diffusion coefficient of passive *tracer* particles in a three-dimensional (3D) solution is given by

$$D_{\rm A} = \frac{n}{60\pi\mu^2\ell_{\rm cut}}(\chi - \chi_{\rm eq}), \tag{2.37}$$

where n is the concentration of active enzymes, μ is viscosity, and $\ell_{\rm cut}$ is a microscopic cut-off length of the order of a protein size. Moreover, we have

$$\chi = \int_0^\infty dt\, C(t)\sigma(t), \tag{2.38}$$

where $C(t)$ is the correlation function of force dipoles corresponding to the enzymes and $\sigma(t)$ is the orientational correlation function for them; $\chi_{\rm eq}$ is given by the same equation, but with $C(t)$ replaced by $C_{\rm eq}(t)$.

The orientational correlation function has the form

$$\sigma(t) = \exp(-t/\tau_{\rm rot}), \tag{2.39}$$

where $\tau_{\rm rot}$ is the orientational correlation time. As seen from Eqs. (2.37), (2.38) and (2.39), the magnitude of diffusion enhancement is sensitive to the relationship between the correlation time of force dipole and the orientational correlation time.

According to the Stokes equation, rotational diffusion coefficient for a spherical particle of radius R is

$$D_{\rm rot} = \frac{k_{\rm B}T}{8\pi\mu R^3}. \tag{2.40}$$

The orientational correlation time is defined as $\tau_{\rm rot} = 1/D_{\rm rot}$. Since proteins

are not spheres, their orientational correlation times are shorter than given by the Stokes estimate. Even in crowded solutions, they do not exceed a microsecond [2.40–2.42]. For active dimers, the orientational correlation times can be estimated by using Eq. (2.40) with $R = \ell_0$.

For the active dimer model, the correlation functions of force dipoles and, therefore, their correlation times were analytically determined at equilibrium [see Eq. (2.17)] and in the limit A [see Eq. (2.18)]. Moreover, they were also numerically determined, as shown in Fig. 2.6. As follows from these results, the correlation times for force dipoles are determined by conformational relaxation times τ_0 and τ_1. In the discussion of conformational relaxation phenomena in proteins in subsection 2.2.4, we have noticed that slow conformational relaxation processes, involving relative domain motions in real enzymes, would usually lie in the microsecond to millisecond range. Hence, correlation times for force dipoles of the enzymes would be typically longer than their orientational correlation times.

Below, we assume that the orientational correlation time is much shorter than the correlation time for force dipoles. By using Eq. (2.39) and putting $C(t) \approx C(0) = \langle \Delta m^2 \rangle$ in Eq. (2.38), we approximately find

$$\chi - \chi_{\rm eq} = \tau_{\rm rot} \langle \Delta m^2 \rangle_{\rm A}. \tag{2.41}$$

Hence, the change in the diffusion coefficient can be estimated as

$$D_{\rm A} = \frac{\tau_{\rm rot} n}{60 \pi \mu^2 \ell_{\rm cut}} \langle \Delta m^2 \rangle_{\rm A}. \tag{2.42}$$

Substituting approximate analytical expressions for $\langle \Delta m^2 \rangle_{\rm A}$ in different limiting regimes, obtained in subsection 2.2.2, or using the numerical data from subsection 2.2.3, we can now estimate and analyze diffusion enhancement.

Particularly, it was found in subsection 2.2.3 that $\langle \Delta m^2 \rangle_{\rm A}$ for active dimers has a Michaelis-Menten dependence on the substrate concentration. As follows from the above equation, the same dependence should hold for $D_{\rm A}$. As could have been expected, the highest diffusion enhancement is reached under the

condition of substrate saturation for the enzymes. Under substrate saturation, the intensity of force dipoles depends, as demonstrated in subsections 2.2.2 and 2.2.3, on the properties of the turnover cycle of an enzyme. The highest intensity is found in regime B, i.e., when there is no long waiting time for product release, and the turnover rates are limited by conformational transitions within the catalytic cycle (adenylate kinase is an example of such an enzyme).

In such asymptotic regime, $\langle \Delta m^2 \rangle_{\mathrm{A}}$ is given by Eq. (2.35) provided that the condition $k\ell_0^2 \gg k_{\mathrm{B}}T$ holds. Substituting this expression into Eq. (2.42), we obtain

$$\frac{D_{\mathrm{A}}}{D_{\mathrm{T}}} = \frac{\nu R_0}{R_0 + \ell_0} \left(\frac{\ell_0}{\Delta\ell}\right)^2 \left(\frac{\ell_0}{\ell}\right)^3 \left(\frac{\Delta E}{k_{\mathrm{B}}T}\right)^2. \tag{2.43}$$

Here, R_0 is the radius of a tracer particle, ℓ_0 is the characteristic size of an enzyme (i.e., the dimer length), $\Delta\ell$ specifies the magnitude of the conformational change, ΔE is the free energy supplied with the substrate and dissipated within each cycle. For the equilibrium diffusion constant D_{T}, the Stokes equation

$$D_{\mathrm{T}} = \frac{k_{\mathrm{B}}T}{6\pi\mu R_0}. \tag{2.44}$$

has been used. Moreover, the microscopic cut-off length is chosen as $\ell_{\mathrm{cut}} = \ell_0 + R_0$ and $\nu = 4\pi\zeta_1/5$ is a numerical factor of order unity.

Equation (2.43) can be employed to estimate the maximum relative diffusion enhancement for passive particles that can be obtained, under substrate saturation, in water solutions of enzymes. For numerical order-of-magnitude estimates, we consider exothermic enzymes with $\Delta E = 10\, k_{\mathrm{B}}T$ and $\Delta\ell = 0.1\ell_0$. As the enzyme concentration, we take $n = 1\,\mu$M. This corresponds to a noncrowded solution where the mean distance between the enzymes is about ten times larger than their size ($\ell \sim 10\ell_0$). Moreover, we consider passive particles with the sizes comparable to that of an enzyme ($R_0 \sim \ell_0$). Under these conditions, we have $D_{\mathrm{A}} \sim 10 D_{\mathrm{T}}$, i.e., diffusion of tracer particles is ten times faster in the solution of catalytically active enzymes.

Dependence of diffusion enhancement on the orientational correlation time

is additionally discussed in Appendix 2.D.

2.3.2 Diffusion effects of active protein inclusions in biomembranes

It is known that, on the length scales shorter than the Saffman-Delbrück length of about a micrometer, lipid bilayers behave as 2D fluids [2.8]. Similar to enzymes in water solutions, active protein inclusions (such as ion pumps or transporters) can cyclically change their shapes inside a lipid bilayer within each ligand turnover cycle. Hence, they behave as hydrodynamical force dipoles within a fluid lipid bilayer. Therefore, diffusion enhancement is expected for biomembranes when nonequilibrium conformational activity of proteins takes place [2.12].

A significant difference to water solution is that, for the biomembranes as 2D fluids, hydrodynamic diffusion enhancement effects are nonlocal. For such systems, Eq. (2.37) is replaced by [2.12, 2.14]

$$D_{\mathrm{A},\alpha\alpha'}(\mathbf{R}) = \frac{1}{32\pi^2\mu_{\mathrm{2D}}^2}(\chi-\chi_{\mathrm{eq}})\int d\mathbf{r}\,\frac{r_\alpha r_{\alpha'}}{r^4}n_{\mathrm{2D}}(\mathbf{R}+\mathbf{r}). \tag{2.45}$$

Here, χ is again given by Eq. (2.38) with $\sigma(t)$ being the planar orientational correlation function for protein inclusions. Moreover, μ_{2D} is the 2D viscosity of the lipid bilayer, related as $\mu_{\mathrm{2D}} = h\mu_{\mathrm{3D}}$ to its 3D viscosity μ_{3D} (where h is the bilayer thickness); n_{2D} is the 2D concentration of active inclusions within the membrane.

For numerical estimates, we assume that active proteins occupy a small circular region (a raft) of radius R_{m} (shorter than the Saffman-Delbrück length) within a membrane. Then, diffusion enhancement for a passive particle of radius R_0 located in the center of the disc is [2.12, 2.14]

$$D_{\mathrm{A}} = \zeta_{\mathrm{m}}\frac{n_{\mathrm{2D}}}{\mu_{\mathrm{2D}}^2}(\chi-\chi_{\mathrm{eq}}), \tag{2.46}$$

where $\zeta_{\mathrm{m}} = (1/32\pi)\ln(R_{\mathrm{m}}/\ell_{\mathrm{cut}})$, $\ell_{\mathrm{cut}} = R_0+\ell_0$, and χ is given by the integral in Eq. (2.38) where, however, $\sigma(t)$ is the planar orientational correlation function

for proteins inside a membrane.

The viscosity μ_{3D} of lipid bilayers is about 10^3 times higher than that of water and, therefore, both translational and rotational diffusion is much slower in them. From experiments, it is known that diffusion constants for proteins in lipid bilayers are about $D_T = 10^{-10}\,\mathrm{cm}^2/\mathrm{s}$, i.e., about 10^3 times smaller than in water for similar proteins. One can therefore expect that rotational diffusion of proteins in lipid bilayers would be slowed by about a factor of 10^3 too, yielding orientational correlation times τ_{rot} that might approach a millisecond, still being shorter than the turnover time of an enzyme.

The magnitude of diffusion enhancement in Eq. (2.46) can be determined by modeling protein inclusions as active dimers that lie flat in the membrane. Then, the same estimate (2.35) for $\langle \Delta m^2 \rangle_A$ can be used. Combining all terms, diffusion enhancement in Eq. (2.46) for a passive particle in the center of a protein raft approximately is

$$D_A = \nu_m \tau_{rot} \left(\frac{\ell_0}{\Delta \ell} \right)^2 \left(\frac{\Delta E}{h \ell_{2D} \mu_{3D}} \right)^2 , \tag{2.47}$$

where the dimensionless prefactor is $\nu_m = \zeta_1 \zeta_m$ and $\ell_{2D} = n_{2D}^{-1/2}$ is the mean distance between inclusions in the membrane.

To obtain a characteristic order-of-magnitude estimate, the 3D viscosity of the lipid bilayer is chosen as $\mu_{3D} = 1\,\mathrm{Pa{\cdot}s}$ and the thickness of the bilayer as $h = 1\,\mathrm{nm}$. For protein inclusions, we assume that $\Delta E = 10\,k_B T$ and $\Delta \ell \sim \ell_0$. The orientational correlation time is taken to be $\tau_{rot} = 100\,\mu\mathrm{s}$ and the mean lateral distance between the proteins is $\ell_{2D} = 10\,\mathrm{nm}$. For such parameter values, the maximal possible diffusion enhancement under substrate saturation conditions is about $D_A = 10^{-9}\,\mathrm{cm}^2/\mathrm{s}$. For comparison, Brownian diffusion constants for proteins in lipid bilayers are of the order of $10^{-10}\,\mathrm{cm}^2/\mathrm{s}$ and diffusion constants for lipids are about $10^{-8}\,\mathrm{cm}^2/\mathrm{s}$.

2.4 Discussion

Using the results of our study, available experimental and computational data on diffusion enhancement in solutions of catalytically active enzymes can be discussed.

2.4.1 Experimental data

Diffusion enhancement for the enzymes has been reported in solutions of several catalytically active enzymes, at the concentrations varying between 1 nM and 10 nM [2.36, 2.43–2.46]. With the exception of aldolase [2.43] (for which, however, the enhancement could not be independently confirmed [2.47]), all these enzymes were exothermic and had high turnover rates of about $10^4\,\mathrm{s}^{-1}$. The enhancement was reported not only for the enzymes themselves, but also for inert molecules (tracers) surrounding them [2.44, 2.45]. The enzyme concentration dependence of the diffusion enhancement effects could *not* however be detected [2.46].

It does not seem plausible that such experimental data can be understood in the framework of the original theory [2.12] and its subsequent extensions, including the present work. The fact that a significant diffusion enhancement (by tens of percent) was observed already at low nanomole concentrations can still be perhaps explained by assuming that, for some reasons, the force dipoles of specific enzymes with high catalytic turnover rates were exceptionally strong. However, the absence of a dependence of the experimentally observed diffusion enhancement on the enzyme concentration clearly contradicts the theory [2.12] where diffusion enhancement arises as a collective hydrodynamic effect. Effectively, diffusion enhancement was observed in the experiments [2.36, 2.43–2.46] already for single molecules of enzymes.

When our study was completed, an interesting publication [2.48] has appeared where diffusion enhancement was demonstrated by a different method for several other reactions. Since catalyst's diffusion was not affected by its concentration, this was again a single-particle property not covered by the the-

ory [2.12].

Experiments on optical tracking of particles in animal cells [2.49] and in bacteria or yeast [2.50] have been furthermore performed. They have shown that, when metabolism was suppressed (by depletion of ATP), diffusion dropped to undetectable levels [2.49, 2.51] or it was much slowed down and replaced by subdiffusion characteristic for a colloidal glass [2.50]. Strong reduction of diffusion under metabolism suppression was moreover found in various cytoplasm extracts [2.52].

It should be also noted that diffusion enhancement has been experimentally observed within chromatin in a living biological cell [2.53]. This was explained by active operation of molecular machines involved in transcription and translation of DNA [2.54].

The cytoplasm of a living cell represents a crowded solution of proteins. In bacteria, the volume fraction of proteins in cytosol is about 30 percent [2.55], with the highest concentrations of the order of $100\,\mu$M reached for glycolysis enzymes. Most of the enzymes in the cell are mechanochemical, i.e., they exhibit conformational changes in their catalytic cycles. Typical turnover times of enzymes in a biological cell are of the order of 10 ms.

According to the previous [2.12] and current estimates, substantial diffusion enhancement due to hydrodynamic collective effects should thus be expected under metabolism in the cytoplasm. There are, however, also other mechanisms that can contribute to diffusion enhancement in the cells.

The cytoskeleton of animal cells represents an active gel, with numerous myosin molecular motors operating within it. It is known that the activity of the motors can lead to development of nonequilibrium fluctuations in the cytoskeleton which induce in turn fluctuations and diffusion enhancement in the cytosol [2.17, 2.51, 2.56]. The skeleton of bacteria and yeast is however passive; moreover, metabolic diffusion enhancement in such cells could also be observed when their skeleton was chemically resolved [2.50]. Therefore, the active gel

mechanism [2.56] cannot account for the effects observed in them.

On the other hand, under high crowding characteristic for cytoplasm, proteins are frequently colliding and direct interactions between them often take place [2.40, 2.42]. It is known that, for dense colloids, glass behavior can be expected, with the transport and relaxation phenomena strongly slowed down in them [2.57]. Indeed, such behavior could be observed both in the cells [2.50] and in the extracts [2.52] in the absence of metabolism.

It has been recently shown that, when the particles forming a glass-like colloid, cyclically change their shapes, the colloid gets fluidized and classical transport properties become restored [2.58, 2.59]. Even in the absence of hydrodynamic interactions, conformational activity of proteins, at the rates of energy supply of about $10\,k_{\mathrm{B}}T$ per a protein molecule per a cycle, can lead to diffusion enhancement by one order of magnitude [2.58]. This provides an additional, non-hydrodynamic, mechanism that can contribute to the experimentally observed diffusion enhancement in living biological cells.

In summary, the analysis of the available experimental data reveals that the predicted diffusion enhancement [2.12] for passive particles caused by collective catalytic activity of enzymes could not so far been reliably confirmed.

2.4.2 Computational data

Large-scale computer simulations for colloids of active dimers have been performed by Dennison, Kapral and Stark [2.20]. In these simulations, the solvent was explicitly included and the multiparticle collision dynamics (MPCD) approximation [2.60] was employed, thus allowing to fully account for hydrodynamic effects.

To facilitate the comparison, we first give a summary of the essential parameter values in the study [2.20], using the current notations employed by us. The natural lengths of the dimer in two ligand states were ℓ_0 and $\ell_1 = \ell_0/2$, and the spring constants were k_0 and $k_1 = 2k_0$. The dimensionless spring constant $k\ell_0^2/(k_{\mathrm{B}}T)$, characterizing stiffness of the dimer, was varied between 144

and 1440. The energy $\Delta E = (1/2)(k_0 + k_1)(\ell_0 - \ell_1)^2$, supplied to a dimer and dissipated by it as heat within a single cycle, was changing therefore between $121.5\, k_{\rm B}T$ and $1215\, k_{\rm B}T$. The simulations were performed under substrate saturation conditions. Product formation and release were possible within a window of half-width $\rho = 0.025\ell_0$ near $x = \ell_1$. The rate v_1 of this transition could be varied in the simulations by a factor of 5.

The Langevin equation (2.5) with viscous friction and thermal noise was not used. Instead, collisions between the two beads of the dimer and the solvent particles were explicitly taken into account in the framework of MPCD. For a single passive dimer, the equilibrium correlation function of force dipoles $C_{\rm eq}(t)$ was computed yielding the correlation time for fluctuations of its force dipole; this function could be well fitted to the theoretical dependence in Eq. (2.17). Note that, when $k_0\ell_0^2/(k_{\rm B}T) \gg 1$, the relaxation time $\tau_0 = (\gamma k_0)^{-1}$ of the dimer should be close to this correlation time. Moreover, we have $\tau_1 = (\gamma k_1)^{-1} = \tau_0/2$. Using such estimates, it can be shown that $w_1\tau_1$ varied between 0.001 and 0.1 in the simulations [2.20]. Because substrate saturation was assumed, conditions $w_0\tau_0 \gg 1$ and $w_1\tau_1 \ll 1$ corresponding to the limit D in Sec. 2.2.2 were therefore approximately satisfied.

For single active dimers, correlation functions $C(t)$ of force dipoles were determined [2.20]. They showed damped oscillations and were similar to the correlation function for $v_0\tau_0 = 3$ in Fig. 2.6. The correlation times varied, but remained of the same order of magnitude as the correlation time of the passive dimer. The force-dipole intensity $\langle \Delta m^2 \rangle$ of active dimers was by about an order of magnitude larger than $\langle \Delta m^2 \rangle_{\rm eq}$ for the passive ones. Depending on the parameters, it scaled as k_0^α with the exponent α in the range between 1.2 and 1.6, comparable with the exponent of 1.5 in Eq. (2.29).

Orientational correlation functions $\sigma(t)$ were furthermore computed for single dimers [2.20]. Remarkably, it was found that the orientational correlation time $\tau_{\rm rot}$ was sensitive to the conformational activity of the dimer, getting shorter by

about an order of magnitude when such activity was switched on. Nonetheless, in all simulations τ_{rot} was larger than the force dipole correlation time.

Multiparticle 3D computer simulations of colloids formed by active dimers were further performed [2.20]. In the simulations, the truncated potential

$$u(r) = 4\epsilon \left[\left(\frac{2r_0}{r} \right)^{48} - \left(\frac{2r_0}{r} \right)^{24} + \frac{1}{4} \right], \tag{2.48}$$

for $r < 2^{1/24}(2r_0)$ and zero otherwise, with $\epsilon = 2.5\, k_{\mathrm{B}}T$ and $r_0 = 1.075\ell_0$, was used to describe steep repulsive interactions between the beads belonging to different dimers. The interaction radius r_0 was chosen as defining the radius of a bead.

Since distances ℓ_0 and $\ell_1 = 0.5\ell_0$ in the open and closed dimer conformations were both smaller than $2r_0 = 2.15\ell_0$, large overlaps between the beads in a dimer were present in the simulations. However, this did not affect the internal dimer dynamics because there were no repulsive interactions between the beads in the same dimer. Additionally, the simulated system included one passive tracer particle of radius $0.5\ell_0$.

The volume fraction ϕ occupied by dimers was determined by taking into account the overlaps, but assuming that all dimers were in the equilibrium open state with the length of ℓ_0. Because, under substrate saturation conditions, they were however mainly found in the closed state with an even stronger overlap, such definition overestimated the actual volume fraction by a factor of up to two.

Due to the crowding effects, diffusion of a passive particle in the system of inactive dimers decreased with the volume fraction of them. The diffusion reduction at the highest taken volume fraction $\phi = 0.266$ was less than ten percent, indicating that this colloidal system was still far from the glass transition threshold [2.57].

When the dimers were active, diffusion of tracers was increasing instead with the dimer volume fraction ϕ. For the most stiff active dimers with $k_0\ell_0^2/(k_{\mathrm{B}}T) =$

1440 and the kinetic regime with $w_1\tau_1$ about 0.1, relative diffusion enhancement of $D_{\rm A}/D_{\rm T} = 0.3$ could be observed [2.20] at the dimer volume fraction of $\phi = 0.266$. For the least stiff dimers with $k_0\ell_0^2/(k_{\rm B}T) = 144$, diffusion enhancement by 5 percent was seen at $\phi = 0.133$.

Thus, collective hydrodynamic effects of active enzymes on diffusion of passive particles could be computationally confirmed. To speed up the calculations, model enzymes in the study [2.20] were chosen however to be unusually rapid (with the turnover times shorter than the rotational diffusion time) and unusually exothermic (with the heat release of hundreds of $k_{\rm B}T$ per a turnover cycle). It would be therefore important to undertake such simulations also for the parameters closer approaching those of the real enzymes.

2.5 Conclusion

To our knowledge, the present work is the first study where hydrodynamic force dipoles of mechanochemical enzymes have been systematically analyzed. Although the analysis has been performed for an idealized model, order-of-magnitude estimates for the intensity of such dipoles for characteristic enzymes, such as adenylate kinase, and for protein machines, such as myosin, have been obtained.

We have also examined for what kinds of enzymes strong hydrodynamic effects may be expected. Our analysis reveals that, in the framework of the investigated model, these should be very rapid, highly exothermic and stiff enzymes, where the energy is dissipated in mechanical motions of a small amplitude. It is interesting to note that these general conditions are indeed satisfied, for example, for catalase or urease.

Using the derived statistical properties of force dipoles in the dimer model, more accurate estimates for diffusion enhancement for surrounding passive particles in solutions of active enzymes were obtained.

Based on these results, currently available experimental and computational

data has been examined. We have concluded that, while the collective hydrodynamic effects of diffusion enhancement have been principally confirmed in the computational study [2.20], further work is needed to bring simulations closer to the parameter region corresponding to real enzymes.

On the experimental side, we have concluded that the data on diffusion enhancement in weak nanomole solutions of several fast exothermic enzymes cannot be explained in the framework of the theory [2.12] and alternative explanations for them should be sought. In experimental studies of diffusion phenomena in living cells and in cellular extracts, additional work is needed to distinguish possible hydrodynamic contributions from the effects of direct collisions between active proteins and the resulting kinetic crowding effects. Large-scale numerical simulations of crowded active colloids including hydrodynamic interactions between the particles are to be performed. It should be also pointed out that, although the effects of diffusion enhancement are also predicted for biomembranes crowded with active protein inclusions, experiments and numerical multiparticle simulations of such phenomena are still missing today; it would be interesting to carry them out.

It was not the aim of the present work to provide a review of all proposed mechanisms for diffusion enhancement effects. Especially, we have not considered possible origins of diffusion enhancement for single catalytically active enzymes, even though this question attracts much attention in view of the recent research [2.45, 2.46, 2.48]. Our focus was on diffusion enhancement for passive particles caused by hydrodynamic collective stirring of the solution by a population of active particles that cyclically change their shapes, but do not propel themselves.

In the future, the active dimer model can be used to develop stochastic thermodynamics of mechanochemical enzymes. It would be important to investigate in detail hydrodynamic effects, accompanying functional conformational transitions, in all-atom or coarse-grained molecular dynamics simulations for specific

enzymes and protein machines.

Appendix 2.A Transition probabilities

When transitions between the states $s = 0$ and $s = 1$ are rare, the solution of the master equations (2.7) and (2.8) can be approximately sought in the form

$$p_s(x,t) = \pi_s(t)p(x,t|s), \tag{2.A1}$$

where $\pi_s(t)$ is the probability to find the dimer in the ligand state s and $p(x,t|s)$ is the probability distribution for distance x provided that the dimer is (permanently) in the state s.

Substituting these expressions into Eqs. (2.7) and (2.8) and integrating over the variable x, one finds that the probabilities π_s obey classical master equations for a two-level system,

$$\frac{d\pi_0}{dt} = w_1\pi_1 - w_0\pi_0, \tag{2.A2}$$

and

$$\frac{d\pi_1}{dt} = w_0\pi_0 - w_1\pi_1. \tag{2.A3}$$

Here w_0 and w_1 are effective rates of transitions between the states given by

$$w_0 = \int_{-\infty}^{\infty} dx\, u_0(x)p(x|s=0), \tag{2.A4}$$

and

$$w_1 = \int_{-\infty}^{\infty} dx\, u_1(x)p(x|s=1). \tag{2.A5}$$

The involved probability distributions in the statistically stationary case are

$$p(x|s=0) = \sqrt{\frac{k_0}{2\pi k_{\rm B}T}}\exp\left[-\frac{k_0}{2k_{\rm B}T}(x-\ell_0)^2\right], \tag{2.A6}$$

and

$$p(x|s=1) = \sqrt{\frac{k_1}{2\pi k_{\rm B}T}}\exp\left[-\frac{k_1}{2k_{\rm B}T}(x-\ell_1)^2\right]. \tag{2.A7}$$

If the transition windows are narrow, approximations in Eq. (2.9) can fur-

thermore be used, so that we obtain

$$w_0 = \nu_0 p(x = \ell_0 | s = 0), \qquad w_1 = \nu_1 p(x = \ell_1 | s = 1). \tag{2.A8}$$

Thus, using the above expressions for distance distributions, we finally get

$$w_0 = 2\rho v_0 \sqrt{\frac{k_0}{2\pi k_\mathrm{B} T}}, \tag{2.A9}$$

and

$$w_1 = 2\rho v_1 \sqrt{\frac{k_1}{2\pi k_\mathrm{B} T}}. \tag{2.A10}$$

In the steady state, the probabilities are

$$\pi_0 = \frac{w_1}{w_0 + w_1}, \qquad \pi_1 = \frac{w_0}{w_0 + w_1}. \tag{2.A11}$$

Appendix 2.B Average force dipole

Let us consider the second statistical moment $\langle x^2 \rangle$. In a steady state, its time derivative is zero. On the other hand, by using Eqs. (2.7) and (2.8) and integrating by parts, we find

$$\begin{aligned} \frac{d\langle x^2 \rangle}{dt} &= 2\gamma \int_{-\infty}^{\infty} dx \left[k_0 x(\ell_0 - x) p_0(x) + k_1 x(\ell_1 - x) p_1(x) \right] \\ &\quad + 2\gamma k_\mathrm{B} T \int_{-\infty}^{\infty} dx \left[p_0(x) + p_1(x) \right] \\ &= 2\gamma \langle m \rangle + 2\gamma k_\mathrm{B} T = 0. \end{aligned} \tag{2.B1}$$

Thus, we straightforwardly obtain that, for an active dimer in any statistically steady state, $\langle m \rangle = -k_\mathrm{B} T$.

Note that here and also in the equations below, the integration limits over x are taken as $+\infty$ and $-\infty$. The actual limits are automatically selected by probability distributions $p_0(x)$ and $p_1(x)$.

Appendix 2.C Force-dipole correlation function

Introducing

$$\mathbf{p}(x,t) = \begin{pmatrix} p_0(x,t) \\ p_1(x,t) \end{pmatrix}, \tag{2.C1}$$

we can write the system of two master equations (2.7) and (2.8) concisely as

$$\frac{d\mathbf{p}}{dt} = -\hat{\mathbf{L}}\mathbf{p}, \tag{2.C2}$$

where

$$\hat{\mathbf{L}} = \begin{pmatrix} \hat{L}_{00} & \hat{L}_{01} \\ \hat{L}_{10} & \hat{L}_{11} \end{pmatrix}, \tag{2.C3}$$

and

$$\hat{L}_{00} = \gamma k_0 \frac{\partial}{\partial x}(\ell_0 - x) - \gamma k_{\mathrm{B}} T \frac{\partial^2}{\partial x^2} + u_0(x), \tag{2.C4}$$

and

$$\hat{L}_{11} = \gamma k_1 \frac{\partial}{\partial x}(\ell_1 - x) - \gamma k_{\mathrm{B}} T \frac{\partial^2}{\partial x^2} + u_1(x), \tag{2.C5}$$

and

$$\hat{L}_{01} = -u_1(x), \qquad \hat{L}_{10} = -u_0(x). \tag{2.C6}$$

The general solution of Eq. (2.C2) is

$$p_s(x,t) = \sum_{n=0}^{\infty} A_n q_s^{(n)}(x) e^{-\lambda_n t} + \text{c.c.} \tag{2.C7}$$

where λ_n and $\mathbf{q}^{(n)}$ are eigenvalues and eigenvectors of the linear operator $\hat{\mathbf{L}}$,

$$\hat{\mathbf{L}}\mathbf{q}^{(n)} = \lambda_n \mathbf{q}^{(n)}, \tag{2.C8}$$

and decomposition coefficients A_n are determined by initial conditions.

Because the master equation must have a stable stationary solution, the operator $\hat{\mathbf{L}}$ should always possess a zero eigenvalue $\lambda_0 = 0$ and, furthermore, condition $\mathrm{Re}\,\lambda_n > 0$ should hold for all other eigenvalues n [2.61]. Generally, the eigenvectors can be ordered according to the increase of $\mathrm{Re}\,\lambda_n$ (and therefore we can enumerate the eigenvalues in such a way that $0 < \mathrm{Re}\,\lambda_1 \leq \mathrm{Re}\,\lambda_2 \leq \mathrm{Re}\,\lambda_3 \leq$ ...). The stationary probability distribution $\bar{\mathbf{p}}(x)$ coincides with the eigenvector $\mathbf{q}^{(0)}(x)$.

The conditional probability $G(x, s, t|x_0, s_0)$ gives the probability to find the dimer in various states (x, s) at time t provided that it was in the state (x_0, s_0)

at time $t = 0$. It represents a special solution of the master equation (2.C2) given by

$$G(x, s, t|x_0, s_0) = \sum_{n=0}^{\infty} a_n(x_0, s_0) q_s^{(n)}(x) e^{-\lambda_n t} + \text{c.c.} \tag{2.C9}$$

where $a_n(x_0, s_0)$ are the coefficients of decomposition of this initial condition over eigenvectors $\mathbf{q}^{(n)}$.

The force dipole m depends on the distance x between the domains and on the dimer state s, i.e., $m(t) = m(x(t), s(t))$. Therefore, in the statistically stationary state we have

$$\langle m(t)m(0)\rangle = \sum_{s,s_0=0,1} \int_{-\infty}^{\infty} dx_0 \int_{-\infty}^{\infty} dx\, m(x_0, s_0) m(x, s) \bar{p}_{s_0}(x_0) G(x, s, t|x_0, s_0). \tag{2.C10}$$

By using Eqs. (2.C9) and (2.C10), we find that, in the statistically stationary state, the correlation function of force dipoles is

$$C(t) = \langle m(t)m(0)\rangle - \langle m^2\rangle = \sum_{n=1}^{\infty} B_n e^{-\lambda_n |t|} + \text{c.c.} \tag{2.C11}$$

where the complex coefficients B_n are

$$B_n = \sum_{s,s_0=0,1} \int_{-\infty}^{\infty} dx_0 \int_{-\infty}^{\infty} dx\, m(x_0, s_0) m(x, s) \bar{p}_{s_0}(x_0) a_n(x_0, s_0) q_s^{(n)}(x). \tag{2.C12}$$

If we retain in this decomposition only the first, most slowly decaying term, this yields

$$C(t) \approx B_1 e^{-\lambda_1 |t|} + \text{c.c.} = \frac{C(0)}{\cos\alpha} e^{-\Gamma|t|} \cos(\Omega|t| - \alpha). \tag{2.C13}$$

Therefore, the normalized correlation function is

$$\frac{C(t)}{C(0)} = \frac{1}{\cos\alpha} e^{-\Gamma|t|} \cos(\Omega|t| - \alpha), \tag{2.C14}$$

where $\Gamma = \operatorname{Re}\lambda_1$, $\Omega = \operatorname{Im}\lambda_1$, and $B_1 = C(0)e^{i\alpha}/\cos\alpha$.

Our numerical simulations, described in Sec. 2.2.3, have shown that, in the regimes approaching a deterministic oscillatory dimer, the correlation functions of force dipoles could be well fitted to the above dependence. This suggests that contributions from the higher, more rapidly decaying relaxation modes $n > 1$

have been indeed relatively small. As generally known [2.62], noisy oscillators possess a slowly relaxing mode that corresponds to diffusion of the oscillation phase. It can be expected that, under chosen conditions, such a mode has been dominating the correlation functions for oscillatory dimers.

Appendix 2.D Dependence on orientational correlation time

Suppose that the force-dipole correlation function $C(t)$ and the orientational correlation function $\sigma(t)$ are given by Eqs. (2.C14) and (2.39). By taking the integral in Eq. (2.38), we find

$$\chi = \frac{1/\tau_{\rm rot} + \Gamma + \Omega \tan\alpha}{(1/\tau_{\rm rot} + \Gamma)^2 + \Omega^2} \langle \Delta m^2 \rangle. \tag{2.D1}$$

This yields a nonmonotonous dependence of χ on the orientational correlation time. If the phase shift α is small and can be neglected (cf. Fig. 2.7), the maximum value $\chi_{\rm max}$ is reached at $\tau_{\rm rot} = (\Omega - \Gamma)^{-1}$ and we have

$$\frac{\chi_{\rm max}}{\chi_\infty} = \frac{\Gamma^2 + \Omega^2}{2\Gamma\Omega}, \tag{2.D2}$$

where

$$\chi_\infty = \frac{\Gamma}{\Gamma^2 + \Omega^2} \langle \Delta m^2 \rangle, \tag{2.D3}$$

is the limit of χ when $\tau_{\rm rot} \gg \Gamma^{-1}$ and $\tau_{\rm rot} \gg \Omega^{-1}$.

These results allow us to discuss how the diffusion enhancement would depend on the orientational correlational time $\tau_{\rm rot}$, not assuming that it is much shorter than the correlation time for force dipoles. If the approximation in Eq. (2.30) holds, diffusion enhancement is determined by Eq. (2.37) where χ is given by Eq. (2.D1). The diffusion enhancement depends nonmonotonously on the orientational correlation time. It increases linearly with $\tau_{\rm rot}$ at short times, then reaches a maximum at $\tau_{\rm rot} = (\Omega - \Gamma)^{-1}$ and finally saturates at large orientational correlation times. For example, if we take the values $\Gamma \approx 1/(2\tau_0)$ and $\Omega \approx \pi/(3\tau_0)$ corresponding to substrate saturation in Fig. 2.7, the maximum

diffusion enhancement would be reached at $\tau_{\rm rot} = 1.8\tau_0$ and, at the maximum, it will be larger by about 30 percent than in the limit $\tau_{\rm rot} \gg \tau_0$.

Appendix 2.E Program: Langevin equation in Eq. (2.5)

Here we present the source code for calculating the discretized Langevin equation of Eq. (2.5). The Euler method is used and the dynamical change of x can be obtained by using this code.

Listing 2.1: Main program (output are not written)

```
import os
from os import path
import datetime
import time
from numpy.random import *
import numpy as np
import datetime
import multiprocessing


start = time.time()


class Write():
    def __init__(self):
        pass

    def write_t_x_m_s(self):
        f = open('%s_%0.2fnu0_no%d.txt'%(output0,nu0,
            nthfile), 'w')
        get_parameters(f)
        f.write('#t␣x␣m␣s\n')
        [f.write( str(ts[item]) +'␣'+ '%0.8f'%(xs[item]) +
            '␣'+ '%0.8f'%(ms[item]) +'␣'+ str(ss[item]) +'␣'
            + '\n') for item in range(trueTT)]
        f.close()

    def write_t_submcorr(self):
        f = open('%s_%0.2fnu0_no%d.txt'%(output0,nu0,
            nthfile), 'r')
        ms = np.loadtxt(f, unpack=True, usecols=[2])
        submcorrs = get_correlation(ms)
        f = open('%s_%0.2fnu0_no%d.txt'%(output1,nu0,
            nthfile), 'w')
```

```
30          get_parameters(f)
31          f.write('#t␣submcorr␣\n')
32          [f.write( str(ts[item]) +'␣'+ "%0.8f"%(submcorrs[
               item]) +'␣'+ '\n') for item in range(trueTT)]
33          f.close()
34
35      def write_t_averagedmcorr(self):
36          for j in range(filenum):
37              f = '%s_%0.2fnu0_no%d.txt'%(output1,nu0,j)
38              submcorrs = np.loadtxt(f, unpack=True, usecols
                   =[1])
39              if j == 0:
40                  sums = np.array([0.]*ndelay)
41              sums += submcorrs[:ndelay]
42
43          averagedmcorrs = sums / filenum
44
45          f = open('%s_%0.2fnu0_%dfiles.txt'%(output2,nu0,
               filenum), 'w')
46          get_parameters(f)
47          f.write('#t␣averagedmcorr\n')
48          [f.write( str(ts[item]) +'␣'+ "%0.8f"%(
               averagedmcorrs[item])  + '\n') for item in range
               (ndelay)]
49          f.close()
50
51          f = open('%s_%0.2fnu0_%dfiles.txt'%(output3,nu0,
               filenum), 'w')
52          get_parameters(f)
53          f.write('#t␣scaledaveragedmcorr\n')
54          [ f.write( str(ts[item]) +'␣'+ "%0.8f"%(
               averagedmcorrs[item]/averagedmcorrs[0])  + '\n')
                for item in range(ndelay)]
55          f.close()
56
57
58
59  nu0s = [40]
60
61
62  # parameters
63  theta = 0.0018
64  A = np.sqrt(2*theta) # magnitude of thermal noise
65  LC = float(0.1) # l_c/l_0
66  L1 = (LC + 1.0) / 2.0 # l_1/l_0
67  nu0 = float(0) # transition rate into s=1
68  nu1 = float(2) # transition rate into s=0
69  WDT = float(10 ** -2) # width of interval for transition
70  DT = float(10 ** -3) # time interval
```

```
71 TT = 10 ** 6  # total steps
72 TOUT = 50 # how often it is printed out
73 trueTT = int(TT/TOUT)
74 SD = np.sqrt(DT) # standard deviation
75 delay = 100 # delay time for correlation function is taken
       up to here
76 ndelay = int((delay/DT)/TOUT) # delay time step for
       correlation function
77 ts = [i*TOUT*DT for i in range(trueTT)]
78 W01 = int(0)
79 W10 = int(0)
80
81
82 # positions
83 t = float(0)
84 x = float(0)
85 s = 0
86 m = float(0)
87 xs = []
88 ss = []
89 ms = []
90
91
92 staato = 0
93 filenum = 10 # number of files
94 data = [i for i in range(0,filenum)]
95 corenumber = 10
96 splitnum = int(filenum/corenumber)
97 split_data = [data[i:i+splitnum] for i in range(staato,
       filenum,splitnum)]
98
99
100 filename = path.basename(__file__)
101 name, ext = path.splitext(filename)
102 cd = path.dirname( path.abspath(__file__))
103 today = datetime.datetime.today()
104 newname = "%s_%s"%(name,today)
105 folders = [ "t_x_m_s", "t_submcorr", "t_averagedmcorr", "
       t_scaledaveragedmcorr"]
106 folder0 = folders[0]
107 folder1 = folders[1]
108 folder2 = folders[2]
109 folder3 = folders[3]
110 cwd = "%s/%s"%(cd,newname) # current working directory
111 os.mkdir(cwd)
112 [ os.mkdir("%s/%s"%(cwd,folders[i])) for i in range(len(
       folders))]
113 output0 = "%s/%s/t_x_m_A%0.2f"%(cwd,folder0,A)
114 output1 = "%s/%s/t_submcorr_A%0.2f"%(cwd,folder1,A)
```

```
115 output2 = "%s/%s/t_avemcorr_A%0.2f"%(cwd,folder2,A)
116 output3 = "%s/%s/t_scaledavemcorr_A%0.2f"%(cwd,folder3,A)
117
118
119 def get_parameters(f):
120     f.write("#source␣filename:%s\n"%(filename))
121     f.write('#theta␣=␣%03.3f\n'%(theta))
122     f.write('#A␣=␣%03.3f\n'%(A))
123     f.write('#LC␣=␣%03.3f\n'%(LC))
124     f.write('#L1␣=␣%03.3f\n'%(L1))
125     f.write('#nu0␣=␣%03.3f\n'%(nu0))
126     f.write('#nu1␣=␣%03.3f\n'%(nu1))
127     f.write('#W01␣=␣%03.3f\n'%(W01))
128     f.write('#W10␣=␣%03.3f\n'%(W10))
129     f.write('#WDT␣=␣%03.3f\n'%(WDT))
130     f.write('#DT␣=␣%03.3f\n'%(DT))
131     f.write('#TT␣=␣%03.3f\n'%(TT))
132     f.write('#TOUT␣=␣%03.3f\n'%(TOUT))
133
134
135 def get_difference():
136     now = int(time.time())
137     seed(now+100*nthfile)
138     dx = - ( (x - 1) + s * (x - LC))* DT + A * SD * randn
           ()
139     return dx
140
141 def get_m():
142     return - x * ( (x - 1.) + s * (x - LC) )
143
144 def get_correlation(X):
145     n = len(X)
146     X = X - np.mean(X)
147     correlation = np.zeros(n)
148     for i in range(ndelay):
149         if i == 0:
150             correlation[0] = np.sum(X*X) / n
151         else:
152             correlation[i] = np.sum(X[i:]*X[:-i]) / (n-i)
153     return correlation
154
155 def worker(data):
156     [calc(x) for x in data]
157
158 def calc(X):
159     global x,m,s,xs,ms,ss,nthfile,W01,W10
160     xs = []
161     ms = []
162     ss = []
```

```
163     x = float(1.0) # initial position
164     s = int(0) # initial state
165     m = get_m()
166     xs.append(x)
167     ms.append(m)
168     ss.append(s)
169 
170     W01 = nu0 * DT # transition probability from s=0 into
            s=1
171     W10 = nu1 * DT # transition probability from s=1 into
            s=0
172 
173     nthfile = X
174 
175     for i in range(1, TT+1):
176         if s == 0 and x > (1-WDT) and x < (1+WDT) and rand
                () < W01:
177             s = 1
178         elif s == 1 and x > (L1-WDT) and x < (L1+WDT) and
                rand() < W10:
179             s = 0
180         x += get_difference()
181         m = get_m()
182         if (i%TOUT) == 0:
183             xs.append(x)
184             ms.append(m)
185             ss.append(s)
186 
187     write.write_t_x_m_s()
188 
189     write.write_t_submcorr()
190 
191 
192 write = Write()
193 
194 
195 for nu0 in nu0s:
196     jobs = []
197     for data in split_data:
198         job = multiprocessing.Process(target=worker, args
                =(data, ))
199         jobs.append(job)
200         job.start()
201 
202     [job.join() for job in jobs]
203 
204     write.write_t_averagedmcorr()
```

References

[2.1] A. Cressman, Y. Togashi, A. S. Mikhailov, and R. Kapral, Phys. Rev. E **77**, 050901 (2008).

[2.2] C. Echeverria, Y. Togashi, A. S. Mikhailov, and R. Kapral, Phys. Chem. Chem. Phys. **13**, 10527 (2011).

[2.3] R. Golestanian and A. Ajdari, Phys. Rev. Lett. **100**, 038101 (2008).

[2.4] R. Golestanian and A. Ajdari, J. Phys.: Cond. Matt. **21**, 204104 (2009).

[2.5] M. Iima and A. S. Mikhailov, EPL **85**, 44001 (2009).

[2.6] T. Sakaue, R. Kapral, and A. S. Mikhailov, Eur. Phys. J. B **75**, 381 (2010).

[2.7] X. Bai and P. Wolynes, J. Chem. Phys. **143**, 165101 (2015).

[2.8] H. Diamant, J. Phys. Soc. Jpn. **78**, 041002 (2009).

[2.9] M.-J. Huang, A. S. Mikhailov, R. Kapral, and H.-Y. Chen, J. Chem. Phys. **137**, 055101 (2012).

[2.10] M.-J. Huang, A. S. Mikhailov, R. Kapral, and H.-Y. Chen, J. Chem. Phys. **138**, 195101 (2013).

[2.11] M.-J. Huang, H.-Y. Chen, and A. S. Mikhailov, Eur. Phys. J. E **35**, 1 (2012).

[2.12] A. S. Mikhailov and R. Kapral, Proc. Natl. Acad. Sci. USA **112**, E3639 (2015).

[2.13] R. Kapral and A. S. Mikhailov, Physica D **318–319**, 104 (2016).

[2.14] A. S. Mikhailov, Y. Koyano, and H. Kitahata, J. Phys. Soc. Jpn. **86**, 101013 (2017).

[2.15] Y. Koyano, H. Kitahata, and A. S. Mikhailov, Phys. Rev. E **94**, 022416 (2016).

[2.16] Y. Hosaka, K. Yasuda, R. Okamoto, and S. Komura, Phys. Rev. E **95**, 052407 (2017).

[2.17] K. Yasuda, R. Okamoto, S. Komura, and A. S. Mikhailov, EPL **117**, 38001 (2017).

[2.18] K. Yasuda, R. Okamoto, and S. Komura, Phys. Rev. E **95**, 032417 (2017).

[2.19] Y. Hosaka, S. Komura, and D. Andelman, Phys. Rev. E **101**, 012610 (2020).

[2.20] M. Dennison, R. Kapral, and H. Stark, Soft Matter **13**, 3741 (2017).

[2.21] F. Kogler, Interactions of artificial molecular machines, Diploma thesis, Technical Univ. of Berlin, Berlin (2012).

[2.22] P. Illien, T. Adeleke-Larodo, and R. Golestanian, EPL **119**, 40002 (2017).

[2.23] H. Flechsig and A. S. Mikhailov, J. Roy. Soc. Interface **16**, 20190244 (2019).

[2.24] J.-H. Prinz, H. Wu, M. Sarich, B. Keller, M. Senne, M. Held, J. D. Chodera, C. Schütte, and F. Noé, J. Chem. Phys. **134**, 174105 (2010).

[2.25] D. E. Shaw, P. Maragakis, K. Lindorff-Larsen, S. Piana, R. O. Dror, M. P. Eastwood, J. A. Bank, J. M. Jumper, J. K. Salmon, Y. Shan, and W. Wriggers, Science **330**, 341 (2010).

[2.26] H. P. Lu, L. Xun, and X. S. Xie, Science **282**, 1887 (1998).

[2.27] H.-P. Lerch, R. Rigler, and A. S. Mikhailov, Proc. Natl. Acad. Sci. USA **102**, 10807 (2005).

[2.28] M. Gur, E. Zomot, and I. Bahar, J. Chem. Phys. **139**, 121912 (2013).

[2.29] K. A. Henzler-Wildman, V. Thai, M. Lei, M. Ott, M. Wolf-Watz, T. Fenn, E. Pozharski, M. A. Wilson, G. A. Petsko, M. Karplus, C. G. Hübner, and D. Kern, Nature **450**, 838 (2007).

[2.30] Y. Togashi and A. S. Mikhailov, Proc. Natl. Acad. Sci. USA **104**, 8697 (2007).

[2.31] H. Flechsig and A. S. Mikhailov, Proc. Natl. Acad. Sci. USA **107**, 20875 (2013).

[2.32] M. Hinczewski, R. Tehver, and D. Thirumalai, Proc. Natl. Acad. Sci. USA **110**, E4059 (2013).

[2.33] K. Shiroguchi, H. F. Chin, D. E. Hannemann, E. Muneyuki, E. M. D. L. Cruz, and K. K. Jr., Proc. Natl. Acad. Sci. USA **9**, e1001031 (2011).

[2.34] N. Kodera, D. Yamamoto, R. Ishikawa, and T. Ando, Nature **468**, 72 (2010).

[2.35] J. M. Berg, L. Stryer, J. Tymoczko, and G. Gatto, *Biochemistry*, 9th ed. (WH Freeman, 2019).

[2.36] C. Riedel, R. Gabizon, C. A. M. Wilson, K. Hamadani, K. Tsekouras, S. Marqusee, S. Pressé, and C. Bustamante, Nature **517**, 227 (2015).

[2.37] R. Inoue, R. Biehl, T. Rosenkranz, J. Fitter, M. Monkenbusch, A. Radulescu, B. Farago, and D. Richter, Biophys. J. **99**, 2309 (2010).

[2.38] J. Schonfield, P. Inder, and R. Kapral, J. Chem. Phys. **136**, 205101 (2012).

[2.39] P. Gouet, H.-M. Jouve, P. A. Williams, I. Andersson, P. Andreoletti, L. Nussaume, and J. Hajdu, Nature Struct. Biol. **3**, 951 (1996).

[2.40] S. von Bülow, M. Siggel, M. Linke, and G. Hummer, Proc. Natl. Acad. Sci. USA **116**, 9843 (2019).

[2.41] Z. Bashardanesh, J. Elf, H. Zhang, and D. van der Spoel, ACS Omega **4**, 20654 (2019).

[2.42] G. Nawrocki, A. Karaboga, Y. Sugita, and M. Feig, Phys. Chem. Chem. Phys. **21**, 876 (2019).

[2.43] P. Illien, X. Zhao, K. Dey, P. J. Butler, A. Sen, and R. Golestanian, Nano Lett. **17**, 4415 (2017).

[2.44] K. K. Dey, Angew. Chem. Int. Ed. **58**, 2208 (2019).

[2.45] A.-Y. Jee, S. Dutta, Y.-K. Cho, T. Tlusty, and S. Granick, Proc. Natl. Acad. Sci. USA **115**, 14 (2018).

[2.46] M. Xu, J. L. Ross, L. Valdez, and A. Sen, Phys. Rev. Lett. **123**, 128101 (2019).

[2.47] Y. Zhang, M. J. Armstrong, N. M. B. Kazeruni, and H. Hess, Nano Lett. **18**, 8025 (2018).

[2.48] H. Wang, M. Park, R. Dong, J. Kim, Y.-K. Cho, T. Tlusty, and S. Granick, Science **369**, 537 (2020).

[2.49] M. Guo, A. J. Ehrlicher, M. H. Jensen, M. Renz, J. R. Moore, R. D. Goldman, J. Lippincott-Schwartz, F. C. MacKintosh, and D. A. Weitz, Cell **158**, 822 (2014).

[2.50] B. R. Parry, I. V. Surovtsev, M. T. Cabeen, C. S. O'Hem, E. R. Dufresne, and C. Jacobs-Wagner, Cell **156**, 183 (2014).

[2.51] E. Fodor, M. Guo, N. S. Gov, P. Visco, D. A. Weitz, and F. van Wijland, EPL **110**, 48005 (2015).

[2.52] K. Nishizawa, K. Fujiwara, N. Ikenaga, N. Nakajo, and D. Mizuno, Sci. Rep. **7**, 15143 (2017).

[2.53] S. C. Weber, A. J. Spakowitz, and J. A. Theriot, Proc. Natl. Acad. Sci. USA **109**, 7338 (2012).

[2.54] R. Bruinsma, A. Y. Grosberg, Y. Rabin, and A. Zidovska, Biophys. J **106**, 1871 (2014).

[2.55] A. Vendeville, D. Lariviere, and E. Fourmentin, FEMS Microbiol. Rev. **35**, 395 (2010).

[2.56] F. C. MacKintosh and A. J. Levine, Phys. Rev. Lett. **100**, 018104 (2008).

[2.57] G. L. Hunter and E. R. Weeks, Rep. Prog. Phys. **75**, 066501 (2012).

[2.58] Y. Koyano, H. Kitahata, and A. S. Mikhailov, EPL **128**, 40003 (2019).

[2.59] N. Oyama, T. Kawasaki, H. Mizuno, and A. Ikeda, Phys. Rev. Research **1**, 032038 (2019).

[2.60] R. Kapral, Adv. Chem. Phys. **140**, 89 (2008).

[2.61] H. Risken, *The Fokker-Planck Equation: Methods of Solution and Applications* (Springer, Berlin, 1989).

[2.62] Y. Kuramoto, *Chemical Oscillations, Waves and Turbulence* (Springer, Berlin, 1984).

Chapter 3

Shear Viscosity of Two-State Enzyme Solutions †

3.1 Introduction

Molecular enzymes are nanometer-size proteins that catalyze chemical reactions in the presence of *substrate* molecules. Here substrates are chemical species that react with enzymes and generate product molecules. Catalytic processes that are carried out by molecular enzymes in the cytoplasm and the membrane are essential for cellular metabolism and homeostasis [3.1]. In the presence of a substrate, enzymes undergo conformational changes in each turnover cycle of the chemical reaction [3.2]. In order to mimic actual enzymes, these conformational dynamics have been simulated using elastic network models [3.3–3.5], and the relationship between conformational dynamics and the chemical reaction stages has been studied recently [3.6].

One of the long-standing and interesting questions in the field is whether a single enzyme exhibits a motile behavior [3.7]. Thanks to recent developments of experimental techniques, diffusion phenomena in enzyme solutions have been studied by several groups. Using fluorescence correlation spectroscopy, Muddana

†The material presented in this chapter was published in: Y. Hosaka, S. Komura, and D. Andelman, Phys. Rev. E **101**, 012610 (2020).

et al. [3.8] reported that diffusion of a single enzyme is enhanced in presence of a substrate. Later on, Riedel *et al.* [3.9] showed that the heat released during turnovers also enhances the enzyme diffusion. Illien *et al.* [3.10] however, revealed experimentally that not only exothermic enzymes but also endothermic ones contribute to the diffusion enhancement. In the presence of a gradient in substrate concentrations, enzymes exhibit collective motions in the direction of higher or lower concentrations [3.11, 3.12]. Moreover, the enhanced diffusion of passive objects in enzymatic solutions have been observed independently [3.13, 3.14].

To understand these experimental findings, several models have been proposed using equilibrium as well as nonequilibrium approaches. Illien *et al.* [3.15] modeled an enzyme consisting of hydrodynamically coupled subunits, and introduced two discrete equilibrium states corresponding to a free enzyme and a substrate-enzyme complex. They showed that diffusion of an enzyme is enhanced due to equilibrium fluctuations [3.15, 3.16]. Within a nonequilibrium framework, Golestanian [3.17] proposed four possible mechanisms leading to diffusion enhancement by enzymes. They included self-thermophoresis, boost in kinetic energy, stochastic swimming, and collective heating. Mikhailov and Kapral [3.18, 3.19] modeled an enzyme as an active force dipole that exerts forces on the surrounding fluid. When such dipoles are immersed in aqueous fluids, hydrodynamic collective effects due to force dipoles can lead to diffusion enhancement [3.18–3.20].

In spite of these extensive studies on enzyme diffusion, a recent experimental work pointed out the difficulty of accounting quantitatively for the observed enhanced diffusion within such models as above [3.21]. Moreover, recent experiments did not observe any change in the diffusion behavior for a specific enzyme that was previously reported to exhibit enhanced diffusion [3.22, 3.23]. It was also noticed that the viscosity of enzyme solutions is locally reduced while a specific enzymatic reaction is taking place [3.7, 3.24]. However, the effect of enzyme

conformational changes on the solution shear viscosity has not been considered theoretically despite its importance.

In this paper, we present an analytical study on the shear viscosity of a dilute enzyme solution under steady shear flow. As a coarse-grained model of catalytic enzymes, we use the two-state dimer model in which conformational changes are induced by substrate binding and product release [3.18]. Our two-state dimer model consists of two hard spheres representing enzymatic domains, which are connected by a harmonic spring [3.18, 3.25, 3.26]. Assuming that the conformational distribution is given by the Boltzmann distribution function, weighted by the waiting time of an enzyme, we obtain analytically the shear viscosity of a two-state dimer solution as a function of the substrate concentration. As a result of the competition between the energy difference of the enzyme two internal states and the substrate concentration, we find that the enzyme solution viscosity exhibits a nonmonotonic behavior that depends on the physical properties of the binding substrates. We shall also connect the obtained viscosity with the diffusion coefficient of a tracer particle in enzyme solutions.

The outline of our manuscript is the following. In Sec. 3.2, we review the derivation of the shear viscosity of dimer solutions originally used to describe polymer solutions. In Sec. 3.3, we discuss the shear viscosity of a two-state dimer solution that represents enzyme solutions. We first introduce the two-state dimer model and discuss the conformational distribution function of dimers. Analytical results for the shear viscosity due to dimers and its limiting expressions are presented. Finally, some discussions and a summary are given in Sec. 3.4.

3.2 Viscosity of dimer solutions

3.2.1 Shear viscosity

We consider a dilute solution of dimers under steady shear flow as schematically depicted in Fig. 3.1. Here the solvent viscosity is $\eta_{\rm s}$ and each dimer is composed of two rigid spheres of radius a, which are connected by an elastic

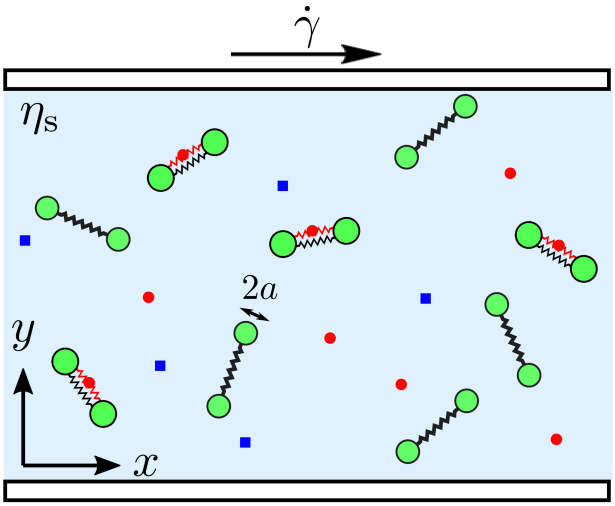

Figure 3.1: A dilute solution of two-state dimers under steady shear flow with shear rate $\dot{\gamma}$. Dimers consist of two green spheres of radius a connected with an elastic spring, and immersed in a Newtonian fluid having viscosity η_s. The enzymatic reaction, in which a dimer, a substrate (red circle) and a product (blue circle) participated, is explained in Fig. 3.2.

spring. The positions of two spheres are denoted by the three-dimensional vectors $\mathbf{r}_1$ and $\mathbf{r}_2$. Then, the force acting between the two spheres within the dimer is given by

$$f_\alpha = -\frac{\partial U(r)}{\partial r_\alpha}, \tag{3.1}$$

where $U(r)$ is the elastic potential energy, $r = |\mathbf{r}| = |\mathbf{r}_2 - \mathbf{r}_1|$ is the distance between the two spheres, and r_α is the α-component of the vector $\mathbf{r} = (r_x, r_y, r_z)$.

In the presence of potential forces, the equation of motion of an overdamped dimer can be written as [3.27, 3.28]

$$\frac{\partial r_\alpha}{\partial t} = \frac{2}{\zeta} f_\alpha - \frac{2k_\mathrm{B}T}{\zeta}\frac{\partial \ln \psi}{\partial r_\alpha} + d_{\alpha\beta} r_\beta, \tag{3.2}$$

where ζ is the friction coefficient of the sphere, k_B is Boltzmann constant, T is the temperature, $\psi(\mathbf{r}, t)$ is the time-dependent configurational distribution of a dimer, and the velocity gradient tensor is given by

$$d_{\alpha\beta} = \frac{\partial v_\alpha}{\partial r_\beta}. \tag{3.3}$$

Notice that v_α is the α-component of the velocity $\mathbf{v} = (v_x, v_y, v_z)$. Throughout

this work, we assume summation over repeated indices. The second and third terms on the right-hand side of Eq. (5.13) represent the velocity due to thermal motion of the solvent and that imposed by the flow field, respectively.

Such models of dimers have been used extensively to model polymer solutions. For polymer solutions, the stress tensor due to the presence of dimers is given [3.27, 3.28]

$$\sigma_{\alpha\beta} = n\langle r_\alpha f_\beta \rangle, \tag{3.4}$$

where n is the number density (per unit volume) of dimers, and $\langle \cdots \rangle$ denotes the thermal average over all dimer configurations. To calculate the statistical average in Eq. (6.3), we introduce the following Fokker-Planck equation for the conformational distribution $\psi(\mathbf{r}, t)$

$$\frac{\partial \psi}{\partial t} = -\frac{\partial}{\partial r_\alpha}\left(\frac{2}{\zeta} f_\alpha \psi - \frac{2k_{\mathrm{B}}T}{\zeta}\frac{\partial \psi}{\partial r_\alpha} + d_{\alpha\beta} r_\beta \psi\right). \tag{3.5}$$

In the above, the continuity equation

$$\frac{\partial \psi}{\partial t} = -\boldsymbol{\nabla} \cdot \left(\frac{\partial \mathbf{r}}{\partial t}\psi\right), \tag{3.6}$$

where $\boldsymbol{\nabla} = (\partial r_x, \partial r_y, \partial r_z)$ and Eq. (5.13) have been used. From the time evolution of $\langle r_\alpha r_\beta \rangle$ in a steady state, the stress tensor in Eq. (6.3) can be written as [3.27, 3.28]

$$\sigma_{\alpha\beta} = nk_{\mathrm{B}}T\delta_{\alpha\beta} + \frac{n\zeta}{4}\Big[d_{\alpha\gamma}\langle r_\beta r_\gamma \rangle + d_{\beta\gamma}\langle r_\alpha r_\gamma \rangle\Big]. \tag{3.7}$$

For simple shear flow whose velocity components are given by $v_x = \dot{\gamma} r_y$, $v_y = v_z = 0$, where $\dot{\gamma}$ is the shear rate (see Fig. 3.1), the viscosity due to dimers has a simple form

$$\eta = \frac{\sigma_{xy}}{\dot{\gamma}} = \frac{n\zeta}{4}\langle r_y^2 \rangle. \tag{3.8}$$

In order to calculate the average $\langle r_y^2 \rangle$, we need to specify the conformational distribution function $\psi(\mathbf{r})$.

3.2.2 Fraenkel dimer model

Let us first discuss a dimer consisting of two spheres that are connected by a harmonic spring having an elastic constant K_0, and a natural length ℓ_0. Its potential energy is then given by

$$U_0(r) = \frac{K_0}{2}(r - \ell_0)^2. \tag{3.9}$$

This is the "*Fraenkel dimer model*" [3.29], and is different than other polymer dynamic models, such as the Hookean dimer model. For Fraenkel dimers, the conformational distribution function, ψ_0, is given by

$$\psi_0(r) = C \exp\left[-\frac{K_0}{2k_{\rm B}T}(r - \ell_0)^2\right], \tag{3.10}$$

where C is the normalization constant. Here, we assume that the characteristic relaxation time of a dimer is much smaller than that of a shear flow, i.e., $\zeta\ell_0^2/(k_{\rm B}T)\dot{\gamma} \ll 1$. The physical meaning of this condition will be separately explained in Sec. 3.4.

Although the shear viscosity of the Fraenkel dimer model was discussed in Ref. [3.30], its explicit expression was not derived. By calculating $\langle r_y^2 \rangle$ in Eq. (3.8) using Eq. (3.10), we obtain the shear viscosity for a Fraenkel dimer solution η_0 as

$$\frac{\eta_0(\epsilon)}{G\tau} = \frac{2\epsilon}{3}\frac{2\epsilon(5+2\epsilon)e^{-\epsilon} + \sqrt{\pi\epsilon}(3+12\epsilon+4\epsilon^2)\left[1+\mathrm{erf}(\sqrt{\epsilon})\right]}{4\epsilon^2 e^{-\epsilon} + 2\sqrt{\pi\epsilon}(\epsilon+2\epsilon^2)\left[1+\mathrm{erf}(\sqrt{\epsilon})\right]}, \tag{3.11}$$

where $\epsilon = K_0\ell_0^2/(2k_{\rm B}T)$ is the dimensionless elastic energy, $G = nk_{\rm B}T$ is the relaxation modulus, $\tau = \zeta/(4K_0)$ is the relaxation time, and $\mathrm{erf}(x) = (2/\sqrt{\pi})\int_0^x dt\, e^{-t^2}$ is the error function [3.31]. Notice that $G\tau$ corresponds to the viscosity of a dimer solution when the natural length of the spring vanishes, i.e., $\epsilon = 0$ [3.28, 3.30].

The limiting behaviors of η_0 for the Hookean, $\epsilon \ll 1$, and stiff Fraenkel

dimers, $\epsilon \gg 1$, are given by [3.27, 3.30]

$$\frac{\eta_0(\epsilon)}{G\tau} = \begin{cases} 1 + \dfrac{4}{3}\sqrt{\dfrac{\epsilon}{\pi}} & \epsilon \ll 1, \\ \dfrac{2}{3}\epsilon & \epsilon \gg 1. \end{cases} \tag{3.12}$$

For $\epsilon \ll 1$, the viscosity is almost constant, indicating that thermal energy dominates over elastic energy. For $\epsilon \gg 1$, on the other hand, the viscosity increases linearly with ϵ.

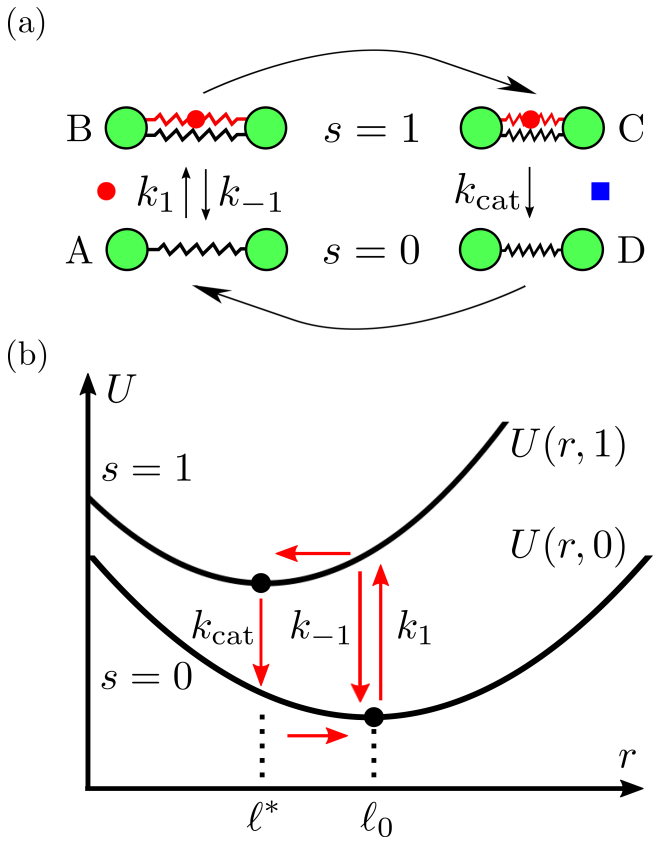

Figure 3.2: (a) The enzymatic cycle of two-state dimer model. A substrate (red circle) binds to a free enzyme ($s = 0$) with the reaction rate k_1 (A→B), while its dissociation also occurs with the reaction rate k_{-1} (B→A). Once the substrate-enzyme complex ($s = 1$) is formed, it starts to contract until the equilibrium conformation is attained (B→C). Then, the product (blue circle) is irreversibly released with the reaction rate $k_{\rm cat}$, and the bare enzyme comes back to its initial conformation. (b) The schematic illustration of the energy for a two-state dimer as described by Eq. (3.13). There are two energy branches $U(r, 0)$ and $U(r, 1)$. The transition between them takes place at $r = \ell_0$ and $r = \ell^*$, which are the equilibrium values of $U(r, 0)$ and $U(r, 1)$, respectively, as are indicated by black circles. This transition is followed by the downhill relaxational motion along each branch. The forward and reverse transition rates, $(s = 0) \rightleftarrows (s = 1)$, are given by k_1,k_{-1}, respectively, and $(s = 1) \to (s = 0)$ is given by $k_{\rm cat}$.

3.3 Two-state dimer solutions

3.3.1 Two-state dimer model

Catalytic enzymes undergo conformational changes in presence of substrate molecules. To model such situations, we use a previously proposed two-state dimer model with a state parameter that can get two values, $s = 0$ or 1 [3.18, 3.25, 3.26]. In Fig 3.2(a), we schematically illustrate an enzymatic cycle that is driven by binding a substrate to an enzyme. In the $s = 0$ state, i.e., the state of the dimer with the elastic constant K_0 and the natural length of the spring ℓ_0, this model corresponds to the Fraenkel dimer model.

When a substrate is supplied to a dimer enzyme whose size is $r = \ell_0$, a transition from $s = 0$ to $s = 1$ occurs with the reaction rate k_1. At the same time, the reverse reaction, namely, the substrate dissociation process, can occur also when $r = \ell_0$ with the reaction rate k_{-1}. For the state $s = 1$, the substrate adds another intra-dimer interaction, which is modeled as an additional spring, whose elastic constant and natural length are K_1 and ℓ_1, respectively. Then, the dimer relaxes to a new equilibrium conformation having the size $r = \ell^*$, as will be explicitly given after Eq. (3.13). Once the substrate molecule is irreversibly converted to a product molecule with the reaction rate $k_{\rm cat}$, a transition from $s = 1$ to $s = 0$ takes place at $r = \ell^*$. Finally, the product is released from the enzyme.

Notice that the reaction rates, k_1, k_{-1} and $k_{\rm cat}$ are the bare rate constants that do not depend on the energy difference between any two states. This also holds for the reaction rates in the cascade reactions discussed in Appendix 3.A. Moreover, the transition of a dimer occurs only when $r = \ell_0$ or $r = \ell^*$; hence, the reaction rates k_1, k_{-1} and $k_{\rm cat}$ are simply taken to be constant in our model.

The state-dependent total potential energy of this two-state dimer can be written as

$$U(r, s) = \frac{K_0}{2}(r - \ell_0)^2 + \frac{sK_1}{2}(r - \ell_1)^2, \tag{3.13}$$

which gives the equilibrium length for $s = 1$ as $\ell^* = (K_0\ell_0 + K_1\ell_1)/(K_0 + K_1)$. In Fig. 3.2(b), we schematically illustrate the energy of a two-state dimer given by Eq. (3.13) when $\ell_0 > \ell_1$. Under this condition, the substrate-enzyme complex shrinks as compared to the bare enzyme [3.18, 3.25, 3.26]. In this work, however, we do not require such a condition. In physiological conditions, the sizes of actual substrate-enzyme complexes either decrease ($\ell_0 > \ell_1$) or increase ($\ell_1 > \ell_0$) upon substrate binding [3.7]. Hereafter, the subscripts "0" and "1" denote physical values for the enzyme and the substrate-enzyme complex, respectively.

As represented by the second term in the r.h.s. of Eq. (5.13), a dimer in our model undergoes conformational fluctuations due to thermal energy. In other words, a free enzyme (or a substrate-enzyme complex) fluctuates around $r = \ell_0$ (or $r = \ell^*$) during turnover cycles. This corresponds to the situation in which enzymes are subject to thermal motion of solvent molecules. Notice, however, that conformational fluctuations between multi-state enzymes [3.32, 3.33] are not considered. This is because the original dimer model [3.18, 3.25, 3.26] that we employ follows the simple Michaelis-Menten kinetics [see Eq. (3.14)] with the advantage that the problem becomes tractable.

3.3.2 Conformational distribution function

The above two-state dimer model describes a chemical equation following the standard Michaelis-Menten reaction [3.34]:

$$\mathrm{E} + \mathrm{S} \underset{k_{-1}}{\overset{k_1}{\rightleftarrows}} \mathrm{ES} \xrightarrow{k_{\mathrm{cat}}} \mathrm{E}_* + \mathrm{P}. \tag{3.14}$$

This chemical reaction equation describes the enzymatic cycle composed of three states of an enzyme: a free enzyme (E), a substrate-enzyme complex (ES), and a free enzyme after the reaction (E_*), as depicted in Fig. 3.2. Furthermore, S and P stand for the substrate and product, respectively. When dimers are connected by elastic springs, the time spent during the transition between these chemical states can be characterized by a relaxation time $\tau = \zeta/(4K_0)$ as introduced after Eq. (3.11).

For a two-state dimer, we assume that the characteristic relaxation time is much smaller than that of a shear flow, i.e., $\zeta\ell_0^2/(k_\mathrm{B}T)\dot{\gamma} \ll 1$ as adopted for the Fraenkel dimer model in Sec. 3.2. We further assume that the transition time spent between enzymatic states is much smaller than the waiting time in each of the states, $s = 0, 1$, i.e., $\tau/W_s \ll 1$, where the waiting time W_s will be defined later in Eq. (3.16). This assumption is justified for enzymes such as adenylate kinase having a relatively large waiting time, $\tau/W_1 \approx 0.1$ [3.6]. For completeness, however, the general case of arbitrary waiting times is discussed in Sec. 3.4. Under these conditions, we can introduce the Boltzmann distribution function that is weighted only by the waiting time in the respective enzymatic states. The validity of this assumption has been confirmed by numerical solutions of the Langevin equation for a single two-state dimer [3.26].

The distribution function for the two-state dimer model for an enzyme is then given by

$$\psi_\mathrm{e}(r) = \frac{W_0 e^{-\beta U(r,0)} + W_1 e^{-\beta U(r,1)}}{\int d\mathbf{r}\, [W_0 e^{-\beta U(r,0)} + W_1 e^{-\beta U(r,1)}]}, \tag{3.15}$$

where $\beta = 1/(k_\mathrm{B}T)$. Here the waiting time in the state s is defined by [3.35, 3.36]

$$W_s = \int_0^\infty dt\, p_s(t), \tag{3.16}$$

where $p_s(t)$ is the time-dependent probability distribution function of an enzyme in state s, which will be explicitly given in Eq. (3.18). The case of a cascade reaction containing N substrate-enzyme complexes is discussed in Appendix 3.A as a generalization, and Eq. (3.15), hence, corresponds to the case $N = 1$.

3.3.3 Waiting times

Since we consider a dilute solution of two-state dimers, we employ a single enzyme kinetics to obtain the waiting time that an enzyme spends at each catalytic step (see also Appendix 3.B). The validity of using a single enzyme kinetics for an enzyme solution will be discussed later in this subsection. For two-state dimers, the corresponding kinetic equations are written in terms of

the probability functions as [3.32, 3.33, 3.37, 3.38]

$$\begin{aligned}\frac{dp_0}{dt} &= k_{-1}p_1 - k_1' p_0,\\ \frac{dp_1}{dt} &= k_1' p_0 - (k_{-1}+k_{\rm cat})p_1,\\ \frac{dp_*}{dt} &= k_{\rm cat}p_1.\end{aligned} \tag{3.17}$$

Here, $p_0(t)$, $p_1(t)$ and $p_*(t)$ are the probability distribution functions for the two-state dimer in one of the two states, $s = 0$, 1, and the free enzyme after the catalysis (E_*), respectively. In the above, we have introduced the pseudo first-order rate constant $k_1' = k_1 c_{\rm S}$, where $c_{\rm S}$ is the time-independent substrate concentration. Such an assumption is justified when $c_{\rm E} \ll c_{\rm S}$ is satisfied, where $c_{\rm E}$ is the enzyme concentration.

By solving the above coupled kinetic equations using the initial conditions, $p_0(0) = 1$ and $p_1(0) = p_*(0) = 0$, under the normalization condition $p_0(t) + p_1(t) + p_*(t) = 1$, the time-dependent probability distributions are obtained [3.37]

$$\begin{aligned}p_0(t) &= \frac{1}{2a}\left[(a+b-k_1')\,e^{(a-b)t} + (a-b+k_1')\,e^{-(a+b)t}\right],\\ p_1(t) &= \frac{k_1'}{2a}\left[e^{(a-b)t} - e^{-(a+b)t}\right],\\ p_*(t) &= \frac{k_1' k_{\rm cat}}{2a}\left[\frac{1}{a-b}e^{(a-b)t} + \frac{1}{a+b}e^{-(a+b)t}\right] + 1,\end{aligned} \tag{3.18}$$

where

$$\begin{aligned}a &= \left[(k_1'+k_{-1}+k_{\rm cat})^2/4 - k_1' k_{\rm cat}\right]^{1/2},\\ b &= (k_1'+k_{-1}+k_{\rm cat})/2.\end{aligned} \tag{3.19}$$

Because $a - b < 0$ and $a + b > 0$, both $p_0(t)$ and $p_1(t)$ decay exponentially for $t \to \infty$, and consequently $p_* \to 1$.

Substituting $p_0(t)$ and $p_1(t)$ of Eq. (3.18) into Eq. (3.16), we obtain the waiting times for $s = 0$ and 1 as

$$W_0 = \frac{k_{-1}+k_{\rm cat}}{k_1' k_{\rm cat}}, \qquad W_1 = \frac{1}{k_{\rm cat}}. \tag{3.20}$$

As a result, the distribution function in Eq. (3.15) can be written as

$$\psi_{\rm e}(r) = \frac{e^{-\beta U(r,0)} + \nu e^{-\beta U(r,1)}}{\int d\mathbf{r}\,\left[e^{-\beta U(r,0)} + \nu\, e^{-\beta U(r,1)}\right]}, \tag{3.21}$$

where we have introduced the dimensionless parameter ν

$$\nu = \frac{k_1}{k_{-1} + k_{\rm cat}} c_{\rm S} = \frac{c_{\rm S}}{K_{\rm M}}, \tag{3.22}$$

and $K_{\rm M}$ is the Michaelis constant [3.1]

$$K_{\rm M} = \frac{k_{-1} + k_{\rm cat}}{k_1}. \tag{3.23}$$

Physically, ν represents the fraction of the $s = 1$ state during one turnover cycle of the enzymatic reaction. It depends only on the substrate concentration and the bare rate constants. In the following analyses, we vary this state parameter ν to investigate the shear viscosity of enzyme solutions. Some numerical estimates of ν are given in the end of this section.

We discuss here the validity of using a single-enzyme kinetics. In our model, we have assumed that the concentration of enzymes is small enough so that hydrodynamic interactions between enzymes are negligible [3.28]. Such a dilute condition corresponds to having only a single enzyme in the system, leading to a renewal process [3.37]. In the renewal process, the probability distribution function is identically and independently distributed [3.39]. This means that in every turnover cycle, waiting times follow the same probability distribution, and hence these times can be uniquely determine as shown in Eq. (3.20).

For systems containing mesoscopic numbers of enzymes, however, stochasticity in enzymatic reactions plays more important roles as discussed in Refs. [3.39, 3.40]. Enzyme stochasticity leads to nonrenewal processes and causes breakdown of the Michaelis-Menten equation in steady state [3.39, 3.40]. Since the waiting time distributions depends on the number of enzymes for nonrenewal processes, one needs to derive master equations for waiting time distributions when a solution of multiple enzymes is considered [3.39]. This is beyond the scope of the present work.

3.3.4 Viscosity of two-state dimer solutions

To calculate the shear viscosity of a two-state enzyme solution, we introduce the following notations: $\kappa = K_1/K_0$, $\lambda = \ell_1/\ell_0$, and $\lambda^* = \ell^*/\ell_0 = (1 + \kappa\lambda)/(1 +$

κ), where $\ell^* = (K_0\ell_0 + K_1\ell_1)/(K_0 + K_1)$ is the effective natural length for a dimer in the $s = 1$ state. In Appendix 3.C, we show that the viscosity of a two-state enzyme solution is given by

$$\eta_e(\nu, \epsilon, \kappa, \lambda) = \eta_0 + (\eta_1 - \eta_0)\,\frac{z\nu}{1 + z\nu}, \tag{3.24}$$

where the quantity η_1 (η_0) corresponds to the viscosity when all the enzymes are in the $s = 1$ ($s = 0$) state

$$\frac{\eta_1(\epsilon, \kappa, \lambda)}{G\tau} = \frac{2\epsilon}{3}\frac{g_4\left(\epsilon(1+\kappa), \lambda^*\right)}{g_2\left(\epsilon(1+\kappa), \lambda^*\right)}, \tag{3.25}$$

and

$$z(\epsilon, \kappa, \lambda) = \exp\left[-\frac{\epsilon\kappa}{1+\kappa}(\lambda - 1)^2\right]\frac{g_2\left(\epsilon(1+\kappa), \lambda^*\right)}{g_2(\epsilon, 1)}. \tag{3.26}$$

See also Eq. (3.11) for the Fraenkel dimer viscosity $\eta_0(\epsilon)$. In the above, $g_m(p, q)$ is given by an integral

$$g_m(p, q) = \int_0^\infty dr\, r^m e^{-p(r-q)^2}, \tag{3.27}$$

and its explicit expression is obtained in Appendix 3.C [see Eq. (3.C6)]. Specifically, the functions $g_2(p, q)$ ($m = 2$) and $g_4(p, q)$ ($m = 4$) are given by

$$g_2(p, q) = \frac{q}{2p}e^{-pq^2} + \frac{\sqrt{\pi}(1 + 2pq^2)[1 + \mathrm{erf}(\sqrt{p}q)]}{4p^{3/2}}, \tag{3.28}$$

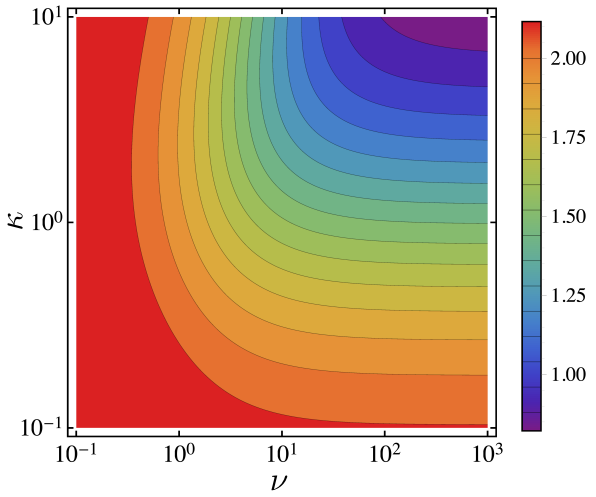

Figure 3.3: Contour plot of $\eta_e/(G\tau)$ as a function of the parameters $\nu = c_S/K_M$ [see Eq. (3.22)] and $\kappa = K_1/K_0$ for $\epsilon = K_0\ell_0^2/(2k_BT) = 1$ and $\lambda = \ell_1/\ell_0 = 1$.

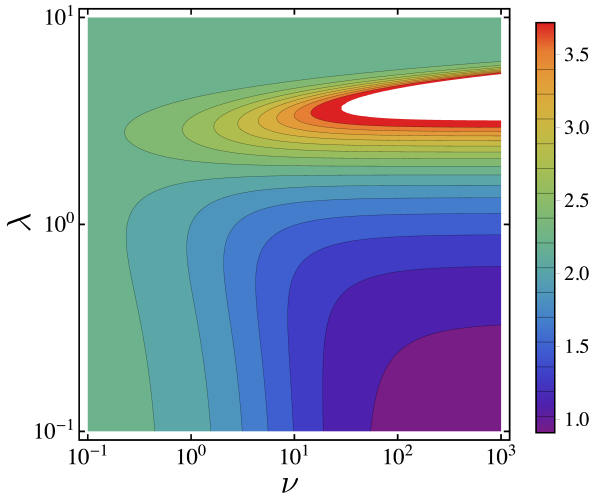

Figure 3.4: Contour plot of $\eta_e/(G\tau)$ as a function of the parameters $\nu = c_S/K_M$ [see Eq. (3.22)] and $\lambda = \ell_1/\ell_0$ for $\epsilon = K_0\ell_0^2/(2k_BT) = 1$ and $\kappa = K_1/K_0 = 1$. The white region corresponds to larger absolute values of η_e.

and

$$g_4(p,q) = \frac{q(5+2pq^2)}{4p^2}e^{-pq^2} + \frac{\sqrt{\pi}(3+12pq^2+4p^2q^4)[1+\mathrm{erf}(\sqrt{p}q)]}{8p^{5/2}}, \qquad (3.29)$$

respectively. Equations (3.24)–(3.29) for the viscosity are the main result of this work.

In Eq. (3.26), the factor $\epsilon\kappa/(1+\kappa)(\lambda-1)^2$ in the exponential function corresponds to the dimensionless energy difference, $U(\ell^*,1) - U(\ell_0,0)$, between the two equilibrium states of a two-state dimer with ℓ_0 and ℓ^*, as shown in Fig. 3.2(b). Although only the bare reaction rates are taken into account, the above energy difference naturally emerges by defining the weighted distribution function as in Eq. (3.21).

When $\nu = 0$, η_e of Eq. (3.24) simply reduces to η_0, the viscosity of the Fraenkel dimer solution [$s = 0$, see Eq. (3.11)]. For $\nu \neq 0$, the enzyme solution viscosity η_e is determined by the ratio between the two viscosities η_0 and η_1. Due to the factor z, however, η_e also depends on the energy difference between the two states of the enzyme. This effect causes a nonmonotonic behavior of the viscosity as we will show later.

Before proceeding to analyze the behavior of η_e, we estimate typical values of

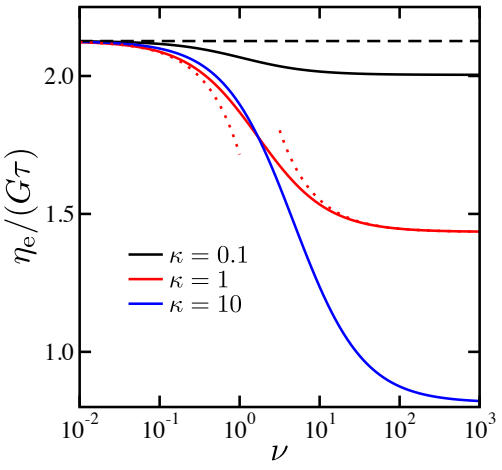

Figure 3.5: Plot of $\eta_e/(G\tau)$ as a function of the parameter ν for $\kappa = K_1/K_0 = 0.1, 1$ and 10. The other parameter values are $\epsilon = K_0\ell_0^2/(2k_BT) = 1$ and $\lambda = \ell_1/\ell_0 = 1$. The black dashed line represents η_0 in Eq. (3.11). The red dotted lines represent the two limiting expressions in Eq. (3.30) for $\kappa = 1$.

$\epsilon = K_0\ell_0^2/(2k_BT)$. The enzymes size can be taken as $\ell_0 \approx 10\,\mathrm{nm}$ [3.1]. Moreover, considering typical forces, 1 pN, generated by a two-state dimer with size ℓ_0, we estimate the spring constant as $K_0 \approx 10^{-4}\,\mathrm{N/m}$ [3.18]. Using these values and $k_BT \approx 4 \times 10^{-21}\,\mathrm{J}$ in physiological conditions, we obtain $\epsilon \approx 1$. Hence, we fix the ϵ value hereafter to $\epsilon = 1$.

In Fig. 3.3, we present the contour plot of the rescaled viscosity due to two-state dimers, $\eta_e/(G\tau)$, as a function of ν and κ for $\epsilon = \lambda = 1$. One can see that η_e becomes smaller for large ν and κ, implying that the viscosity decreases when enzymatic reactions occur more frequently and substrates are stiffer (large K_1). Notice that stiff dimers lead to a decrease of η_e because its stiffness suppresses the enzyme size fluctuation. In Fig. 3.4, we plot the rescaled viscosity, $\eta_e/(G\tau)$, as a function of ν and λ for $\epsilon = \kappa = 1$. Here we see a nonmonotonic behavior of the viscosity in λ characterized by a peak around $\lambda \approx 3.2$. Note that for larger λ values, η_e becomes independent of ν.

To see more detailed behavior, we plot in Fig. 3.5 the rescaled viscosity, $\eta_e/(G\tau)$, as a function of ν for $\kappa = 0.1$, 1 and 10, while keeping $\epsilon = \lambda = 1$. The dashed line corresponds to the constant viscosity for a Fraenkel dimer solution,

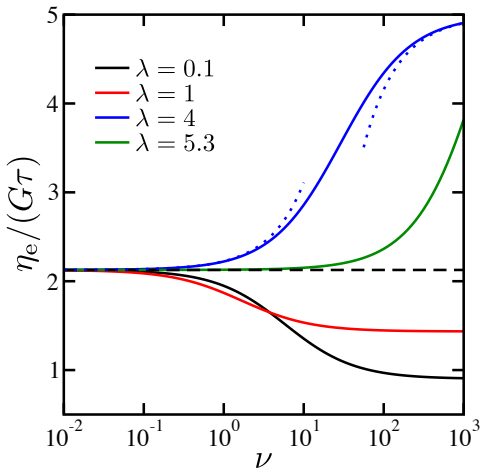

Figure 3.6: Plot of $\eta_e/(G\tau)$ as a function of the parameter ν for $\lambda = \ell_1/\ell_0 = 0.1, 1, 4$ and 5.3. The other parameter values are $\epsilon = K_0\ell_0^2/(2k_BT) = 1$ and $\kappa = K_1/K_0 = 1$. The black dashed line represents η_0 in Eq. (3.11). The blue dotted lines represent the two limiting expressions in Eq. (3.30) for $\lambda = 4$.

i.e., $\eta_0/(G\tau) \approx 2.13$. We see that η_e decreases with increasing ν for all the κ values. The decrease of η_e is more enhanced for larger κ values.

In Fig. 3.6, we plot η_e as a function of ν for $\lambda = 0.1$, 1, 4 and 5.3, while keeping $\epsilon = \kappa = 1$. We see that η_e shows both increasing and decreasing dependency as a function of ν depending on the value of λ. When $\lambda = 0.1$, 1, and 4, the viscosity η_e increases with λ, reflecting the fact that larger enzymes lead to higher viscosity. For larger λ such as $\lambda = 5.3$, however, η_e becomes smaller, and as λ is further increased, the viscosity approaches the value of η_0 as indicated by the dashed line. In this limit, both Fraenkel dimer solutions and two-state enzyme solutions exhibit the same viscosity even when ν is very large.

We discuss now the nonmonotonic behavior of η_e that is seen in Fig. 3.6. Such a behavior occurs because z in Eq. (3.26) increases for smaller λ, but strongly decreases for larger λ due to the Gaussian function of Eq. (3.26). The factor $\epsilon\kappa(\lambda-1)^2/(1+\kappa)$ in the Gaussian function corresponds to the rescaled energy difference between the $s = 0$ and $s = 1$ states. Hence, it can be regarded as an Arrhenius' equation that determines the transition rate from the $s = 0$ to $s = 1$ state.

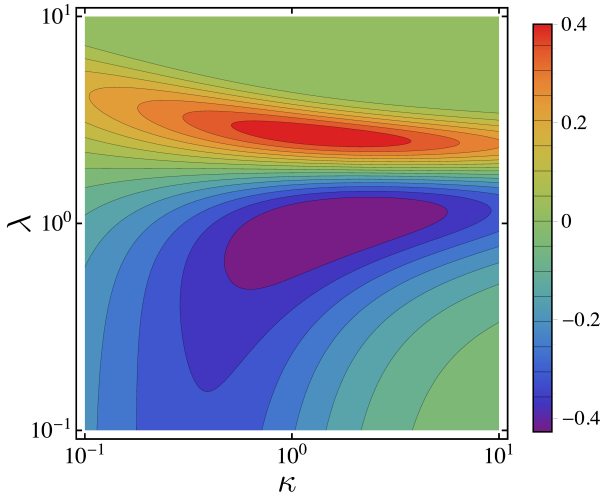

Figure 3.7: Contour plot of $C_1/(G\tau)$ [see Eq. (3.30)] as a function of $\kappa = K_1/K_0$ and $\lambda = \ell_1/\ell_0$ for $\epsilon = K_0\ell_0^2/(2k_BT) = 1$ under the condition $\nu \ll 1$. The quantity C_1 changes its sign from negative to positive around $\lambda \approx 2$.

3.3.5 Limiting expressions

Next, we present the limiting expressions of η_e for small and large values of the ν parameter, $\nu \ll 1$ and $\nu \gg 1$. The viscosity of two-state dimer solution in Eq. (3.24) becomes

$$\eta_e(\nu,\epsilon,\kappa,\lambda) \approx \begin{cases} \eta_0 + C_1\nu, & \nu \ll 1 \\ \eta_1 + \dfrac{C_2}{\nu}, & \nu \gg 1 \end{cases} \tag{3.30}$$

where $C_1(\epsilon,\kappa,\lambda) = (\eta_1 - \eta_0)z$ and $C_2(\epsilon,\kappa,\lambda) = (\eta_0 - \eta_1)/z$. In Figs. 3.5 and 3.6, we have plotted the above limits by the red (for $\kappa = 1$) and blue (for $\lambda = 4$) dotted line, respectively.

In Fig. 3.7, we study the $\nu \ll 1$ behavior and plot the coefficient $C_1 = (\eta_1 - \eta_0)z$ of ν in Eq. (3.30) as a function of κ and λ for $\epsilon = 1$. The behavior of C_1 is nonmonotonic, having a minimum and a maximum around $(\kappa,\lambda) \approx (1,1)$ and $(\kappa,\lambda) \approx (1,2.5)$, respectively. The quantity C_1 vanishes for large λ values, because the Gaussian function in z, Eq. (3.26), dominates over the viscosity difference, $\eta_0 - \eta_1$. Notice that C_1 changes its sign from negative to positive around $\lambda \approx 2$, where the switching from decreasing to increasing behavior of η_e

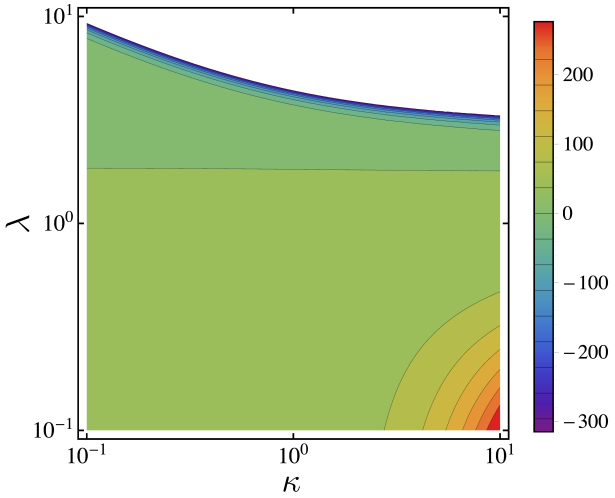

Figure 3.8: Contour plot of $C_2/(G\tau)$ [see Eq. (3.30)] as a function of $\kappa = K_1/K_0$ and $\lambda = \ell_1/\ell_0$ for $\epsilon = K_0\ell_0^2/(2k_BT) = 1$ under the condition $\nu \gg 1$. The quantity C_2 changes its sign from positive to negative around $\lambda \approx 2$. The white region corresponds to larger absolute values of C_2.

as a function of ν occurs.

In Fig. 3.8, we study the $\nu \gg 1$ behavior and plot the coefficient $C_2 = (\eta_0 - \eta_1)/z$ of ν^{-1} in Eq. (3.30) as a function of κ and λ when $\epsilon = 1$. Here C_2 exhibits a monotonic behavior in κ and λ, and changes its sign from positive to negative around $\lambda \approx 2$. Since η_e is inversely proportional to ν in Eq. (3.30), positive C_2 leads to a decreasing behavior of η_e, whereas negative C_2 results in an increasing behavior.

3.3.6 Numerical estimates

To end this section, we give some numerical estimates of the parameter $\nu = c_S/K_M$ in Eq. (3.22). The experimentally accessible substrate concentration is $10^{-6}\,\mathrm{M} < c_S < 10^{-3}\,\mathrm{M}$ [3.12, 3.14]. On the other hand, the value of the Michaelis constant K_M differs between fast and slow enzymes. For fast enzymes, such as urease and catalase, it is given by $K_M \approx 10^{-3}\,\mathrm{M}$ [3.9, 3.12]. For slow enzymes, such as aldolase and adenylate kinase, it is $K_M \approx 10^{-6}\,\mathrm{M}$ [3.6, 3.10]. Hence, the ν range is estimated as $10^{-3} < \nu < 1$ and $1 < \nu < 10^3$, respectively, for fast and slow enzymes. These estimates imply that the limiting expressions

derived for $\nu \ll 1$ and $\nu \gg 1$ in Eq. (3.30) correspond to these two types of enzymes for $c_{\rm S} < 10^{-4}\,{\rm M}$ and $c_{\rm S} > 10^{-5}\,{\rm M}$, respectively.

Next we discuss the values of κ and λ in order to estimate the viscosity $\eta_{\rm e}$ for typical physiological conditions. Since an enzyme consists of a large complex of macromolecules, the size of substrate molecules is typically smaller than that of enzymes [3.1]. Due to this size difference, the condition $\lambda < 1$ holds generally. Noncovalent bonds, such as hydrogen bonds, van der Waals attractions and hydrophobic forces, are responsible for the formation of macromolecular assemblies. On the other hand, covalent bonds are responsible for the formation of substrate molecules. Then, the molecular flexibilities for the substrates compared with the enzymes are different, which leads to the condition $\kappa > 1$.

From the above argument, we choose $\lambda = 0.1$ and $\kappa = 10$. Using these values and setting $\epsilon = 1$, we obtain $\eta_{\rm e}/(G\tau) \approx 2.11$ and $\eta_{\rm e}/(G\tau) \approx 0.39$ for fast and slow enzymes, respectively, assuming that the maximum substrate concentration $c_{\rm S} = 10^{-3}\,{\rm M}$ is attained. Since $\eta_0/(G\tau) \approx 2.13$ for $\epsilon = 1$, the difference between the enzyme solution with substrates $\eta_{\rm e}$ and that without substates η_0 is negligible for fast enzymes, whereas the viscosity $\eta_{\rm e}$ is approximately five times smaller than η_0 for slow enzymes.

3.4 Discussion and conclusion

In this paper, we have investigated the viscosity of dilute two-state enzyme solutions under steady shear flow. We have obtained the shear viscosity by taking into account the enzyme conformational changes in a solution with a supply of substrates. The waiting times, which correspond to the respective conformations of the enzyme, are connected to the reaction rates in the enzymatic cycle by using the single enzyme kinetics [3.37]. In our approach, the two-state dimer model [3.18, 3.25, 3.26] and the polymer dimer model [3.27–3.29] are combined.

When the enzyme has the same structural properties as the substrate, the shear viscosity decreases as the substrate concentration becomes higher (see

Fig. 3.5). For a substrate larger than the enzyme, the viscosity increases with substrate concentrations (see Fig. 3.6). When the substrate is large enough, however, the viscosity reduces to that of a Fraenkel dimer solution. Furthermore, we have obtained the limiting expressions of the viscosity for fast and slow enzymes [see Eq. (3.30)]. For slow enzymes, the coefficient shows only a monotonic behavior. For fast enzymes, on the other hand, the coefficient of the substrate concentration exhibits a nonmonotonic behavior as functions of the stiffness and size of the substrate.

Next, we comment on the connection between the viscosity of a two-state dimer solution and the diffusion coefficient of a tracer particle in such a solution. By following the discussion in Refs. [3.41, 3.42], the diffusion coefficient of a passive spherical particle of radius R can be given by Einstein's relation

$$D_{\mathrm{e}} = \frac{k_{\mathrm{B}}T}{6\pi(\eta_{\mathrm{s}} + \eta_{\mathrm{e}})R}, \tag{3.31}$$

where we have assumed $R \gg \ell_0$. In terms of the enzyme volume fraction $\phi = 4\pi(\ell_0/2)^3 n/3$, D_{e} can be expanded up to first order in ϕ as

$$D_{\mathrm{e}} \approx \frac{k_{\mathrm{B}}T}{6\pi\eta_{\mathrm{s}}R}\left(1 - \frac{9a\eta_{\mathrm{e}}}{2\ell_0 G\tau}\phi\right). \tag{3.32}$$

Hence, the relative change of the diffusion coefficient with respect to that of a Fraenkel dimer solution (denoted by D_0) is

$$\delta D = D_{\mathrm{e}} - D_0 = \frac{3k_{\mathrm{B}}T}{4\pi\eta_{\mathrm{s}}R}\frac{a(\eta_0 - \eta_{\mathrm{e}})}{\ell_0 G\tau}\phi. \tag{3.33}$$

Since $\eta_0 > \eta_{\mathrm{e}}$ holds for both fast and slow enzymes as estimated before, catalytic enzymes give rise to the diffusion enhancement under physiological conditions. Moreover, we see that δD increases as c_{S} is increased in the limits of fast and slow enzymes (see Figs. 3.7 and 3.8). This behavior qualitatively agrees with experiments for both tracers and enzymes [3.8, 3.14, 3.21]. More specifically, using values such as $c_{\mathrm{S}} = 10^{-3}\,\mathrm{M}$, $a/\ell_0 = 0.2$, $\phi = 0.1$, we obtain that the diffusion increases for slow enzymes as $\delta D/D_0 \approx 0.15$. In existing experiments, however, ϕ is typically of the order of 10^{-5}, and hence experimental

measurements using higher $c_{\rm E}$ concentration are needed for a more accurately checking of the validity of our model.

Here we discuss how the obtained viscosity is modified by hydrodynamic effects that have been neglected so far. In the presence of hydrodynamic interactions, the equation of motion, Eq. (5.13), can be rewritten as [3.43]

$$\frac{\partial r_\alpha}{\partial t} = (\delta_{\alpha\beta} - \zeta G_{\alpha\beta}) \left(\frac{2}{\zeta} f_\beta - \frac{2k_{\rm B}T}{\zeta} \frac{\partial \ln \psi}{\partial r_\beta} \right) + d_{\alpha\beta} r_\beta, \tag{3.34}$$

where $G_{\alpha\beta}(r) = (\delta_{\alpha\beta} + r_\alpha r_\beta / r^2) / (8\pi\eta_{\rm s} r)$ is the hydrodynamic Oseen tensor [3.44]. If we assume all orientations to be equally probable, an equilibrium-averaged hydrodynamic interaction can be defined by taking the average of $G_{\alpha\beta}(r)$ over all orientations [3.45]

$$h = \frac{1}{3} {\rm Tr} \left(\frac{\int d\mathbf{r}\, \psi(r) G_{\alpha\beta}(r)}{\int d\mathbf{r}\, \psi(r)} \right), \tag{3.35}$$

where Tr denotes the trace operation. This is called the pre-averaging approximation [3.44]. Then, the equation of motion can be approximated as

$$\frac{\partial r_\alpha}{\partial t} \approx \frac{2(1-\zeta h)}{\zeta} \left(f_\alpha - k_{\rm B}T \frac{\partial \ln \psi}{\partial r_\alpha} \right) + d_{\alpha\beta} r_\beta. \tag{3.36}$$

Comparing Eqs. (5.13) and (3.36), one finds that the change over from negligible hydrodynamic interactions to equilibrium-averaged ones can be accomplished by replacing ζ with $\zeta/(1-\zeta h)$. Hence, for a single-state dimer as in Eq. (3.8), the hydrodynamic interaction modifies the viscosity by a factor of $1/(1-\zeta h)$. In Appendix 3.D, we derive h for the Fraenkel dimer model. When $a/\ell_0 = 0.2$ and $\epsilon = 1$, for example, we find that the viscosity is about 20% larger as compared to the negligible hydrodynamic case. For the two-state dimers, hydrodynamic effects do not affect the ν-dependence of $\eta_{\rm e}$ although some geometrical factors such as κ and λ can enter in h.

In this study, we have assumed that the distribution functions do not depend on shear flow [see Eqs. (3.10) and (3.15)]. Here we discuss how these distribution functions are modified by an external flow and the regime where the flow does not affect the distributions as assumed in this paper. For a steady-state

homogeneous potential flow, Eq. (3.5) has an analytical solution [3.27]

$$\psi(r) = C' \exp\left[-\frac{U(r)}{k_{\mathrm{B}}T}\right] \exp\left[\frac{\zeta}{k_{\mathrm{B}}T} r_\alpha d_{\alpha\beta} r_\beta\right], \tag{3.37}$$

where C' is the normalization constant.

For a simple shear flow characterized by a shear rate $\dot{\gamma}$, the distribution function becomes

$$\psi(r, \theta, \phi, \dot{\gamma}) = C' \exp\left[-\frac{U(r)}{k_{\mathrm{B}}T}\right] \exp\left[\frac{\zeta r^2 \dot{\gamma}}{2k_{\mathrm{B}}T} \sin^2\theta \sin 2\phi\right], \tag{3.38}$$

where $r_x = r\sin\theta\cos\phi$ and $r_y = r\sin\theta\sin\phi$. When the length of a dimer is $r = \ell_0$, the characteristic relaxation time is given by $\zeta\ell_0^2/(k_{\mathrm{B}}T)$ [3.29]. Hence, the shear flow does not affect the distribution functions when $\zeta\ell_0^2/(k_{\mathrm{B}}T)\dot{\gamma} \ll 1$.

We have assumed that the transition time spent from one enzymatic species to another is much smaller than the waiting time, i.e., $\tau/W_s \ll 1$. Here, we consider the general case of arbitrary waiting time. Because the total times in state $s = 0$ and $s = 1$ are given by $W_0 + \tau$ and $W_1 + \tau_1$, respectively, the modified parameter ν becomes

$$\nu = \frac{k_1(1 + k_{\mathrm{cat}}\tau_1)c_{\mathrm{S}}}{k_{-1} + k_{\mathrm{cat}}(1 + k_1\tau c_{\mathrm{S}})}, \tag{3.39}$$

where $\tau = \zeta/(4K_0)$ as before and $\tau_1 = \zeta/(4K_1)$. Since the reverse reaction rate k_{-1} is negligible in general but may have a finite value, we set it to be a constant. There are only four relevant time scales, namely, k_{cat}^{-1}, $(k_1 c_{\mathrm{S}})^{-1}$, τ, and τ_1, and Eq. (3.39) has four limiting expressions. When the transition rates are vanishingly small, the modified parameter coincides with ν in Eq. (3.22) as it should. For the two intermediate regimes, Eq. (3.39) shows linear and inverse dependences on the transition time. When the transition time is infinitely large, we have $\nu \sim \kappa^{-1}$, indicating that the transition dynamics is governed only by the relative stiffness between the enzyme and substrate.

The transition rates can depend on κ and/or λ for general enzymatic solutions although these effects were not considered in this work. Using Kramers' reaction-rate theory [3.46], Aviram *et al.* [3.6] obtained free-energy profiles of

enzymes by experimentally measuring the transition rates. In the presence of such an effect, the enzyme solution viscosity may exhibit more complicated dependences on κ and/or λ. Finally, we have assumed that the viscosity due to enzymes does not depend on the shear rate. Since the dimer model with finite natural lengths predicts a viscosity that depends on the shear rate [3.27, 3.30], one can extend the present model to a nonNewtonian enzymatic fluid.

Appendix 3.A Probability distribution function for multiple-state enzymes

In this Appendix, we generalize the dimer-enzyme into a N-mer one. We derive the probability distribution function for a single enzyme that has multiple intermediate states in catalytic chemical reactions. We consider the following cascade reaction containing N intermediate substrate-enzyme complexes:

$$\mathrm{E}+\mathrm{S}\underset{k_{-1}}{\overset{k_1}{\rightleftarrows}}(\mathrm{ES})_1\underset{k_{-2}}{\overset{k_2}{\rightleftarrows}}\cdots(\mathrm{ES})_s\cdots\underset{k_{-N}}{\overset{k_N}{\rightleftarrows}}(\mathrm{ES})_N\xrightarrow{k_{\mathrm{cat}}}\mathrm{E}_*+\mathrm{P}. \tag{3.A1}$$

Here $(\mathrm{ES})_s$ denotes the s-th intermediate complex in the reaction, and k_s and k_{-s} are the forward and backward reaction rates to the states s and $s-1$, respectively. At the final step, the complex is irreversibly converted to an enzyme and a product with the reaction rate k_{cat}. The enzyme after the catalysis is denoted by E_*.

Since we assume that a substrate having the energy E_s binds to $(\mathrm{ES})_{s-1}$ with the reaction rate k_s, the energy of an enzyme in the state s can be written as

$$U(r,s)=E_0+\sum_{s'=1}^{s}E_{s'}, \tag{3.A2}$$

where E_0 is the energy of the free enzyme. Then, the waiting time-weighted distribution functions is given by

$$\psi_N(r)=\frac{\sum_{s=0}^{N}W_s e^{-\beta U(r,s)}}{\sum_{s=0}^{N}W_s\int d\mathbf{r}\, e^{-\beta U(r,s)}}. \tag{3.A3}$$

Here W_s is the waiting time in the state s, which is defined in Eq. (3.16).

In order to obtain the viscosity of dimer solutions using Eq. (3.8), we need

to calculate the second moment $\langle r_y^2 \rangle$. In general, the average of any function $f(\mathbf{r})$ over the distribution function, Eq. (3.A3), can be written as

$$\langle f(\mathbf{r}) \rangle_N = \langle f(\mathbf{r}) \rangle_0 + \sum_{s=1}^{N} \left[\langle f(\mathbf{r}) \rangle_s - \langle f(\mathbf{r}) \rangle_0 \right] \frac{z_{s0} w_{s0}}{1 + \sum_{s'=1}^{N} z_{s'0} w_{s'0}}, \tag{3.A4}$$

where $\langle f(\mathbf{r}) \rangle_s$ denotes the average of $f(\mathbf{r})$ over all configurations in the state s

$$\langle f(\mathbf{r}) \rangle_s = \frac{\int d\mathbf{r}\, f(\mathbf{r}) e^{-\beta U(r,s)}}{\int d\mathbf{r}\, e^{-\beta U(r,s)}}, \tag{3.A5}$$

while $z_{ss'}$ and $w_{ss'}$ are defined by

$$z_{ss'} = \frac{\int d\mathbf{r}\, e^{-\beta U(r,s)}}{\int d\mathbf{r}\, e^{-\beta U(r,s')}}, \qquad w_{ss'} = \frac{\int_0^\infty dt\, p_s(t)}{\int_0^\infty dt\, p_{s'}(t)}. \tag{3.A6}$$

Notice that the quantity z in Eq. (3.26) corresponds to z_{10} in the above notation.

Appendix 3.B Michaelis-Menten kinetics and single enzyme kinetics

In this Appendix, we briefly review the Michaelis-Menten kinetics [3.34] and the single-enzyme kinetics. In the two-state dimer model, the cascade reaction in Eq. (3.A1) reduces to the Michaelis-Menten reaction [see Eq. (3.14)]. In the ensemble of enzymatic experiments, the corresponding kinetic equations become

$$\begin{aligned} \frac{dc_{\rm E}}{dt} &= k_{-1} c_{\rm ES} - k_1 c_{\rm E} c_{\rm S}, \\ \frac{dc_{\rm ES}}{dt} &= k_1 c_{\rm E} c_{\rm S} - (k_{-1} + k_{\rm cat}) c_{\rm ES}, \\ \frac{dc_{\rm P}}{dt} &= k_{\rm cat} c_{\rm ES}, \end{aligned} \tag{3.B1}$$

where $c_{\rm E}$ and $c_{\rm S}$ were defined before, whereas $c_{\rm ES}$ and $c_{\rm P}$ are the concentrations of substrate-enzyme complex and product, respectively. By replacing the concentrations of the chemical species with the probability distributions, we obtain the kinetic equations for a single enzyme as in Eq. (3.17). In the steady sate, $dc_{\rm ES}/dt = 0$, the enzymatic velocity is given by

$$V = \frac{dc_{\rm P}}{dt} = \frac{V_{\rm max} c_{\rm S}}{K_{\rm M} + c_{\rm S}}, \tag{3.B2}$$

where $V_{\rm max} = k_{\rm cat}(c_{\rm E} + c_{\rm ES})$ is the maximum enzymatic velocity and $K_{\rm M} = (k_{-1} + k_{\rm cat})/k_1$ is the Michaelis constant defined in Eq. (3.23).

For a single-enzyme, the corresponding reaction velocity can be obtained from the inverse of the total waiting time during one catalytic cycle. With the use of Eq. (3.20), this velocity becomes

$$\frac{1}{W} = \frac{1}{W_0 + W_1} = \frac{k_{\rm cat} c_{\rm S}}{K_{\rm M} + c_{\rm S}}, \tag{3.B3}$$

which is termed the single-molecule Michaelis-Menten equation [3.32]. Comparison of Eqs. (3.B2) and (3.B3) yields the relation

$$\frac{V}{c_{\rm E} + c_{\rm ES}} = \frac{1}{W}. \tag{3.B4}$$

This relation originates from the equivalence between the average over a single molecule's long-time trace and that over a large ensemble of identical molecules, i.e., the ergodicity [3.32, 3.33].

Appendix 3.C Derivation of $\eta_{\rm e}$

In this Appendix, we present the derivation of $\eta_{\rm e}$ in Eq. (3.24). Using Eq. (3.21), we calculate $\langle r_y^2 \rangle$ in Eq. (3.8) as

$$\eta_{\rm e} = \frac{n\zeta}{4} \frac{\int d\mathbf{r} \, \left[r_y^2 e^{-\beta U(r,0)} + \nu r_y^2 e^{-\beta U(r,1)} \right]}{\int d\mathbf{r} \, \left[e^{-\beta U(r,0)} + \nu e^{-\beta U(r,1)} \right]}. \tag{3.C1}$$

With the use of Eq. (3.A4) for $N = 1$, we obtain

$$\eta_{\rm e} = \frac{n\zeta}{4} \left(\langle r_y^2 \rangle_0 + \left[\langle r_y^2 \rangle_1 - \langle r_y^2 \rangle_0 \right] \frac{z\nu}{1 + z\nu} \right). \tag{3.C2}$$

Since $n\zeta \langle r_y^2 \rangle_0 / 4 = \eta_0$ and $n\zeta \langle r_y^2 \rangle_1 / 4 = \eta_1$, we obtain Eq. (3.24). The viscosity of a Fraenkel dimer solution η_0 is given by Eq. (3.11).

Next we calculate η_1 in Eq. (3.25) as

$$\eta_1 = \frac{n\zeta}{4} \frac{\int d\mathbf{r} \, r_y^2 e^{-\beta U(r,1)}}{\int d\mathbf{r} \, e^{-\beta U(r,1)}} = \frac{n\zeta}{12} \frac{\int_0^\infty dr \, r^4 e^{-\beta U(r,1)}}{\int_0^\infty dr \, r^2 e^{-\beta U(r,1)}}. \tag{3.C3}$$

For a harmonic potential, the integration of r^m can be generally expressed as

$$\begin{aligned} g_m(p,q) &= \int_0^\infty dr \, r^m e^{-p(r-q)^2} \\ &= \int_{-q}^\infty du \, (u+q)^m e^{-pu^2} \\ &= \sum_{n=0}^m \frac{m!}{(m-n)!n!} q^{m-n} \int_{-q}^\infty du \, u^n e^{-pu^2}. \end{aligned} \tag{3.C4}$$

The last integral can be further performed as follows.

$$\begin{aligned}
&\int_{-q}^{0} du\, u^n e^{-pu^2} + \int_{0}^{\infty} du\, u^n e^{-pu^2} \\
&= \frac{p^{-(n+1)/2}}{2}\left[(-1)^n \int_0^{pq^2} dt\, t^{(n+1)/2-1} e^{-t} + \int_0^{\infty} dt\, t^{(n+1)/2-1} e^{-t}\right], \\
&= \frac{p^{-(n+1)/2}}{2}\left[[1+(-1)^n]\int_0^{\infty} dt\, t^{(n+1)/2-1} e^{-t} - (-1)^n \int_{pq^2}^{\infty} dt\, t^{(n+1)/2-1} e^{-t}\right].
\end{aligned} \tag{3.C5}$$

Finally, $g_m(p,q)$ becomes

$$\begin{aligned}
g_m(p,q) = \frac{1}{2}\sum_{n=0}^{m} \frac{m!}{(m-n)!n!} p^{-(n+1)/2} q^{m-n} \\
\times \left[[1+(-1)^n]\,\Gamma\left(\frac{n+1}{2}\right) - (-1)^n \Gamma\left(\frac{n+1}{2}, pq^2\right)\right],
\end{aligned} \tag{3.C6}$$

where $\Gamma(x) = \int_0^{\infty} dt\, t^{x-1}e^{-t}$ and $\Gamma(x,\alpha) = \int_{\alpha}^{\infty} dt\, t^{x-1}e^{-t}$ are the gamma function and the incomplete gamma function of the second kind, respectively [3.31].

Appendix 3.D Hydrodynamic interactions between two spheres

In this Appendix, we present the calculation of Eq. (3.35) for the Fraenkel dimer model. With the assumption that the fluid is isotropic, the Oseen tensor becomes $\delta_{\alpha\beta}/(6\pi\eta_{\mathrm{s}} r)$. Substituting it into Eq. (3.35) yields

$$h = \frac{1}{6\pi\eta_{\mathrm{s}}} \frac{\int d\mathbf{r}\, \psi_0(r)/r}{\int d\mathbf{r}\, \psi_0(r)}. \tag{3.D1}$$

By taking $m = 1, 2$ in $g_m(p,q)$, Eq. (3.C6), the dimensionless combination ζh is obtained as

$$\zeta h(\epsilon) = \frac{a}{\ell_0}\frac{g_1(\epsilon,1)}{g_2(\epsilon,1)} = \frac{a}{\ell_0}\frac{e^{-\epsilon} + \sqrt{\pi\epsilon}\,[1+\mathrm{erf}\,(\sqrt{\epsilon})]}{e^{-\epsilon} + \sqrt{\pi\epsilon}[1+1/(2\epsilon)]\,[1+\mathrm{erf}\,(\sqrt{\epsilon})]}. \tag{3.D2}$$

For large dimers, $a/\ell_0 \ll 1$, the hydrodynamic effects become negligible. The limiting behavior of h for the Hookean, $\epsilon \ll 1$, and stiff Fraenkel dimers, $\epsilon \gg 1$,

is given, respectively, by

$$\zeta h(\epsilon) = \begin{cases} \dfrac{2a}{\ell_0}\sqrt{\dfrac{\epsilon}{\pi}} & \epsilon \ll 1, \\ \dfrac{a}{\ell_0}\dfrac{1}{1+1/(2\epsilon)} & \epsilon \gg 1. \end{cases} \tag{3.D3}$$

References

[3.1] B. Alberts, A. Johnson, P. Walter, J. Lewis, and M. Raff, *Molecular Biology of the Cell* (Garland Science, New York, 2008).

[3.2] M. Gerstein, A. M. Lesk, and C. Chothia, Biochemistry **33**, 6739 (1994).

[3.3] Y. Togashi and A. S. Mikhailov, Proc. Natl. Acad. Sci. (USA) **104**, 8697 (2007).

[3.4] T. Sakaue, R. Kapral, and A. S. Mikhailov, Eur. Phys. J. B **75**, 381 (2010).

[3.5] C. Echeverria, Y. Togashi, A. S. Mikhailov, and R. Kapral, Phys. Chem. Chem. Phys. **13**, 10527 (2011).

[3.6] H. Y. Aviram, M. Pirchi, H. Mazal, Y. Barak, I. Riven, and G. Haran, Proc. Natl. Acad. Sci. (USA) **115**, 3243 (2018).

[3.7] Y. Zhang and H. Hess, ACS Cent. Sci. **5**, 939 (2019).

[3.8] H. S. Muddana, S. Sengupta, T. E. Mallouk, A. Sen, and P. J. Butler, J. Am. Chem. Soc. **132**, 2110 (2010).

[3.9] C. Riedel, R. Gabizon, C. A. M. Wilson, K. Hamadani, K. Tsekouras, S. Marqusee, S. Pressé, and C. Bustamante, Nature **517**, 227 (2015).

[3.10] P. Illien, X. Zhao, K. K. Dey, P. J. Butler, A. Sen, and R. Golestanian, Nano Lett. **17**, 4415 (2017).

[3.11] S. Sengupta, K. K. Dey, H. S. Muddana, T. Tabouillot, M. E. Ibele, P. J. Butler, and A. Sen, J. Am. Chem. Soc. **135**, 1406 (2013).

[3.12] A.-Y. Jee, S. Dutta, Y.-K. Cho, T. Tlusty, and S. Granick, Proc. Natl. Acad. Sci. (USA) **115**, 14 (2018).

[3.13] K. K. Dey, F. Y. Pong, J. Breffke, R. Pavlick, E. Hatzakis, C. Pacheco, and A. Sen, Angew. Chem. Int. Ed. **55**, 1113 (2016).

[3.14] X. Zhao, K. K. Dey, S. Jeganathan, P. J. Butler, U. M. Córdova-Figueroa, and A. Sen, Nano Lett. **17**, 4807 (2017).

[3.15] P. Illien, T. Adeleke-Larodo, and R. Golestanian, EPL **119**, 40002 (2017).

[3.16] T. Adeleke-Larodo, P. Illien, and R. Golestanian, Eur. Phys. J. E **42**, 39 (2019).

[3.17] R. Golestanian, Phys. Rev. Lett. **115**, 108102 (2015).

[3.18] A. S. Mikhailov and R. Kapral, Proc. Natl. Acad. Sci. (USA) **112**, E3639 (2015).

[3.19] R. Kapral and A. S. Mikhailov, Physica D **318-319**, 100 (2016).

[3.20] Y. Hosaka, K. Yasuda, R. Okamoto, and S. Komura, Phys. Rev. E **95**, 052407 (2017).

[3.21] M. Xu, J. L. Ross, L. Valdez, and A. Sen, Phys. Rev. Lett. **123**, 128101 (2019).

[3.22] Y. Zhang, M. J. Armstrong, N. M. B. Kazeruni, and H. Hess, Nano Lett. **18**, 8025 (2018).

[3.23] J.-P. Günther, G. Majer, and P. Fischer, J. Chem. Phys. **150**, 124201 (2019).

[3.24] V. Armoškaitė, K. Ramanauskienė, and V. Briedis, Afr. J. Pham. Pharmacol. **6**, 1685 (2012).

[3.25] H. Flechsig and A. S. Mikhailov, J. R. Soc. Interface **16**, 20190244 (2019).

[3.26] Y. Hosaka, S. Komura, and A. S. Mikhailov, unpublished.

[3.27] R. B. Bird, R. C. Armstrong, O. Hassager, and C. F. Curtiss, *Dynamics of Polymeric Liquids, Vol. 2* (Wiley, New York, 1987).

[3.28] M. Doi, *Soft Matter Physics* (Oxford University, Oxford, 2013).

[3.29] G. K. Fraenkel, J. Chem. Phys. **20**, 642 (1952).

[3.30] R. B. Bird, C. F. Curtiss, and K. J. Beers, Rheol. Acta. **36**, 269 (1997).

[3.31] M. Abramowitz and I.A. Stegun, *Handbook of Mathematical Functions* (Dover, New York, 1972).

[3.32] S. C. Kou, B. J. Cherayil, W. Min, B. P. English, and X. S. Xie, J. Phys. Chem. **109**, 19068 (2005).

[3.33] B. P. English, W. Min, A. M. van Oijen, K. T. Lee, G. Luo, H. Sun, B. J. Cherayil, S. C. Kou, and X. S. Xie, Nature Chem. Bio. **2**, 87 (2006).

[3.34] L. Michaelis and M. L. Menten, Biochem. Z. **49**, 333-369 (1913).

[3.35] J. Cao, J. Phys. Chem. B **115**, 5493 (2011).

[3.36] N. G. van Kampen, *Stochastic processes in physics and chemistry* (Elsevier Science, New York, 1992).

[3.37] H. P. Lu, L. Xun, and X. S. Xie, Science **282**, 1877 (1998).

[3.38] S. Xie, Single Mol. **2**, 229 (2001).

[3.39] S. Saha, S. Ghose, R. Adhikari, and A. Dua, Phys. Rev. Lett. **107**, 218301 (2011).

[3.40] R. Grima, Phys. Rev. Lett. **102**, 218103 (2009).

[3.41] N. Oppenheimer and H. Diamant, Biophys. J. **96**, 3041 (2009).

[3.42] N. Oppenheimer and H. Diamant, Phys. Rev. E **82**, 041912 (2010).

[3.43] R. B. Bird and H. R. Warner, Trans. Soc. Rheol. **15**, 741 (1971).

[3.44] M. Doi and S. F. Edwards, *The Theory of Polymer Dynamics* (Oxford University Press, New York, 1986).

[3.45] H. R. Warner, Ind. Eng. Chem. Fundam., **11**, 379 (1972).

[3.46] P. Hänggi, P. Talkner, and M. Brokovec, Rev. Mod. Phys. **62**, 251 (1990).

Chapter 4

Lateral Diffusion Induced by Enzymes in a Biomembrane †

4.1 Introduction

Biomembranes that consist of lipid bilayers can be regarded as thin two-dimensional (2D) fluids, and membrane protein molecules as well as lipid molecules are allowed to move laterally [4.1, 4.2]. These membrane inclusions are subject to the thermal motion of lipid molecules, leading to random positional fluctuations. Such a Brownian motion plays important roles in various life processes such as transportation of materials or reaction between chemical species [4.3]. In order to describe lateral diffusion of membrane proteins, a drag coefficient of a cylindrical disc moving in a 2D fluid sheet has been theoretically studied in various membrane environments [4.4–4.10]. The obtained drag coefficient was used to estimate the diffusion coefficients of membrane proteins through Einstein's relation under the assumption that the system is in thermal equilibrium [4.11].

In recent experiments, however, it has been shown that motions of particles inside cells are dominantly driven by random nonthermal forces rather than thermal fluctuations [4.12, 4.13]. In these experimental works, they found that

†The material presented in this chapter was published in: Y. Hosaka, K. Yasuda, R. Okamoto, and S. Komura, Phys. Rev. E **95**, 052407 (2017).

nonthermal forces in biological cells are generated by active proteins undergoing conformational changes with a supply of adenosine triphosphate (ATP). These active fluctuations lead to enhanced diffusion of molecules in the cytoplasm [4.14, 4.15]. Biomembranes also contain various active proteins which, for example, act as ion pumps by changing their shapes to exert forces to the adjacent membrane and solvent [4.2]. Lipid bilayers containing such active proteins have been called "active membranes", and their out-of-plane fluctuations (deformations) have already been investigated both experimentally and theoretically [4.16–4.18]. However, lateral motions of inclusions in membranes that are induced by active proteins have not yet been considered. Since such active forces give rise to enhanced diffusion, one needs to take into account both active nonthermal fluctuations as well as passive thermal ones to calculate diffusion in membranes.

Recently, Mikhailov and Kapral discussed an enhanced diffusion due to nonthermal fluctuating hydrodynamic flows which are induced by oscillating active force dipoles [see Fig. 4.1(a)] [4.19, 4.20]. They calculated the active diffusion coefficient of a passive particle immersed either in a three-dimensional (3D) cytoplasm or in a 2D membrane, and showed that it exhibits a logarithmic size dependence for the 2D case. Moreover, a chemotaxis-like drift of a passive particle was predicted when gradients of active proteins or ATP are present [4.19]. Later Koyano *et al.* showed that lipid membrane rafts, in which active proteins are concentrated, can induce a directed drift velocity near the interface of a domain [4.21]. In these works, they considered membranes that are smaller in size than the hydrodynamic screening length. Huang *et al.* performed coarse-grained simulations of active protein inclusions in lipid bilayers [4.22, 4.23]. In Ref. [4.23], they showed that active proteins undergoing conformational motions not only affect the membrane shape but also laterally stir the lipid bilayer so that lipid flows are induced. Importantly, the flow pattern induced by an immobilized protein resembles the 2D fluid velocity fields that are created by a force

dipole.

Following Refs. [4.19, 4.20], we assume that an active protein behaves as an oscillating force dipole which acts on the surroundings to generate hydrodynamic flows that can induce motions of passive particles in the fluid. In this paper, we investigate active diffusion and drift velocity of a particle in "free" and "confined" membranes which are completely flat and infinitely large. In the free membrane case, a thin 2D fluid sheet is embedded in a 3D solvent having typically a lower viscosity than that of the membrane. Whereas in the confined case, which mimics a supported membrane [4.24], a membrane is sandwiched by two rigid walls separated by a finite but small distance from it. For both the free and confined membrane cases, we employ general mobility tensors that take into account the hydrodynamic effects mediated by the surrounding 3D solvent [4.25–4.28]. Using the general mobility tensors, we numerically calculate the active diffusion coefficient and the drift velocity as a function of the diffusing particle size for the entire length scales. Furthermore, several asymptotic expressions are also derived in order to compare with numerical estimates and thermal contributions. Importantly, our result leads to characteristic length scales describing a crossover from nonthermal to thermal diffusive behaviors for large scales.

In the next section, we present the expressions for the active diffusion coefficient and the drift velocity in 2D membranes [4.19]. We also review the general mobility tensors for the free and confined membrane cases [4.25–4.28]. Using these expressions, we calculate in Sec. 4.3 the active diffusion coefficient for the two geometries. In Sec. 4.4, we compare the thermal diffusion coefficient with the obtained nonthermal diffusion coefficient, and discuss the characteristic crossover lengths. In Sec. 4.5, we obtain the drift velocities as a function of the particle size. The summary of our work and some numerical estimates for the obtained quantities are given in Sec. 4.6.

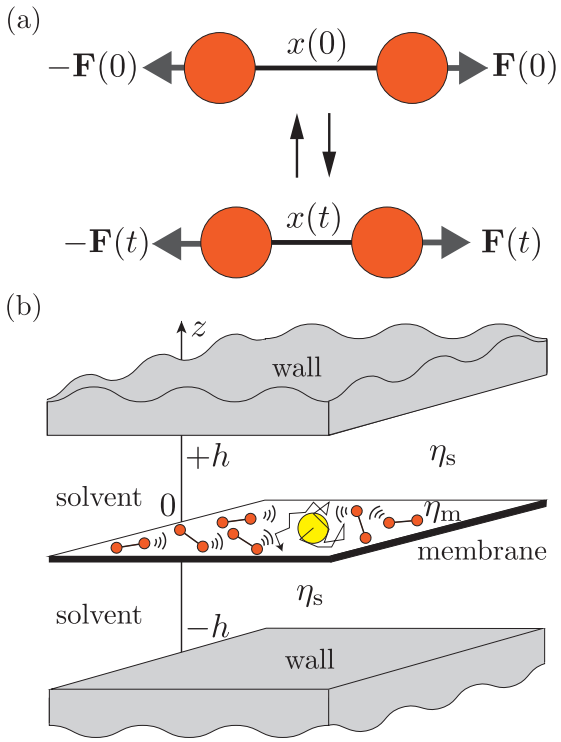

Figure 4.1: (a) The conformational change of an oscillating force dipole representing an active protein. Within a turnover cycle of the force dipole separated by a distance $x(t)$, it exerts two oppositely directed forces $\pm\mathbf{F}(t)$ at time t. The integral intensity of a force dipole is S (see the text). (b) Schematic picture showing a flat and infinitely large membrane of 2D viscosity η_m that is located at $z = 0$. The membrane is surrounded by a bulk solvent of 3D viscosity η_s, and the two flat walls are located at $z = \pm h$. The solvent velocity is assumed to vanish at the surfaces of these walls. The "free membrane" and the "confined membrane" cases correspond to the limits of $h \to \infty$ and $h \to 0$, respectively. The yellow passive particle undergoes Brownian motion due to thermal and non-thermal fluctuations. The latter contribution is induced by active force dipoles which are homogeneously distributed in the membrane with a 2D concentration c_0.

4.2 Active transport and mobility tensors in membranes

4.2.1 Active diffusion coefficient

Active proteins in a 2D biological membrane, modeled as oscillating force dipoles, produce nonequilibrium fluctuations and cause an enhancement of the lateral diffusion of a passive particle. We assume that the spatially fixed force dipoles are homogeneously and isotropically distributed in the membrane, and they exert only in-plane lateral forces. The total diffusion coefficient is given by $D = D_{\mathrm{T}} + D_{\mathrm{A}}$, where D_{T} is the thermal contribution and determined by Einstein's relation (which will be discussed in Sec. 4.4), and D_{A} is the active nonthermal contribution given by [4.19]

$$D_{\mathrm{A}} = \frac{Sc_0}{2}\Omega_{\beta\beta'\gamma\gamma'}\int \mathrm{d}^2 r\, \frac{\partial G_{\alpha\beta}(\mathbf{r})}{\partial r_\gamma}\frac{\partial G_{\alpha\beta'}(\mathbf{r})}{\partial r_{\gamma'}}, \tag{4.1}$$

where $\mathbf{r} = (x, y)$ denotes a 2D vector and we have introduced a notation

$$\Omega_{\beta\beta'\gamma\gamma'} = \frac{1}{8}(\delta_{\beta\beta'}\delta_{\gamma\gamma'} + \delta_{\beta\gamma}\delta_{\beta'\gamma'} + \delta_{\beta\gamma'}\delta_{\beta'\gamma}). \tag{4.2}$$

Throughout this paper, the summation over repeated greek indices is assumed. In Eq. (4.1), S is the integral intensity of a force dipole, c_0 is the constant 2D concentration of active proteins, and $G_{\alpha\beta}(\mathbf{r})$ is the membrane mobility tensor which will be discussed later separately.

Within a fluctuating "dimer model" as presented in Fig. 4.1(a), the magnitude of a force dipole is given by $m(t) = x(t)F(t)$, where $x(t)$ is the distance between the two spheres and $F(t)$ is the magnitude of the oppositely directed forces. The statistical average of the dipole magnitude vanishes, i.e., $\langle m(t)\rangle = 0$, whereas the integral intensity S of a force dipole is given by $S = \int_0^\infty \mathrm{d}t\, \langle m(t)m(0)\rangle$ [4.19]. Since we assume that active proteins are homogeneously distributed in the membrane as shown in Fig. 4.1(b), it is sufficient to consider only the isotropic diffusion as given by Eq. (4.1).

In deriving Eq. (4.1), the size of a dipole is assumed to be much smaller than

the distance between the passive particle and active force dipoles [4.19]. At large distances, almost any object that changes its shape would create a flow field that corresponds to some force dipole. It should be noted, however, that the above expression is not accurate when the distance between them becomes smaller. As for the mobility tensor in 3D fluids, it is known that the Rotne-Prager mobility tensor takes into account higher order corrections to the Oseen mobility tensor and gives more accurate approximation at short distances [4.20]. Such a better approximation has not been worked out so far for 2D fluid membranes, and we shall only consider the lowest order contribution (see later calulations). In the above, we have also assumed that force dipoles are spatially fixed in the membrane. Since no forces are applied to fix the dipoles, such an approximation is justified when the dynamics of force dipoles is much slower than that of the passive particle.

4.2.2 Drift velocity

Although we have assumed above that c_0 is constant, active proteins are often distributed inhomogeneously in the membrane due to heterogeneous structures such as sphingolipid-enriched domains [4.29, 4.30]. According to the "lipid raft" hypothesis, theses domains act as platforms for membrane signaling and traffcking [4.31]. Hence it is also important to consider the effects of nonuniform spatial distribution of active proteins and to see how it affects the lateral dynamics in membranes.

When a spatial concentration gradient ∇c of active protein is present, it gives rise to an unbalanced induced forces between two points in the membrane. Hence passive particles are subjected to a drift toward either lower or higher concentration of active proteins, and a chemotaxis-like drift can occur. When the absolute value of the concentration gradient $|\nabla c|$ is assumed to be constant, the induced drift velocity of a passive particle in the direction ∇c is given by [4.19]

$$V = -S|\nabla c|\Omega_{\beta\beta'\gamma\gamma'} \int \mathrm{d}^2 r\, \hat{n}_\alpha \frac{\partial^2 G_{\alpha\beta}(\mathbf{r})}{\partial r_\gamma \partial r_\delta} \frac{\partial G_{\delta\beta'}(\mathbf{r})}{\partial r_{\gamma'}} (\mathbf{r}\cdot\hat{\mathbf{n}}). \tag{4.3}$$

Here, the unit vector $\hat{\mathbf{n}} = \nabla c/|\nabla c|$ denotes the direction of the concentration gradient of active proteins. We shall employ the above expression to obtain the lateral drift velocity in a membrane by using the membrane mobility tensor as discussed below.

4.2.3 Membrane mobility tensors

Since we discuss active diffusion in an infinitely large flat membrane, we use the 2D membrane mobility tensor which also takes into account the hydrodynamic effects of the surrounding 3D solvent. We consider a general situation as depicted in Fig. 4.1(b), where a fluid membrane of 2D shear viscosity η_{m} is surrounded by a solvent of 3D shear viscosity η_{s}. Furthermore, we consider the case in which there are two walls located symmetrically at an arbitrary distance h from the flat membrane [4.25–4.28].

We denote the in-plane velocity vector of the fluid membrane by $\mathbf{v}(\mathbf{r})$ and the lateral pressure by $p(\mathbf{r})$. Assuming that the incompressibility condition holds for the fluid membrane, we write its hydrodynamic equations as

$$\nabla \cdot \mathbf{v} = 0, \tag{4.4}$$

$$\eta_{\mathrm{m}} \nabla^2 \mathbf{v} - \nabla p + \mathbf{f}_{\mathrm{s}} + \mathbf{F} = 0. \tag{4.5}$$

The second equation is the 2D Stokes equation, where $\mathbf{f}_{\mathrm{s}}$ is the force exerted on the membrane by the surrounding solvent, and $\mathbf{F}$ is any external force acting on the membrane. If we denote the upper and lower solvents with the superscripts $\pm$, the two solvent velocities $\mathbf{v}^{\pm}(\mathbf{r}, z)$ and pressures $p^{\pm}(\mathbf{r}, z)$ obey the following hydrodynamic equations, respectively

$$\widehat{\nabla} \cdot \mathbf{v}^{\pm} = 0, \tag{4.6}$$

$$\eta_{\mathrm{s}} \widehat{\nabla}^2 \mathbf{v}^{\pm} - \widehat{\nabla} p^{\pm} = 0, \tag{4.7}$$

where $\widehat{\nabla}$ stands for the 3D differential operator.

We assume that the surrounding solvent cannot permeate the membrane, and impose the no-slip boundary condition between the membrane and the sur-

rounding solvent at $z = 0$ [4.4, 4.5, 4.25–4.28]. Hence we require the conditions

$$v_z^{\pm}(\mathbf{r}, 0) = 0, \qquad v_\alpha(\mathbf{r}) = v_\alpha^{\pm}(\mathbf{r}, 0), \tag{4.8}$$

where $\alpha = x, y$. Furthermore, the solvent velocity vanishes at the walls located at $z = \pm h$, i.e., $v_\alpha^{\pm}(\mathbf{r}, \pm h) = 0$.

By solving the above coupled hydrodynamic equations in Fourier space with $\mathbf{k} = (k_x, k_y)$ being the 2D wavevector, the 2D mobility tensor $G_{\alpha\beta}(\mathbf{k})$ defined through $v_\alpha(\mathbf{k}) = G_{\alpha\beta}(\mathbf{k})F_\beta(\mathbf{k})$ can be obtained as [4.25–4.28]

$$G_{\alpha\beta}(\mathbf{k}) = \frac{\delta_{\alpha\beta} - \hat{k}_\alpha \hat{k}_\beta}{\eta_{\rm m}\left[k^2 + \nu k \coth(kh)\right]}, \tag{4.9}$$

where $k = |\mathbf{k}|$ and $\hat{k}_\alpha = k_\alpha/k$, and the ratio of the two viscosities $\nu^{-1} = \eta_{\rm m}/(2\eta_{\rm s})$ defines the Saffman–Delbrück (SD) hydrodynamic screening length [4.4, 4.5]. Notice that $\eta_{\rm m}$ and $\eta_{\rm s}$ have different dimensions, and ν^{-1} has a dimension of length.

In order to perform analytical calculations, the two limiting cases of Eq. (4.9) are considered, i.e., the "free membrane" case and the "confined membrane" case corresponding to the limits of $h \to \infty$ and $h \to 0$, respectively [4.26–4.28]. For the free membrane case, we take the limit $kh \gg 1$ in Eq. (4.9) and obtain the following asymptotic expression

$$G_{\alpha\beta}^{\rm F}(\mathbf{k}) = \frac{\delta_{\alpha\beta} - \hat{k}_\alpha \hat{k}_\beta}{\eta_{\rm m}(k^2 + \nu k)}. \tag{4.10}$$

Hereafter, we shall denote the quantities for the free membrane case with the superscript "F". For the confined membrane case, on the other hand, we take the opposite limit $kh \ll 1$ and obtain

$$G_{\alpha\beta}^{\rm C}(\mathbf{k}) = \frac{\delta_{\alpha\beta} - \hat{k}_\alpha \hat{k}_\beta}{\eta_{\rm m}(k^2 + \kappa^2)}, \tag{4.11}$$

where $\kappa^{-1} = (h/\nu)^{1/2}$ is the Evans–Sackmann (ES) screening length [4.7], and we use the superscript "C" for the quantities related to the confined membrane case. We note that the ES screening length κ^{-1} is the geometric mean of ν^{-1} and h so that we typically have $\kappa^{-1} < \nu^{-1}$.

Taking the inverse Fourier transform of Eqs. (4.10) and (4.11), we obtain the

mobility tensors in the real space for the two limiting cases as [4.26–4.28]

$$G^{\mathrm{F}}_{\alpha\beta}(\mathbf{r}) = \frac{1}{4\eta_{\mathrm{m}}}\left[\mathbf{H}_0(\nu r) - Y_0(\nu r) + \frac{2}{\pi\nu^2 r^2} - \frac{\mathbf{H}_1(\nu r)}{\nu r} + \frac{Y_1(\nu r)}{\nu r}\right]\delta_{\alpha\beta} + \frac{1}{4\eta_{\mathrm{m}}}\left[-\frac{4}{\pi\nu^2 r^2} + \frac{2\mathbf{H}_1(\nu r)}{\nu r} - \frac{2Y_1(\nu r)}{\nu r} - \mathbf{H}_0(\nu r) + Y_0(\nu r)\right]\hat{r}_\alpha\hat{r}_\beta, \tag{4.12}$$

and

$$G^{\mathrm{C}}_{\alpha\beta}(\mathbf{r}) = \frac{1}{2\pi\eta_{\mathrm{m}}}\left[K_0(\kappa r) + \frac{K_1(\kappa r)}{\kappa r} - \frac{1}{\kappa^2 r^2}\right]\delta_{\alpha\beta} + \frac{1}{2\pi\eta_{\mathrm{m}}}\left[-K_0(\kappa r) - \frac{2K_1(\kappa r)}{\kappa r} + \frac{2}{\kappa^2 r^2}\right]\hat{r}_\alpha\hat{r}_\beta, \tag{4.13}$$

respectively, where we have used the notations $r = |\mathbf{r}|$ and $\hat{r}_\alpha = r_\alpha/r$. In the above, $\mathbf{H}_n(z)$ are the Struve functions, $Y_n(z)$ the Bessel functions of the second kind, and $K_n(z)$ the modified Bessel functions of the second kind. The physical meaning of the above expressions was also discussed in Refs. [4.32–4.34]. We note that if there is only one wall instead of two walls, the definition of the ES length needs to be modified as $\kappa^{-1} \to (2h/\nu)^{1/2}$ [4.34]. In the next sections, we shall use Eqs. (4.12) and (4.13) to calculate the active diffusion coefficients and the drift velocity.

4.3 Active diffusion coefficient

4.3.1 Free membranes

We first calculate the active diffusion coefficient for the free membrane case by substituting Eq. (4.12) into Eq. (4.1). Since the integrand in Eq. (4.1) diverges logarithmically at short distances, we need to introduce a small cutoff length ℓ_{c}. Physically, ℓ_{c} is given by the sum of the size of a passive particle (undergoing lateral Brownian motion) and that of a force dipole [4.20]. In the following, we generally assume that force dipoles are smaller than the diffusing object whose size is represented by ℓ_{c}. This is further justified when we consider lateral diffusion of a passive object that is larger than the SD or ES screening lengths.

Introducing a dimensionless vector $\mathbf{z} = \nu\mathbf{r}$ scaled by the SD length, we can

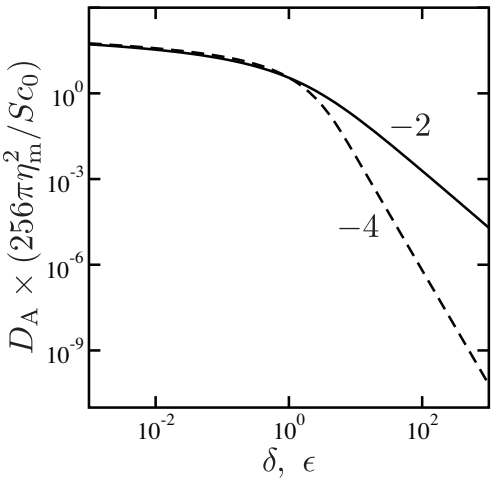

Figure 4.2: The plot of the scaled active diffusion coefficient D_A as a function of the scaled cutoff length $\delta = \nu\ell_c$ and $\epsilon = \kappa\ell_c$ for the free membrane case [solid line, see Eq. (4.14)] and the confined membrane case [dashed line, see Eq. (4.19)], respectively. Here D_A is scaled by $Sc_0/(256\pi\eta_m^2)$. The numbers in this plot indicate the slope of the curves and represent the powers of the algebraic dependencies.

write the active diffusion coefficient for the free membrane case as

$$D_A^F = \frac{Sc_0}{32\pi^2\eta_m^2}\Omega_{\beta\beta'\gamma\gamma'}\int_\delta^\infty d^2z\,\frac{\partial g_{\alpha\beta}^F(\mathbf{z})}{\partial z_\gamma}\frac{\partial g_{\alpha\beta'}^F(\mathbf{z})}{\partial z_{\gamma'}}, \tag{4.14}$$

where $\delta = \nu\ell_c$ is the dimensionless cutoff, and $g_{\alpha\beta}^F(\mathbf{z}) = 4\pi\eta_m G_{\alpha\beta}^F$ is the corresponding dimensionless mobility tensor [see Eq. (4.12)]. We have first evaluated the above integral numerically. In Fig. 4.2, we plot the obtained D_A^F as a function of $\delta = \nu\ell_c$ by the solid line. We see that the active diffusion coefficient depends only weakly on the particle size at small scales, whereas it shows a stronger size dependence described by a power-law behavior at large scales. The crossover between these two behaviors is set by the condition $\delta \approx 1$.

In order to understand the above behaviors, we next discuss the asymptotic behaviors of D_A^F for both small and large δ values. Expanding the mobility tensor in Eq. (4.12) for $\nu r \ll 1$ and $\nu r \gg 1$, we have [4.34]

$$g_{\alpha\beta}^F(\mathbf{z}) \approx \left(\ln\frac{2}{z} - \gamma - \frac{1}{2}\right)\delta_{\alpha\beta} + \hat{z}_\alpha\hat{z}_\beta, \tag{4.15}$$

and

$$g^{\mathrm{F}}_{\alpha\beta}(\mathbf{z}) \approx \frac{2}{z}\hat{z}_\alpha \hat{z}_\beta, \tag{4.16}$$

respectively, where $\gamma \approx 0.5772$ is Euler's constant. By substituting Eqs. (4.15) and (4.16) into Eq. (4.14), we can analytically obtain the asymptotic forms of the active diffusion coefficient as a function of $\delta = \nu \ell_{\mathrm{c}}$.

As obtained in Ref. [4.19], we find for $\delta \ll 1$

$$D^{\mathrm{F}}_{\mathrm{A}} \approx \frac{Sc_0}{32\pi\eta^2_{\mathrm{m}}} \ln \frac{L}{\ell_{\mathrm{c}}}, \tag{4.17}$$

where a large cutoff length L is introduced because the integral in Eq. (4.14) also diverges logarithmically at large distances. In order to match with the numerical estimation, we obtain $L \approx 0.682\nu^{-1}$. The above logarithmic dependence on ℓ_{c} means that $D^{\mathrm{F}}_{\mathrm{A}}$ depends only weakly on the particle size. We also note that the above expression contains only the membrane viscosity η_{m}, and does not depend on the solvent viscosity η_{s}. This is because the hydrodynamics at small scales is primarily dominated by the 2D membrane property.

In the opposite limit of $\delta \gg 1$, on the other hand, we show in the Appendix A that the active diffusion coefficient becomes

$$D^{\mathrm{F}}_{\mathrm{A}} \approx \frac{5Sc_0}{256\pi\eta^2_{\mathrm{s}}} \frac{1}{\ell^2_{\mathrm{c}}}, \tag{4.18}$$

which is an important result of this paper. This asymptotic expression decays as $1/\ell^2_{\mathrm{c}}$ and depends now only on η_{s}, indicating that the membrane lateral dynamics is governed by the surrounding 3D fluid at large scales. From the obtained asymptotic expressions in Eqs. (4.17) and (4.18), the behavior of $D^{\mathrm{F}}_{\mathrm{A}}$ in Fig. 4.2 is explained as a crossover from a logarithmic dependence to an algebraic dependence with a power of -2.

4.3.2 Confined membranes

Next we consider the confined membrane case. With the use of Eq. (4.13) the active diffusion coefficient can be written as

$$D_{\rm A}^{\rm C} = \frac{Sc_0}{32\pi^2\eta_{\rm m}^2}\Omega_{\beta\beta'\gamma\gamma'}\int_{\epsilon}^{\infty} {\rm d}^2 w\, \frac{\partial g_{\alpha\beta}^{\rm C}(\mathbf{w})}{\partial w_\gamma}\frac{\partial g_{\alpha\beta'}^{\rm C}(\mathbf{w})}{\partial w_{\gamma'}}, \tag{4.19}$$

where $\mathbf{w} = \kappa\mathbf{r}$ is a different dimensionless variable, $\epsilon = \kappa\ell_{\rm c}$ is a differently scaled cutoff, and $g_{\alpha\beta}^{\rm C}(\mathbf{w}) = 4\pi\eta_{\rm m}G_{\alpha\beta}^{\rm C}$ is the corresponding dimensionless mobility tensor [see Eq. (4.13)]. Performing the numerical integration of Eq. (4.19), we plot in Fig. 4.2 the active diffusion coefficient $D_{\rm A}^{\rm C}$ as a function of $\epsilon = \kappa\ell_{\rm c}$ by the dashed line. For small ϵ values, the behavior of $D_{\rm A}^{\rm C}$ is similar to that of $D_{\rm A}^{\rm F}$, while $D_{\rm A}^{\rm C}$ decays much faster than $D_{\rm A}^{\rm F}$ for large ϵ values.

To discuss these size dependencies, we use the asymptotic expressions of Eq. (4.13) for $\kappa r \ll 1$ and $\kappa r \gg 1$ given by [4.34]

$$g_{\alpha\beta}^{\rm C}(\mathbf{w}) \approx \left(\ln\frac{2}{w} - \gamma - \frac{1}{2}\right)\delta_{\alpha\beta} + \hat{w}_\alpha\hat{w}_\beta, \tag{4.20}$$

and

$$g_{\alpha\beta}^{\rm C}(\mathbf{w}) \approx -\frac{2}{w^2}(\delta_{\alpha\beta} - 2\hat{w}_\alpha\hat{w}_\beta), \tag{4.21}$$

respectively. Note that Eq. (4.20) is identical to Eq. (4.15) when w is replaced by z. Hence, in the limit of $\epsilon \ll 1$, the active diffusion coefficient for the confined membrane case should be identical to Eq. (4.17) and is given by [4.19]

$$D_{\rm A}^{\rm C} \approx \frac{Sc_0}{32\pi\eta_{\rm m}^2}\ln\frac{L}{\ell_{\rm c}}. \tag{4.22}$$

The large cutoff length should be taken here as $L \approx 1.12\kappa^{-1}$. As mentioned before, the 2D hydrodynamic effect is more important at small scales, and $D_{\rm A}^{\rm C}$ is logarithmically dependent on the particle size.

In the large size limit of $\epsilon \gg 1$, on the other hand, we also show in the Appendix A that $D_{\rm A}^{\rm C}$ asymptotically behaves as

$$D_{\rm A}^{\rm C} \approx \frac{Sc_0}{16\pi\eta_{\rm s}^2}\frac{h^2}{\ell_{\rm c}^4}, \tag{4.23}$$

which is another important result. The obtained expression decays as $1/\ell_{\rm c}^4$

which is much stronger than Eq. (4.18) for the free membrane case. According to Eqs. (4.22) and (4.23), the behavior of $D_{\mathrm{A}}^{\mathrm{C}}$ in Fig. 4.2 can be understood as a crossover from a logarithmic dependence to an algebraic dependence with a power of -4.

4.4 Total diffusion coefficient

Having obtained the active diffusion coefficients for the free and the confined membrane cases, we now discuss the total lateral diffusion coefficients in membranes by considering both thermal and nonthermal contributions. Concerning the thermal diffusion coefficient $D_{\mathrm{T}}^{\mathrm{F}}$ for the free membrane case, we use an empirical expression obtained by Petrov and Schwille [4.35, 4.36]

$$D_{\mathrm{T}}^{\mathrm{F}}(\delta) = \frac{k_{\mathrm{B}}T}{4\pi\eta_{\mathrm{m}}}\left[\ln\frac{2}{\delta} - \gamma + \frac{4\delta}{\pi} - \frac{\delta^2}{2}\ln\frac{2}{\delta}\right]\left[1 - \frac{\delta^3}{\pi}\ln\frac{2}{\delta} + \frac{c_1\delta^{b_1}}{1+c_2\delta^{b_2}}\right]^{-1}, \quad (4.24)$$

where k_{B} is the Boltzmann constant, T is the temperature, and the four numerical constants are chosen as $c_1 = 0.73761$, $b_1 = 2.74819$, $c_2 = 0.52119$, and $b_2 = 0.51465$ [4.36]. For the free membrane case, there is no exact analytical expression of the thermal diffusion coefficient which covers the entire size range, except for the case where a 2D polymer chain is confined in a fluid membrane [4.26]. Equation (4.24) is known to recover the correct asymptotic limits of the thermal diffusion coefficients both for $\delta \ll 1$ [4.4, 4.5] and $\delta \gg 1$ [4.6].

On the other hand, the thermal diffusion coefficient $D_{\mathrm{T}}^{\mathrm{C}}$ for the confined membrane case was explicitly calculated by Evans *et al.* [4.7] and also by Ramachandran *et al.* [4.8–4.11]. In this case, the resulting expression is given by

$$D_{\mathrm{T}}^{\mathrm{C}}(\epsilon) = \frac{k_{\mathrm{B}}T}{4\pi\eta_{\mathrm{m}}}\left[\frac{\epsilon^2}{4} + \frac{\epsilon K_1(\epsilon)}{K_0(\epsilon)}\right]^{-1}. \quad (4.25)$$

In Fig. 4.3, we plot $D_{\mathrm{T}}^{\mathrm{F}}$ as a function of the particle size δ by the solid line, and $D_{\mathrm{T}}^{\mathrm{C}}$ as a function of ϵ by the dashed line for the whole size range. Their asymptotic behaviors are separately discussed below.

When we consider the total diffusion coefficient $D = D_{\mathrm{T}} + D_{\mathrm{A}}$, we shall neglected the contribution from thermal fluctuations of force dipoles. These

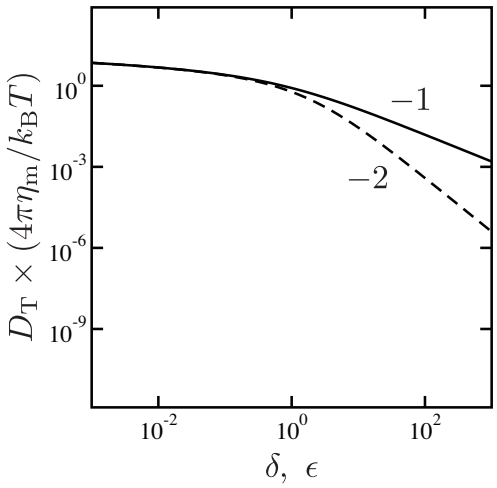

Figure 4.3: The plot of the scaled thermal diffusion coefficient $D_{\rm T}$ as a function of the scaled cutoff length $\delta = \nu\ell_{\rm c}$ and $\epsilon = \kappa\ell_{\rm c}$ for the free membrane case [solid line, see Eq. (4.24)] and the confined membrane case [dashed line, see Eq. (4.25)], respectively. Here $D_{\rm T}$ is scaled by $k_{\rm B}T/(4\pi\eta_{\rm m})$. The numbers in this plot indicate the slope of the curves and represent the powers of the algebraic dependencies.

fluctuations can arise when force dipoles contain structural internal degrees of freedom. However, such a contribution to the diffusion coefficient is small compared to $D_{\rm T}$ because it should be proportional to the product of $k_{\rm B}T$ and the concentration of force dipoles c_0.

4.4.1 Free membranes

For the free membrane case, the total diffusion coefficient is given by $D^{\rm F} = D^{\rm F}_{\rm T} + D^{\rm F}_{\rm A}$, where the active nonthermal contribution $D^{\rm F}_{\rm A}$ was discussed in the previous section. Using Eqs. (4.24) and (4.17) in the limit of $\delta \ll 1$, we asymptotically have [4.4, 4.5]

$$D^{\rm F} \approx \frac{k_{\rm B}T}{4\pi\eta_{\rm m}}\left(\ln\frac{2}{\nu\ell_{\rm c}} - \gamma\right) + \frac{Sc_0}{32\pi\eta_{\rm m}^2}\ln\frac{L}{\ell_{\rm c}}, \tag{4.26}$$

where both contributions are proportional to $\ln(1/\ell_{\rm c})$.

For $\delta \gg 1$, on the other hand, we obtain from Eqs. (4.24) and (4.18) [4.6]

$$D^{\rm F} \approx \frac{k_{\rm B}T}{16\eta_{\rm s}}\frac{1}{\ell_{\rm c}} + \frac{5Sc_0}{256\pi\eta_{\rm s}^2}\frac{1}{\ell_{\rm c}^2}. \tag{4.27}$$

Since the $\ell_{\rm c}$-dependencies in Eq. (4.27) are different between the thermal and

nonthermal contributions, we can introduce a new crossover length defined by

$$\ell^* = \frac{5Sc_0}{16\pi k_{\rm B}T\eta_{\rm s}}. \tag{4.28}$$

This length scale characterizes a crossover from the $1/\ell_{\rm c}^2$-dependence to $1/\ell_{\rm c}$-dependence. When $\ell_{\rm c} \ll \ell^*$ (but still $\nu^{-1} \ll \ell_{\rm c}$), the nonthermal contribution dominates over the thermal one, while in the opposite limit of $\ell_{\rm c} \gg \ell^*$, the thermal contribution is of primary importance.

4.4.2 Confined membranes

In the case of confined membranes, the total diffusion coefficient now becomes $D^{\rm C} = D_{\rm T}^{\rm C} + D_{\rm A}^{\rm C}$. In the limit of $\epsilon \ll 1$, we have from Eqs. (4.25) and (4.22) [4.7, 4.8]

$$D^{\rm C} \approx \frac{k_{\rm B}T}{4\pi\eta_{\rm m}}\left(\ln\frac{2}{\kappa\ell_{\rm c}} - \gamma\right) + \frac{Sc_0}{32\pi\eta_{\rm m}^2}\ln\frac{L}{\ell_{\rm c}}, \tag{4.29}$$

where both contributions exhibit a logarithmic dependence on $\ell_{\rm c}$ as in the free membrane case.

In the opposite limit of $\epsilon \gg 1$, we find from Eqs. (4.25) and (4.23) [4.7, 4.8]

$$D^{\rm C} \approx \frac{k_{\rm B}T}{2\pi\eta_{\rm s}}\frac{h}{\ell_{\rm c}^2} + \frac{Sc_0}{16\pi\eta_{\rm s}^2}\frac{h^2}{\ell_{\rm c}^4}. \tag{4.30}$$

Similar to the free membrane case, we can consider another characteristic length defined by

$$\ell^{**} = \left(\frac{Sc_0 h}{8k_{\rm B}T\eta_{\rm s}}\right)^{1/2}. \tag{4.31}$$

This length scale characterizes a crossover from the $1/\ell_{\rm c}^4$-dependence to $1/\ell_{\rm c}^2$-dependence. We note that ℓ^{**} is essentially the geometric mean of ℓ^* and h. Numerical estimates of these two characteristic length scales will be discussed in Sec. 4.6.

4.5 Drift velocity

4.5.1 Free membranes

In this section, we calculate the drift velocity V of a passive particle due to a concentration gradient of active force dipoles. For the free membrane case, we

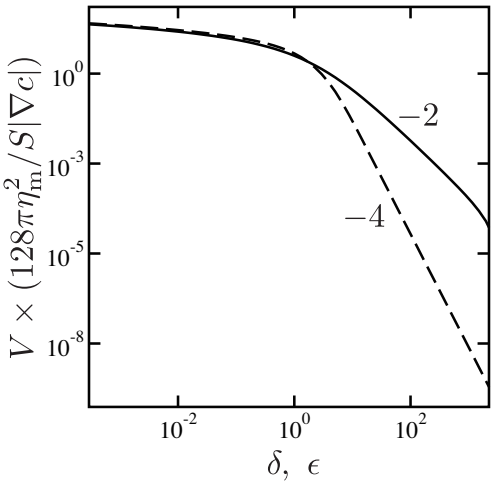

Figure 4.4: The plot of the scaled drift velocity V as a function of the scaled cutoff length $\delta = \nu\ell_c$ and $\epsilon = \kappa\ell_c$ for the free membrane case [solid line, see Eq. (4.32)] and the confined membrane case [dashed line, see Eq. (4.35)], respectively. Here V is scaled by $S|\nabla c|/(128\pi\eta_m^2)$. The numbers in this plot indicate the slope of the curves and represent the powers of the algebraic dependencies.

substitute Eq. (4.12) into Eq. (4.3) and obtain

$$V^F = -\frac{S|\nabla c|}{16\pi^2\eta_m^2}\Omega_{\beta\beta'\gamma\gamma'}\int_\delta^\infty d^2z\,\hat{n}_\alpha\frac{\partial^2 g^F_{\alpha\beta}(\mathbf{z})}{\partial z_\gamma\partial z_\delta}\frac{\partial g^F_{\delta\beta'}(\mathbf{z})}{\partial z_{\gamma'}}(\mathbf{z}\cdot\hat{\mathbf{n}}), \tag{4.32}$$

where $\delta = \nu\ell_c$ and $g^F_{\alpha\beta}(\mathbf{z}) = 4\pi\eta_m G^F_{\alpha\beta}$ as before. Performing the numerical integration of Eq. (4.32), we plot in Fig. 4.4 the drift velocity V^F as a function of δ by the solid line. Similar to the active diffusion coefficient D^F_A, the drift velocity V^F depends weakly on the particle size at small scales, while it exhibits a stronger size dependence at large scales. Such a crossover also occurs around $\delta \approx 1$.

We next discuss the asymptotic behaviors of V^F for small and large δ values. With the use of Eqs. (4.15) and (4.16), we show in the Appendix B that the asymptotic behaviors of V for $\delta \ll 1$ and $\delta \gg 1$ are

$$V^F \approx \frac{S|\nabla c|}{32\pi\eta_m^2}\ln\frac{L}{\ell_c}, \tag{4.33}$$

and

$$V^F \approx \frac{13S|\nabla c|}{256\pi\eta_s^2}\frac{1}{\ell_c^2}, \tag{4.34}$$

respectively, where we choose $L \approx 1.85\nu^{-1}$. Note that Eq. (4.33) was previously derived in Ref. [4.19] for a 2D membrane, while Eq. (4.34) is a new result. As we see in Eqs. (4.33) and (4.34), there is a crossover from a logarithmic to an algebraic dependence with a power of -2 when δ is increased. These behaviors are consistent with the numerical plot in Fig. 4.4 for the free membrane case.

4.5.2 Confined membranes

Finally we calculate the drift velocity for the confined membrane case. Substituting Eq. (4.13) into Eq. (4.3), we now obtain

$$V^{\mathrm{C}} = -\frac{S|\nabla c|}{16\pi^2\eta_{\mathrm{m}}^2}\Omega_{\beta\beta'\gamma\gamma'}\int_{\epsilon}^{\infty} \mathrm{d}^2 w\, \hat{n}_\alpha \frac{\partial^2 g^{\mathrm{C}}_{\alpha\beta}(\mathbf{w})}{\partial w_\gamma \partial w_\delta}\frac{\partial g^{\mathrm{C}}_{\delta\beta'}(\mathbf{w})}{\partial w_{\gamma'}}(\mathbf{w}\cdot\hat{\mathbf{n}}), \tag{4.35}$$

where $\epsilon = \kappa\ell_{\mathrm{c}}$ and $g^{\mathrm{C}}_{\alpha\beta}(\mathbf{w}) = 4\pi\eta_{\mathrm{m}} G^{\mathrm{C}}_{\alpha\beta}$ as before. In Fig. 4.4, we present numerically calculated V^{C} as a function of ϵ by the dashed line. As ϵ is increased, we see a crossover from a logarithmic to an algebraic dependence, although V^{C} decays faster than V^{F} at large scales.

The asymptotic behaviors of V^{C} for small and large ϵ values can be discussed similarly. Using Eqs. (4.20) and (4.21), we obtain in the Appendix B the asymptotic expressions of V^{C} for $\epsilon \ll 1$ and $\epsilon \gg 1$ as

$$V^{\mathrm{C}} \approx \frac{S|\nabla c|}{32\pi\eta_{\mathrm{m}}^2}\ln\frac{L}{\ell_{\mathrm{c}}}, \tag{4.36}$$

and

$$V^{\mathrm{C}} \approx \frac{3S|\nabla c|}{16\pi\eta_{\mathrm{s}}^2}\frac{h^2}{\ell_{\mathrm{c}}^4}, \tag{4.37}$$

respectively, and we choose $L \approx 3.05\kappa^{-1}$ to coincide with the numerical integration. We note that Eqs. (4.33) and (4.36) are identical and depend only on η_{m} for small sizes [4.19].

From Fig. 4.4 and Eqs. (4.33), (4.34), (4.36) and (4.37), we see that the drift velocity V is always positive. This means that passive particles move toward higher concentrations of active proteins, and a chemotaxis-like drift takes place in the presence of protein concentration gradients [4.19–4.21]. The dominant viscosity dependence of V switches from η_{m} to η_{s} as the particle size exceeds the

Table 4.1: Summary of the asymptotic dependencies of the thermal diffusion coefficient D_{T}, the active diffusion coefficient D_{A}, and the drift velocity V on the passive particle size ℓ_{c}. The numbers after the asymptotic expressions correspond to the equation numbers in this paper.

Cases	Limits	D_{T}	D_{A}	V
free membrane	$\nu\ell_{\mathrm{c}} \ll 1$	$\ln(1/\ell_{\mathrm{c}})$ (4.26)	$\ln(1/\ell_{\mathrm{c}})$ (4.17)	$\ln(1/\ell_{\mathrm{c}})$ (4.33)
$(hk \gg 1)$	$\nu\ell_{\mathrm{c}} \gg 1$	$1/\ell_{\mathrm{c}}$ (4.27)	$1/\ell_{\mathrm{c}}^2$ (4.18)	$1/\ell_{\mathrm{c}}^2$ (4.34)
confined membrane	$\kappa\ell_{\mathrm{c}} \ll 1$	$\ln(1/\ell_{\mathrm{c}})$ (4.29)	$\ln(1/\ell_{\mathrm{c}})$ (4.22)	$\ln(1/\ell_{\mathrm{c}})$ (4.36)
$(hk \ll 1)$	$\kappa\ell_{\mathrm{c}} \gg 1$	$1/\ell_{\mathrm{c}}^2$ (4.30)	$1/\ell_{\mathrm{c}}^4$ (4.23)	$1/\ell_{\mathrm{c}}^4$ (4.37)

corresponding hydrodynamic screening length, namely, ν^{-1} or κ^{-1}.

4.6 Discussion and conclusion

In this paper, we have investigated lateral diffusion induced by active force dipoles embedded in a biomembrane. In particular, we have calculated the active diffusion coefficient and the drift velocity for the free and the confined membrane cases by taking into account the hydrodynamic coupling between the membrane and the surrounding bulk solvent. The force dipole model in Refs. [4.19, 4.20] and the general membrane mobility tensors obtained in Refs. [4.25–4.28] have been employed in our work. When the size of a passive diffusing particle is small, the active diffusion coefficients for the free and the confined membranes represent the same logarithmic size dependence, as shown in Eqs. (4.17) and (4.22), respectively [4.19]. In the opposite large size limit, we find algebraic dependencies with powers -2 and -4 for the two cases, as given by Eqs. (4.18) and (4.23), respectively. These are the important outcomes of this paper and are also summarized in Table 5.1 together with other asymptotic expressions.

In our work, we have assumed that the total diffusion coefficient is provided by the sum of thermal and nonthermal contributions. For small particle sizes, we have shown that both the total D^{F} and D^{C} exhibit a logarithmic size dependence [4.19], whereas different contributions have different size dependencies for large particle sizes. From this result, we have obtained two characteristic length scales that describe the crossover from nonthermal to thermal behaviors when

the particle size is larger than the hydrodynamic screening length. The drift velocity in the presence of a concentration gradient of active proteins exhibits the same size dependencies as the active diffusion coefficient for the two membrane geometries.

Here we give some numerical estimates of the obtained crossover length scales. Using typical values such as $k_{\rm B}T \approx 4 \times 10^{-21}\,{\rm J}$, $\eta_{\rm s} \approx 10^{-3}\,{\rm Pa{\cdot}s}$, $h \approx 10^{-9}\,{\rm m}$, $S \approx 10^{-42}\,{\rm J^2{\cdot}s}$, and $c_0 \approx 10^{14}\,{\rm m^{-2}}$ [4.19], we obtain $\ell^* \approx 2 \times 10^{-6}\,{\rm m}$ [see Eq. (4.28)] and $\ell^{**} \approx 6 \times 10^{-8}\,{\rm m}$ [see Eq. (4.31)]. On the other hand, the SD and the ES screening lengths are typically $\nu^{-1} \approx 5 \times 10^{-7}\,{\rm m}$ and $\kappa^{-1} \approx 2 \times 10^{-8}\,{\rm m}$, respectively [4.4, 4.5, 4.7, 4.8]. Hence ℓ^* and ℓ^{**} are typically larger than ν^{-1} and κ^{-1}, respectively. Moreover, the values of S and c_0 can vary significantly in one membrane to another as pointed out in Ref. [4.19]. For example, when active proteins are confined in raft domains [4.29–4.31], the 2D concentration c_0 can be much larger. When, for example, $c_0 \approx 10^{15}\,{\rm m^{-2}}$ (while S is the same as above) [4.21], the crossover length can be estimated as $\ell^* \approx 2 \times 10^{-5}\,{\rm m}$ and $\ell^{**} \approx 2 \times 10^{-7}\,{\rm m}$. If ℓ^* and ℓ^{**} are much larger than the screening lengths ν^{-1} and κ^{-1}, respectively, as in this case, the three different scaling regimes of the total diffusion coefficient are expected as the particle size is increased, i.e., $\ln(1/\ell_{\rm c}) \to 1/\ell_{\rm c}^2 \to 1/\ell_{\rm c}$ for the free membrane case, and $\ln(1/\ell_{\rm c}) \to 1/\ell_{\rm c}^4 \to 1/\ell_{\rm c}^2$ for the confined membrane case.

Momentum in a membrane is conserved over distances smaller than the hydrodynamic screening length (either ν^{-1} or κ^{-1}), whereas it leaks to the surrounding fluid beyond that length scale [4.32–4.34]. Within a membrane, the velocity decays as $\ln(1/r)$ at short distances, as shown in Eqs. (4.15) and (4.20), due to the momentum conservation in 2D. These 2D behaviors also lead to the logarithmic dependence of the active diffusion coefficients in Eqs. (4.17) and (4.22). For the free membrane case, the velocity decays as $1/r$ at large scales as shown in Eq. (4.16) due to the momentum conservation in the 3D bulk. This behavior is reflected in the first term of Eq. (4.27) for the thermal diffusion

coefficient [4.6]. As shown in Eq. (4.21), however, the velocity decays as $1/r^2$ at large scales for the confined membrane case. This behavior essentially arises from the mass conservation in 2D while the total momentum is not conserved due to the presence of the walls which break the translational symmetry of the system [4.32–4.34]. The corresponding contribution is the first term of Eq. (4.30) for the thermal diffusion coefficient [4.7, 4.8].

The active diffusion coefficient $D_{\rm A}^{\rm F}$ obtained in Eq. (4.18) for the free membrane case essentially reflects the hydrodynamics of the surrounding bulk 3D solvent. Hence our result can be compared with that in Ref. [4.19] obtained for a purely 3D fluid system:

$$D_{\rm A}^{\rm 3D} \approx \frac{S c_0^{\rm 3D}}{60\pi\eta_{\rm s}^2}\frac{1}{\ell_{\rm c}}, \tag{4.38}$$

which decays as $1/\ell_{\rm c}$ and is different from Eq. (4.18). In fact, such a difference arises from the different dimensions of the dipole concentrations, i.e., c_0 is the 2D concentration in our case, while $c_0^{\rm 3D}$ is the 3D concentration in Ref. [4.19]. A similar comparison can be also made for the drift velocity of free membranes in Eq. (4.34) and that in Ref. [4.19] for a 3D fluid system:

$$V^{\rm 3D} \approx \frac{S|\nabla c^{\rm 3D}|}{30\pi\eta_{\rm s}^2}\frac{1}{\ell_{\rm c}}. \tag{4.39}$$

The same reason holds for the different $\ell_{\rm c}$-dependence.

At this stage, we also comment that both the active diffusion coefficient $D_{\rm A}$ and the drift velocity V exhibit the same $\ell_{\rm c}$-dependence. Although the integrands in Eqs. (4.1) and (4.3) look apparently different, their physical dimensions are identical because the first derivative of the mobility tensor in Eq. (4.1) corresponds to the product of the second derivative and $(\mathbf{r}\cdot\hat{\mathbf{n}})$ in Eq. (4.3). This is the simple reason that they exhibit the same $\ell_{\rm c}$-dependence. One can also easily confirm that V is positive when we make use of the membrane mobility tensor, because the integrand in Eq. (4.3) is the product of the first and the second derivatives of the mobility tensor which have opposite signs. This leads to $V > 0$ indicating a chemotaxis-like drift as mentioned before.

In this work, we have assumed that active proteins generate forces only in the lateral directions. On the other hand, actual active motors such as bacteriorhodopsin can also exert forces to the surrounding solvent [4.16–4.18]. Although we did not take into account such normal forces which induce membrane undulation, consideration of normal forces as well as lateral ones will provide us with a general understanding of active diffusion in biomembranes [4.37].

We have also assumed that the force dipoles are fixed in a membrane and are distributed homogeneously. It would be interesting to consider the case when active proteins can also move laterally in the membrane and even interact with each other through a nematic-like interaction [4.38]. The full equation of motion now involves potential-of-mean-force interactions in the multi-particle diffusion equations that describe the combined motions of the passive particle and active proteins in the membrane. Although the dynamics of the active protein concentration is essentially determined by a diffusion equation, it is a complicated problem because not only thermal diffusion but also active nonthermal diffusion should be taken into account. Our work is the first step toward such a full description of very rich biomembrane dynamics.

Appendix 4.A Derivation of Eqs. (4.18) and (4.23)

Since Eqs. (4.17) and (4.22) have been obtained in Ref. [4.19], we show here the derivation of Eqs. (4.18) and and (4.23). Substituting Eq. (4.16) into Eq. (4.14), we get

$$D_{\rm A}^{\rm F} = \frac{Sc_0}{8\pi^2\eta_{\rm m}^2}\int_\delta^\infty {\rm d}^2 z\, \Omega_{\beta\beta'\gamma\gamma'}\frac{\partial}{\partial z_\gamma}\left(\frac{\hat{z}_\alpha\hat{z}_\beta}{z}\right)\frac{\partial}{\partial z_{\gamma'}}\left(\frac{\hat{z}_\alpha\hat{z}_{\beta'}}{z}\right), \tag{4.A1}$$

where $\mathbf{z} = \nu\mathbf{r}$. Since

$$\frac{\partial}{\partial z_\gamma}\left(\frac{\hat{z}_\alpha\hat{z}_\beta}{z}\right) = \frac{1}{z^3}(\delta_{\alpha\gamma}z_\beta + \delta_{\beta\gamma}z_\alpha) - \frac{3}{z^5}z_\alpha z_\beta z_\gamma, \tag{4.A2}$$

the integrand in Eq. (4.A1) becomes

$$\frac{\partial}{\partial z_\gamma}\left(\frac{\hat{z}_\alpha\hat{z}_\beta}{z}\right)\frac{\partial}{\partial z_{\gamma'}}\left(\frac{\hat{z}_\alpha\hat{z}_{\beta'}}{z}\right) = \frac{1}{z^4}\delta_{\beta\gamma}\delta_{\beta'\gamma'} + \frac{1}{z^6}[\delta_{\gamma\gamma'}z_\beta z_{\beta'} - 2(\delta_{\beta\gamma}z_{\beta'}z_{\gamma'} + \delta_{\beta'\gamma'}z_\beta z_\gamma)]$$

$$+\frac{3}{z^8}z_\beta z_{\beta'}z_\gamma z_{\gamma'}. \tag{4.A3}$$

By operating $\Omega_{\beta\beta'\gamma\gamma'}$, we have

$$\Omega_{\beta\beta'\gamma\gamma'}\frac{\partial}{\partial z_\gamma}\left(\frac{\hat{z}_\alpha\hat{z}_\beta}{z}\right)\frac{\partial}{\partial z_{\gamma'}}\left(\frac{\hat{z}_\alpha\hat{z}_{\beta'}}{z}\right)=\frac{5}{8z^4}. \tag{4.A4}$$

After the integration, we obtain Eq. (4.18).

Similarly, we substitute Eq. (4.21) into Eq. (4.19) and obtain

$$D_{\rm A}^{\rm C}=\frac{Sc_0}{8\pi^2\eta_{\rm m}^2}\int_\epsilon^\infty {\rm d}^2w\,\Omega_{\beta\beta'\gamma\gamma'}\frac{\partial}{\partial w_\gamma}\left(\frac{\delta_{\alpha\beta}-2\hat{w}_\alpha\hat{w}_\beta}{w^2}\right)\frac{\partial}{\partial w_{\gamma'}}\left(\frac{\delta_{\alpha\beta'}-2\hat{w}_\alpha\hat{w}_{\beta'}}{w^2}\right), \tag{4.A5}$$

where $\mathbf{w}=\kappa\mathbf{r}$. Since

$$\frac{\partial}{\partial w_\gamma}\left(\frac{\delta_{\alpha\beta}-2\hat{w}_\alpha\hat{w}_\beta}{w^2}\right)=-\frac{2}{w^4}(\delta_{\alpha\beta}w_\gamma+\delta_{\beta\gamma}w_\alpha+\delta_{\alpha\gamma}w_\beta)+\frac{8}{w^6}w_\alpha w_\beta w_\gamma, \tag{4.A6}$$

we obtain

$$\begin{aligned}&\frac{\partial}{\partial w_\gamma}\left(\frac{\delta_{\alpha\beta}-2\hat{w}_\alpha\hat{w}_\beta}{w^2}\right)\frac{\partial}{\partial w_{\gamma'}}\left(\frac{\delta_{\alpha\beta'}-2\hat{w}_\alpha\hat{w}_{\beta'}}{w^2}\right)\\&=\frac{4}{w^6}\delta_{\beta\gamma}\delta_{\beta'\gamma'}+\frac{4}{w^8}[\delta_{\beta\beta'}w_\gamma w_{\gamma'}+\delta_{\beta'\gamma}w_\beta w_{\gamma'}+\delta_{\beta\gamma'}w_{\beta'}w_\gamma+\delta_{\gamma\gamma'}w_\beta w_{\beta'}\\&-2(\delta_{\beta\gamma}w_{\beta'}w_{\gamma'}+\delta_{\beta'\gamma'}w_\beta w_\gamma)].\end{aligned} \tag{4.A7}$$

By operating $\Omega_{\beta\beta'\gamma\gamma'}$, we have

$$\Omega_{\beta\beta'\gamma\gamma'}\frac{\partial}{\partial w_\gamma}\left(\frac{\delta_{\alpha\beta}-2\hat{w}_\alpha\hat{w}_\beta}{w^2}\right)\frac{\partial}{\partial w_{\gamma'}}\left(\frac{\delta_{\alpha\beta'}-2\hat{w}_\alpha\hat{w}_{\beta'}}{w^2}\right)=\frac{4}{w^6}. \tag{4.A8}$$

After the integration, we obtain Eq. (4.23).

Appendix 4.B Derivation of Eqs. (4.34) and (4.37)

In this Appendix, we show the derivation of Eqs. (4.34) and (4.37). Substituting Eq. (4.16) into Eq. (4.32), we obtain

$$V^{\rm F}=-\frac{S|\nabla c|}{4\pi^2\eta_{\rm m}^2}\int_\delta^\infty {\rm d}^2z\,\Omega_{\beta\beta'\gamma\gamma'}\hat{n}_\alpha\frac{\partial^2}{\partial z_\gamma\partial z_\delta}\left(\frac{\hat{z}_\alpha\hat{z}_\beta}{z}\right)\frac{\partial}{\partial z_{\gamma'}}\left(\frac{\hat{z}_\delta\hat{z}_{\beta'}}{z}\right)(\mathbf{z}\cdot\hat{\mathbf{n}}). \tag{4.B1}$$

In the above, the derivatives are

$$\begin{aligned}\frac{\partial^2}{\partial z_\gamma\partial z_\delta}\left(\frac{\hat{z}_\alpha\hat{z}_\beta}{z}\right)&=\frac{1}{z^3}(\delta_{\alpha\delta}\delta_{\beta\gamma}+\delta_{\alpha\gamma}\delta_{\beta\delta})-\frac{3}{z^5}(\delta_{\alpha\delta}z_\beta z_\gamma+\delta_{\beta\delta}z_\alpha z_\gamma+\delta_{\alpha\gamma}z_\beta z_\delta+\delta_{\beta\gamma}z_\alpha z_\delta\\&+\delta_{\gamma\delta}z_\alpha z_\beta)+\frac{15}{z^7}z_\alpha z_\beta z_\gamma z_\delta,\end{aligned} \tag{4.B2}$$

and

$$\begin{aligned}
&\frac{\partial^2}{\partial z_\gamma \partial z_\delta}\left(\frac{\hat{z}_\alpha \hat{z}_\beta}{z}\right)\frac{\partial}{\partial z_{\gamma'}}\left(\frac{\hat{z}_\delta \hat{z}_{\beta'}}{z}\right)\\
&= -\frac{1}{z^6}[2\delta_{\beta'\gamma'}(\delta_{\alpha\gamma}z_\beta + \delta_{\beta\gamma}z_\alpha) - (\delta_{\alpha\gamma'}\delta_{\beta\gamma} + \delta_{\alpha\gamma}\delta_{\beta\gamma'})z_{\beta'}]\\
&- \frac{3}{z^8}[(\delta_{\alpha\gamma'}z_\beta z_\gamma + \delta_{\beta\gamma'}z_\alpha z_\gamma - \delta_{\alpha\gamma}z_\beta z_{\gamma'} - \delta_{\beta\gamma}z_\alpha z_{\gamma'}\\
&+ \delta_{\gamma\gamma'}z_\alpha z_\beta)z_{\beta'} - 2\delta_{\beta'\gamma'}z_\alpha z_\beta z_\gamma] - \frac{3}{z^{10}}z_\alpha z_\beta z_{\beta'} z_\gamma z_{\gamma'}.
\end{aligned} \tag{4.B3}$$

By operating $\Omega_{\beta\beta'\gamma\gamma'}$, we have

$$\Omega_{\beta\beta'\gamma\gamma'}\frac{\partial^2}{\partial z_\gamma \partial z_\delta}\left(\frac{\hat{z}_\alpha \hat{z}_\beta}{z}\right)\frac{\partial}{\partial z_{\gamma'}}\left(\frac{\hat{z}_\delta \hat{z}_{\beta'}}{z}\right) = -\frac{13 z_\alpha}{8z^6}. \tag{4.B4}$$

After the integration, we obtain Eq. (4.34).

Next we substitute Eq. (4.21) into Eq. (4.35) and find

$$\begin{aligned}
V^{\mathrm{C}} = &-\frac{S|\nabla c|}{4\pi^2\eta_{\mathrm{m}}^2}\int_\epsilon^\infty \mathrm{d}^2 w\, \Omega_{\beta\beta'\gamma\gamma'}\hat{n}_\alpha \frac{\partial^2}{\partial w_\gamma \partial w_\delta}\left(\frac{\delta_{\alpha\beta} - 2\hat{w}_\alpha\hat{w}_\beta}{w^2}\right)\\
&\times \frac{\partial}{\partial w_{\gamma'}}\left(\frac{\delta_{\delta\beta'} - 2\hat{w}_\delta\hat{w}_{\beta'}}{w^2}\right)(\mathbf{w}\cdot\hat{\mathbf{n}}).
\end{aligned} \tag{4.B5}$$

Here the derivatives are

$$\begin{aligned}
\frac{\partial^2}{\partial w_\gamma \partial w_\delta}\left(\frac{\delta_{\alpha\beta} - 2\hat{w}_\alpha\hat{w}_\beta}{w^2}\right) = &-\frac{2}{w^4}(\delta_{\alpha\beta}\delta_{\gamma\delta} + \delta_{\alpha\gamma}\delta_{\beta\delta} + \delta_{\alpha\delta}\delta_{\beta\gamma})\\
&+ \frac{8}{w^6}(\delta_{\alpha\beta}w_\gamma w_\delta + \delta_{\beta\delta}w_\alpha w_\gamma + \delta_{\alpha\delta}w_\beta w_\gamma + \delta_{\alpha\gamma}w_\beta w_\delta\\
&+ \delta_{\beta\gamma}w_\alpha w_\delta + \delta_{\gamma\delta}w_\alpha w_\beta) - \frac{48}{w^8}w_\alpha w_\beta w_\gamma w_\delta,
\end{aligned} \tag{4.B6}$$

and

$$\begin{aligned}
&\frac{\partial^2}{\partial w_\gamma \partial w_\delta}\left(\frac{\delta_{\alpha\beta} - 2\hat{w}_\alpha\hat{w}_\beta}{w^2}\right)\frac{\partial}{\partial w_{\gamma'}}\left(\frac{\delta_{\delta\beta'} - 2\hat{w}_\delta\hat{w}_{\beta'}}{w^2}\right)\\
&= -\frac{4}{w^8}[3\delta_{\beta'\gamma'}(\delta_{\alpha\beta}w_\gamma + \delta_{\alpha\gamma}w_\beta + \delta_{\beta\gamma}w_\alpha) - (\delta_{\alpha\beta}\delta_{\gamma\beta'} + \delta_{\alpha\gamma}\delta_{\beta\beta'} + \delta_{\alpha\beta'}\delta_{\beta\gamma})w_{\gamma'}\\
&- (\delta_{\alpha\beta}\delta_{\gamma\gamma'} + \delta_{\alpha\gamma}\delta_{\beta\gamma'} + \delta_{\alpha\gamma'}\delta_{\beta\gamma})w_{\beta'}] + \frac{16}{w^{10}}[(\delta_{\alpha\beta}w_{\beta'}w_\gamma - \delta_{\beta\beta'}w_\alpha w_\gamma - \delta_{\alpha\beta'}w_\beta w_\gamma\\
&+ \delta_{\alpha\gamma}w_\beta w_{\beta'} + \delta_{\beta\gamma}w_\alpha w_{\beta'} - \delta_{\beta'\gamma}w_\alpha w_\beta)w_{\gamma'} - (\delta_{\beta\gamma'}w_\alpha w_\gamma + \delta_{\alpha\gamma'}w_\beta w_\gamma + \delta_{\gamma\gamma'}w_\alpha w_\beta)w_{\beta'}\\
&+ 3\delta_{\beta'\gamma'}w_\alpha w_\beta w_\gamma].
\end{aligned} \tag{4.B7}$$

By operating $\Omega_{\beta\beta'\gamma\gamma'}$, we find

$$\Omega_{\beta\beta'\gamma\gamma'}\frac{\partial^2}{\partial w_\gamma \partial w_\delta}\left(\frac{\delta_{\alpha\beta} - 2\hat{w}_\alpha\hat{w}_\beta}{w^2}\right)\frac{\partial}{\partial w_{\gamma'}}\left(\frac{\delta_{\delta\beta'} - 2\hat{w}_\delta\hat{w}_{\beta'}}{w^2}\right) = -\frac{12 w_\alpha}{w^8}. \tag{4.B8}$$

After the integration, we obtain Eq. (4.37).

References

[4.1] S. J. Singer and G. L. Nicolson, Science **175**, 720 (1972).

[4.2] B. Alberts, A. Johnson, P. Walter, J. Lewis, and M. Raff, *Molecular Biology of the Cell* (Garland Science, New York, 2008).

[4.3] R. Lipowsky and E. Sackmann, *Structure and Dynamics of Membranes* (Elsevier, Amsterdam, 1995).

[4.4] P. G. Saffman and M. Delbrück, Proc. Natl. Acad. Sci. USA. **72**, 3111 (1975).

[4.5] P. G. Saffman, J. Fluid Mech. **73**, 593 (1976).

[4.6] B. D. Hughes, B. A. Pailthorpe, and L.R. White, J. Fluid Mech. **110**, 349 (1981).

[4.7] E. Evans and E. Sackmann, J. Fluid Mech. **194**, 553 (1988).

[4.8] S. Ramachandran, S. Komura, M. Imai, and K. Seki, Eur. Phys. J. E **31**, 303-310 (2010).

[4.9] K. Seki, S. Ramachandran, and S. Komura, Phys. Rev. E **84**, 021905 (2011).

[4.10] K. Seki, S. Mogre, and S. Komura, Phys. Rev. E **89**, 022713 (2014).

[4.11] S. Komura, S. Ramachandran, and M. Imai, in *Non-Equilibrium Soft Matter Physics*, edited by S. Komura and T. Ohta (World Scientific, Singapore, 2012), p. 197.

[4.12] B. R. Parry, I. V. Surovtsev, M. T. Cabeen, C. S. O'Hern, E. R. Dufresne, and C. Jacobs-Wagner, Cell **156**, 183 (2014).

[4.13] M. Guo, A. J. Ehrlicher, M. H. Jensen, M. Renz, J. R. Moore, R. D. Goldman, J. Lippincott-Schwartz, F. C.Mackintosh, and D. A.Weitz, Cell **158**, 822 (2014).

[4.14] K. Yasuda, R. Okamoto, S. Komura, and A. S. Mikhailov, EPL **117**, 38001 (2017).

[4.15] K. Yasuda, R. Okamoto, and S. Komura, Phys. Rev. E. **95**, 032417 (2017).

[4.16] J.-B. Manneville, P. Bassereau, D. Lévy, and J. Prost, Phys. Rev. Lett. **82**, 4356 (1999).

[4.17] J.-B. Manneville, P. Bassereau, S. Ramaswamy, and J. Prost, Phys. Rev. E **64**, 021908 (2001).

[4.18] S. Ramaswamy, J Toner, and J. Prost, Phys. Rev. Lett. **84**, 3494 (2000).

[4.19] A. S. Mikhailov and R. Kapral, Proc. Nat. Acad. Sci. USA **112**, E3639 (2015).

[4.20] R. Kapral and A. S. Mikhailov, Physica D **318-319**, 100 (2016).

[4.21] Y. Koyano, H Kitahata, and A. S. Mikhailov, Phys. Rev. E **94**, 022416 (2016).

[4.22] M.-J. Huang, A. S. Mikhailov, and H.-Y. Chen, Eur. Phys. J. E **35**, 119 (2012).

[4.23] M.-J. Huang, R. Kapral, A. S. Mikhailov, and H.-Y. Chen, J. Chem. Phys. **138**, 195101 (2013).

[4.24] M. Tanaka and E. Sackmann, Nature **437**, 656 (2005).

[4.25] K. Inaura and Y. Fujitani, J. Phys. Soc. Jpn. **77**, 114603 (2008).

[4.26] S. Ramachandran, S. Komura, K. Seki, and G. Gompper, Eur. Phys. J. E **34**, 46 (2011).

[4.27] S. Ramachandran, S. Komura, K. Seki, and M. Imai, Soft Matter **7**, 1524 (2011).

[4.28] S. Komura, S. Ramachandran, K. Seki, and M. Imai, Advances in Planar Lipid Bilayers and Liposomes **16**, 129 (2012).

[4.29] K. Simons and E. Ikonen, Science **290**, 1721 (1997).

[4.30] S. Komura and D. Andelman, Adv. Colloid Interface Sci. **208**, 34 (2014).

[4.31] D. Lingwood and K. Simons, Science **327**, 46 (2010).

[4.32] H. Diamant, J. Phys. Soc. Jpn. **78**, 041002 (2009).

[4.33] N. Oppenheimer and H. Diamant, Biophys. J. **96**, 3041 (2009).

[4.34] N. Oppenheimer and H. Diamant, Phys. Rev. E **82**, 041912 (2010).

[4.35] E. P. Petrov and P. Schwille, Biophys. J. **94**, L41 (2008).

[4.36] E. P. Petrov and P. Schwille, Soft Matter **8**, 7552 (2012).

[4.37] S. Komura, K. Yasuda, and R. Okamoto, J. Phys.: Condens. Matter **27**, 432001 (2015).

[4.38] A. W. C. Lau and T. C. Lubensky, Phys. Rev. E **80**, 011917 (2009).

Chapter 5

Nonreciprocal Response of a Two-Dimensional Fluid with Odd Viscosity †

5.1 Introduction

Two-dimensional (2D) active chiral fluids have been predicted to have a new rheological property called *odd viscosity* [5.1]. Over two decades ago, Avron has shown that when time-reversal and parity symmetries are broken, the viscosity tensor of a 2D isotropic fluid could have an anti-symmetric (odd) part that does not result in dissipation [5.1, 5.2]. The origin of the odd viscosity is explained by coarse-grained theories, such as Onsager's reciprocal relations [5.1] and Green-Kubo relations for viscosity coefficients [5.3–5.5]. Furthermore, in microscopic approaches, it was shown that active chiral fluids composed of self-spinning objects also exhibit odd viscosity [5.2, 5.6].

In order to observe odd viscosity in physical systems, several protocols have been proposed. For incompressible fluids, it was predicted that odd viscosity can emerge at a dynamical boundary that is subjected to no-stress boundary

†The material presented in this chapter was published in: Y. Hosaka, S. Komura, and D. Andelman, Phys. Rev. E **103**, 042610 (2021).

conditions [5.7, 5.8]. Experimentally, Soni *et al.* measured odd viscosity in active chiral fluids by observing the boundary dynamics of a fluid [5.9]. Odd viscosity has also been measured by using molecular dynamics simulations and its Green-Kubo representation [5.4, 5.5].

In addition, more fundamental phenomena in active chiral systems, such as responses to point forces or finite-size bodies, have been studied theoretically [5.7, 5.10–5.14]. Recently, the nonreciprocity of the point force response was investigated in a 3D anisotropic fluid with odd viscosity [5.10] as well as in an active solid material [5.11, 5.12]. As for the finite-size body response, lift force was observed in active chiral granular media [5.13] and in a 2D fluid with inertia [5.14], whereas no such force was found in the incompressible limit [5.7]. Despite these intensive findings, very little is known about the linear hydrodynamic response of a 2D active chiral fluid.

In this paper, we discuss the hydrodynamic response of a 2D isotropic compressible fluid with odd viscosity, which can be regarded as a 2D active chiral fluid [5.1–5.3]. Taking into account the 3D bulk fluid coupled to the 2D fluid layer and employing the lubrication approximation for the 3D fluid [5.15–5.17], we analytically obtain the asymmetric mobility tensor of the 2D fluid in the presence of odd viscosity. Because of such a nonreciprocal hydrodynamic response, a perpendicular fluid flow develops and breaks the axial symmetry of the flow with respect to the driving force. Extending the point force response, we derive viscous forces on a rigid disk that moves laterally in the 2D active chiral fluid. As a consequence of the nonreciprocal hydrodynamic response due to odd viscosity, we find that lift force acts on the driven disk.

There are two reasons that motivated us to consider a 2D compressible fluid with odd viscosity in contact with an underlying 3D fluid. As pointed out in Ref. [5.7], the velocity field is independent of the odd viscosity in a 2D incompressible fluid, when nonslip boundary conditions are imposed on a moving object. This means that the effects of odd viscosity cannot be directly seen in a

Table 5.1: The components associated with the three viscosity coefficients $\eta_{\rm d}$ (dilatation), $\eta_{\rm s}$ (shear), and $\eta_{\rm o}$ (odd) in the $\eta_{ijk\ell}$ tensor under index permutations [see Eq. (5.2)]. The $+$ $(-)$ sign denotes that the components are symmetric (anti-symmetric) under a given index permutation. Components that include even (odd) number of ϵ_{ij} are symmetric (anti-symmetric) under the parity transformation in a 2D system ($x \to -x$, $y \to y$) [5.3].

Viscosity coefficients	Components	$i \leftrightarrow j$	$k \leftrightarrow \ell$	$ij \leftrightarrow k\ell$	Parity
$\eta_{\rm d}$	$\delta_{ij}\delta_{k\ell}$	$+$	$+$	$+$	$+$
$\eta_{\rm s}$	$\delta_{ik}\delta_{j\ell} + \delta_{i\ell}\delta_{jk} - \delta_{ij}\delta_{k\ell}$	$+$	$+$	$+$	$+$
$\eta_{\rm o}$	$\epsilon_{ik}\delta_{j\ell} + \epsilon_{j\ell}\delta_{ik} + \epsilon_{i\ell}\delta_{jk} + \epsilon_{jk}\delta_{i\ell}$	$+$	$+$	$-$	$-$

2D incompressible fluid. Moreover, for a pure 2D fluid at low Reynolds number, a linear relation between the velocity and the viscous drag force acting on a translating disk cannot be obtained [5.18, 5.19]. This is known as the Stokes paradox that originates from the constraint of momentum conservation in a pure 2D system. This paradox can be resolved, e.g., by considering momentum decay to an underlying 3D fluid [5.20–5.25].

In the next section, we review the concept of the odd viscosity [5.1–5.3]. Then, we introduce in Sec. 5.3 the hydrodynamic equations for the 2D active chiral fluid layer by taking into account the coupling to the underlying 3D bulk fluid [5.15–5.17]. In Sec. 5.4, we derive the corresponding mobility tensor and calculate the velocity fields induced by a point force or a force dipole. In Sec. 5.5, we discuss the force and torque acting on a moving disk of a finite size. Finally, a summary of our work and some further comments are given in Sec. 5.6.

5.2 Odd viscosity

Here we briefly review the concept of odd viscosity and its contribution to the fluid stress tensor in two dimensions [5.1–5.3]. First, the strain rate tensor is defined as $v_{k\ell} = (\partial_k v_\ell + \partial_\ell v_k)/2$, where v_i is the 2D velocity component, $\partial_i = \partial/\partial r_i$ is the 2D differential operator component, and $\mathbf{r} = (x, y)$. The general linear relation between $v_{k\ell}$ and the fluid stress tensor σ_{ij} is given by

$$\sigma_{ij} = \eta_{ijk\ell} v_{k\ell}, \tag{5.1}$$

where $\eta_{ijk\ell}$ is the fourth-rank viscosity tensor. Throughout our work, we assume summation over repeated indices. Notice that the choice of the Cartesian coordinates is just done for convenience and is not a requirement.

In an isotropic fluid, rotational invariance of the system requires the symmetry of the stress tensor under the exchange of indices $i \leftrightarrow j$, i.e., $\sigma_{ij} = \sigma_{ji}$. This enforces the symmetry relation of the viscosity tensor $\eta_{ijk\ell} = \eta_{jik\ell}$, as inferred from Eq. (5.1). Since $v_{k\ell}$ is a symmetric tensor by definition, the symmetry under the exchange $k \leftrightarrow \ell$ always holds, leading to the symmetry relation $\eta_{ijk\ell} = \eta_{ij\ell k}$.

Extending the above symmetry argument, Avron introduced a new type of index exchange $ij \leftrightarrow k\ell$, which implies time-reversal transformation [5.1–5.3]. In light of such a pair exchange, the viscosity tensor can generally be split into symmetric (even) and anti-symmetric (odd) parts $\eta_{ijk\ell} = \eta^{\mathrm{S}}_{ijk\ell} + \eta^{\mathrm{A}}_{ijk\ell}$, where $\eta^{\mathrm{S}}_{ijk\ell} = \eta^{\mathrm{S}}_{k\ell ij}$ and $\eta^{\mathrm{A}}_{ijk\ell} = -\eta^{\mathrm{A}}_{k\ell ij}$. The anti-symmetric term $\eta^{\mathrm{A}}_{ijk\ell}$ exists as a consequence of broken time-reversal symmetry in a 2D fluid. Under the assumption that σ_{ij} is isotropic, the general viscosity tensor can be written as [5.2, 5.3]

$$\eta_{ijk\ell} = \\ \eta_{\mathrm{d}}\delta_{ij}\delta_{k\ell} + \eta_{\mathrm{s}}\left(\delta_{ik}\delta_{j\ell} + \delta_{i\ell}\delta_{jk} - \delta_{ij}\delta_{k\ell}\right) + \frac{1}{2}\eta_{\mathrm{o}}\left(\epsilon_{ik}\delta_{j\ell} + \epsilon_{j\ell}\delta_{ik} + \epsilon_{i\ell}\delta_{jk} + \epsilon_{jk}\delta_{i\ell}\right), \tag{5.2}$$

where $\eta_{\mathrm{d}}, \eta_{\mathrm{s}}$, and η_{o} are 2D dilatational, shear, and odd viscosities, respectively, δ_{ij} is the Kronecker delta, and ϵ_{ij} is the 2D Levi-Civita tensor with $\epsilon_{xx} = \epsilon_{yy} = 0$ and $\epsilon_{xy} = -\epsilon_{yx} = 1$.

The above viscosity tensor $\eta_{ijk\ell}$ is symmetric under the parity transformation in a 2D system ($x \to -x$, $y \to y$) [5.3], and hence it is parity-even. This is because both σ_{ij} and $v_{k\ell}$ are parity-even in Eq. (5.1). On the other hand, terms that include odd number of ϵ_{ij} are parity-odd. Hence, one concludes from Eq. (5.2) that η_{o} exists only if both time-reversal and parity symmetries are broken [5.2]. In Table 5.1, the above permutations of the viscosity-tensor

components are summarized.

Substituting Eq. (5.2) into Eq. (5.1), we obtain the stress tensor of a 2D compressible fluid with odd viscosity as

$$\sigma_{ij} = (\eta_{\rm d} - \eta_{\rm s})\delta_{ij}\partial_k v_k + \eta_{\rm s}(\partial_j v_i + \partial_i v_j) + \frac{1}{2}\eta_{\rm o}\left(\partial_j v_i^* + \partial_i v_j^* + \partial_j^* v_i + \partial_i^* v_j\right), \tag{5.3}$$

where $v_i^* \equiv \epsilon_{ik} v_k$ is the velocity vector rotated clockwise by $\pi/2$ and $\partial_i^* \equiv \epsilon_{ik}\partial_k$. Since the odd viscosity does not contribute to the energy dissipation, $(\partial_i v_j)\sigma_{ij}$, the sign of $\eta_{\rm o}$ can be either positive or negative.

5.3 Active chiral fluid

We consider a 2D layer of an active chiral compressible fluid particularly having odd viscosity, which is flat, thin, infinitely large and overlays a 3D bulk fluid (e.g. water). One of the realizations of such a system is schematically depicted in Fig. 6.1. The bulk fluid has a 3D shear viscosity η and is in contact with an impermeable flat wall located at $z = 0$, where the fluid velocity vanishes. In order to clearly see the odd viscosity effect [5.7], we suppose that the 2D fluid layer is compressible, so that it has both 2D dilatational and shear viscosities, $\eta_{\rm d}$ and $\eta_{\rm s}$, respectively. In physical systems, such a fluid can be realized by a monolayer of amphiphiles that are loosely packed on the interface at $z = h$ [5.15–5.17]. More details on the physical realization of our model will be discussed in Sec. 5.6.

In addition to the above viscosity coefficients, we assume that the 2D layer has odd viscosity, $\eta_{\rm o}$, that is an important measure of how far the fluid departs from passive fluids. We will not specifically focus on the origin of the odd viscosity, but it can be attributed, for example, to self-spinning objects immersed in the 2D fluid layer that break both time-reversal and parity symmetries [5.2, 5.26]. In this case, one has to assume that the active rotors are homogeneously distributed in the 2D fluid layer and their concentration is small enough. Under this condition, the 2D layer can be regarded as a layer of a continuum active

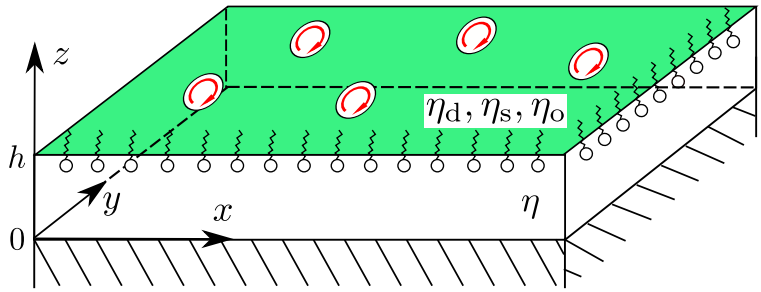

Figure 5.1: Schematic sketch of an active chiral fluid characterized by odd viscosity. An infinitely large, flat, and thin 2D fluid layer (green) (e.g., a monolayer formed by amphiphiles) is located at $z = h$ having 2D dilatational, shear, and odd viscosities, η_d, η_s, and η_o, respectively. The fluid interface is in contact with air ($z > h$) and a 3D fluid underneath ($0 < z < h$) having a 3D shear viscosity η. The 3D fluid is bounded by an impermeable flat wall located at $z = 0$, and its velocity is assumed to vanish at $z = 0$. On the 2D fluid layer at $z = h$, both time-reversal and parity symmetries are broken (e.g., due to the self-spinning objects injecting energy into the fluid), giving rise to the possibility of an odd viscosity, η_o, in the 2D layer.

chiral fluid with a constant odd viscosity, η_o.

For the 2D fluid layer introduced above, the momentum balance equation at low Reynolds number can be written as

$$-\nabla\Pi + \nabla\cdot\boldsymbol{\sigma} + \mathbf{f}_b + \mathbf{F} = 0, \tag{5.4}$$

where $\nabla = (\partial_x, \partial_y)$ stands for the 2D gradient operator, Π is the 2D hydrostatic pressure, $\boldsymbol{\sigma}$ is the stress tensor given in Eq. (6.3) that includes the odd viscosity η_o, $\mathbf{f}_b$ is the force exerted on the 2D fluid layer by the underlying 3D bulk fluid, and $\mathbf{F}$ is any other force density acting on the 2D fluid.

The bulk underneath the 2D fluid layer is a pure 3D fluid. We denote its velocity field by the vector $\mathbf{u}(\mathbf{r}, z)$ and the 3D hydrostatic pressure by $p(\mathbf{r}, z)$. The corresponding Stokes equation is

$$\eta\tilde{\nabla}^2\mathbf{u} - \tilde{\nabla}p = 0, \tag{5.5}$$

with η being the 3D shear viscosity of the bulk fluid and $\tilde{\nabla}$ being the 3D gradient

operator. The incompressibility condition for $\mathbf{u}$ reads

$$\tilde{\nabla} \cdot \mathbf{u} = 0. \tag{5.6}$$

In order to obtain $\mathbf{f}_\mathrm{b}$, we solve the hydrodynamic equations for the bulk fluid in Eqs. (5.5) and (5.6) [5.15–5.17]. The boundary conditions on the 3D bulk velocity $\mathbf{u}(\mathbf{r}, z)$ are the stick (nonslip) conditions at the bottom surface of the bulk fluid ($z = 0$) and at its top surface ($z = h$):

$$\mathbf{u}(\mathbf{r}, 0) = 0, \qquad \mathbf{u}(\mathbf{r}, h) = \mathbf{v}(\mathbf{r}), \tag{5.7}$$

with $\mathbf{v}(\mathbf{r})$ being the in-plane velocity vector of the fluid layer at $z = h$. We now use the lubrication approximation where the vertical component of the velocity, u_z, is neglected compared to the in-plane components and the vertical pressure gradient vanishes, i.e., $\partial p/\partial z = 0$. This assumption is justified as long as h is smaller than any horizontal characteristic length scale of the bulk fluid velocity. Under these assumptions, the 3D Stokes equation (5.5) reduces to

$$\eta \frac{\partial^2}{\partial z^2} \begin{pmatrix} u_x \\ \\ u_y \end{pmatrix} - \nabla p = 0. \tag{5.8}$$

Taking into account the boundary conditions in Eq. (5.7), the above equation can be integrated to give

$$\mathbf{u}(\mathbf{r}, z) = \frac{z^2 - zh}{2\eta} \nabla p(\mathbf{r}) + \frac{z}{h} \mathbf{v}(\mathbf{r}). \tag{5.9}$$

Then, the force exerted on the 2D fluid layer by the bulk fluid beneath is calculated as [5.15–5.17]

$$\mathbf{f}_\mathrm{b} = -\eta \left. \frac{\partial \mathbf{u}}{\partial z} \right|_{z=h} = -\frac{h}{2} \nabla p - \frac{\eta}{h} \mathbf{v}. \tag{5.10}$$

Substituting the obtained $\mathbf{f}_\mathrm{b}$ into Eq. (6.1), one can show that the hydrodynamic equation for the active chiral layer is

$$-\nabla \Pi + \eta_\mathrm{d} \nabla (\nabla \cdot \mathbf{v}) + \eta_\mathrm{s} \nabla^2 \mathbf{v} + \eta_\mathrm{o} \nabla^2 \mathbf{v}^* - \frac{h}{2} \nabla p - \frac{\eta}{h} \mathbf{v} + \mathbf{F} = 0, \tag{5.11}$$

where the divergence of the in-plane velocity is given by the following rela-

tion [5.15, 5.17]

$$\nabla \cdot \mathbf{v} = \frac{h^2}{6\eta}\nabla^2 p. \tag{5.12}$$

This relation can be derived by taking the divergence of Eq. (5.9) and integrating over the lubrication layer ($0 \leq z \leq h$) under the incompressibility condition of Eq. (5.6) and the boundary conditions of Eq. (5.7). The fourth term on the left-hand-side of Eq. (5.11) indicates that odd viscosity contributes to the fluid flow that is perpendicular to the one generated by shear viscosity [5.2].

5.4 Hydrodynamic response of a point force

5.4.1 Mobility tensor

We derive the mobility tensor for the hydrodynamic response of the 2D fluid layer with odd viscosity. The second-rank mobility tensor $\mathbf{G}(\mathbf{r})$ connects the force density $\mathbf{F}$ acting on the fluid layer at position $\mathbf{r}'$ with its induced velocity at position $\mathbf{r}$:

$$v_i(\mathbf{r}) = \int \mathrm{d}^2 r'\, G_{ij}(\mathbf{r} - \mathbf{r}') F_j(\mathbf{r}'). \tag{5.13}$$

In order to derive $G_{ij}(\mathbf{r})$, we solve the hydrodynamic equations (5.11) and (5.12) in Fourier space and obtain $G_{ij}[\mathbf{k}]$, where $\mathbf{k} = (k_x, k_y)$, and the square brackets indicate a function in Fourier space. We introduce two orthogonal unit vectors

$$\hat{\mathbf{k}} = (k_x/k, k_y/k), \qquad \bar{\mathbf{k}} = (-k_y/k, k_x/k), \tag{5.14}$$

with $k = |\mathbf{k}|$.

In Appendix 5.A, we show that $G_{ij}[\mathbf{k}]$ has the following expression

$$G_{ij}[\mathbf{k}] = \frac{\eta_\mathrm{s}(k^2+\kappa^2)\hat{k}_i\hat{k}_j + (\eta_\mathrm{s}+\eta_\mathrm{d})(k^2+\lambda^2)\bar{k}_i\bar{k}_j - \eta_\mathrm{o}k^2\epsilon_{ij}}{\eta_\mathrm{s}(\eta_\mathrm{s}+\eta_\mathrm{d})(k^2+\kappa^2)(k^2+\lambda^2) + \eta_\mathrm{o}^2 k^4}, \tag{5.15}$$

where

$$\kappa^2 = \frac{\eta}{h\eta_\mathrm{s}}, \qquad \lambda^2 = \frac{4\eta}{h(\eta_\mathrm{s}+\eta_\mathrm{d})}. \tag{5.16}$$

Note that the ratio, η/η_s, gives the inverse length scale because the 2D viscosity, η_s, has the dimension of Pa·s·m, while that of η is Pa·s. The lengths scales, κ^{-1}

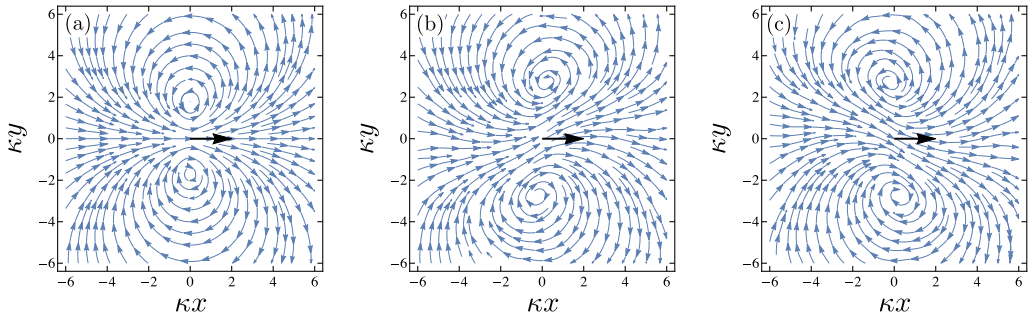

Figure 5.2: Streamlines of the velocity $\mathbf{v}(x, y)$ rescaled by $F/(2\pi\eta_s)$ and generated by a point force, $\mathbf{F} = F\hat{\mathbf{e}}_x\delta(\mathbf{r})$, as a function of κx and κy while keeping $\eta_d = 3\eta_s$. The force along the x-axis is applied at the origin (the black horizontal arrow) for (a) $\mu = \eta_o/\eta_s = 0$, (b) $\mu = 3$, and (c) $\mu = -3$ [see Eqs. (5.13) and (5.19)]. The blue arrows indicate the flow direction.

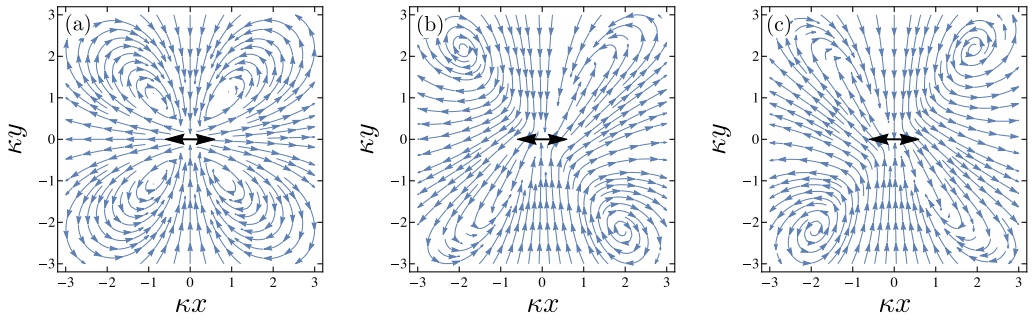

Figure 5.3: Streamlines of the velocity $\mathbf{v}(x, y)$ rescaled by $F\kappa\ell/(2\pi\eta_s)$ and generated by a force dipole as a function of κx and κy while keeping $\eta_d = 3\eta_s$. The force dipole along the x-axis ($\hat{\mathbf{d}} = \hat{\mathbf{e}}_x$) is centered at the origin (the black double arrow) for (a) $\mu = \eta_o/\eta_s = 0$, (b) $\mu = 3$, and (c) $\mu = -3$ [see Eq. (5.23)]. The blue arrows indicate the flow direction.

and λ^{-1}, correspond to the hydrodynamic screening lengths beyond which the 2D layer exchanges momentum with the underlying bulk fluid. Importantly, the numerator of Eq. (5.15) includes an anti-symmetric tensor ϵ_{ij}.

For simplicity sake, we hereafter assume $\kappa = \lambda$ (or equivalently $\eta_d = 3\eta_s$) in Eq. (5.15) and consider the following simplified mobility tensor

$$G_{ij}[\mathbf{k}] = \frac{(k^2+\kappa^2)(4\delta_{ij} - 3\hat{k}_i\hat{k}_j) - \mu k^2\epsilon_{ij}}{\eta_s\left[4(k^2+\kappa^2)^2 + \mu^2k^4\right]}, \tag{5.17}$$

where

$$\mu = \frac{\eta_o}{\eta_s}. \tag{5.18}$$

The above dimensionless parameter, μ, is a measure of how far the 2D active

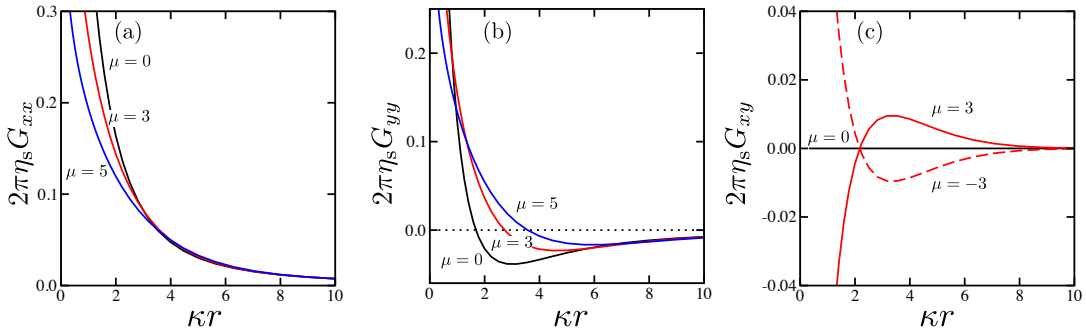

Figure 5.4: Plots of the mobility coefficients rescaled by $2\pi\eta_s$ as a function of κr for various values of μ. (a) The longitudinal mobility coefficient G_{xx} for $\mu = 0$, 3, and 5 (black, red, and blue lines). (b) The transverse mobility coefficient G_{yy} for $\mu = 0$, 3, and 5 (black, red, and blue lines). (c) The anti-symmetric mobility coefficient G_{xy} for $\mu = -3$, 0, and 3 (red dashed, black solid, and red solid lines).

chiral fluid departs from the passive fluid, e.g., due to the self-spinning active objects.

As shown in Appendix 5.B, the real space representation of the mobility tensor can be obtained by the inverse Fourier transform of Eq. (5.17) [5.27]

$$G_{ij}(\mathbf{r}) = C_1(r)\delta_{ij} + C_2(r)\hat{r}_i\hat{r}_j + C_3(r)\epsilon_{ij}, \tag{5.19}$$

where $\hat{\mathbf{r}} = \mathbf{r}/r$ is a unit vector ($r = |\mathbf{r}|$), and the three coefficients are given by

$$C_1(r) = \frac{1}{2\pi\eta_s}\int_0^\infty \mathrm{d}k\, \frac{k(k^2+\kappa^2)}{4(k^2+\kappa^2)^2+\mu^2k^4}\left[4J_0(kr) - \frac{3J_1(kr)}{kr}\right], \tag{5.20}$$

$$C_2(r) = \frac{1}{2\pi\eta_s}\int_0^\infty \mathrm{d}k\, \frac{3k(k^2+\kappa^2)}{4(k^2+\kappa^2)^2+\mu^2k^4}\left[-J_0(kr) + \frac{2J_1(kr)}{kr}\right], \tag{5.21}$$

$$C_3(r) = -\frac{\mu}{2\pi\eta_s}\int_0^\infty \mathrm{d}k\, \frac{k^3J_0(kr)}{4(k^2+\kappa^2)^2+\mu^2k^4}. \tag{5.22}$$

In the above, $J_n(x)$ is the Bessel function of the first kind [5.28]. When $\eta_o = 0$ (or $\mu = 0$), C_3 vanishes and $G_{ij}(\mathbf{r})$ reduces to that of a 2D passive compressible fluid, $G^0_{ij}(\mathbf{r})$, which we analytically derive in Appendix 5.B [see Eq. (5.B5)]. Hereafter, the superscript "0" denotes quantities when $\mu = 0$ (vanishing odd viscosity). Under the exchange $\eta_o \leftrightarrow -\eta_o$, C_1 and C_2 of Eqs. (5.20) and (5.21) remain unchanged, whereas C_3 of Eq. (5.22) changes its sign.

We briefly discuss the symmetry property of the mobility tensor obtained in Eq. (5.19). From G^0_{ij} in Eq. (5.B5), one sees that the mobility tensor of passive fluids satisfies the symmetry property $G^0_{ij} = G^0_{ji}$, whereas for active chiral fluids, such a symmetry does not hold, i.e., $G_{ij} \neq G_{ji}$ as shown in Eq. (5.19). This asymmetry gives rise to the fluid velocity perpendicular to an applied force that results from the nonreciprocal hydrodynamic response.

5.4.2 Velocity field

With the obtained mobility tensor, we first investigate the velocity field induced by a point force acting on a 2D fluid layer with odd viscosity. Substituting Eq. (5.19) into Eq. (5.13), we calculate the velocity field induced by a point force at the origin, $\mathbf{F} = F\hat{\mathbf{e}}_x\delta(\mathbf{r})$, with $\hat{\mathbf{e}}_x$ being a unit vector in the x-direction. The obtained velocity field is plotted in Fig. 5.2 for $\mu = 0$, 3, and -3. When $\mu = 0$, we see axisymmetric streamlines that pass through the applied force (the black horizontal arrow), as in Fig. 5.2(a). There are two vortices whose center is located at $(\kappa x, \kappa y) \approx (0, \pm 2.0)$. They result from the nature of the 2D fluid layer with the hydrodynamic screening length, κ^{-1}.

When μ is finite, however, a perpendicular flow in the y-direction starts to develop and accordingly, the axial symmetry breaks down, as shown in Figs. 5.2(b) and (c). This behavior results from the nonreciprocal hydrodynamic response in the presence of the odd viscosity. When $\mu = \pm 3$, the vortices approach to the positions $(0, \pm 3.0)$, meaning that finite values of μ causes an effective increase in the hydrodynamic length, κ^{-1}.

We next calculate the flow field generated by a hydrodynamic force dipole that is composed of two point forces directed oppositely to each other. When a force dipole at the origin is directed along a given unit vector $\hat{\mathbf{d}}$, its induced velocity field is given by [5.29]

$$v_i(\mathbf{r}) = -F\ell\hat{d}_k\partial_k G_{ij}(\mathbf{r})\hat{d}_j. \tag{5.23}$$

Here, F is the force magnitude, ℓ is the distance between the two point forces,

and the limit $\ell \ll r$ is assumed. In Fig. 5.3, we plot the force dipole along the x-axis (i.e., $\hat{\mathbf{d}} = \hat{\mathbf{e}}_x$) for $\mu = 0$, 3, and -3. When $\mu = 0$, the streamlines have an axial symmetry along the x-direction as well as the y-direction, as shown in Fig. 5.3(a). For $\mu = \pm 3$, however, flows perpendicular to the applied forces become dominant, and both mirror symmetries are broken, as shown in Fig. 5.3(b) and (c).

5.4.3 Mobility coefficients

Next, we investigate each component of the mobility tensor in Eq. (5.19). If we choose the x-axis, without loss of generality, along the r direction, i.e., $\mathbf{r} = r\hat{\mathbf{e}}_x$, the longitudinal, transverse, and anti-symmetric mobility coefficients are given by $G_{xx} = C_1 + C_2$, $G_{yy} = C_1$, and $G_{xy} = -G_{yx} = C_3$, respectively. The nonzero mobility coefficient G_{xy} is characteristic of the active chiral fluid with finite odd viscosity, while G_{xx} and G_{yy} remain in the limit of $\eta_{\rm o} \to 0$. Note that both G_{xx} and G_{yy} also depend on $\eta_{\rm o}$, as seen in Eqs. (5.20) and (5.21).

In Fig. 5.4, we plot G_{xx}, G_{yy}, and G_{xy} as a function of κr for various values of μ, while keeping $\eta_{\rm d} = 3\eta_{\rm s}$. We see that G_{xx} decreases monotonically with κr for all the μ values, as shown in Fig. 5.4(a). The decrease of G_{xx} is more enhanced for lager μ, whereas G_{xx} weakly depends on μ for larger κr. This reflects the fact that, for $\kappa r \gg 1$, the 3D hydrodynamic effect becomes more important, and G_{xx} is almost independent of the odd viscosity $\eta_{\rm o}$. In Fig. 5.4(b), on the other hand, G_{yy} takes negative values because the 2D fluid layer can flow in the direction opposite to the applied force [5.23]. Such a behavior results from the two vortices shown in Fig. 5.2.

The mobility coefficient G_{xy} describes the nonreciprocal hydrodynamic response because it gives the relation between the applied force F_y and induced velocity v_x. When $\mu = 0$, G_{xy} is always zero as it should be, whereas for $\mu = \pm 3$, it exhibits nonmonotonic behavior, as shown in Fig. 5.4(c). This means that when the system is active, an applied force in the 2D fluid layer generates a perpendicular flow, giving rise to the broken mirror symmetry with respect to

the force direction, even when the fluid layer is isotropic. When η_o is positive, G_{xy} takes negative ($\kappa r < 2$) and positive values ($\kappa r > 2$), corresponding to the attractive and repulsive flows, respectively, and vice versa for negative η_o. These flow patterns can lead to either convergence or dispersion of surrounding inclusions, and the specific behavior depends on the hydrodynamic screening length, κ^{-1}.

5.5 Hydrodynamic response of a rigid disk

5.5.1 Boundary integral equation

So far, we have discussed the hydrodynamic response induced by a point force and a force dipole in a 2D fluid layer with odd viscosity using the mobility tensor in Eq. (5.19). Here we generalize the discussion to the situation where the response is induced by a finite-size body moving in the 2D fluid layer. For a passive fluid, the force acting on such a body can be calculated by using a boundary integral equation that is based on the Lorentz reciprocal theorem [5.30, 5.31]. In Appendix 5.C, we first generalize this theorem for a 2D compressible fluid with finite η_o. Then, in Appendix 5.D, we derive the corresponding boundary integral equation that is used in the following analysis.

Consider a circular rigid disk of radius R, which translates and rotates in the 2D fluid. We assume that a no-slip boundary condition holds at the disk perimeter and further consider the limit of $\kappa R \ll 1$. As detailed in Appendix 5.D, the velocity at any point on the disk perimeter ($\mathbf{R} = R\hat{\mathbf{r}}$) can be expressed in terms of the following boundary integral equation

$$U_i + \epsilon_{ijk}\Omega_j R_k = -\int_{C_u} \mathrm{d}s(R')\, f_j\left(\mathbf{R}'\right) G_{ji}\left(\mathbf{R}-\mathbf{R}'\right), \tag{5.24}$$

where $\mathbf{U}$ and $\boldsymbol{\Omega}$ are the lateral and angular velocities of the rigid disk, respectively, and ϵ_{ijk} is the 3D Levi-Civita tensor. The right-hand-side of Eq. (5.24) is a line integral over an unspecified closed curve C_u, and $\mathrm{d}s(R')$ indicates that $\mathbf{R}'$ is the integration variable. The boundary integral equation (5.24) relates

the velocities of the disk moving in the 2D fluid layer with the accompanying unknown force distribution $\mathbf{f}$.

5.5.2 Translational and rotational frictions

Since the governing hydrodynamic equation (5.11) is linear in $\mathbf{v}$, the translational motion is decoupled from the rotational one. Hence, the following linear relations hold

$$\mathbf{F}^{\mathrm{d}} = -\boldsymbol{\Gamma} \cdot \mathbf{U}, \qquad \mathbf{T}^{\mathrm{d}} = -\Lambda \boldsymbol{\Omega}, \tag{5.25}$$

where $F_i^{\mathrm{d}} = \int_{C_{\mathrm{u}}} \mathrm{d}s(R')\, f_i(\mathbf{R}')$ and $T_i^{\mathrm{d}} = \epsilon_{ijk} \int_{C_{\mathrm{u}}} \mathrm{d}s(R')\, R'_j f_k(\mathbf{R}')$ are the force and torque acting on the disk, respectively, while $\boldsymbol{\Gamma}$ is the translational friction tensor and Λ is the rotational friction coefficient. The minus signs in Eq. (5.25) take into account that the force and torque act opposite to the velocities. Note that Λ is a scalar because both $\mathbf{T}^{\mathrm{d}}$ and $\boldsymbol{\Omega}$ must point to the z-direction in a 2D system.

Using the assumption $|\mathbf{R}'| \ll |\mathbf{R}|$ in Eq. (5.24) [5.22], we obtain the expressions for $\boldsymbol{\Gamma}$ and Λ as

$$\boldsymbol{\Gamma} = \frac{1}{(C_1 + C_2/2)^2 + C_3^2} \begin{pmatrix} C_1 + C_2/2 & C_3 \\ -C_3 & C_1 + C_2/2 \end{pmatrix}, \tag{5.26}$$

$$\Lambda = \frac{2R^2}{C_2 - R(\partial C_1/\partial R)}. \tag{5.27}$$

See Appendix 5.E for the derivation. In the above, the arguments of the three coefficients are omitted, $C_n \equiv C_n(R)$ $(n = 1, 2, 3)$, in order to keep the notation compact. For passive fluids, the translational friction tensor must be symmetric and positive definite according to the requirement that the dissipated energy is positive [5.32]. For the considered fluid with η_{o}, however, the translational friction tensor is allowed to be asymmetric when C_3 is nonzero. Notice that the energy dissipation calculated from Eq. (5.26) is $U_i \Gamma_{ij} U_j \sim (C_1 + C_2/2)U^2$ and the anti-symmetric part does not contribute to the dissipation.

For a disk translating with the velocity $\mathbf{U} = (U, 0)$, we have the viscous drag

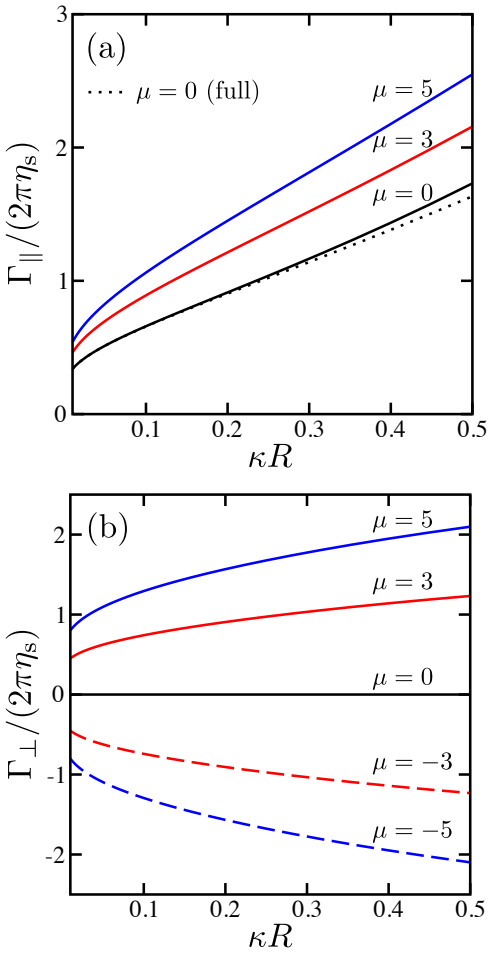

Figure 5.5: Plots of the drag ($\Gamma_\parallel$) and lift ($\Gamma_\perp$) coefficients rescaled by $2\pi\eta_s$ as a function of the rescaled disk radius κR. (a) The drag coefficient $\Gamma_\parallel$ for $\mu = 0$, 3, and 5 (black, red, and blue solid lines). The dotted line represents the full expression $\Gamma_\parallel^0$ for the drag coefficient when $\mu = 0$ reported in Ref. [5.15] (see the text for the specific expression). (b) The lift coefficient $\Gamma_\perp$ for $\mu = -5$, -3, 0, 3, and 5 (blue dashed, red dashed, black solid, red solid, and blue solid lines).

and lift coefficients as $\Gamma_\parallel = \Gamma_{xx}$ and $\Gamma_\perp = \Gamma_{yx}$, respectively. In Fig. 5.5, we plot $\Gamma_\parallel$ and $\Gamma_\perp$ as a function of the dimensionless radius κR for various values of μ. We see that $\Gamma_\parallel$ increases monotonically with increasing the disk size for all μ values, as seen in Fig. 5.5(a). For a fixed disk size, $\Gamma_\parallel$ is larger for larger μ values. The dotted line in Fig. 5.5(a) is the full analytical result for $\mu = 0$ (2D passive compressible fluid) [5.15], $\Gamma_\parallel^0/(2\pi\eta_s) = \frac{4}{5}(\kappa R)^2 K_2(\kappa R)/K_0(\kappa R)$, where $K_n(x)$ is the modified Bessel function of the second kind [5.28]. Our result obtained by using the boundary integral equation (5.24) coincides with the analytical one

when $\kappa R \ll 1$.

In Fig. 5.5(b), we see that $\Gamma_\perp$ shows both increasing and decreasing dependencies on κR for positive and negative values of μ, respectively. However, when $\mu = 0$, $\Gamma_\perp$ is always zero, as it should be. Finite values of $\Gamma_\perp$ mean that the disk translated along the x-axis presents a lift motion along the y-direction. For a fixed disk size, the absolute value of $\Gamma_\perp$ increases and the lift force is more enhanced as the absolute value of μ increases.

Assuming that the disk is rotating with velocity $\mathbf{\Omega} = (0, 0, \Omega)$, we obtain the rotational friction coefficient Λ that is plotted in Fig. 5.6 as a function of κR. We see that Λ shows an increasing dependency on κR for all the μ values. The dotted line in Fig. 5.6 represents the full analytical expression for $\mu = 0$ (2D passive incompressible fluid) [5.20], $\kappa^2\Lambda^0/(4\pi\eta_s) = (\kappa R)^2 + \frac{1}{2}(\kappa R)^3 K_0(\kappa R)/K_1(\kappa R)$. The solid black line and the dotted line coincide in the limit of $\kappa R \ll 1$, because the disk rotation contributes neither to the compression nor to the expansion of fluids.

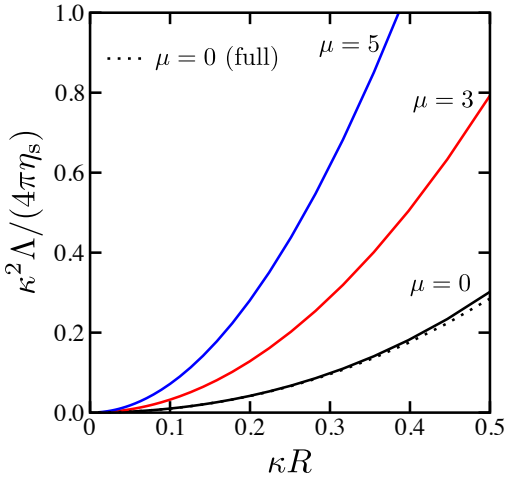

Figure 5.6: Plot of the rotational friction coefficient (Λ) rescaled by $4\pi\eta_s/\kappa^2$ as a function of the rescaled disk radius κR for $\mu = 0$, 3, and 5 (black, red, and blue solid lines). The dotted line represents the full expression Λ^0 for the rotational coefficient when $\mu = 0$ reported in Ref. [5.20] (see the text for the specific expression).

5.6 Discussion and conclusion

We have investigated the linear hydrodynamic response of a 2D fluid layer with broken time-reversal and parity symmetries. Such a 2D active fluid presents a special rheological property called *odd viscosity*, characterizing the deviation of the system from a passive fluid. In our approach, we combine the concept of the odd viscosity [5.1–5.3] and the hydrodynamic model of a 2D compressible fluid derived by using the lubrication approximation [5.15–5.17]. In contrast to well-studied 2D fluids characterized by a shear viscosity [5.20–5.25], the additional odd viscosity η_o leads to anomalous flow behavior, i.e., nonreciprocal hydrodynamic response.

In the case of a point force and a force dipole, the symmetry of the velocity field in terms of the force direction is broken, generating flow perpendicular to the applied force (see Figs. 5.2 and 5.3). We also analyzed the effects of the odd viscosity on the mobility tensor, as derived in Eq. (5.19). In particular, we investigated the behavior of the anti-symmetric mobility coefficient G_{xy} that exists only for nonvanishing η_o, as shown in Eq. (5.22). As for the hydrodynamic response of finite-size bodies, we have investigated the forces acting on a translating and rotating disk in a 2D fluid layer, using the boundary integral equation (5.24). We found that small disks ($\kappa R \ll 1$) not only undergo a drag force, but also a lift force, which cannot be seen in an isotropic passive fluid (see Fig. 5.5) [5.1].

As a possible biological application, we can relate the 2D fluid layer to a monolayer with a low concentration of active motor proteins, such as ion pumps [5.33]. Rheological properties of these system can be investigated by surface microrheology techniques [5.34]. For typical values such as $\eta \approx 10^{-3}\,\mathrm{Pa{\cdot}s}$, $\eta_\mathrm{s} \approx 10^{-6}\,\mathrm{Pa{\cdot}s{\cdot}m}$, and $h \approx 1\,\mathrm{nm}$, we find that the obtained drag and lift forces could be observed in experiments using a sub-micrometer probe, i.e., $R < 0.1\,\mu\mathrm{m}$.

In this paper, we have considered a 2D compressible fluid, which is in contact

with a 3D bulk fluid. Such a compressible 2D system can be realized by a dilute Gibbs monolayer, which is composed of soluble amphiphiles that can dissolve into the underlying bulk fluid [5.15, 5.16]. When the adsorption and desorption processes of soluble amphiphiles are instantaneous, surface concentration gradients can be eliminated rapidly. This is the situation that we consider in the present work. When the amphiphile is insoluble, on the other hand, the concentration gradient is sustained, giving rise to a Marangoni flow [5.17, 5.35]. Although the Marangoni convection is outside the scope of this paper, it would be interesting to investigate the effects of odd viscosity on such convective phenomena.

In general, odd viscosity can depend on the density of self-spinning objects, although such an effect was not considered in the present work. By using the 2D Faxén laws, effective shear viscosity of a fluid membrane with finite-size suspensions was derived [5.22, 5.23]. Hence, it is of interest to see how the nonreciprocal flow field of the 2D fluid with an odd viscosity η_o changes with the rotor concentration. Moreover, for a passive fluid at equilibrium, the disk drag coefficient is connected to its diffusion constant through Einstein's relation. However, such an evident relation does not exist in active chiral fluids and one has to extend the fluctuation dissipation theorem [5.36–5.39]. These interesting questions are left for future investigations.

Appendix 5.A Derivation of Eq. (5.15)

We derive the mobility tensor in Fourier space $\mathbf{G}[\mathbf{k}]$ as given by Eq. (5.15). The Fourier transform of $\mathbf{v}(\mathbf{r})$ is defined by

$$\mathbf{v}(\mathbf{r}) = \int \frac{\mathrm{d}^2 k}{(2\pi)^2}\, \mathbf{v}[\mathbf{k}] \exp(i\mathbf{k}\cdot\mathbf{r}), \tag{5.A1}$$

with $\mathbf{k} = (k_x, k_y)$, and similarly for the 3D pressure $p(\mathbf{r})$ and the force density $\mathbf{F}(\mathbf{r})$. In the Fourier space, Eq. (5.11) becomes

$$-\eta_\mathrm{s} k^2 \mathbf{v}[\mathbf{k}] - \eta_\mathrm{d} k^2 \hat{\mathbf{k}}\hat{\mathbf{k}}\cdot\mathbf{v}[\mathbf{k}] - \eta_\mathrm{o} k^2 (\hat{\mathbf{k}}\bar{\mathbf{k}}\cdot\mathbf{v}[\mathbf{k}] - \bar{\mathbf{k}}\hat{\mathbf{k}}\cdot\mathbf{v}[\mathbf{k}])$$

$$-\frac{ih}{2}kp[\mathbf{k}]\hat{\mathbf{k}}-\frac{\eta}{h}\mathbf{v}[\mathbf{k}]+\mathbf{F}[\mathbf{k}]=0, \tag{5.A2}$$

or equivalently

$$-\eta_{\rm s}k^2\mathbf{v}[\mathbf{k}]-\eta_{\rm d}k^2v_{\parallel}[\mathbf{k}]\hat{\mathbf{k}}-\eta_{\rm o}k^2(v_{\perp}[\mathbf{k}]\hat{\mathbf{k}}-v_{\parallel}[\mathbf{k}]\bar{\mathbf{k}})-\frac{ih}{2}kp[\mathbf{k}]\hat{\mathbf{k}}-\frac{\eta}{h}\mathbf{v}[\mathbf{k}]+\mathbf{F}[\mathbf{k}]=0, \tag{5.A3}$$

where $v_{\parallel}[\mathbf{k}]=\hat{\mathbf{k}}\cdot\mathbf{v}[\mathbf{k}]$ and $v_{\perp}[\mathbf{k}]=\bar{\mathbf{k}}\cdot\mathbf{v}[\mathbf{k}]$. For Eq. (5.12), we have

$$ik\hat{\mathbf{k}}\cdot\mathbf{v}[\mathbf{k}]=ikv_{\parallel}[\mathbf{k}]=-\frac{h^2}{6\eta}k^2p[\mathbf{k}]. \tag{5.A4}$$

In the derivation of Eq. (5.A2), we have assumed that the 2D fluid layer is quickly equilibrated with the 3D bulk, and hence the 2D pressure is homogeneous in space, i.e., $\nabla\Pi=0$ [5.15, 5.17].

Substituting Eq. (5.A4) into Eq. (5.A2) to eliminate $p[\mathbf{k}]$, we obtain

$$-\eta_{\rm s}k^2\mathbf{v}[\mathbf{k}]-\eta_{\rm d}k^2v_{\parallel}[\mathbf{k}]\hat{\mathbf{k}}-\eta_{\rm o}k^2(v_{\perp}[\mathbf{k}]\hat{\mathbf{k}}-v_{\parallel}[\mathbf{k}]\bar{\mathbf{k}})-\frac{3\eta}{h}v_{\parallel}[\mathbf{k}]\hat{\mathbf{k}}-\frac{\eta}{h}\mathbf{v}[\mathbf{k}]+\mathbf{F}[\mathbf{k}]=0. \tag{5.A5}$$

Hence, $\mathbf{F}[\mathbf{k}]$ can be written as

$$\begin{pmatrix}F_{\parallel}[\mathbf{k}]\\F_{\perp}[\mathbf{k}]\end{pmatrix}=\begin{pmatrix}(\eta_{\rm s}+\eta_{\rm d})k^2+4\eta/h & \eta_{\rm o}k^2\\ -\eta_{\rm o}k^2 & \eta_{\rm s}k^2+\eta/h\end{pmatrix}\begin{pmatrix}v_{\parallel}[\mathbf{k}]\\v_{\perp}[\mathbf{k}]\end{pmatrix}. \tag{5.A6}$$

Since the mobility tensor in the Fourier space satisfies the relation $\mathbf{v}[\mathbf{k}]=\mathbf{G}[\mathbf{k}]\cdot\mathbf{F}[\mathbf{k}]$, we obtain Eq. (5.15).

Appendix 5.B Derivation of Eq. (5.19) and $\mathbf{G}^0(\mathbf{r})$

Here we perform the inverse Fourier transform of $\mathbf{G}[\mathbf{k}]$ in Eq. (5.15) to obtain $\mathbf{G}(\mathbf{r})$. By calculating G_{ii}, $G_{ij}\hat{r}_i\hat{r}_j$, and $G_{ij}\epsilon_{ij}$, we obtain [5.27]

$$\begin{aligned}2C_1+C_2&=\int\frac{{\rm d}^2k}{(2\pi)^2}\frac{\eta_{\rm s}(k^2+\kappa^2)+(\eta_{\rm s}+\eta_{\rm d})(k^2+\lambda^2)}{\eta_{\rm s}(\eta_{\rm s}+\eta_{\rm d})(k^2+\kappa^2)(k^2+\lambda^2)+\eta_{\rm o}^2k^4}\exp(i\mathbf{k}\cdot\mathbf{r})\\&=\frac{1}{2\pi}\int_0^{\infty}{\rm d}k\,k\frac{\eta_{\rm s}(k^2+\kappa^2)+(\eta_{\rm s}+\eta_{\rm d})(k^2+\lambda^2)}{\eta_{\rm s}(\eta_{\rm s}+\eta_{\rm d})(k^2+\kappa^2)(k^2+\lambda^2)+\eta_{\rm o}^2k^4}J_0(kr),\end{aligned} \tag{5.B1}$$

$$C_1+C_2=\int\frac{{\rm d}^2k}{(2\pi)^2}\frac{\eta_{\rm s}(k^2+\kappa^2)\cos^2\theta+(\eta_{\rm s}+\eta_{\rm d})(k^2+\lambda^2)(1-\cos^2\theta)}{\eta_{\rm s}(\eta_{\rm s}+\eta_{\rm d})(k^2+\kappa^2)(k^2+\lambda^2)+\eta_{\rm o}^2k^4}\exp(i\mathbf{k}\cdot\mathbf{r})$$

$$= \frac{1}{2\pi}\int_0^\infty \mathrm{d}k\, k \frac{\eta_\mathrm{s}(k^2+\kappa^2)[J_0(kr) - J_1(kr)/(kr)] + (\eta_\mathrm{s}+\eta_\mathrm{d})(k^2+\lambda^2)J_1(kr)/(kr)}{\eta_\mathrm{s}(\eta_\mathrm{s}+\eta_\mathrm{d})(k^2+\kappa^2)(k^2+\lambda^2)+\eta_\mathrm{o}^2k^4}, \tag{5.B2}$$

$$\begin{aligned} C_3 &= -\int \frac{\mathrm{d}^2k}{(2\pi)^2} \frac{\eta_\mathrm{o}k^2}{\eta_\mathrm{s}(\eta_\mathrm{s}+\eta_\mathrm{d})(k^2+\kappa^2)(k^2+\lambda^2)+\eta_\mathrm{o}^2k^4} \exp(i\mathbf{k}\cdot\mathbf{r}) \\ &= -\frac{\eta_\mathrm{o}}{2\pi}\int_0^\infty \mathrm{d}k\, \frac{k^3 J_0(kr)}{\eta_\mathrm{s}(\eta_\mathrm{s}+\eta_\mathrm{d})(k^2+\kappa^2)(k^2+\lambda^2)+\eta_\mathrm{o}^2k^4}, \end{aligned} \tag{5.B3}$$

respectively, where θ is the angle between the vectors $\mathbf{k}$ and $\mathbf{r}$. Solving Eqs. (5.B1) and (5.B2) when $\kappa = \lambda$, we obtain Eqs. (5.20), (5.21), and (5.22).

Next, we analytically derive the mobility tensor $\mathbf{G}^0(\mathbf{r})$ in the absence of the odd viscosity, i.e., $\mu = 0$. In this case, we have from Eq. (5.15)

$$G^0_{ij}[\mathbf{k}] = \frac{\delta_{ij} - \hat{k}_i\hat{k}_j}{\eta_\mathrm{s}(k^2+\kappa^2)} + \frac{\hat{k}_i\hat{k}_j}{(\eta_\mathrm{s}+\eta_\mathrm{d})(k^2+\lambda^2)}. \tag{5.B4}$$

The real-space mobility tensor $\mathbf{G}^0(\mathbf{r})$ can be obtained by assuming

$$G^0_{ij}(\mathbf{r}) = B_1(r)\delta_{ij} + B_2(r)\hat{r}_i\hat{r}_j, \tag{5.B5}$$

with two coefficients B_1 and B_2.

By calculating G^0_{ii} and $G^0_{ij}\hat{r}_i\hat{r}_j$, we have

$$\begin{aligned} 2B_1 + B_2 &= \frac{1}{2\pi}\int_0^\infty \mathrm{d}k\, \left[\frac{k}{\eta_\mathrm{s}(k^2+\kappa^2)} + \frac{k}{(\eta_\mathrm{s}+\eta_\mathrm{d})(k^2+\lambda^2)}\right] J_0(kr) \\ &= \frac{1}{2\pi\eta_\mathrm{s}}K_0(\kappa r) + \frac{1}{2\pi(\eta_\mathrm{s}+\eta_\mathrm{d})}K_0(\lambda r), \end{aligned} \tag{5.B6}$$

$$\begin{aligned} B_1 + B_2 &= \frac{1}{2\pi}\int_0^\infty \mathrm{d}k\, \left[\frac{J_1(kr)}{\eta_\mathrm{s}r(k^2+\kappa^2)} + \frac{k}{(\eta_\mathrm{s}+\eta_\mathrm{d})(k^2+\lambda^2)}\left(J_0(kr) - \frac{J_1(kr)}{kr}\right)\right] \\ &= \frac{1}{2\pi\eta_\mathrm{s}}\left[-\frac{K_1(\kappa r)}{\kappa r} + \frac{1}{(\kappa r)^2}\right] + \frac{1}{2\pi(\eta_\mathrm{s}+\eta_\mathrm{d})}\left[K_0(\lambda r) + \frac{K_1(\lambda r)}{\lambda r} - \frac{1}{(\lambda r)^2}\right]. \end{aligned} \tag{5.B7}$$

Solving Eqs. (5.B6) and (5.B7), we obtain

$$B_1(r) = \frac{1}{2\pi\eta_\mathrm{s}}\left[K_0(\kappa r) + \frac{K_1(\kappa r)}{\kappa r} - \frac{1}{(\kappa r)^2}\right] + \frac{1}{2\pi(\eta_\mathrm{s}+\eta_\mathrm{d})}\left[-\frac{K_1(\lambda r)}{\lambda r} + \frac{1}{(\lambda r)^2}\right], \tag{5.B8}$$

$$B_2(r) = \frac{1}{2\pi\eta_\mathrm{s}}\left[-K_0(\kappa r) - \frac{2K_1(\kappa r)}{\kappa r} + \frac{2}{(\kappa r)^2}\right]$$

$$+\frac{1}{2\pi(\eta_{\rm s}+\eta_{\rm d})}\left[K_0(\lambda r)+\frac{2K_1(\lambda r)}{\lambda r}-\frac{2}{(\lambda r)^2}\right]. \tag{5.B9}$$

Appendix 5.C Generalized Lorentz reciprocal theorem

The Lorentz reciprocal theorem gives a relation regarding the resistance of finite-size bodies moving in a passive fluid [5.31, 5.32]. Here we generalize this theorem for a 2D compressible fluid with finite odd viscosity. Let unprimed and primed symbols represent the variables for any two arbitrary types of flows satisfying the following equations

$$\partial_j\sigma_{ij}+b_i=0, \qquad \partial_j\sigma'_{ij}+b'_i=0, \tag{5.C1}$$

where $\mathbf{b}$ and $\mathbf{b}'$ are the arbitrary body force densities and the associated velocity fields are given by $\mathbf{v}$ and $\mathbf{v}'$, respectively. In the above, σ_{ij} is the stress tensor in Eq. (6.3) that also includes the 2D isotropic pressure term, $-\Pi\delta_{ij}$ (similarly for σ'_{ij}). The divergence of $\sigma'_{ij}v_j-\sigma_{ij}v'_j$ becomes [5.40]

$$\begin{aligned}&\partial_i[(\sigma'_{{\rm S},ij}+\sigma'_{{\rm A},ij})v_j]-\partial_i\left[(\sigma_{{\rm S},ij}-\sigma_{{\rm A},ij})v'_j\right]\\&=v'_jb_j-v_jb'_j-\Pi'\partial_jv_j+\Pi\partial_jv'_j+2v'_j\partial_i\sigma_{{\rm A},ij},\end{aligned} \tag{5.C2}$$

where

$$\begin{aligned}\sigma_{{\rm S},ij}&=-\Pi\delta_{ij}+(\eta_{\rm d}-\eta_{\rm s})\delta_{ij}\partial_kv_k+\eta_{\rm s}(\partial_jv_i+\partial_iv_j),\\\sigma_{{\rm A},ij}&=\frac{1}{2}\eta_{\rm o}\left(\partial_jv_i^*+\partial_iv_j^*+\partial_j^*v_i+\partial_i^*v_j\right),\end{aligned} \tag{5.C3}$$

with $\sigma_{ij}=\sigma_{{\rm S},ij}+\sigma_{{\rm A},ij}$. Integrating the above equation over the fluid area A, we obtain the integral identity as

$$\begin{aligned}&\int_C{\rm d}s\,n_i(\sigma'_{{\rm S},ij}+\sigma'_{{\rm A},ij})v_j-\int_C{\rm d}s\,n_i(\sigma_{{\rm S},ij}-\sigma_{{\rm A},ij})v'_j\\&=-\int_A{\rm d}A\,v'_jb_j+\int_A{\rm d}A\,v_jb'_j+\int_A{\rm d}A\,\Pi'\partial_jv_j-\int_A{\rm d}A\,\Pi\partial_jv'_j-2\int_A{\rm d}A\,v'_j\partial_i\sigma_{{\rm A},ij},\end{aligned} \tag{5.C4}$$

where C denotes the curve bounding the area A and the unit vector $\mathbf{n}$ is directed into that area. We note that Eq. (5.C4) is not invariant under the exchange of

the unprimed and primed variables when $\eta_{\rm o} \neq 0$. When $\eta_{\rm o} = 0$, on the other hand, Eq. (5.C4) reduces to the Lorentz reciprocal theorem for a 2D compressible fluid [5.40].

Appendix 5.D Derivation of Eq. (5.24)

Here we derive the boundary integral equation in Eq. (5.24). When $\Pi = \Pi' = 0$, we consider the following two types of unprimed and primed flows

$$\partial_j \sigma_{ij} = 0, \quad \partial_j \sigma'_{ij} + F'_i \delta(\mathbf{R} - \mathbf{R}') = 0. \tag{5.D1}$$

Suppose that a circular rigid disk is moving in the fluid area A, Eq. (5.C4) with the use of Eq. (5.D1) becomes [5.30, 5.31]

$$\begin{aligned}\int_{C_{\rm d}} {\rm d}s(R)\, n_i(\sigma_{{\rm S},ij} - \sigma_{{\rm A},ij}) v'_j = \int_{C_{\rm d}} {\rm d}s(R)\, n_i(\sigma'_{{\rm S},ij} + \sigma'_{{\rm A},ij}) v_j \\ - F'_j \int_A {\rm d}A(R)\, v_j \delta(\mathbf{R} - \mathbf{R}'),\end{aligned} \tag{5.D2}$$

where $C_{\rm d}$ is the circular curve bounding the moving disk, as schematically depicted in Fig. 5.7. The notations, ${\rm d}s(R)$ and ${\rm d}A(R)$, indicate that $\mathbf{R}$ is the integration variable. Assuming a nonslip boundary condition at the disk perimeter and using the form of the point-force solution, $v'_i(\mathbf{R}) = G_{ij}(\mathbf{R} - \mathbf{R}')F'_j$, we obtain [5.31]

$$\int_A {\rm d}A(R)\, v_\ell(\mathbf{R}) \delta(\mathbf{R} - \mathbf{R}') = -\int_{C_{\rm u}} {\rm d}s(R)\, f_j(\mathbf{R}) G_{j\ell}(\mathbf{R} - \mathbf{R}'), \tag{5.D3}$$

where $C_{\rm u}$ denotes the domain of the unknown force distribution, $\mathbf{f}$, and we have assumed that the force distribution can be defined as $f_j = n_i(\sigma_{{\rm S},ij} - \sigma_{{\rm A},ij})$. Interchanging $\mathbf{R}$ and $\mathbf{R}'$, we finally obtain Eq. (5.24).

Appendix 5.E Derivation of Eqs. (5.26) and (5.27)

We derive the translational friction tensor $\mathbf{\Gamma}$ and the rotational friction coefficient Λ in Eqs. (5.26) and (5.27), respectively. If we assume $|\mathbf{R}'| \ll |\mathbf{R}|$ [5.22], the right-hand-side of Eq. (5.24) can be expanded up to first order in $\mathbf{R}'$ as

$$U_i + \epsilon_{ijk}\Omega_j R_k \approx -\int_{C_{\rm u}} {\rm d}s(R')\, f_j(\mathbf{R}') \left[G_{ji}(R) - R'_k \frac{\partial G_{ji}(R)}{\partial R_k} \right]. \tag{5.E1}$$

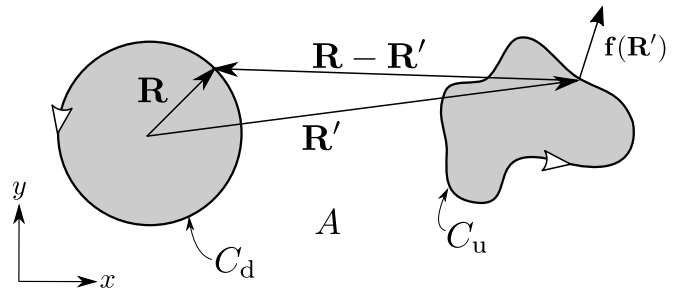

Figure 5.7: Sketch of the circular curve, C_{d}, and the unspecified curve, C_{u}, with the accompanying unknown force distribution, $\mathbf{f}$, while A is the fluid area bounded by both C_{d} and C_{u} (white area). The curves, C_{d} and C_{u}, are parameterized by the vectors $\mathbf{R}$ and $\mathbf{R}'$, respectively and the two arrows represent the direction of the line integral. In the sketch, we have $|\mathbf{R}'| > |\mathbf{R}|$ only for presentation purposes. In actual calculations where the condition $|\mathbf{R}'| \ll |\mathbf{R}|$ is used, the two curves overlap with each other.

Integrating Eq. (5.E1) over the circular disk perimeter, C_{d}, parametrized by $\mathbf{R}$, we obtain the relation between the velocity and the force as

$$U_i = -\frac{1}{2\pi R}\int_{C_{\mathrm{u}}} \mathrm{d}s(R')\, f_j(\mathbf{R}') \int_{C_{\mathrm{d}}} \mathrm{d}s(R)\, G_{ji}(R) = -[(C_1 + C_2/2)\delta_{ij} - C_3\epsilon_{ij}]F_j^{\mathrm{d}}, \tag{5.E2}$$

where $F_i^{\mathrm{d}} = \int_{C_{\mathrm{u}}} \mathrm{d}s(R')\, f_i(\mathbf{R}')$ is the force acting on the disk. In the above, the integrals of the odd terms in $\mathbf{R}$ vanish because of the symmetry of the disk. Hence, we obtain Eq. (5.26).

Next, we multiply both sides of Eq. (5.E1) by $\mathbf{R}$ and integrate over C_{d}

$$\pi R^3 \epsilon_{\ell ij}\Omega_j = \int_{C_{\mathrm{u}}} \mathrm{d}s(R')\, R'_k f_j\,(\mathbf{R}') \int_{C_{\mathrm{d}}} \mathrm{d}s(R)\, R_\ell \frac{\partial G_{ji}(R)}{\partial R_k}. \tag{5.E3}$$

We further multiply both sides of the above equation by $\epsilon_{\ell in}$ and obtain

$$\Omega_n = \frac{1}{2R}\left[\left(\frac{\partial C_1}{\partial R} - \frac{C_2}{R}\right)\epsilon_{nkj} - \frac{\partial C_3}{\partial R}\epsilon_{nki}\epsilon_{ij}\right] \int_{C_{\mathrm{u}}} \mathrm{d}s(R')\, R'_k f_j\,(\mathbf{R}')\,. \tag{5.E4}$$

On the right-hand-side, the term with C_3 represents the radial pressure acting on the disk [5.1]. As this term does not contribute to the torque, it vanishes and the relation between the angular velocity and the torque becomes

$$\mathbf{\Omega} = \frac{1}{2R}\left(\frac{\partial C_1}{\partial R} - \frac{C_2}{R}\right)\mathbf{T}^{\mathrm{d}}, \tag{5.E5}$$

where $T_i^{\mathrm{d}} = \epsilon_{ijk}\int_{C_{\mathrm{u}}} \mathrm{d}s(R')\, R'_j f_k\,(\mathbf{R}')$ is the torque on the disk. Hence, we obtain

Eq. (5.27).

References

[5.1] J. E. Avron, J. Stat. Phys. **92**, 543 (1998).

[5.2] D. Banerjee, A. Souslov, A. G. Abanov, and V. Vitelli, Nat. Commun. **8**, 1573 (2017).

[5.3] J. M. Epstein and K. K. Mandadapu, Phys. Rev. E **101**, 052614 (2020).

[5.4] C. Hargus, K. Klymko, J. M. Epstein, and K. K. Mandadapu, J. Chem. Phys. **152**, 201102 (2020).

[5.5] M. Han, M. Fruchart, C. Scheibner, S. Vaikuntanathan, J. J. de Pablo, and V. Vitelli, Nat. Phys. **17**, 1260 (2021).

[5.6] T. Markovich and T. C. Lubensky, Phys. Rev. Lett. **127**, 048001 (2021).

[5.7] S. Ganeshan and A. G. Abanov, Phys. Rev. Fluids **2**, 094101 (2017).

[5.8] A. Abanov, T. Can, and S. Ganeshan, SciPost Phys. **5**, 010 (2018).

[5.9] V. Soni, E. S. Bililign, S. Magkiriadou, S. Sacanna, D. Bartolo, M. J. Shelley, and W. T. M. Irvine, Nat. Phys. **15**, 1188 (2019).

[5.10] T. Khain, C. Scheibner, M. Fruchart, and V. Vitelli, arXiv preprint arXiv:2011.07681 (2020).

[5.11] L. Braverman, C. Scheibner, and V. Vitelli, arXiv preprint arXiv:2011.11543 (2020).

[5.12] C. Scheibner, A. Souslov, D. Banerjee, P. Surówka, W. T. M. Irvine, and V. Vitelli, Nat. Phys. **16**, 475 (2020).

[5.13] C. Reichhardt and C. J. O. Reichhardt, Phys. Rev. E **100**, 012604 (2019).

[5.14] E. Kogan, Phys. Rev. E **94**, 043111 (2016).

[5.15] C. Barentin, C. Ybert, J.-M. di Meglio, and J.-F. Joanny, J. Fluid Mech. **397**, 331 (1999).

[5.16] C. Barentin, P. Muller, C. Ybert, J.-F. Joanny, and J.-M. di Meglio, Eur. Phys. J. E **2**, 153 (2000).

[5.17] G. J. Elfring, L. G. Leal, and T. M. Squires, J. Fluid Mech. **792**, 712 (2016).

[5.18] H. Lamb, *Hydrodynamics* (Cambridge University Press, New York, 1975).

[5.19] L. D. Landau and E. M. Lifshitz, *Fluid mechanics* (Pergamon Press, Oxford, 1987).

[5.20] E. Evans and E. Sackmann, J. Fluid Mech. **194**, 553 (1988).

[5.21] H. Diamant, J. Phys. Soc. Jpn. **78**, 041002 (2009).

[5.22] N. Oppenheimer and H. Diamant, Biophys. J. **96**, 3041 (2009).

[5.23] N. Oppenheimer and H. Diamant, Phys. Rev. E **82**, 041912 (2010).

[5.24] S. Ramachandran, S. Komura, M. Imai, and K. Seki, Eur. Phys. J. E **31**, 303 (2010).

[5.25] S. Ramachandran, S. Komura, K. Seki, and G. Gompper, Eur. Phys. J. E **34**, 46 (2011).

[5.26] A. Souslov, K. Dasbiswas, M. Fruchart, S. Vaikuntanathan, and V. Vitelli, Phys. Rev. Lett. **122**, 128001 (2019).

[5.27] M. Doi and S. F. Edwards, *The Theory of Polymer Dynamics* (Oxford University Press, New York, 1986).

[5.28] M. Abramowitz and I. A. Stegun, *Handbook of Mathematical Functions* (Dover, New York, 1972).

[5.29] S. E. Spagnolie and E. Lauga, J. Fluid Mech. **700**, 105 (2012).

[5.30] C. Pozrikidis, *Boundary Integral and Singularity Methods for Linearized Viscous Flow* (Cambridge University Press, New York, 1992).

[5.31] H. Masoud and H. A. Stone, J. Fluid Mech. **879**, 1 (2019).

[5.32] J. Happel and H. Brenner, *Low Reynolds Number Hydrodynamics: With Special Applications to Particulate Media* (Kluwer Academic Publishers, Netherlands, 1991).

[5.33] B. Alberts, A. Johnson, J. Lewis, M. Raff, K. Roberts, and P. Walter, *Molecular Biology of the Cell* (Garland Science, New York, 2008).

[5.34] A. Maestro, L. J. Bonales, H. Ritacco, T. M. Fischer, R. G. Rubio, and F. Ortega, Soft Matter **7**, 7761 (2011).

[5.35] H. Manikantan and T. M. Squires, J. Fluid Mech. **892** (2020).

[5.36] K. Yasuda, R. Okamoto, and S. Komura, Phys. Rev. E **95**, 032417 (2017).

[5.37] Y. Hosaka, K. Yasuda, R. Okamoto, and S. Komura, Phys. Rev. E **95**, 052407 (2017).

[5.38] K. Yasuda, R. Okamoto, S. Komura, and A. S. Mikhailov, EPL **117**, 38001 (2017).

[5.39] Y. Hosaka, S. Komura, and A. S. Mikhailov, Soft Matter **16**, 10734 (2020).

[5.40] F. R. Cunha, A. J. de Sousa, and M. Loewenberg, Comput. Appl. Math. **22**, 53 (2003).

Chapter 6

Hydrodynamic Lift of a Two-Dimensional Liquid Domain with Odd Viscosity †

6.1 Introduction

Biological membranes play an important role in various life-sustaining processes such as the transportation of materials or the reaction between chemical species, which are essential for cellular metabolism and homeostasis [6.1]. Biomembranes are composed of two layers of lipid molecules, cholesterol, and various types of proteins that can move laterally due to the membrane fluidity [6.2]. Since lipid bilayers are extremely thin, as compared to their lateral size, they have been modeled as two-dimensional (2D) fluids, and their transport properties have been investigated both theoretically and experimentally. For instance, the drag coefficient of a disk-like domain (protein) moving in a 2D fluid sheet has been studied for various membrane geometries [6.3–6.6]. Using fluorescence correlation spectroscopy, Ramadurai *et al.* measured the lateral mobility of proteins in lipid bilayers and confirmed a logarithmic dependence of

†The material presented in this chapter was published: Y. Hosaka, S. Komura, and D. Andelman, Phys. Rev. E **104**, 064613 (2021).

the mobility on the protein size in agreement with predictions [6.7].

In an actual biological environment, the presence of active protein molecules plays an important role because they induce nonequilibrium hydrodynamic effects to the surrounding fluid [6.8–6.11]. For example, there are active rotating proteins such as ion pumps, that allow materials to pass through the membrane [6.12, 6.13]. Their inherent nonequilibrium nature due to continuous energy consumption violates the time-reversal symmetry and drives the membrane into out-of-equilibrium situations [6.14]. In addition, rotating proteins further break the parity symmetry because of their unidirectional motion, so that the membrane with autonomous rotors can be viewed as an active chiral system [6.15–6.18]. Moreover, active proteins are often inhomogeneously distributed in the membrane to form active protein-rich domains that are called lipid rafts [6.19–6.21]. Due to the presence of such condensed active rotor proteins, biomembranes can be regarded as a heterogeneous active chiral fluid rather than just a uniform and passive 2D fluid.

Active chiral fluids are generally characterized by a peculiar rheological property called *odd viscosity* [6.22], which accounts for the fluid flow perpendicular to the velocity gradient and does not contribute to energy dissipation. It is known that odd viscosity gives rise to anomalous hydrodynamic phenomena such as surface waves [6.23] or topological edge modes [6.24–6.26] at fluid boundaries. Furthermore, it leads to an instability of a viscous film [6.27, 6.28] and asymmetric mobility [6.29]. In an incompressible fluid, however, the odd viscosity can be absorbed into the hydrostatic pressure term [6.17, 6.22] and does not affect the flow profile [6.30, 6.31]. To clearly see the odd viscosity effect, one should include either the violation of the incompressibility condition or the appropriate boundaries in 2D fluids [6.29, 6.30].

To reveal the odd viscosity effect, the hydrodynamic forces acting on various objects have been studied in the presence of odd viscosity [6.29–6.32]. For a laterally moving rigid disk, it was found that odd viscosity causes a hydrody-

namic lift force for a compressible 2D fluid [6.29]. Moreover, odd viscosity is responsible for the torque acting on objects with time-varying area such as an expanding bubble with a no-stress boundary condition [6.30–6.32]. From the experimental point of view, odd viscosity was measured for a fluid consisting of self-spinning particles [6.33, 6.34]. Although odd viscosity may exist in biological systems [6.17, 6.35], hydrodynamic responses in heterogeneous active chiral fluids have not been discussed and the role of odd viscosity in biomembranes remains largely unexplored.

In this paper, we discuss the hydrodynamic forces acting on a circular liquid domain that moves laterally in a supported membrane in the presence of odd viscosity [6.22]. To investigate active heterogeneous structures relevant to lipid rafts in biomembranes, we consider a situation where the odd viscosity is different between the inside and outside of the liquid domain. Taking into account the momentum leakage from the 2D fluid to the underlying substrate [6.6, 6.36–6.41], we analytically obtain the velocity field induced by the domain motion and discuss its dependence on the odd viscosity difference. We then calculate the drag and lift forces acting on a moving liquid domain. We show that a dissipationless lift force acting on the domain emerges when only the odd viscosity difference is present, while it vanishes when the odd viscosity is uniform in space. We further obtain various limiting expressions of the drag and lift coefficients for small and large domain sizes, which deviate from those obtained for the passive case [6.6].

In the next section, we introduce the hydrodynamic equations for a 2D active chiral fluid with momentum decay and show a general solution in the presence of odd viscosity. In Sec. 6.3, we obtain the velocity field and stress tensor needed to investigate the flow profile induced by the domain motion. In Sec. 6.4, we calculate the hydrodynamic drag and lift forces acting on the liquid domain and examine their limiting expressions, by changing either the domain size or odd viscosity difference. A summary and further discussion are given in Sec. 6.5.

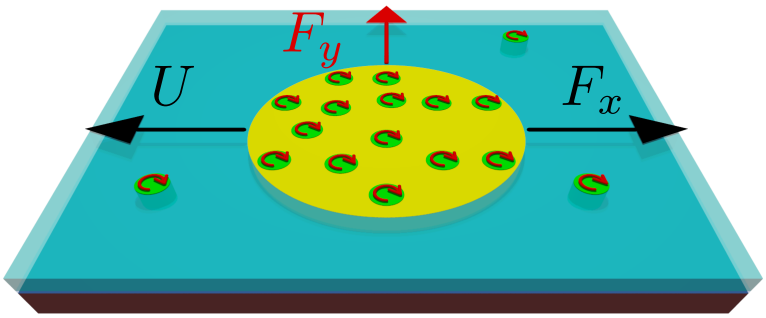

Figure 6.1: Schematic drawing of a fluid membrane (blue), which is flat, thin, incompressible, and supported by a rigid substrate (brown). The membrane has a 2D even (shear) viscosity η, odd viscosity η_o, and friction parameter λ. A circular liquid domain (yellow) of radius R has a 2D even (shear) viscosity η', odd viscosity η'_o, and friction parameter λ'. The odd viscosity reflects the presence of active rotor proteins (green) within the membrane that accumulate inside the liquid domain. Hence, in general, η_o can be different from η'_o. The liquid domain that moves laterally with a velocity $\mathbf{U} = (-U, 0)$ experiences a hydrodynamic force $\mathbf{F} = (F_x, F_y)$, where F_x and F_y are the drag and lateral lift forces, respectively.

6.2 Two-dimensional hydrodynamic equations with momentum decay

Biological membranes are formed as condensed lipid molecules with very small area compressibility [6.42] and they have been modeled as incompressible fluids [6.3–6.5]. For an incompressible 2D fluid in which momentum is strictly conserved, one cannot obtain a linear relation between the velocity and viscous force acting on an embedded object. This is the well-known Stokes' paradox [6.43, 6.44]. One way to circumvent this problem is to introduce a momentum decay mechanism in the 2D fluid [6.5, 6.6]. Such a momentum leakage occurs, for example, due to the friction between the supported membrane and the underlying rigid substrate [6.45], as shown in Fig. 6.1.

Let us denote any 2D vector by $\mathbf{r} = (x, y)$ and the 2D velocity by $\mathbf{v}(\mathbf{r})$. The steady-state linearized hydrodynamic equation for an active chiral fluid in the low Reynolds number limit can be written as [6.6, 6.36–6.41]

$$\nabla \cdot \boldsymbol{\sigma} - \lambda \mathbf{v} = 0. \tag{6.1}$$

Here, $\nabla = (\partial_x, \partial_y)$ stands for the 2D gradient operator, $\boldsymbol{\sigma}$ is the 2D fluid stress tensor as given below in Eq. (6.3), and λ is the friction parameter accounting for the momentum decay (see also Sec. 6.5 later for an estimate of λ). In addition, we assume that the 2D fluid is incompressible satisfying the condition:

$$\nabla \cdot \mathbf{v} = 0. \tag{6.2}$$

The Stokes' paradox can be eliminated in the presence of the momentum decay mechanism, and one can consistently solve the above hydrodynamic equations under appropriate boundary conditions.

For an incompressible 2D fluid with odd viscosity, the stress tensor is given by [6.17, 6.29, 6.46]

$$\sigma_{ij} = -p\delta_{ij} + \eta\left(\partial_j v_i + \partial_i v_j\right) + \frac{1}{2}\eta_{\rm o}\left(\partial_j v_i^* + \partial_i v_j^* + \partial_j^* v_i + \partial_i^* v_j\right), \tag{6.3}$$

where p is the 2D hydrostatic pressure with δ_{ij} being the Kronecker delta, η and $\eta_{\rm o}$ are the 2D even (shear) and odd viscosities, respectively, and $v_i^* = \epsilon_{ij} v_j$ and $\partial_i^* = \epsilon_{ij}\partial_j$ with ϵ_{ij} being the 2D Levi-Civita antisymmetric tensor ($\epsilon_{xx} = \epsilon_{yy} = 0$ and $\epsilon_{xy} = -\epsilon_{yx} = 1$). Hence, the vector $\mathbf{v}^*$ is obtained by rotating $\mathbf{v}$ by $\pi/2$ in a clockwise direction.

In our work, we do not specify the microscopic origin of odd viscosity, but it can be attributed, for example, to self-spinning objects representing active rotor proteins [6.17, 6.35]. Their continuous energy consumption and autonomous rotation break both time-reversal and parity symmetries, giving rise to odd viscosity in a 2D fluid with active rotor proteins. Although even viscosity η is always positive, odd viscosity $\eta_{\rm o}$ can be either positive or negative depending on the protein rotational direction. Substituting Eq. (6.3) into Eq. (6.1), we obtain the 2D hydrodynamic equation as

$$-\nabla p + \eta\nabla^2\mathbf{v} + \eta_{\rm o}\nabla^2\mathbf{v}^* - \lambda\mathbf{v} = 0, \tag{6.4}$$

together with the incompressibility condition of Eq. (6.2).

Within an infinitely extended 2D fluid characterized by η, $\eta_{\rm o}$, and λ, we

consider now a circular liquid domain of radius R having a 2D even (shear) viscosity η' and friction parameter λ' [6.6], as schematically presented in Fig. 6.1. Moreover, we assume that the fluid inside the domain has an odd viscosity $\eta'_{\rm o}$ that can be different from $\eta_{\rm o}$. The difference in the odd viscosities, $\eta_{\rm o} \neq \eta'_{\rm o}$, reflects the fact that active rotor proteins can accumulate and have a denser concentration in the liquid domain [6.19]. In general, both $\eta_{\rm o}$ and $\eta'_{\rm o}$ can be either positive or negative. Notice that the domain perimeter is assumed to be impermeable, so that the fluids inside and outside the domain do not mix with each other [6.6]. In addition, we assume that the deformation of the circular liquid domain can be neglected. This is justified when the line tension at the domain boundary is large enough compared to the viscous force [6.6, 6.44].

Throughout this work, we adopt the notation convention that quantities with prime refer to those inside the domain, while quantities without prime correspond to those outside the domain. Any 2D fluid velocity can be expressed as the sum of a gradient of a scalar potential ϕ and a curl of a vector potential $\mathbf{A} = (0, 0, A)$, where the z-component, A, corresponds to the stream function [6.6, 6.43]. Then, the 2D velocities outside/inside the domain are expressed as

$$\mathbf{v} = -\nabla\phi + \nabla \times \mathbf{A}, \qquad \mathbf{v}' = -\nabla\phi' + \nabla \times \mathbf{A}'. \tag{6.5}$$

Substituting Eq. (6.5) into Eq. (6.2), we obtain

$$\nabla^2\phi = 0, \qquad \nabla^2\phi' = 0, \tag{6.6}$$

which are the 2D Laplace equations.

One can also show that Eq. (6.4) is satisfied if the outside/inside pressures are given by

$$p = \eta\kappa^2\phi - \eta_{\rm o}\kappa^2 A, \qquad p' = \eta'\kappa'^2\phi' - \eta'_{\rm o}\kappa'^2 A', \tag{6.7}$$

while A and A' obey the 2D Helmholtz equations:

$$(\nabla^2 - \kappa^2)A = 0, \qquad (\nabla^2 - \kappa'^2)A' = 0. \tag{6.8}$$

Here, we have defined the inverse hydrodynamic screening lengths for the outside/inside fluids as $\kappa = (\lambda/\eta)^{1/2}$ and $\kappa' = (\lambda'/\eta')^{1/2}$. As seen in Eq. (6.7), the effect of odd viscosity can be taken into account through the modified pressure [6.17, 6.22, 6.30, 6.32], reflecting the fact that the odd viscosity does not contribute to the dissipation. In the next section, we shall derive the solutions to Eqs. (6.6) and (6.8) under the appropriate boundary conditions for a laterally moving liquid domain.

6.3 The velocity field of a moving liquid domain

6.3.1 Velocity and stress tensor

For convenience, we use the 2D polar coordinates (r, θ) defined by $x = r\cos\theta$ and $y = r\sin\theta$ with the origin fixed at the domain center. First, we consider the region outside the domain ($r > R$). Under the condition that the velocity and pressure vanish at large distances $r \to \infty$, we write down the solutions to Eqs. (6.6) and (6.8) as follows:

$$\phi = \frac{C_1}{r}\cos\theta + \frac{C_3}{r}\sin\theta, \tag{6.9}$$

$$A = C_2 K_1(\kappa r)\sin\theta + C_4 K_1(\kappa r)\cos\theta. \tag{6.10}$$

Here, $C_1, \cdots, C_4$ are unknown coefficients that will be determined from the boundary conditions, and $K_1(z)$ is the first-order modified Bessel function of the second kind [6.47].

From Eq. (6.5), the radial and tangential components of the velocity for $r > R$ are given by

$$v_r = \left[\frac{C_3}{r^2} - \frac{C_4}{r}K_1(\kappa r)\right]\sin\theta + \left[\frac{C_1}{r^2} + \frac{C_2}{r}K_1(\kappa r)\right]\cos\theta, \tag{6.11}$$

and

$$\begin{aligned} v_\theta = &\left[\frac{C_1}{r^2} + C_2\kappa K_0(\kappa r) + \frac{C_2}{r}K_1(\kappa r)\right]\sin\theta \\ &+ \left[-\frac{C_3}{r^2} + C_4\kappa K_0(\kappa r) + \frac{C_4}{r}K_1(\kappa r)\right]\cos\theta, \end{aligned} \tag{6.12}$$

respectively. Then, with the use of Eq. (6.3), the two components of the stress tensor can be obtained as

$$\begin{aligned}\sigma_{rr} = &-\left[\eta\left(\frac{4C_3}{r^3}+\frac{C_3\kappa^2}{r}-\frac{2C_4\kappa}{r}K_2(\kappa r)\right)\right.\\ &\left.+\eta_{\mathrm{o}}\left(\frac{4C_1}{r^3}+\frac{2C_2\kappa}{r}K_2(\kappa r)\right)\right]\sin\theta\\ &-\left[\eta\left(\frac{4C_1}{r^3}+\frac{C_1\kappa^2}{r}+\frac{2C_2\kappa}{r}K_2(\kappa r)\right)\right.\\ &\left.+\eta_{\mathrm{o}}\left(-\frac{4C_3}{r^3}+\frac{2C_4\kappa}{r}K_2(\kappa r)\right)\right]\cos\theta,\end{aligned} \tag{6.13}$$

and

$$\begin{aligned}\sigma_{r\theta} = &-\left[\eta\left(\frac{4C_1}{r^3}+C_2\kappa^2K_1(\kappa r)+\frac{2C_2\kappa}{r}K_2(\kappa r)\right)\right.\\ &\left.+\eta_{\mathrm{o}}\left(-\frac{4C_3}{r^3}+\frac{2C_4\kappa}{r}K_2(\kappa r)\right)\right]\sin\theta\\ &-\left[\eta\left(-\frac{4C_3}{r^3}+\frac{2C_4\kappa}{r}K_2(\kappa r)+C_4\kappa^2K_1(\kappa r)\right)\right.\\ &\left.+\eta_{\mathrm{o}}\left(-\frac{4C_1}{r^3}-\frac{2C_2\kappa}{r}K_2(\kappa r)\right)\right]\cos\theta.\end{aligned} \tag{6.14}$$

Inside the domain ($r < R$), on the other hand, the solutions to Eqs. (6.6) and (6.8) under the condition that they are finite at the origin ($r = 0$) are given by

$$\phi' = C_1' r\cos\theta + C_3' r\sin\theta, \tag{6.15}$$

$$A' = C_2' I_1(\kappa' r)\sin\theta + C_4' I_1(\kappa' r)\cos\theta. \tag{6.16}$$

Here, $C_1', \cdots, C_4'$ are the other unknown coefficients, and $I_1(z)$ is the first-order modified Bessel function of the first kind [6.47]. Although the general solutions to Eqs. (6.6) and (6.8) for ϕ, ϕ', A, and A' can be expressed as a series expansion in terms of r and θ, we have kept only the smallest number of terms satisfying the boundary conditions that will be discussed in the next subsection.

Then, the corresponding radial and tangential components of the velocity for $r < R$ become

$$v_r' = \left[-C_3' - \frac{C_4'}{r}I_1(\kappa' r)\right]\sin\theta - \left[C_1' - \frac{C_2'}{r}I_1(\kappa' r)\right]\cos\theta, \tag{6.17}$$

and

$$v'_\theta = \left[C'_1 - C'_2\kappa' I_0(\kappa' r) + \frac{C'_2}{r} I_1(\kappa' r)\right] \sin\theta + \left[-C'_3 - C'_4\kappa' I_0(\kappa' r) + \frac{C'_4}{r} I_1(\kappa' r)\right] \cos\theta, \tag{6.18}$$

respectively, and the two components of the stress tensor are given by

$$\sigma'_{rr} = -\left[\eta'\left(C'_3\kappa'^2 r + \frac{2C'_4\kappa'}{r} I_2(\kappa' r)\right) - \eta'_{\mathrm{o}}\frac{2C'_2\kappa'}{r} I_2(\kappa' r)\right] \sin\theta - \left[\eta'\left(C'_1\kappa'^2 r - \frac{2C'_2\kappa'}{r} I_2(\kappa' r)\right) - \eta'_{\mathrm{o}}\frac{2C'_4\kappa'}{r} I_2(\kappa' r)\right] \cos\theta, \tag{6.19}$$

and

$$\begin{aligned}\sigma'_{r\theta} = &-\left[\eta' C'_2\left(\kappa'^2 I_1(\kappa' r) - \frac{2\kappa'}{r} I_0(\kappa' r) + \frac{4}{r^2} I_1(\kappa' r)\right)\right. \\ &\left.+\eta'_{\mathrm{o}} C'_4\left(-\frac{2\kappa'}{r} I_0(\kappa' r) + \frac{4}{r^2} I_1(\kappa' r)\right)\right] \sin\theta \\ &-\left[\eta' C'_4\left(-\frac{2\kappa'}{r} I_0(\kappa' r) + \kappa'^2 I_1(\kappa' r) + \frac{4}{r^2} I_1(\kappa' r)\right)\right. \\ &\left.+\eta'_{\mathrm{o}} C'_2\left(\frac{2\kappa'}{r} I_0(\kappa' r) - \frac{4}{r^2} I_1(\kappa' r)\right)\right] \cos\theta.\end{aligned} \tag{6.20}$$

These velocities and stress tensor components for the inside and outside of the domain should be connected through the appropriate boundary conditions at the domain perimeter.

6.3.2 Boundary conditions at the liquid domain perimeter

As mentioned in the previous section, we consider the situation in which the liquid domain is laterally moving with a constant velocity $\mathbf{U} = (-U, 0)$. At $r = R$, the radial component of the fluid velocity should be equal to the domain velocity, while the tangential components of the fluid velocity and the stress tensor should be continuous [6.6, 6.44]. These conditions are written as

$$v_r = -U\cos\theta, \tag{6.21}$$

$$v'_r = -U\cos\theta, \tag{6.22}$$

$$v_\theta = v'_\theta, \tag{6.23}$$

$$\sigma_{r\theta} = \sigma'_{r\theta}. \tag{6.24}$$

Since we consider the circular liquid domain without deformation, there exists a finite line tension at the domain boundary, which dominates over a viscous force. The line tension gives rise to the 2D Laplace pressure at the domain perimeter, so that the normal stress condition inside and outside the domain is automatically satisfied [6.6, 6.44]. Hence, one does not need the condition, $\sigma_{rr} = \sigma'_{rr}$, in addition to Eqs. (6.21)-(6.24). Using the above boundary conditions, we can determine the eight coefficients $C_1, \cdots, C_4, C'_1, \cdots, C'_4$, whose explicit expressions are provided in Appendix 6.A. Since each of Eqs. (6.21)-(6.24) includes both $\sin\theta$ and $\cos\theta$ that are orthogonal to each other, one boundary condition provides two constraints. Therefore, the four boundary conditions lead to eight constraints that are sufficient to determine the eight unknown coefficients.

Notice that for the passive case without odd viscosity ($\eta_o = \eta'_o = 0$), the coefficients, C_3, C_4, C'_3, and C'_4, in Eqs. (6.9), (6.10), (6.15), and (6.16) are not required to satisfy the boundary conditions of Eqs. (6.21)-(6.24) [6.6]. This is because the odd viscosity contributes to the fluid stress perpendicular to the velocity gradient, as can be recognized in Eq. (6.3). More details on the passive case will be summarized in Appendix 6.B.

6.3.3 Flow profile

Having fixed all the coefficients in Eqs. (6.11), (6.12), (6.17), and (6.18), we next investigate the fluid flow induced by the lateral translational motion of the liquid domain. For simplicity, we assume $\eta = \eta'$ and $\lambda = \lambda'$ (or equivalently $\kappa = \kappa'$). In Fig. 6.2, the velocity field $\mathbf{v} - \mathbf{U}$ is plotted for (a) $\eta_o = \eta'_o = \eta$ (uniform odd viscosity), (b) $\eta_o = \eta$ and $\eta'_o = 0$ (vanishing odd viscosity inside the domain), and (c) $\eta_o = 0$ and $\eta'_o = \eta$ (vanishing odd viscosity outside the domain). In Fig. 6.3, we also plot $\mathbf{v} - \mathbf{U}$ for (a) $\eta_o = -\eta'_o = \eta$ and (b) $-\eta_o = \eta'_o = \eta$. In these plots, the domain size is fixed to $\kappa R = 0.1$ (circular black line).

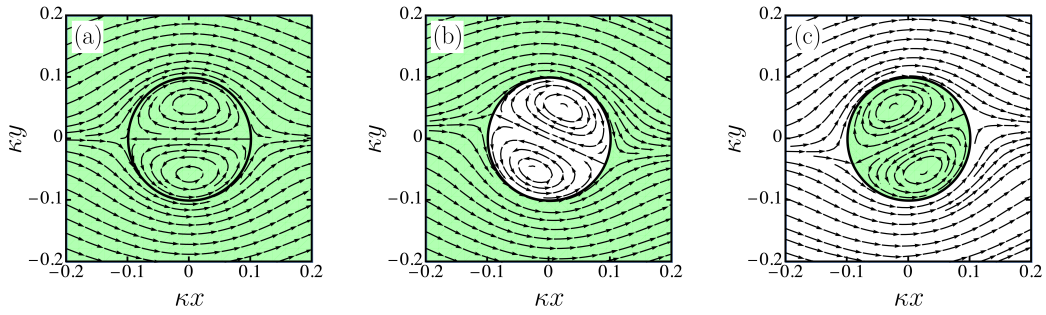

Figure 6.2: Streamlines (black arrows) of the fluid velocity, $\mathbf{v}-\mathbf{U}$, as a function of κx and κy when (a) $\eta_o = \eta'_o = \eta$ (uniform odd viscosity), (b) $\eta_o = \eta$ and $\eta'_o = 0$ (vanishing odd viscosity inside the domain), and (c) $\eta_o = 0$ and $\eta'_o = \eta$ (vanishing odd viscosity outside the domain) [see Eqs. (6.11), (6.12), (6.17), and (6.18)]. The green (light gray) region represents fluids with nonvanishing odd viscosity, while the white region represents vanishing odd viscosity. We also have chosen $\eta = \eta'$, $\lambda = \lambda'$, and $\epsilon = \kappa R = 0.1$. The domain moves laterally in the negative x-direction with a velocity $\mathbf{U} = (-U, 0)$. The circular black line represents the domain perimeter.

When the odd viscosity is spatially uniform ($\eta_o = \eta'_o$), as in Fig. 6.2(a), we see that the flow streamlines induced by the domain motion are symmetric with respect to the direction of motion. Such a symmetric profile is also seen for the passive case in which odd viscosity does not exist [6.6]. When $\eta_o \neq \eta'_o$, as in Figs. 6.2(b) and 6.2(c), the flow inside the domain is rotated with respect to the x-axis and the above symmetry breaks down. When $\eta_o/\eta'_o < 0$, as in Fig. 6.3, the flow inside the domain is more rotated compared to Figs. 6.2(b) and 6.2(c). This implies that the negative odd viscosity enhances the rotation in the flow field. Figure 6.2(c) is relevant to a lipid domain enriched with active rotor proteins, while Fig. 6.3 represents active proteins rotating oppositely inside and outside the domain. In the next section, we show that such a flow-field asymmetry leads to a lateral lift force acting on the domain.

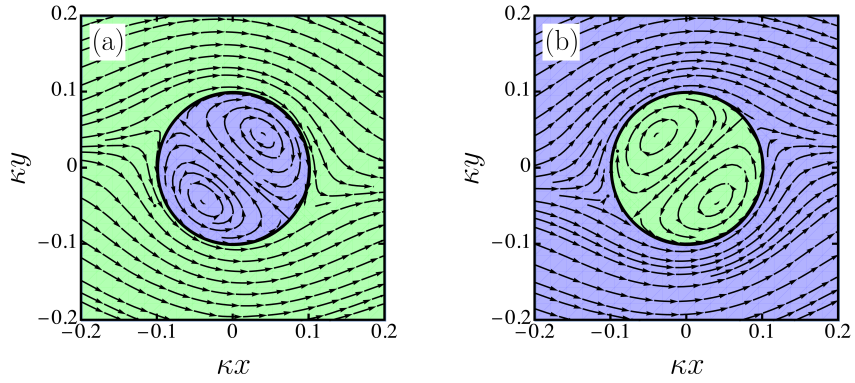

Figure 6.3: Streamlines (black arrows) of the fluid velocity, $\mathbf{v}-\mathbf{U}$, as a function of κx and κy when (a) $\eta_o = -\eta_o' = \eta$ and (b) $-\eta_o = \eta_o' = \eta$ [see the caption of Fig. 6.2 for the other conditions]. The green (light gray) region represents fluids with positive odd viscosity, while the blue (gray) region represents negative odd viscosity.

6.4 Hydrodynamic forces acting on a moving liquid domain

6.4.1 Drag and lift forces

For a liquid domain laterally moving with a velocity $\mathbf{U} = (-U, 0)$, the forces acting in the x- and y- directions, $\mathbf{F} = (F_x, F_y)$, are given by [6.6, 6.44]

$$F_x = R\int_0^{2\pi} d\theta\ (\sigma_{rr}\cos\theta - \sigma_{r\theta}\sin\theta) = \pi\eta(\kappa R)^2\left[-\frac{C_1}{R^2} + \frac{C_2 K_1(\kappa R)}{R}\right], \quad (6.25)$$

and

$$F_y = R\int_0^{2\pi} d\theta\ (\sigma_{rr}\sin\theta + \sigma_{r\theta}\cos\theta) = -\pi\eta(\kappa R)^2\left[\frac{C_3}{R^2} + \frac{C_4 K_1(\kappa R)}{R}\right], \quad (6.26)$$

respectively. In the above, the already determined coefficients $C_1, \cdots, C_4$ are substituted as given in Appendix 6.A. In addition, the full expressions of F_x and F_y are also given in Appendix 6.A.

For the sake of simplicity, we consider as before the case $\eta = \eta'$ and $\lambda = \lambda'$ (or equivalently $\kappa = \kappa'$) in Eqs. (6.25) and (6.26). We introduce a dimensionless domain radius, $\epsilon \equiv \kappa R$, and the arguments of the modified Bessel functions are omitted as in $K_n = K_n(\epsilon)$ and $I_n = I_n(\epsilon)$ to keep the notations more compact. Then, the expressions for the drag coefficient $\Gamma_\parallel = F_x/U$ and the lateral lift

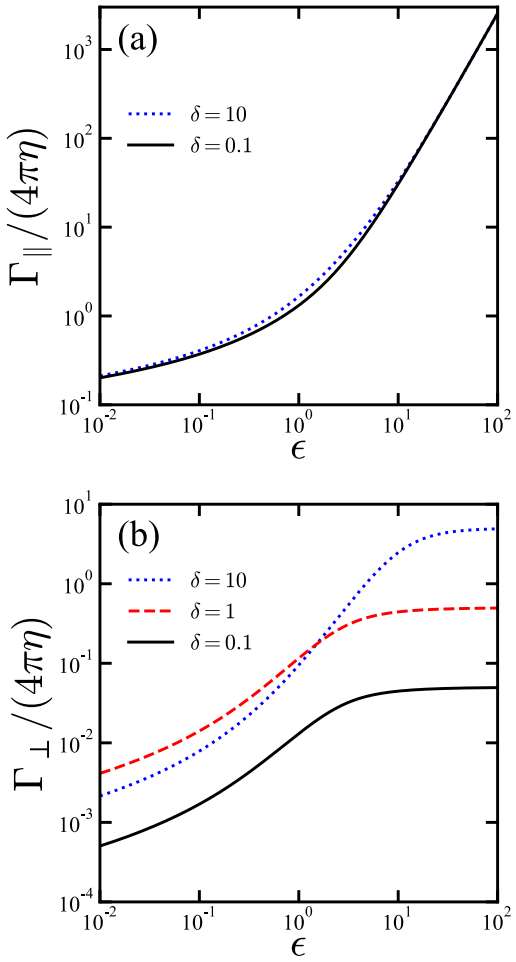

Figure 6.4: Plots of (a) the rescaled drag coefficient $\Gamma_\parallel$ and (b) the rescaled lift coefficient $\Gamma_\perp$ as a function of the rescaled domain radius $\epsilon = \kappa R$ for various values of the odd viscosity difference $\delta = (\eta_o - \eta_o')/\eta$. In (a), $\delta = 0.1$ and 10 are presented by the solid black and dotted blue lines, respectively. In (b), $\delta = 0.1, 1$, and 10 are presented by the solid black, dashed red, and dotted blue lines, respectively.

coefficient $\Gamma_\perp = F_y/U$ become

$$\frac{\Gamma_\parallel}{4\pi\eta} = \frac{\epsilon^2}{4} + \frac{\epsilon K_1}{K_0}\left[1 - \frac{\epsilon^2(K_0I_1 + K_1I_2)K_1I_2}{\epsilon^2(K_0I_1 + K_1I_2)^2 + 4(\delta K_0 I_2)^2}\right], \tag{6.27}$$

and

$$\frac{\Gamma_\perp}{4\pi\eta} = \frac{2\delta(\epsilon K_1 I_2)^2}{\epsilon^2(K_0I_1 + K_1I_2)^2 + 4(\delta K_0 I_2)^2}. \tag{6.28}$$

In the above, we have introduced the dimensionless difference in odd viscosity, δ, between the inside and outside of the domain

$$\delta = \frac{\eta_o - \eta_o'}{\eta}. \tag{6.29}$$

Equations (6.27) and (6.28) are the main results of our work.

Both the drag $\Gamma_\parallel$ and lift $\Gamma_\perp$ coefficients depend on the odd viscosity difference δ, and are even and odd functions of δ, respectively. As the domain moves in the negative x-direction, it exhibits a lateral lift motion along the $y > 0$ direction when $\delta > 0$, and also along the $y < 0$ direction for $\delta < 0$. Notice that the passive case without odd viscosity ($\eta_o = \eta'_o = 0$) is recovered by setting $\delta = 0$ [6.6] [see Eq. (6.B2) in Appendix 6.B for the specific expression]. For the uniform case with $\eta_o = \eta'_o \neq 0$ or $\delta = 0$, the drag coefficient $\Gamma_\parallel$ reduces to that of the passive case [6.6], whereas the lift coefficient $\Gamma_\perp$ vanishes. Since the lift force does not exist for the passive case [6.3–6.6], the finite lift force reflects not only the existence of odd viscosity, but also its difference ($\delta \neq 0$) between the inside and outside of the domain.

6.4.2 Dependence on the domain size ϵ

To discuss the dependence of the drag coefficient $\Gamma_\parallel$ and the lateral lift coefficient $\Gamma_\perp$ on the domain size ϵ for arbitrary δ, it is useful to obtain their asymptotic expressions in the small and large ϵ limits. The dependence on δ will be separately discussed in the next subsection. For $\epsilon \ll 1$, they become

$$\frac{\Gamma_\parallel}{4\pi\eta} \approx \frac{4[\ln(2/\epsilon) - \gamma + 1/4] + \delta^2[\ln(2/\epsilon) - \gamma]}{4[\ln(2/\epsilon) - \gamma + 1/4]^2 + \delta^2[\ln(2/\epsilon) - \gamma]^2}, \tag{6.30}$$

and

$$\frac{\Gamma_\perp}{4\pi\eta} \approx \frac{\delta}{8[\ln(2/\epsilon) - \gamma + 1/4]^2 + 2\delta^2[\ln(2/\epsilon) - \gamma]^2}, \tag{6.31}$$

where $\gamma \approx 0.5772$ is Euler's constant. Hence, both $\Gamma_\parallel$ and $\Gamma_\perp$ depend only logarithmically on the rescaled domain size ϵ. In the opposite limit of $\epsilon \gg 1$, the asymptotic expressions become

$$\frac{\Gamma_\parallel}{4\pi\eta} \approx \frac{\epsilon^2}{4}, \tag{6.32}$$

and

$$\frac{\Gamma_\perp}{4\pi\eta} \approx \frac{\delta}{2}. \tag{6.33}$$

Here, $\Gamma_\parallel$ is proportional to ϵ^2 and independent of δ, while $\Gamma_\perp$ is independent of ϵ and is determined solely by δ.

In Fig. 6.4, we plot $\Gamma_\parallel$ and $\Gamma_\perp$ of Eqs. (6.27) and (6.28), respectively, as a function of the rescaled domain size $\epsilon = \kappa R$ for various values of δ. These plots are consistent with the above asymptotic behaviors of $\Gamma_\parallel$ and $\Gamma_\perp$. We also see that the crossover between the two limiting cases is reasonably given for $\epsilon \approx 1$. In Fig. 6.4(a), $\Gamma_\parallel$ is slightly larger when δ is increased, whereas it hardly depends on δ for larger ϵ. In Fig. 6.4(b), we see that the lift coefficient $\Gamma_\perp$ increases logarithmically for $\epsilon \ll 1$, while it becomes independent of the domain size for $\epsilon \gg 1$.

Let us discuss the physical interpretation of the above limiting behaviors of $\Gamma_\parallel$ and $\Gamma_\perp$ [6.41, 6.48]. The momentum in the 2D fluid is conserved over distances smaller than the hydrodynamic screening length, $r \ll \kappa^{-1}$, and the stress decays as $1/r$ due to the momentum conservation. Since the stress scales as $\sigma \sim \eta v/r$, we have $v \sim 1/\eta$ [6.48]. This explains the weak (logarithmic) size dependence of $\Gamma_\parallel$ and $\Gamma_\perp$ in Eqs. (6.30) and (6.31), respectively. For larger length scales, $r \gg \kappa^{-1}$, the momentum is not conserved, and the only contribution to the velocity is from mass conservation. In a 2D fluid, a mass monopole (source) will create a velocity that decays as $1/r$ [6.48]. Hence, the velocity due to a mass dipole (source and sink) decays as $1/r^2$, explaining the scaling $\Gamma_\parallel \sim \epsilon^2$ in Eq. (6.32). Such a strong size dependence is not observed for $\Gamma_\perp$ in Eq. (6.33) as the friction parameter λ does not cause any momentum leakage along the rotated velocity $\mathbf{v}^*$.

6.4.3 Dependence on the odd viscosity difference δ

Next, we show how $\Gamma_\parallel$ and $\Gamma_\perp$ depend on the odd viscosity difference δ for arbitrary ϵ. The asymptotic expressions of Eqs. (6.27) and (6.28) for $|\delta| \ll 1$ are

$$\frac{\Gamma_\parallel}{4\pi\eta} \approx \frac{\epsilon^2}{4} + \frac{\epsilon K_1 I_1}{K_0 I_1 + K_1 I_2}, \tag{6.34}$$

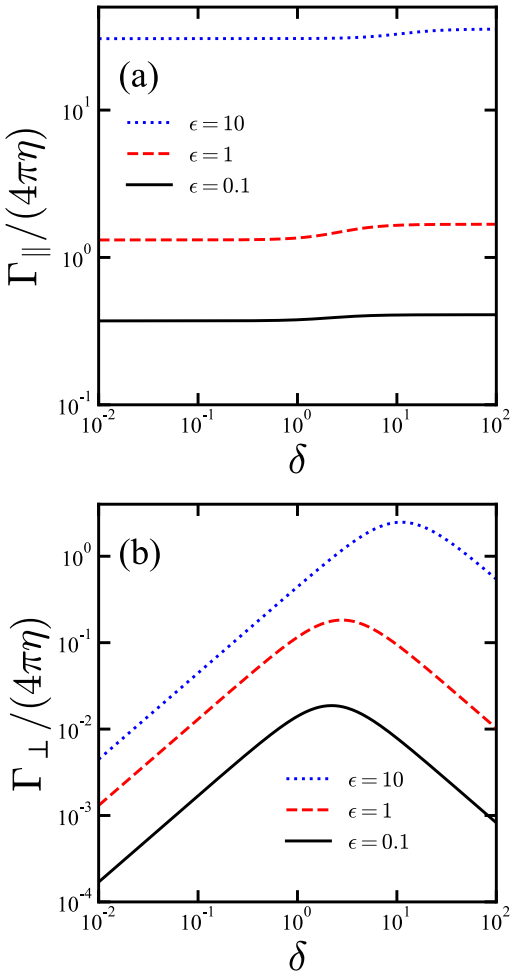

Figure 6.5: Plots of (a) the rescaled drag coefficient $\Gamma_{\parallel}$ and (b) the rescaled lift coefficient $\Gamma_{\perp}$ as a function of the odd viscosity difference $\delta = (\eta_o - \eta_o')/\eta$ for various values of the rescaled domain radius $\epsilon = \kappa R$. In both plots, $\epsilon = 0.1, 1,$ and 10 are presented by the solid black, dashed red, and dotted blue lines, respectively.

and

$$\frac{\Gamma_{\perp}}{4\pi\eta} \approx 2\delta \left(\frac{K_1 I_2}{K_0 I_1 + K_1 I_2} \right)^2, \tag{6.35}$$

showing that $\Gamma_{\parallel}$ is independent of δ and $\Gamma_{\perp}$ is proportional to only δ. As mentioned before, Eq. (6.34) coincides with the passive drag coefficient of a liquid domain [6.6] [see Eq. (6.B2)].

When $|\delta| \gg 1$, on the other hand, we obtain

$$\frac{\Gamma_{\parallel}}{4\pi\eta} \approx \frac{\epsilon^2}{4} + \frac{\epsilon K_1}{K_0}, \tag{6.36}$$

and

$$\frac{\Gamma_\perp}{4\pi\eta} \approx \frac{1}{2\delta}\left(\frac{\epsilon K_1}{K_0}\right)^2. \tag{6.37}$$

Here, $\Gamma_\parallel$ is also independent of δ, while $\Gamma_\perp$ decays as $1/\delta$. Interestingly, Eq. (6.36) coincides with the result by Evans and Sackmann for the drag coefficient of a rigid disk in a passive supported membrane [6.5].

In Fig. 6.5, we plot $\Gamma_\parallel$ and $\Gamma_\perp$ in Eqs. (6.27) and (6.28), respectively, as a function of the odd viscosity difference δ for various values of ϵ. As can be seen in Fig. 6.5(a), $\Gamma_\parallel$ is almost independent of δ. However, Fig. 6.5(b) shows that $\Gamma_\perp$ changes nonmonotonically, in accordance with Eqs. (6.35) and (6.37). The maximum of $\Gamma_\perp$ shifts to higher values of δ as ϵ is increased.

6.5 Discussion and conclusion

In this paper, we have investigated the hydrodynamic forces acting on a 2D liquid domain that moves laterally in a supported membrane characterized by an odd viscosity. We combined the momentum decay mechanism of a 2D fluid [6.6, 6.36–6.41] with the concept of odd viscosity [6.22]. Since active rotor proteins can accumulate inside the lipid domain, we have focused on the difference in odd viscosity between the inside and outside of the domain. Taking into account the momentum decay mechanism of the incompressible 2D fluid, we have analytically obtained the fluid flow induced by a lateral domain motion. In the presence of odd viscosity difference, the flow field due to the domain motion is rotated with respect to its direction, as shown in Fig. 6.2.

Using the obtained flow field, we have calculated the hydrodynamic forces acting on the moving domain. The resulting drag and lift coefficients are given in Eqs. (6.27) and (6.28). In contrast to the passive case that does not have an odd viscosity [6.3–6.6], the existence of a lateral lift force is predicted when the odd viscosity difference is present. We have discussed in detail the dependence of the drag coefficient $\Gamma_\parallel$ and lift coefficient $\Gamma_\perp$ on the domain size ϵ and the odd viscosity difference δ. The appearance of a finite lift force indicates not only the

existence of the odd viscosity, but also its asymmetry between the inside and outside of the domain.

In addition to the asymmetry condition, $\eta_o \neq \eta'_o$, discussed in this work, we briefly summarize other conditions for finite lift force in incompressible 2D fluids with odd viscosity. For a laterally moving rigid disk with a nonslip boundary, no lift was observed [6.30], while it was reported to exist within the Oseen approximation [6.49]. For a bubble with a no-stress boundary condition, lift and torque forces, respectively, emerge for a moving and expanding bubble [6.30–6.32]. The forces of rigid disks and bubbles are discussed in more detail below.

Since the governing hydrodynamic equations (6.2) and (6.4) are linear in $\mathbf{v}$, the force $\mathbf{F}$ acting on a circular domain can be generally written as

$$\mathbf{F} = -\boldsymbol{\Gamma} \cdot \mathbf{U}, \tag{6.38}$$

where $\boldsymbol{\Gamma}$ is the domain friction tensor and $\mathbf{U}$ is the domain velocity in an arbitrary direction. Following a similar calculation as before, we find that $\boldsymbol{\Gamma}$ can be expressed as

$$\Gamma_{ij} = \Gamma_{\parallel}\delta_{ij} - \Gamma_{\perp}\epsilon_{ij}, \tag{6.39}$$

where the coefficients $\Gamma_{\parallel}$ and $\Gamma_{\perp}$ are, respectively, given by Eqs. (6.27) and (6.28) for the simple case ($\eta = \eta'$ and $\lambda = \lambda'$), or Eqs. (6.A4) and (6.A5) for the general case ($\eta \neq \eta'$ and $\lambda \neq \lambda'$). When $\delta = 0$, the lift coefficient $\Gamma_{\perp}$ vanishes and the friction tensor satisfies the reciprocal relation $\Gamma_{ij} = \Gamma_{ji}$. According to the Lorentz reciprocal theorem [6.50–6.52], such a reciprocal property is guaranteed for an arbitrarily shaped object in a passive fluid. When $\delta \neq 0$, the hydrodynamic response becomes nonreciprocal, i.e., $\Gamma_{ij} \neq \Gamma_{ji}$, leading to a dissipationless lift force. This is one of the distinctive features of an active chiral fluid characterized by odd viscosity [6.29].

In Ref. [6.30], it was shown that a lift force does not exist for an object in an incompressible 2D fluid with odd viscosity when nonslip boundary conditions are imposed. This is the case when the boundary conditions include only the

continuity of velocity as we have used in Eqs. (6.21)-(6.23). However, in the case of a liquid domain, we also have employed the boundary condition for the stress continuity as in Eq. (6.24). Then, the obtained lift force depends on the odd viscosity difference δ.

Some numerical estimates of the physical quantities in the model can be given [6.6]. For a fluid membrane supported by a rigid substrate, the friction parameter in Eq. (6.1) can be identified as $\lambda = \eta_{\rm w}/h$, where $\eta_{\rm w}$ is the 3D viscosity of the surrounding water and h is the thickness of a thin layer of lubricating water between the membrane and the substrate [6.5]. Then, the hydrodynamic screening length is given by $\kappa^{-1} = (\eta h/\eta_{\rm w})^{1/2}$. For typical values such as $h \approx 10^{-8}\,{\rm m}$, $\eta_{\rm w} \approx 10^{-3}\,{\rm Pa{\cdot}s}$, and $\eta \approx 10^{-9}\,{\rm Pa{\cdot}s{\cdot}m}$, we find $\kappa^{-1} \approx 10^{-7}\,{\rm m}$. Since the size of a lipid domain (raft) is roughly 10 nm–100 nm [6.19, 6.53], the dimensionless domain size $\epsilon = \kappa R$ is estimated to be $0.1 \leq \epsilon \leq 1$. Hence, the limiting expressions derived in Eqs. (6.30) and (6.31) for $\epsilon \ll 1$ are the appropriate ones for the drag and lift coefficients.

Next we discuss the value of the domain odd viscosity $\eta_{\rm o}'$ for typical physiological conditions. Consider the situation where disk-like active rotor proteins concentrate only inside the domain, i.e., $\eta_{\rm o} = 0$ and $\eta_{\rm o}' \neq 0$, while $\eta = \eta'$ as was assumed above. In microscopic approaches [6.17, 6.35], it was shown that odd viscosity is related to the angular-momentum density of rotor proteins through the relation, $\eta_{\rm o}' \simeq IT/\zeta$. Here, I and T are the moment-of-inertia and torque densities, respectively, and ζ is the rotational friction coefficient of a rotor.

For an active rotor protein of radius a and mass m driven by the torque τ, one can estimate [6.5, 6.34] $I = m\rho/\pi$, $T = \rho\tau/(\pi a^2)$, and $\zeta = \eta'\rho/\pi$, which lead to $\eta_{\rm o}' \simeq m\rho\tau/(\pi\eta' a^2)$. Here, $\rho = N\pi a^2/(\pi R^2)$ is the area fraction of N rotors inside the domain. Using typical values such as $m \approx 10^{-21}\,{\rm kg}$, $\rho \approx 0.3$, $\tau \approx 10^{-19}\,{\rm N{\cdot}m}$, and $a \approx 10^{-8}\,{\rm m}$ [6.1, 6.11, 6.15, 6.18] and assuming that the domain is filled with water ($\eta' \approx 10^{-12}\,{\rm Pa{\cdot}s{\cdot}m}$), we obtain $\eta_{\rm o}' \approx 10^{-13}\,{\rm Pa{\cdot}s{\cdot}m}$. Then, the odd viscosity ratio is given by $\delta = -\eta_{\rm o}'/\eta \approx -0.1$ and the limiting

expressions of Eqs. (6.34) and (6.35) for $|\delta| \ll 1$ can be used here for the drag and lift coefficients.

As a special case of a liquid domain, we discuss the hydrodynamic forces acting on a circular bubble of radius R that moves laterally in an incompressible 2D fluid with odd viscosity. In Appendix 6.C, we obtain the drag and lift coefficients by requiring that $\eta' = 0$ and $\eta'_{\rm o} = 0$, while η and $\eta_{\rm o}$ for the outside of the domain are kept finite. For a moving bubble, $\Gamma_\parallel$ and $\Gamma_\perp$ depend on the viscosity ratio $\mu = \eta_{\rm o}/\eta$. The asymptotic behaviors of the drag and lift coefficients are similar to those of a liquid domain. In the previous studies, it was reported that the effect of odd viscosity can be seen as a torque acting on an expanding bubble [6.30–6.32]. Our results show that the forces due to odd viscosity exist even for an undeformable object.

In the opposite limit $\eta' \to \infty$, the general drag and lift forces in Eqs. (6.A4) and (6.A5) reduce to those acting on a rigid disk. In this case, the drag coefficient becomes identical to that for a passive supported membrane [6.5] as in Eq. (6.36), while the lift coefficient vanishes. This is reasonable because the boundary conditions at the disk perimeter can be constructed without the stress continuity of Eq. (6.24) [6.6] and the odd viscosity does not enter in the forces on the disk [6.30, 6.31].

When the odd viscosity is spatially uniform ($\delta = 0$), it does not affect either the velocity field or the forces acting on the domain. This implies that the effect of odd viscosity can be seen in biomembranes when active rotor proteins concentrate locally inside specific domains and the odd viscosity becomes nonuniform. It would be interesting to investigate experimentally the diffusion of such active domains by using microrheology techniques [6.54]. When a membrane is in thermal equilibrium, the drag coefficient can be connected to the diffusion coefficient of the liquid domain through Einstein's relation. In active fluids, however, such a relation no longer holds and one needs to generalize the fluctuation-dissipation theorem in the presence of active protein molecules [6.11, 6.55–6.60]. Through

molecular-dynamics simulations of a particle diffusing in an active chiral fluid, the applicability of Einstein's relation was evaluated [6.59]. For the Langevin equation with odd viscosity, the asymmetric diffusion tensor is obtained, and is characterized by the ratio of the drag to lift coefficients [6.60]. A more detailed discussion of such diffusion phenomena in the active chiral fluid will be given elsewhere [6.60].

Appendix 6.A General drag and lift forces

The coefficients $C_1, \cdots, C_4, C_1', \cdots, C_4'$ are determined by the boundary conditions in Eqs. (6.21)-(6.24) and given by

$$\begin{aligned}
C_1 &= -RU\left(\kappa' RI_0 - 2I_1\right)\left[\eta\kappa^2 R^2 K_1 + 2(\eta-\eta')\left(\kappa R K_0 + 2K_1\right)\right] D_1/(\kappa D) \\
&\quad - \eta'\kappa'^2 R^3 U\left(\kappa R K_0 + 2K_1\right) I_1 D_1/(\kappa D) - R^2 U K_2 D_2/D, \\
C_2 &= 2U\left[2(\eta-\eta')(\kappa' RI_0 - 2I_1) + \eta'\kappa'^2 R^2 I_1\right] D_1/(\kappa D) + 2UD_2/(\kappa D), \\
C_3 &= -4\eta(\eta_\mathrm{o} - \eta_\mathrm{o}')\kappa'^2 R^4 U K_1^2 I_2^2/D, \\
C_4 &= -4\eta(\eta_\mathrm{o} - \eta_\mathrm{o}')\kappa'^2 R^3 U K_1 I_2^2/D,
\end{aligned} \tag{6.A1}$$

and

$$\begin{aligned}
C_1' &= U\Big[K_0 D_2 + \eta^2\kappa^2\kappa'^2 R^4 K_1^2 I_0 I_2 \\
&\quad + 2\eta\kappa R K_0 K_1(\kappa' RI_0 - I_1)\left\{2(\eta-\eta')(\kappa' RI_0 - 2I_1) + \eta'\kappa'^2 R^2 I_1\right\} \\
&\quad + \left\{2(\eta-\eta')(\kappa' RI_0 - 2I_1) + \eta'\kappa'^2 R^2 I_1\right\}^2 K_0^2\Big]/D, \\
C_2' &= 2\eta\kappa R^2 U K_1 D_1/D, \\
C_3' &= -4\eta(\eta_\mathrm{o} - \eta_\mathrm{o}')\kappa\kappa' R^2 U K_0 K_1 I_1 I_2/D, \\
C_4' &= 4\eta(\eta_\mathrm{o} - \eta_\mathrm{o}')\kappa\kappa' R^3 U K_0 K_1 I_2/D,
\end{aligned} \tag{6.A2}$$

where

$$\begin{aligned}
D &= D_1^2 + K_0 D_2, \\
D_1 &= 2(\eta-\eta')(\kappa' RI_0 - 2I_1)K_0 + \kappa' R^2\left(\eta'\kappa' K_0 I_1 + \eta\kappa K_1 I_2\right), \\
D_2 &= 4(\eta_\mathrm{o} - \eta_\mathrm{o}')^2\kappa'^2 R^2 K_0 I_2^2.
\end{aligned} \tag{6.A3}$$

In the above, we have used the notations $K_n = K_n(\kappa R) = K_n(\epsilon)$ and $I_n = I_n(\kappa' R) = I_n(\epsilon')$. In the main text, we consider the case $\eta = \eta'$ and $\lambda = \lambda'$ (or equivalently $\kappa = \kappa'$), and the function $I_n(\kappa R) = I_n(\epsilon)$ is written as I_n.

Substituting C_1 and C_2 into Eq. (6.25) and C_3 and C_4 into Eq. (6.26), we obtain the general drag and lift forces as

$$\begin{aligned}\frac{F_x}{4\pi\eta} &= U\epsilon(\delta\epsilon' I_2)^2(\epsilon K_0 + 4K_1)K_0/M \\ &\quad + (U\epsilon/4)\left[2(\nu-1)K_0(2I_1 - \epsilon' I_0) + \epsilon'\left(\epsilon K_1 I_2 + \nu\epsilon' K_0 I_1\right)\right] \\ &\quad \times \left[\left\{\nu\epsilon'^2 I_1 + 2(\nu-1)(2I_1 - \epsilon' I_0)\right\}(\epsilon K_0 + 4K_1) - \epsilon^2 K_1(2I_1 - \epsilon' I_0)\right]/M,\end{aligned} \tag{6.A4}$$

and

$$\frac{F_y}{4\pi\eta} = 2U\delta(\epsilon\epsilon' K_1 I_2)^2/M, \tag{6.A5}$$

where $\nu = \eta'/\eta$, $\delta = (\eta_o - \eta_o')/\eta$, and

$$M = \left[2(\nu-1)K_0(2I_1 - \epsilon' I_0) + \epsilon'\left(\epsilon K_1 I_2 + \nu\epsilon' K_0 I_1\right)\right]^2 + 4(\delta\epsilon' K_0 I_2)^2. \tag{6.A6}$$

When $\eta = \eta'$ and $\lambda = \lambda'$ (or equivalently $\nu = 1$ and $\epsilon = \epsilon'$), we obtain Eqs. (6.27) and (6.28).

Appendix 6.B Drag and lift coefficients for a 2D liquid domain when $\eta_o = \eta_o' = 0$

We summarize the passive case without odd viscosity, which was studied in Ref. [6.6]. When $\eta_o = \eta_o' = 0$ (while $\nu \neq 1$ or $\eta \neq \eta'$), the coefficients, C_3, C_4, C_3', and C_4', become zero, as can be seen in Eqs. (6.A1)-(6.A3). Then, the scalar and vector potentials in Eqs. (6.9), (6.10), (6.15), and (6.16) reduce to

$$\phi = \frac{C_1}{r}\cos\theta, \qquad A = C_2 K_1(\kappa r)\sin\theta, \qquad \phi' = C_1' r\cos\theta, \qquad A' = C_2' I_1(\kappa' r)\sin\theta, \tag{6.B1}$$

respectively. Calculating the corresponding velocity fields and stress tensors and applying the boundary conditions of Eqs. (6.21)-(6.24), one can obtain the drag and lift coefficients as

$$\frac{\Gamma_{\parallel}}{4\pi\eta} = \frac{\epsilon^2}{4} + \frac{\epsilon K_1 \left[\nu\left(4+\epsilon'^2\right) I_1 - 2\nu\epsilon' I_0 + 2\left(\epsilon' I_0 - 2I_1\right)\right]}{\nu K_0 \left[\left(4+\epsilon'^2\right) I_1 - 2\epsilon' I_0\right] + \left(2K_0 + \epsilon K_1\right)\left(\epsilon' I_0 - 2I_1\right)}, \tag{6.B2}$$

and $\Gamma_{\perp} = 0$, respectively. When $\nu = 1$ or $\eta = \eta'$, Eq. (6.B2) coincides with the drag coefficient derived in Eq. (6.34) for $|\delta| \ll 1$.

Appendix 6.C Drag and lift coefficients for a 2D bubble

We derive the hydrodynamic forces acting on a moving bubble of radius R. By setting $\eta' = 0$ and $\eta'_{\rm o} = 0$ in Eqs. (6.A4) and (6.A5), we obtain the drag and lift coefficients as

$$\begin{aligned} \frac{\Gamma_{\parallel}}{4\pi\eta} &= \frac{\epsilon^2}{4} + \frac{2\epsilon K_1}{2K_0 + \epsilon K_1}\left[1 + \frac{2\mu^2 \epsilon K_0 K_1}{(2K_0+\epsilon K_1)^2 + 4(\mu K_0)^2}\right], \\ \frac{\Gamma_{\perp}}{4\pi\eta} &= \frac{2\mu(\epsilon K_1)^2}{(2K_0+\epsilon K_1)^2 + 4(\mu K_0)^2}, \end{aligned} \tag{6.C1}$$

with $\mu = \eta_{\rm o}/\eta$. In the limits of $\epsilon \ll 1$ and $\epsilon \gg 1$, we obtain respectively for arbitrary μ

$$\begin{aligned} \frac{\Gamma_{\parallel}}{4\pi\eta} &\approx \frac{\ln(2/\epsilon) - \gamma + 1/2 + \mu^2[\ln(2/\epsilon) - \gamma]}{[\ln(2/\epsilon) - \gamma + 1/2]^2 + \mu^2[\ln(2/\epsilon) - \gamma]^2}, \\ \frac{\Gamma_{\perp}}{4\pi\eta} &\approx \frac{\mu}{2[\ln(2/\epsilon) - \gamma + 1/2]^2 + 2\mu^2[\ln(2/\epsilon) - \gamma]^2}, \end{aligned} \tag{6.C2}$$

and

$$\begin{aligned} \frac{\Gamma_{\parallel}}{4\pi\eta} &\approx \frac{\epsilon^2}{4}, \\ \frac{\Gamma_{\perp}}{4\pi\eta} &\approx 2\mu. \end{aligned} \tag{6.C3}$$

References

[6.1] B. Alberts, A. Johnson, J. Lewis, M. Raff, K. Roberts, and P. Walter, *Molecular Biology of the Cell* (Garland Science, New York, 2008).

[6.2] S. J. Singer and G. L. Nicolson, Science **175**, 720 (1972).

[6.3] P. G. Saffman and M. Delbrück, Proc. Natl. Acad. Sci. (USA) **72**, 3111 (1975).

[6.4] P. G. Saffman, J. Fluid Mech. **73**, 593 (1976).

[6.5] E. Evans and E. Sackmann, J. Fluid Mech. **194**, 553 (1988).

[6.6] S. Ramachandran, S. Komura, M. Imai, and K. Seki, Eur. Phys. J. E **31**, 303 (2010).

[6.7] S. Ramadurai, A. Holt, V. Krasnikov, G. van den Bogaart, J. A. Killian, and B. Poolman, J. Am. Chem. Soc. **131**, 12650 (2009).

[6.8] A. S. Mikhailov and R. Kapral, Proc. Natl. Acad. Sci. (USA) **112**, E3639 (2015).

[6.9] R. Kapral and A. S. Mikhailov, Physica D **318**, 100 (2016).

[6.10] Y. Koyano, H. Kitahata, and A. S. Mikhailov, Phys. Rev. E **94**, 022416 (2016).

[6.11] Y. Hosaka, K. Yasuda, R. Okamoto, and S. Komura, Phys. Rev. E **95**, 052407 (2017).

[6.12] J.-B. Manneville, P. Bassereau, D. Levy, and J. Prost, Phys. Rev. Lett. **82**, 4356 (1999).

[6.13] J.-B. Manneville, P. Bassereau, S. Ramaswamy, and J. Prost, Phys. Rev. E **64**, 021908 (2001).

[6.14] G. Gompper, R. G. Winkler, T. Speck, A. Solon, C. Nardini, F. Peruani, H. Löwen, R. Golestanian, U. B. Kaupp, L. Alvarez, *et al.*, J. Phys.: Condens. Matter **32**, 193001 (2020).

[6.15] P. Lenz, J.-F. Joanny, F. Jülicher, and J. Prost, Eur. Phys. J. E **13**, 379 (2004).

[6.16] S. Fürthauer, M. Strempel, S. W. Grill, and F. Jülicher, Eur. Phys. J. E **35**, 1 (2012).

[6.17] D. Banerjee, A. Souslov, A. G. Abanov, and V. Vitelli, Nat. Commun. **8**, 1573 (2017).

[6.18] N. Oppenheimer, D. B. Stein, and M. J. Shelley, Phys. Rev. Lett. **123**, 148101 (2019).

[6.19] K. Simons and E. Ikonen, Nature **387**, 569 (1997).

[6.20] S. L. Veatch and S. L. Keller, Biophys. Acta **1746**, 172 (2005).

[6.21] S. Komura and D. Andelman, Adv. Colloid Interface Sci. **208**, 34 (2014).

[6.22] J. E. Avron, J. Stat. Phys. **92**, 543 (1998).

[6.23] A. Abanov, T. Can, and S. Ganeshan, SciPost Phys. **5**, 010 (2018).

[6.24] A. Souslov, K. Dasbiswas, M. Fruchart, S. Vaikuntanathan, and V. Vitelli, Phys. Rev. Lett. **122**, 128001 (2019).

[6.25] C. Tauber, P. Delplace, and A. Venaille, J. Fluid Mech. **868**, R2 (2019).

[6.26] C. Tauber, P. Delplace, and A. Venaille, Phys. Rev. Res. **2**, 013147 (2020).

[6.27] G. Bao and Y. Jian, Phys. Rev. E **103**, 013104 (2021).

[6.28] S. Mukhopadhyay and A. Mukhopadhyay, Eur. J. Mech. B Fluids **89**, 161 (2021).

[6.29] Y. Hosaka, S. Komura, and D. Andelman, Phys. Rev. E **103**, 042610 (2021).

[6.30] S. Ganeshan and A. G. Abanov, Phys. Rev. Fluids **2**, 094101 (2017).

[6.31] A. Souslov, A. Gromov, and V. Vitelli, Phys. Rev. E **101**, 052606 (2020).

[6.32] M. F. Lapa and T. L. Hughes, Phys. Rev. E **89**, 043019 (2014).

[6.33] V. Soni, E. S. Bililign, S. Magkiriadou, S. Sacanna, D. Bartolo, M. J. Shelley, and W. T. M. Irvine, Nat. Phys. **15**, 1188 (2019).

[6.34] Q. Yang, H. Zhu, P. Liu, R. Liu, Q. Shi, K. Chen, N. Zheng, F. Ye, and M. Yang, Phys. Rev. Lett. **126**, 198001 (2021).

[6.35] T. Markovich and T. C. Lubensky, Phys. Rev. Lett. **127**, 048001 (2021).

[6.36] K. Seki and S. Komura, Phys. Rev. E **47**, 2377 (1993).

[6.37] S. Komura and K. Seki, J. Phys. II France **5**, 5 (1995).

[6.38] K. Seki, S. Komura, and M. Imai, J. Phys.: Condens. Matter **19**, 072101 (2007).

[6.39] S. Ramachandran, S. Komura, and G. Gompper, Europhys. Lett. **89**, 56001 (2010).

[6.40] S. Ramachandran, S. Komura, K. Seki, and M. Imai, Soft Matter **7**, 1524 (2011).

[6.41] S. Ramachandran, S. Komura, K. Seki, and G. Gompper, Eur. Phys. J. E **34**, 1 (2011).

[6.42] E. Evans and D. Needham, J. Phys. Chem. **91**, 4219 (1987).

[6.43] H. Lamb, *Hydrodynamics* (Cambridge University Press, New York, 1975).

[6.44] L. D. Landau and E. M. Lifshitz, *Fluid Mechanics* (Pergamon Press, Oxford, 1987).

[6.45] M. Tanaka and E. Sackmann, Nature **437**, 656 (2005).

[6.46] J. M. Epstein and K. K. Mandadapu, Phys. Rev. E **101**, 052614 (2020).

[6.47] M. Abramowitz and I. A. Stegun, *Handbook of Mathematical Functions* (Dover, New York, 1972).

[6.48] H. Diamant, J. Phys. Soc. Jpn **78**, 041002 (2009).

[6.49] E. Kogan, Phys. Rev. E **94**, 043111 (2016).

[6.50] C. Pozrikidis, *Boundary Integral and Singularity Methods for Linearized Viscous Flow* (Cambridge University Press, New York, 1992).

[6.51] J. Happel and H. Brenner, *Low Reynolds Number Hydrodynamics: With Special Applications to Particulate Media* (Kluwer Academic Publishers, Netherlands, 1991).

[6.52] H. Masoud and H. A. Stone, J. Fluid Mech. **879**, 1 (2019).

[6.53] L. J. Pike, J. Lipid Res. **50**, S323 (2009).

[6.54] E. M. Furst and T. M. Squires, *Microrheology* (Oxford University Press, 2017).

[6.55] K. Yasuda, R. Okamoto, and S. Komura, Phys. Rev. E **95**, 032417 (2017).

[6.56] K. Yasuda, R. Okamoto, S. Komura, and A. S. Mikhailov, Europhys. Lett. **117**, 38001 (2017).

[6.57] Y. Hosaka, S. Komura, and D. Andelman, Phys. Rev. E **101**, 012610 (2020).

[6.58] Y. Hosaka, S. Komura, and A. S. Mikhailov, Soft Matter **16**, 10734 (2020).

[6.59] C. Hargus, J. M. Epstein, and K. K. Mandadapu, Phys. Rev. Lett. **122**, 178001 (2021).

[6.60] K. Yasuda, K. Ishimoto, L.-S. Lin, A. Kobayashi, Y. Hosaka, and S. Komura, in preparation.

Chapter 7

Concluding Remarks

7.1 Summary of the thesis

In recent years, to better understand the nonequilibrium complex phenomena observed in living systems, modelings of biological nanomachines have been conducted extensively. Experimental results demonstrate that biological nanomachines or enzymes give rise to nonequilibrium transport phenomena such as diffusion enhancement, chemotaxis, and substantial change in rheological properties. Although several theories have been proposed to treat these phenomena, there has been no unifying theory that quantitatively accounts for the observed results. Moreover, equilibrium concepts do not hold in living systems and hence further developments in universal physical properties that characterize the systems are needed.

In Chap. 1, we have reviewed the general background on biological nanomachines and relevant nonequilibrium phenomena in living systems that include active transport in living cells, the rheology of the cytoplasm, and emergent macroscopic behavior in active chiral systems. We then have provided a review of several models of enzymatic molecules and the concept of nonreciprocity that has attracted much attention recently. In the last part of the chapter, experimental and theoretical findings related to the peculiar transport coefficient

called odd viscosity have been illustrated.

In Chap. 2, we have discussed statistical properties of a single biological nanomachine by using the active force dipole model. A dipole, consisting of two domains connected with an elastic spring of its constant k_0 and natural length ℓ_0, exhibits the conformational dynamics, where the enzyme-substrate complex is characterized by the elastic spring of the constant k_1 and natural length ℓ_1. First, we analytically calculated the force dipole magnitude m by considering the four regimes that are determined by the competition between the thermal energy $k_{\rm B}T$ and the elastic energies, $k_0\ell_0^2$ and $k_1\ell_1^2$. Then, we performed numerical simulations of the Langevin equation where there is no explicit hydrodynamics and the solvent effects are considered through the viscous friction and thermal noise terms. The statistical data reveal that equilibrium and nonequilibrium properties of an active force dipole can be characterized by exponentially and oscillatory decaying correlation functions, respectively. To our knowledge, the present work is the first study where hydrodynamic force dipoles of mechanochemical enzymes have been systematically analyzed and order-of-magnitude estimates for the intensity of such dipoles for characteristic enzymes have been obtained.

In Chap. 3, we have considered force dipoles immersed in a solvent of viscosity $\eta_{\rm s}$ and discussed the effective shear viscosity of an enzymatic solution $\eta_{\rm e}$. Employing the Boltzmann distribution weighted by the waiting times of enzymatic species in each catalytic cycle, we have obtained $\eta_{\rm e}$ as a function of substrate concentration and its physical properties. As a result of the competition between the energy difference of the enzyme two internal states and the substrate concentration, we have shown that the enzyme solution viscosity exhibits a nonmonotonic behavior that depends on the physical properties of the binding substrates. We emphasize that this work sheds light on the influence of biological nanomachines on the rheological properties of suspending fluids.

In Chap. 4, we have discussed the hydrodynamic collective effects due to

active force dipoles that are immersed in lipid bilayer membranes. Specifically, the obtained diffusion coefficients D_{A} and drift velocities V of a passive particle were obtained in the enzyme solution for free and confined membrane geometries. Since the model accounts for the bulk solvent, the hydrodynamic screening lengths ν^{-1} and κ^{-1} enter in the results and give rise to the rich dependencies of D_{A} and V on the probe size. Due to the interplay between the thermal and non-thermal contributions to the diffusive dynamics, we have shown that the three different scaling regimes of the total diffusion coefficient are expected with the increasing particle size, i.e., $\ln(\ell_{\mathrm{c}}) \to 1/\ell_{\mathrm{c}}^2 \to 1/\ell_{\mathrm{c}}$ for the free membrane case and $\ln(\ell_{\mathrm{c}}) \to 1/\ell_{\mathrm{c}}^4 \to 1/\ell_{\mathrm{c}}^2$ for the confined membrane case. These behaviors of the diffusion coefficient would be observed in active membranes by tuning the size of a probe particle with microrheology techniques.

In Chap. 5, we have discussed the hydrodynamic response of a point force and a finite-size object in a 2D compressible fluid with odd viscosity. The viscosity coefficient reflects that the time-reversal and parity symmetries are broken in aqueous environments. Taking into account the hydrodynamic coupling to the underlying bulk fluid, we have obtained the odd viscosity-dependent mobility tensor G_{ij}, which is responsible for the nonreciprocal hydrodynamic response to a point force, i.e., $G_{ij} \neq G_{ji}$. Furthermore, we have extended the point-force response to a finize-size disk response, which moves laterally in the fluid and demonstrated that the resistance tensor Γ_{ij} exhibits the nonreciprocal relation, $\Gamma_{ij} \neq \Gamma_{ji}$. This nonreciprocity leads to a lift force on the disk in addition to the drag one and would be observed in biological monolayers with active constituents such as rotary motor proteins.

Finally in Chap. 6, we have discussed hydrodynamic forces acting on a 2D liquid domain that moves laterally within an incompressible fluid membrane in the presence of odd viscosity. Since active rotating proteins can accumulate inside the domain, we have focused on the difference in odd viscosity between the inside (η_{o}') and outside (η_{o}) of the domain. Taking into account the momentum

leakage from a 2D fluid to the underlying substrate, we have calculated the fluid flow induced by the lateral domain motion, and derived the domain resistance tensor that turned out to be nonreciprocal, i.e., $\Gamma_{ij} \neq \Gamma_{ji}$ only when $\eta_{\rm o} \neq \eta'_{\rm o}$. As before, the nonreciprocal relation leads to a lift force on the domain. Our results have shown that odd viscosity would be observed in biological membranes in which rotating proteins are heterogeneously distributed, which is in sharp contrast to the case of compressible fluids studied in Chap. 5.

7.2 Future prospects

For future work, the active force dipole model can be extended to active rotating proteins that exert torque along their axes rather than force dipoles. Such a theory can serve as a base to study the parity-breaking effects on the nonequilibrium transport phenomena such as diffusion enhancement (see Chaps. 2-4) and chemotaxis (see Chap. 4). It will be also useful to investigate how these physical quantities are modified due to the concentration of biological nanomachines. A possible approach is to consider stresses that are exerted by rigid particles on surrounding fluids (see, e.g., Ref. [7.1]).

Furthermore, it is possible to consider active force dipoles to model cytoplasmic streaming that is directional flows observed mainly in plant cells and plays roles in their growth [7.2]. By introducing force dipoles in the vicinity of a cellular membrane and taking into account hydrodynamic flows induced by the dipoles, one can obtain the macroscopic flow, which can be compared with cytoplasmic streaming. In addition, the flow may exhibit unidirectional flows that would depend on the order parameter defined by the average direction of the dipoles. These edge currents have been observed in an odd-viscous fluid (see Chaps. 5 and 6) and the odd transport coefficient is expected to play an important role in the model.

In addition, it is possible to consider the bulk solvent effect on the resistance tensor of a disk in a compressible fluid with odd viscosity. In Chap. 5, the

obtained drag and lift forces are valid in the limit of $\kappa R \ll 1$ as we have ignored the body force densities in the Lorentz reciprocal theorem. To obtain the expressions for $\kappa R \gg 1$, one has to consider other approaches, e.g., numerical simulations of the boundary integral equations [7.3] or the full derivation of the solutions of the hydrodynamic equations for a 2D chiral fluid [7.4].

More generally, it can be useful to reveal the existence of odd viscosity in microscopic approaches. Numerically, active chiral systems with rotating constituents have been investigated in light of phase separation dynamics [7.5] and an inertial lift force [7.6]. However, there have been less studies that aim at extracting the odd transport coefficient in such systems. On the other hand, collective behavior of enzymes in active chiral media deserve attention as well. In the presence of thermal noise, one has to consider the generalization of the fluctuation-dissipation theorem as well as the Langevin equation with multiplicative noise when the friction coefficient depends on the position [7.7]. These interesting questions are left for future investigations.

References

[7.1] N. Oppenheimer and H. Diamant, Biophys. J. **96**, 3041 (2009).

[7.2] R. E. Goldstein and J.-W. van de Meent, Interface Focus **5**, 20150030 (2015).

[7.3] C. Pozrikidis, *Boundary Integral and Singularity Methods for Linearized Viscous Flow* (Cambridge University Press, New York, 1992).

[7.4] H. Hayakawa, Phys. Rev. E **61**, 5477 (2000).

[7.5] N. H. Nguyen, D. Klotsa, M. Engel, and S. C. Glotzer, Phys. Rev. Lett. **112**, 075701 (2014).

[7.6] Y. Goto and H. Tanaka, Nat. Commun. **6**, 1 (2015).

[7.7] A. W. Lau and T. C. Lubensky, Phys. Rev. E **76**, 011123 (2007).